UNIVERSITÀ DEGLI STUDI DI MILANO
Facoltà di Scienze Matematiche, Fisiche e Naturali
Scuola di Dottorato "Terra, Ambiente e Biodiversità"
Dottorato di Ricerca in Scienze della Terra - Ciclo XXIV

MODELLING THE EARTH:
COMPRESSIBLE VISCOELASTODYNAMICS, GRAVITATIONAL SEISMOLOGY AND TRUE POLAR WANDER

Tesi di Dottorato di Ricerca di

GABRIELE CAMBIOTTI
Matricola R08031

Tutor	**Anno Accademico**	Coordinatore
Prof. Roberto Sabadini	**2011 / 2012**	**Prof. Elisabetta Erba**

to my beloved country
my family
and friends

Contents

Abstract

This thesis reviews and sheds new light on compressible Earth models and theories for the modelling of megathrust earthquakes and rotational instabilities caused by glacial isostatic adjustments and mantle convection. The basic theory is outlined in the first chapter, where we discuss the response of a self-gravitating Earth to external forces and loads seated at its surface or interior and we focus on elastic static perturbations and the transition between the elastic and fluid behaviours of the Earth that occurs on thousand and million years time scales.

In the first part of this thesis, we derive the analytical solution of the momentum and Poisson equations for a spherically symmetric viscoelastic Earth model that accounts for compressibility both at the initial state of hydrostatic equilibrium and during the perturbations. This constitutes a step ahead with respect to all previous analytical solutions, which actually neglect compressibility in some aspects, and allows to gain deep insight into the relaxation spectrum of compressible viscoelastic Earth models.

In the second part, we discuss long-wavelength gravity anomalies caused by the 2004 Sumatra earthquake and detected by the Gravity Recovery And Climate Experiment (GRACE) space mission. We extend the classic theory in order to interpret gravity anomalies in terms of volume changes within the solid Earth, advection of the initial density field and ocean water redistribution caused by perturbations of the ocean floor and surface topographies. This physics is then exploited in order to develop a novel procedure for the inversion of the principal seismic source parameters (hypocentre and moment tensor) of large earthquakes relying solely on space gravity data. This procedure, which complements traditional seismology and which we shall name Gravitational Centroid Moment Tensor (GCMT) analysis, is applied for the first time to the 2011 Tohoku earthquake.

In the third part of the thesis, we discuss issues related to long time scale instabilities of the Earth's rotation. The slow motion of the rotation axis with respect to the mantle, called True Polar Wander (TPW), has continuously been debated after the pioneering works i the sixties by Munk, MacDonald and Gold. We thus discuss TPW due to variations of surface loading from ice ages on hundreds of thousand year time scales, its sensitivity to the elastic or viscoelastic rheologies of the lithosphere and the stabilizing role of mantle density heterogeneities. Also, we face the problem of TPW driven by mantle convection on the million years time scale. Most studies have assumed that on this long time scale the planet readjusts without delay and that the Earth's rotation axis and the maximum inertia direction of mantle convection coincide. We herein overcome this approximation and we provide a novel treatment of the Earth's rotation, which clearly explains the interaction between mantle convection and rotational bulge readjustments, and the physical laws for the characteristic times controlling the polar motion in the directions of the intermediate and minimum principal axes of the mantle convection inertia tensor. We thus clarify a fundamental issue related to mantle mass heterogeneities and TPW dynamics.

Chapter 1

Self–gravitating compressible Maxwell Earth models

The following mathematical model describes the response of a self–gravitating Earth to external forces and loads seated at its surface or interior. We focus on elastic static perturbations and the transition between the elastic and fluid behaviours of the Earth that occurs on thousand and million year timescales. We assume that the undeformed Earth is in non-rotating hydrostatic equilibrium and spherically symmetric. Rotation will be discussed as an external force: the centrifugal force in the rotating reference frame of Earth. We also assume that the rheological laws are linear and that the strain are infinitesimal.

1.1 Momentum and Poisson equations

For long time scale processes the inertial forces vanish and the conservation of linear momentum requires that the body force $\mathbf{F}$ per unit volume acting on the infinitesimal element of the continuum body are balanced by the stress acting on the surface of the element. At any instant of time t, we thus have for the Cauchy stress tensor $\boldsymbol{\sigma}$ acting on the infinitesimal element

$$\boldsymbol{\nabla} \cdot \boldsymbol{\sigma} + \mathbf{F} = \mathbf{0} \tag{1.1}$$

The body force $\mathbf{F}$ accounts for gravitation due to the Earth, internal and surface loads, and external bodies responsible for tidal forces. It also accounts for all kinds of other contributions like centrifugal and seismic forces. We decompose the body force $\mathbf{F}$ into a non-conservative force $\mathbf{M}$ (i.e., seismic forces) and a conservative force that we express in terms of the gradient of the potential ϕ

$$\mathbf{F} = \mathbf{M} - \left(\rho + \rho^L\right) \boldsymbol{\nabla}\phi \tag{1.2}$$

where ρ and ρ^L are the densities of the Earth and loads, and the potential ϕ consists of the gravitational, tidal, and centrifugal potentials

$$\phi = \phi^G + \phi^T + \phi^C \tag{1.3}$$

The gravitational potential ϕ^G is due to the density of the Earth ρ and loads ρ^L, while the tidal potential is due to the density of external bodies ρ^T. They satisfy the following Poisson equations

$$\nabla^2 \phi^G = 4\,\pi\,G\,\left(\rho + \rho^L\right) \tag{1.4}$$

$$\nabla^2 \phi^T = 4\,\pi\,G\,\rho^T \tag{1.5}$$

where G is the universal gravitational constant. Note that the density ρ^T does not enter the momentum equation (1.1) via eq. (1.2) because, by definition, external bodies do not load the Earth, i.e., the balance of forces acting on external bodies does not involve surface forces from the Earth. The centrifugal potential ϕ^C due to the Earth's rotation is defined by

$$\phi^C = \frac{1}{2}\,\left[(\boldsymbol{\omega}\cdot\boldsymbol{r})^2 - \omega^2\,r^2\right] \tag{1.6}$$

where $\boldsymbol{\omega}$ and $\boldsymbol{r}$ are the angular velocity of the Earth and the position vector, and $\omega = |\boldsymbol{\omega}|$ and $r = |\boldsymbol{r}|$ are the rotation rate and the radial distance from the Earth centre.

The potential ϕ thus solve the Poisson equation

$$\nabla^2 \phi = 4\,\pi\,G\,\left(\rho + \rho^L + \rho^T\right) - 2\,\omega^2 \tag{1.7}$$

where the latter term in the right-hand side (RHS) results from the Laplacian of the centrifugal potential.

Within the Lagrangian approach, we describe the deformed Earth in terms of displacements of the particles of the continuum body

$$\boldsymbol{r} = \boldsymbol{x} + \boldsymbol{u}(\boldsymbol{x}, t) \tag{1.8}$$

where t is the time, and $\boldsymbol{x}$ and $\boldsymbol{r}$ denote the initial and current positions of the particle

subjected to the displacement $\boldsymbol{u}$. Following the work of Wolf (1991), we then introduce the decomposition of scalar, vector and tensor fields into initial fields, (i.e., the fields at the initial time) and local and material incremental fields

$$f(\boldsymbol{r},t) = f_0(\boldsymbol{r}) + f^{\Delta}(\boldsymbol{r},t) \tag{1.9}$$

$$f(\boldsymbol{r},t) = f_0(\boldsymbol{x}) + f^{\delta}(\boldsymbol{x},t) \tag{1.10}$$

where f stands for the generic field. The initial field f_0 (denoted with the subscript 0) describes the initial state of the undeformed Earth. The local incremental field f^{Δ} (denoted with the superscript Δ) is the increment of the field at point $\boldsymbol{r}$ with respect to the initial field at the same position $\boldsymbol{r}$. The material incremental field f^{δ} (denoted with the superscript δ) is the increment of the field at point $\boldsymbol{r}$ with respect to the initial field at point $\boldsymbol{x}$, which is the initial position of the particle that is currently located at $\boldsymbol{r}$, eq. (1.8).

Local and material incremental fields only differ for the so called advective incremental field, which is the difference between the initial field evaluated at the current and initial positions of the particle. Particularly, within the assumption of infinitesimal deformations, this difference is a first–order term that cannot be neglected

$$f^{\delta} = f^{\Delta} + \boldsymbol{u} \cdot \boldsymbol{\nabla} f_0 \tag{1.11}$$

This relation holds both in Lagrangian and Eulerian formulations, i.e., when the incremental fields are functions of the initial and current positions of the particle, because differences for incremental fields are of the second order and may be ignored.

Because the undeformed Earth is in non-rotating hydrostatic equilibrium, the initial potential ϕ_0 is the gravitational potential due to the initial density ρ_0, i.e., the density of the undeformed Earth, and satisfies the Poisson equation

$$\nabla^2 \phi_0 = 4\,\pi\,G\,\rho_0 \tag{1.12}$$

Also, the initial Cauchy stress tensor $\boldsymbol{\sigma}_0$ is the initial hydrostatic stress

$$\boldsymbol{\sigma}_0 = -p_0\,\mathbf{1} \tag{1.13}$$

where $\mathbf{1}$ and p_0 are the identity matrix and the initial hydrostatic pressure, entering with the minus sign according to the convention that stress are positive when they act in the same direction as the outward normal to the surface. From the momentum equation at the initial time, we thus find the condition of non-rotating hydrostatic equilibrium

$$-\boldsymbol{\nabla} p_0 - \rho_0\,\boldsymbol{\nabla}\phi_0 = \mathbf{0} \tag{1.14}$$

In the following, we describe perturbations of the Cauchy stress tensor $\boldsymbol{\sigma}$ in terms of material increment

$$\boldsymbol{\sigma}(\boldsymbol{r},t) = -p_0(\boldsymbol{x})\,\mathbf{1} + \boldsymbol{\sigma}^{\delta}(\boldsymbol{x},t) \tag{1.15}$$

for which the constitutive equations of elastic and viscoelastic materials are expressed as functions of strain and strain rate. Differently, the natural choice for perturbations of the potential ϕ and the density ρ are the local increments

$$\phi(\boldsymbol{r},t) = \phi_0(\boldsymbol{r}) + \phi^{\Delta}(\boldsymbol{r},t) \tag{1.16}$$

$$\rho(\boldsymbol{r},t) = \rho_0(\boldsymbol{r}) + \rho^{\Delta}(\boldsymbol{r},t) \tag{1.17}$$

for which, after substitution of eqs (1.2) and (1.15)–(1.17) into eqs (1.1) and (1.7), the momentum and Poisson equations keep the following simpler forms

$$\boldsymbol{\nabla}\cdot\boldsymbol{\sigma}^{\delta} + \boldsymbol{\nabla}\left(\boldsymbol{u}\cdot\boldsymbol{\nabla} p_0\right) - \rho_0\,\boldsymbol{\nabla}\phi^{\Delta} - \rho^{\Delta}\,\boldsymbol{\nabla}\phi_0 - \rho^{L}\,\boldsymbol{\nabla}\phi_0 + \mathbf{M} = \mathbf{0} \tag{1.18}$$

$$\nabla^2\phi = 4\,\pi\,G\,\left(\rho^{\Delta} + \rho^{L} + \rho^{T}\right) - 2\,\omega^2 \tag{1.19}$$

The first term in eq. (1.18) describes the contribution from the material incremental stress and the second term the advection of the initial hydrostatic stress which results from eq. (1.14) and

$$-\boldsymbol{\nabla} p_0(\boldsymbol{x}) - \rho_0(\boldsymbol{r})\,\boldsymbol{\nabla}\phi_0(\boldsymbol{r}) = \boldsymbol{\nabla}\left(\boldsymbol{u}(\boldsymbol{x},t)\cdot\boldsymbol{\nabla} p_0(\boldsymbol{x},t)\right) \tag{1.20}$$

Furthermore, the third term describes gravity perturbations (i.e., self–gravitation) and tidal and centrifugal forces, the fourth term buoyancy forces due to density changes (i.e., compressibility), and the fifth and sixth terms account for the weight of loads and non-conservative forces.

For self–gravitating Earth models, the local incremental potential ϕ^{Δ} must be obtained self–consistently with the local incremental density ρ^{Δ}. This couples the momentum and Poisson equations, eqs (1.18)–(1.19), via the continuity equation of mass written as

$$\rho^{\Delta} = -\boldsymbol{\nabla}\cdot(\rho_0\,\boldsymbol{u}) = -\rho_0\,\Delta - \boldsymbol{u}\cdot\boldsymbol{\nabla}\rho_0 \tag{1.21}$$

Here, the first term of the RHS describes the density perturbation due to the volume variation Δ of the particle

$$\Delta = \boldsymbol{\nabla}\cdot\boldsymbol{u} \tag{1.22}$$

and the second term the advection of the initial density field. In this respect, the first term of the RHS of eq. (1.21) is the material incremental density ρ^{δ}

$$\rho^{\delta} = -\rho_0\,\Delta \tag{1.23}$$

1.1.1 The linear Maxwell solid

The equations above need to be supplemented by the constitutive equation describing how material incremental stress and strain (or strain rate) are related to each other. Within the first–order perturbation theory, the strain tensor $\boldsymbol{\epsilon}$ is defined by

$$\boldsymbol{\epsilon} = \frac{1}{2}\left[\boldsymbol{\nabla} \otimes \boldsymbol{u} + \boldsymbol{u} \otimes \boldsymbol{\nabla}\right] \tag{1.24}$$

where $\otimes$ stands for the algebraic product. This representation bases on the dyadic formulation, which we discuss in Appendix A.2. This allows the definition of stress and strain without choosing a specif coordinate system, and to obtain general expressions for the gradient and curl of vectors and the divergence of tensors that hold in any coordinate system. This makes easier the study of the momentum equation.

In the following, we will assume linear and isotropic constitutive equations and we focus on the viscoelastic rheology. We also assume that perturbations are isentropic and isochemical because viscoelastic relaxation processes of the Earth occur on time scales much smaller than those of heat diffusion and changes in the chemical composition of the rock. Particularly, we consider the viscoelastic Maxwell rheology defined by the following constitutive equation

$$\boldsymbol{\sigma}^{\delta} = \kappa\, \Delta\, \mathbf{1} + 2\, q \star \partial_t \boldsymbol{\epsilon}_D \tag{1.25}$$

where ∂_t and $\star$ stand for the partial derivative with respect to time t and the time convolution

$$\left(q \star \partial_t \boldsymbol{\epsilon}_D\right)(t) = \int_0^t q(t-t')\, \partial_{t'} \boldsymbol{\epsilon}_D(t')\, dt' \tag{1.26}$$

and κ, q and $\boldsymbol{\epsilon}_D$ are the adiabatic bulk modulus, the shear relaxation function and the deviatoric strain tensor

$$\boldsymbol{\epsilon}_D = \boldsymbol{\epsilon} - \frac{\Delta}{3}\mathbf{1} \tag{1.27}$$

For the Maxwell solid, the shear relaxation function takes the following form

$$q(t) = \begin{cases} \mu \, \exp\left(-\frac{t}{\tau}\right) & t \geq 0 \\ 0 & t < 0 \end{cases} \tag{1.28}$$

where τ is the Maxwell time defined by the ratio of the viscosity ν over the shear modulus μ

$$\tau = \frac{\nu}{\mu} \tag{1.29}$$

By means of the Maxwell rheology, we describe the transition from the elastic to the Newtonian fluid behaviours of the Earth that occurs on the timescale given by the Maxwell time τ. Despite the constitutive equations of both elastic and Newtonian fluid bodies relating stress at a given time to only strain and strain rate at that time, the Maxwell rheology relates the viscoelastic stress at a given time to the whole strain rate history before that time, as pointed out by the time convolution between the shear relaxation function and the deviatoric strain rate in eq. (1.25).

Note that, instead, the Maxwell solid does not account for bulk relaxation and the adiabatic bulk modulus κ is defined from the partial derivative of the density state function ρ with respect to pressure p, at fixed entropy s and chemical composition c,

$$\left.\frac{\partial \rho}{\partial p}\right|_{s,c} = \frac{\rho}{\kappa} \tag{1.30}$$

In this respect, the adiabatic bulk modulus relates the material incremental density ρ^δ and pressure p^δ, and the first term in the RHS of eq. (1.25) describes the isotropic stress due to the material incremental pressure

$$p^\delta = -\kappa \, \Delta \tag{1.31}$$

By definition, there are no volume changes Δ within incompressible materials. However, incompressible materials must be able to react to isotropic stresses. From eq.

(1.31), we thus require that the bulk modulus κ is infinitely large in order that the incremental pressure p^δ remains finite in the limit of Δ going to zero and of κ going to infinity (Love, 1911, section 154)

$$p^\delta = \lim_{\Delta \to 0 \, \kappa \to \infty} (-\kappa \, \Delta) \tag{1.32}$$

In this respect, the bulk modulus is sometimes called modulus of incompressibility. On the contrary, compressible materials are characterized by a finite bulk modulus.

1.1.2 The Correspondence Principle

The Laplace transform of a function $f(t)$ is formally defined by

$$\mathcal{L}[f] = \int_0^\infty f(t) e^{-st} dt, \tag{1.33}$$

with $\mathcal{L}$, t and s beint the Laplace transform operator, time and Laplace variable (which has dimension of inverse time). Introducing $\tilde{f}(s) = \mathcal{L}[f]$ for brevity, it is straightforward to show that the Laplace transform of the time derivative of the function $f(t)$ yields

$$\mathcal{L}[\partial_t f] = s \, \tilde{f}(s) - f(0) \tag{1.34}$$

and that the Laplace transform of the time convolution of two functions $f(t)$ and $h(t)$ yields the product of the Laplace transforms $\tilde{f}(s)$ and $\tilde{h}(s)$

$$\mathcal{L}[f \star h] = \tilde{f}(s) \, \tilde{h}(s) \tag{1.35}$$

with $\star$ denoting the time convolution operator.

In the following we will consider external forcings and loading that act on the Earth starting immediately after the initial time, at $t = 0^+$, and we restrict our attention on right-handed functions that differs from zero only for $t > 0$

$$f_+(t) = f(t)\, H(t - 0^+) \tag{1.36}$$

Here $H(t)$ is the Heaviside function. It is a discontinuous function, whose value is zero for negative arguments and one for positive arguments, and its derivative yields the Dirac delta function $\delta(t)$

$$\partial_t H(t) = \delta(t) \tag{1.37}$$

The Laplace transform of the right-handed function $f_+(t)$ is the same of the original function $f(t)$

$$\tilde{f}_+(s) = \tilde{f}(s) \tag{1.38}$$

while its Laplace transform yields

$$\mathcal{L}[\partial_t f_+(t)] = s\, \tilde{f}(s) \tag{1.39}$$

because the second term of the RHS of eq. (1.34) disappears due to the step-like discontinuity of $f_+(t)$ at $t = 0^+$. From now on, we intend time-dependent functions describing forcings and perturbations as right-handed functions, even though the subscript $+$ will be omitted in order not to overwhelm the text.

By making use of eq. (1.39), the Laplace transform of the constitutive equation for the Maxwell solid, eq. (1.25), yields

$$\tilde{\boldsymbol{\sigma}}^{\delta}(s) = \kappa\, \tilde{\Delta}(s)\, \mathbf{1} + 2\, \hat{\mu}(s)\, \tilde{\boldsymbol{\epsilon}}_D(s) \tag{1.40}$$

with $\hat{\mu}(s)$ being the following function of the Laplace variable s

$$\hat{\mu}(s) = \frac{\mu\, s}{s + \frac{1}{\tau}} \tag{1.41}$$

Note that eq. (1.40) has the same form of the Hooke's law for linear elastic solids

$$\boldsymbol{\sigma}^{\delta} = \kappa\,\Delta\,\mathbf{1} + 2\,\mu\,\boldsymbol{\epsilon}_D \tag{1.42}$$

where $\hat{\mu}(s)$ and the Laplace transforms of the fields are replaced by the shear modulus μ and the same fields in the time domain. So we can derive equations for viscoelastic bodies in the Laplace domain with formulas for elastic bodies. Particularly, after Laplace transformation, the momentum and Poisson equations for the the viscoelastic body are formally equivalent to those for the elastic solid. We thus solve the equivalent elastic problem in the Laplace domain and, only at the last stage, we will perform the inverse Laplace transform of the solution to obtain the viscoelastic solution in the time domain. In this respect, we will also refer to the viscoelastic solution in the Laplace domain as the associated elastic solution.

The so-called Correspondence Principle (Peltier, 1975; Wu and Peltier, 1982) states that the time dependent viscoelastic solution of the momentum and Poisson equations can by found in a unique way after the inverse Laplace transformation of the associated elastic solution. In the light of this analogy between the elastic and viscoelastic problems, afterwards we will omit the tilde to denote Laplace transforms and we do not distinguish between the shear modulus μ and the function $\hat{\mu}(s)$, eq. (1.41). In this respect, the following results can be seen both as the solution of the elastic static problem and the associated elastic solution.

1.2 Spherical harmonic expansion

In the following we will consider spherically symmetric Earth models composed of several concentric layers as the core, the lower and upper mantle and the lithosphere. Within each layer the material parameters, consisting of the initial density ρ_0, the bulk modulus κ, the shear modulus μ and the viscosity ν, are continuous functions of the only radial distance from the Earth centre r. At the internal boundaries separating two layers of the Earth, these parameters may have step-like discontinuities due to the specific chemical compositions and phases of the rock of each layer.

The most widely used spherically symmetric Earth model is the Preliminary Refer-

ence Earth Model (PREM, Dziewonski and Anderson, 1981) that specifies the material parameters of the main layers of the Earth in terms of polynomials of the radial distance from the Earth centre r. It thus accounts for the continuous variations of the material parameters and discontinuities at the interfaces between the layers. As it concerns the rheology, we will consider models with a fluid core, a viscoelastic mantle, with viscosity of about 10^{21} Pa s, and an elastic or viscoelastic (but more viscous than the mantle) lithosphere of about 100 km.

The spherical symmetry of the Earth model is herein exploited to further simplify the incremental momentum and Poisson equations and discuss fundamental aspects of the style of deformation. We thus consider the spherical reference frame and we denote with r, θ and φ the radial distance from the Earth centre, the colatitude and the longitude, and with $\boldsymbol{e}_r$, $\boldsymbol{e}_\theta$ and $\boldsymbol{e}_\varphi$ the respective unit vectors (see Appendix A.1).

In view of the spherical symmetry, the initial density, potential and pressure only depend on the radial distance from the Earth centre r and their gradients have no angular components

$$\boldsymbol{\nabla}\rho_0 = \partial_r\rho_0\,\boldsymbol{e}_r \tag{1.43}$$

$$-\boldsymbol{\nabla}p_0 = \rho_0\,\boldsymbol{\nabla}\phi_0 = \rho_0\,g\,\boldsymbol{e}_r \tag{1.44}$$

where g is the initial gravity acceleration

$$g(r) = \frac{4\,\pi\,G}{r^2}\int_0^r \rho_0(x)\,x^2\,dx \tag{1.45}$$

The incremental momentum and Poisson equations (1.18)–(1.19) thus become

$$\boldsymbol{\nabla}\cdot\boldsymbol{\sigma}^\delta + \boldsymbol{\nabla}\left(\rho_0\,g\,\boldsymbol{u}\cdot\boldsymbol{e}_r\right) - \rho_0\,\boldsymbol{\nabla}\phi^\Delta - \rho^\Delta\,g\,\boldsymbol{e}_r - \rho^L\,g\,\boldsymbol{e}_r + \mathbf{M} = \mathbf{0} \tag{1.46}$$

$$\nabla^2\phi = -4\,\pi\,G\,\left(\rho_0\,\Delta + \partial_r\rho_0\,\boldsymbol{u}\cdot\boldsymbol{e}_r\right) + 4\,\pi\,G\,\left(\rho^L + \rho^T\right) - 2\,\omega^2 \tag{1.47}$$

We also introduce the spherical harmonic expansions of the potential ϕ and the decomposition of the displacement $\boldsymbol{u}$ into spheroidal, $\boldsymbol{u}_S$, and toroidal, $\boldsymbol{u}_T$, displacements

$$\phi^{\Delta}(r,\theta,\varphi) = \sum_{\ell=0}^{\infty} \Phi_{\ell m}(r)\, Y_{\ell m}(\theta,\varphi) \tag{1.48}$$

$$\boldsymbol{u} = \boldsymbol{u}_S + \boldsymbol{u}_T \tag{1.49}$$

with

$$\boldsymbol{u}_S(r,\theta,\varphi) = \sum_{\ell=0}^{\infty} \left[U_{\ell m}(r)\, \mathbf{R}_{\ell m}(\theta,\varphi) + V_{\ell m}(r)\, \mathbf{S}_{\ell m}(\theta,\varphi)\right] \tag{1.50}$$

$$\boldsymbol{u}_T(r,\theta,\varphi) = \sum_{\ell=0}^{\infty} W_{\ell m}(r)\, \mathbf{T}_{\ell m}(\theta,\varphi) \tag{1.51}$$

Here, $Y_{\ell m}$ are the spherical harmonics of harmonic degree $\ell = 0, \cdots, \infty$ and order $m = -\ell, \cdots, \ell$, and $\mathbf{R}_{\ell m}$, $\mathbf{S}_{\ell m}$ and $\mathbf{T}_{\ell m}$ are the spherical harmonic vectors defined by

$$\mathbf{R}_{\ell m} = Y_{\ell m}\, \boldsymbol{e}_r \tag{1.52}$$

$$\mathbf{S}_{\ell m} = r\, \boldsymbol{\nabla} Y_{\ell m} = \partial_\theta Y_{\ell m}\, \boldsymbol{e}_\theta + \frac{\partial_\varphi Y_{\ell m}}{\sin\theta}\, \boldsymbol{e}_\varphi \tag{1.53}$$

$$\mathbf{T}_{\ell m} = \boldsymbol{\nabla} \times (\boldsymbol{r}\, Y_{\ell m}) = \frac{\partial_\varphi Y_{\ell m}}{\sin\theta}\, \boldsymbol{e}_\theta - \partial_\theta Y_{\ell m}\, \boldsymbol{e}_\varphi \tag{1.54}$$

with $\boldsymbol{r} = r\, \boldsymbol{e}_r$ being the position vector. Also, the scalars $\Phi_{\ell m}$, $U_{\ell m}$, $V_{\ell m}$ and $W_{\ell m}$ are the respective spherical harmonic coefficients and we will simply refer to them as the potential, the radial and tangential spheroidal displacements, and the toroidal displacement.

Further details about spherical harmonics and spherical harmonics vectors are discussed in Ben–Menahem and Singh (1981). Here we only explicit the definition of

spherical harmonics

$$Y_{\ell m}(\theta, \varphi) = P_{\ell m}(\cos\theta)\, e^{i\, m\, \varphi} \tag{1.55}$$

where $P_{\ell m}$ are the associated Legendre polynomials. The latter, for $m \geq 0$, are given by

$$P_{\ell m}(x) = \frac{1}{2^\ell\, \ell!}\, \left(1 - x^2\right)^{m/2}\, \frac{d^{\ell+m}\left(x^2 - 1\right)^\ell}{dx} \tag{1.56}$$

and, for $m < 0$,

$$P_{\ell m}(x) = (-1)^m\, \frac{(\ell + m)!}{(\ell - m)!}\, P_{\ell -m}(x) \tag{1.57}$$

We also recall that the spherical harmonics are eigenfunctions of the Laplacian operator

$$\nabla^2 Y_{\ell m} = \frac{\ell(\ell+1)}{r^2}\, Y_{\ell m} \tag{1.58}$$

1.2.1 Volume changes and surface forces

After substitution of eqs (1.49)–(1.51) into (1.22), we obtain the spherical harmonic expansions of the volume change Δ

$$\Delta = \boldsymbol{\nabla} \cdot \boldsymbol{u} = \sum_{\ell m} \chi_{\ell m}\, Y_{\ell m} \tag{1.59}$$

where the scalar $\chi_{\ell m}$ is given by

$$\chi_{\ell m} = \partial_r U_{\ell m} + \frac{2}{r}\, U_{\ell m} - \frac{\ell\,(\ell+1)}{r}\, V_{\ell m} \tag{1.60}$$

It is noteworthy that the toroidal displacement does not contribute to volume changes, i.e., $\boldsymbol{\nabla} \cdot \boldsymbol{u}_T = 0$. Furthermore, because the toroidal displacement has no component

along $\boldsymbol{e}_r$, it does not contribute to the advection of the initial density field of the Earth models, which can be only radial for eq. (1.43). This means that the local incremental density is only due to spheroidal deformations

$$\rho^{\Delta} = -\rho_0 \, \boldsymbol{\nabla} \cdot \boldsymbol{u}_S - \partial_r \rho_0 \, \boldsymbol{u}_S \cdot \boldsymbol{e}_r \tag{1.61}$$

and that toroidal deformations do not directly contribute to the local incremental potential ϕ^{Δ}. Actually, as we will show in a while, toroidal deformations are completely decoupled from spheroidal deformations and perturbations of the potential. They can be studied separately.

Let us now consider the spherical harmonic expansion of the material incremental stress $\boldsymbol{\sigma}^{\delta} \cdot \boldsymbol{e}_r$ acting on a surface element with outward normal $\boldsymbol{e}_r$. From the definition of the strain tensor, eq. (1.24), and the Hooke's law, eq. (1.42) or, equivalently, the consitutive equation for the Maxwell solid in the Laplace domain, eq. (1.40), after some straightforward algebra we obtain

$$\boldsymbol{\sigma}^{\delta} \cdot \boldsymbol{e}_r = \lambda \, \Delta \, \boldsymbol{e}_r + \mu \, [\boldsymbol{\nabla} \, (\boldsymbol{u} \cdot \boldsymbol{e}_r) - (\boldsymbol{\nabla} \boldsymbol{e}_r) \cdot \boldsymbol{u} + (\boldsymbol{e}_r \cdot \boldsymbol{\nabla}) \, \boldsymbol{u}] \tag{1.62}$$

where λ is the second Lamé parameters that is expressed in terms of the shear modulus μ (also known as first Lamé parameter) and the bulk modulus κ

$$\lambda = \kappa - \frac{2}{3} \, \mu \tag{1.63}$$

Then, by substituting the spherical harmonic expansions for displacements and volume changes, eqs (1.49)–(1.51) and (1.59), we obtain

$$\boldsymbol{\sigma} \cdot \boldsymbol{e}_r = \sum_{\ell m} \left(R_{\ell m} \, \mathbf{R}_{\ell m} + S_{\ell m} \, \mathbf{S}_{\ell m} + T_{\ell m} \, \mathbf{T}_{\ell m} \right) \tag{1.64}$$

where the spherical harmonic coefficients $R_{\ell m}$, $S_{\ell m}$ and $T_{\ell m}$ are given by

$$R_{\ell m} = \lambda \, \chi_{\ell m} + 2 \, \mu \, \partial_r U_{\ell m} \tag{1.65}$$

$$S_{\ell m} = \mu \left(\partial_r V_{\ell m} + \frac{U_{\ell m} - V_{\ell m}}{r} \right) \tag{1.66}$$

$$T_{\ell m} = \mu \left(\partial_r W_{\ell m} - \frac{W_{\ell m}}{r} \right) \tag{1.67}$$

We will simply refer to $R_{\ell m}$ and $S_{\ell m}$ as the radial and tangential spheroidal stresses, and to $T_{\ell m}$ as the toroidal stress.

1.2.2 Spheroidal and toroidal deformations

The divergence of the material incremental Cauchy stress tensor, assuming the elastic or the viscoelastic rheology, eqs (1.40) and (1.42), and using the definition of the strain tensor, eq. (1.24), can be arranged as follow

$$\boldsymbol{\nabla} \cdot \boldsymbol{\sigma}^{\delta} = \lambda \, \boldsymbol{\nabla} \Delta + \Delta \, \boldsymbol{\nabla} \lambda + \mu \, \left(\nabla^2 \boldsymbol{u} + \boldsymbol{\nabla} \Delta \right) + \boldsymbol{\nabla} \mu \cdot \left(\boldsymbol{\nabla} \otimes \boldsymbol{u} + \boldsymbol{u} \otimes \boldsymbol{\nabla} \right) \tag{1.68}$$

which simplifies into

$$\boldsymbol{\nabla} \cdot \boldsymbol{\sigma}^{\delta} = \lambda \, \boldsymbol{\nabla} \Delta + \partial_r \lambda \, \Delta \, \boldsymbol{e}_r + \mu \, \left(\nabla^2 \boldsymbol{u} + \boldsymbol{\nabla} \Delta \right) + \partial_r \mu \, \left[2 \, \partial_r \boldsymbol{u} + \boldsymbol{e}_r \times \left(\boldsymbol{\nabla} \times \boldsymbol{u} \right) \right] \tag{1.69}$$

owing to the spherical symmetry of the Earth model, i.e., $\boldsymbol{\nabla} \mu = \partial_r \mu \, \boldsymbol{e}_r$ and $\boldsymbol{\nabla} \lambda = \partial_r \mu \, \boldsymbol{e}_r$.

By making use of eq. (1.69) and expanding in spherical harmonics eq. (1.46)–(1.47), we obtain the spherical harmonic coefficients of the radial and tangential spheroidal components of the momentum equation,

$$-\rho_0 \, \partial_r \Phi_{\ell m} - \rho_0 \, \partial_r \left(g \, U_{\ell m} \right) + \rho_0 \, g \, \chi_{\ell m} + \partial_r \left(\lambda \, \chi_{\ell m} + 2 \, \mu \, \partial_r U_{\ell m} \right)$$

$$+\frac{1}{r^2}\,\mu\,\left[4\,r\,\partial_r U_{\ell m} - 4\,U_{\ell m} + \ell(\ell+1)(3\,V_{\ell m} - U_{\ell m} - r\,\partial_r V_{\ell m})\right]$$

$$-\rho^L_{\ell m}\,g + m^R_{\ell m} = 0 \tag{1.70}$$

$$-\rho_0\,\Phi_{\ell m} - \rho_0\,g\,U_{\ell m} + \lambda\,\chi_{\ell m} + r\,\partial_r\left[\mu\,\left(\partial_r V_{\ell m} + \frac{1}{r}U_{\ell m} - \frac{1}{r}\,V_{\ell m}\right)\right]$$

$$\frac{1}{r}\,\mu\,\left[5\,U_{\ell m} + 3\,r\,\partial_r V_{\ell m} - V_{\ell m} - 2\,\ell(\ell+1)\,V_{\ell m}\right] + m^S_{\ell m} = 0 \tag{1.71}$$

the toroidal component,

$$\partial_r\left[\mu\,\left(\partial_r W_{\ell m} - \frac{W_{\ell m}}{r}\right)\right] + \mu\,\left(\frac{3}{r}\,\partial_r W_{\ell m} - \frac{1+\ell(\ell+1)}{r^2}\,W_{\ell m}\right) + m^T_{\ell m} = 0 \tag{1.72}$$

and the Poisson equation

$$\nabla^2_r \Phi_{\ell m} = -4\,\pi\,G\,\left(\rho_0\,\chi_{\ell m} + U_{\ell m}\,\partial_r\rho_0\right) + 4\,\pi\,G\,\left(\rho^L_{\ell m} + \rho^T_{\ell m}\right) \tag{1.73}$$

Here $\rho^L_{\ell m}$, $\rho^T_{\ell m}$, $m^R_{\ell m}$, $m^S_{\ell m}$ and $m^T_{\ell m}$ are the spherical harmonic coefficients of the densities of loads and external bodies, and of the non-conservative forces

$$\rho^L = \sum_{\ell m} \rho^L_{\ell m}\,Y_{\ell m} \tag{1.74}$$

$$\rho^T = \sum_{\ell m} \rho^T_{\ell m}\,Y_{\ell m} \tag{1.75}$$

$$\mathbf{M} = \sum_{\ell m} \left(m^R_{\ell m}\, \mathbf{R}_{\ell m} + m^S_{\ell m}\, \mathbf{S}_{\ell m} + m^T_{\ell m}\, \mathbf{T}_{\ell m} \right) \tag{1.76}$$

and ∇^2_r is the radial part of the Laplacian operator ∇^2

$$\nabla^2_r = \partial^2_r + \frac{2}{r}\,\partial_r - \frac{\ell(\ell+1)}{r^2} \tag{1.77}$$

Furthermore, the spheroidal tangential and toroidal components of the momentum equation have been multiplied by r in order to simplify the following treatment.

Eqs (1.70)–(1.73) only hold for harmonic degree ℓ greater than 0. The case of degree–0 perturbations need a specific treatment that we do not discuss as it has little relevance in the geophysical processes considered in this thesis. Note that the term $-2\,\omega^2$ entering the Poisson equation (1.47) does not enter eq. (1.73) because it only contribute to the degree–0 spherical harmonic coefficient.

The radial and tangential spheroidal components of the momentum equation, eqs (1.70)–(1.71), and the Poisson equation, eq. (1.73), are decoupled from the toroidal component of the momentum equation, eq. (1.72). In this respect, spheroidal and toroidal deformations can be studied separately. Furthermore, it is also noteworthy that spheroidal perturbations are triggered by all kind of forcing that we are considering (loads and tidal, centrifugal and seismic forces), while toroidal deformations are triggered only by seismic forces. This reflects the fact that loading and tidal and centrifugal forcings are axially symmetric. Because we will study earthquakes only as it concerns gravity changes (see Chapter 3 and 4), which are not affected by toroidal deformations, we will omit to further discuss toroidal deformations in this thesis.

The radial and tangential spheroidal components of the momentum equation and the Poisson equation constitute a system of three differential equation of the second order in the unknowns $U_{\ell m}$, $V_{\ell m}$ and $\Phi_{\ell m}$. This differential system must be solved for each harmonic degree, but for $\ell = 0$, and order from the centre to the surface of the Earth where proper boundary conditions uniquely determine the solution. Analytical solutions of these differential equations will be considered in Chapter 2, with some restriction on the material parameter of the Earth model. Here, in order to define proper boundary conditions and compute numerical solutions of the viscoelastic problem for general

spherically symmetric Earth models, we cast these differential equations into the form of six differential equations of the first–order that are suitable for numerical integration in the radial variable r by means of algorithms like the Runge-Kutta method. We thus introduce the spheroidal 6–vector solution $\boldsymbol{y}_{\ell m}$

$$\boldsymbol{y}_{\ell m} = (U_{\ell m},\, V_{\ell m},\, R_{\ell m},\, S_{\ell m},\, \Phi_{\ell m},\, Q_{\ell m})^T \tag{1.78}$$

where the first and second components are the radial and tangential displacements, the third and fourth components the radial and tangential stresses, the fifth component the potential and the sixth component the so called 'potential stress'. The latter is defined by

$$Q_{\ell m} = \partial_r \Phi_{\ell m} + \frac{\ell + 1}{r}\, \Phi_{\ell m} + 4\,\pi\, G\, \rho_0\, U_{\ell m} \tag{1.79}$$

and its meaning will be clarified in section 1.3, when we discuss the boundary conditions at the internal interfaces and the surface of the Earth.

From the radial and tangential spheroidal components of the momentum equation, eqs (1.70)–(1.71), the Poisson equation, eq. (1.73), and the definition of radial, tangential and potential stresses, eqs (1.65)–(1.66) and (1.79), after some straightforward algebra we obtain the following linear differential system for the spheroidal vector solution

$$\frac{d\boldsymbol{y}_{\ell m}(r)}{dr} = \mathbf{A}_\ell(r)\, \boldsymbol{y}_{\ell m}(r) - \boldsymbol{f}_{\ell m}(r) \tag{1.80}$$

where $\mathbf{A}_\ell$ is the 6×6–matrix depending on the material parameters of the Earth model, on the radial distance from the Earth centre r and on the harmonic degree ℓ

$$\mathbf{A}_\ell(r) =$$

$$\begin{pmatrix} -\frac{2\,\lambda}{r\,\beta} & \frac{\ell(\ell+1)\,\lambda}{r\,\beta} & \frac{1}{\beta} & 0 & 0 & 0 \\ -\frac{1}{r} & \frac{1}{r} & 0 & \frac{1}{\mu} & 0 & 0 \\ \frac{4}{r}\left(\frac{3\,\kappa\,\mu}{r\,\beta}-\rho_0\,g\right) & \frac{\ell(\ell+1)}{r}\left(\rho_0\,g-\frac{6\,\kappa\,\mu}{r\,\beta}\right) & -\frac{4\,\mu}{r\,\beta} & \frac{\ell(\ell+1)}{r} & -\frac{\rho_0\,(\ell+1)}{r} & \rho_0 \\ \frac{1}{r}\left(\rho_0\,g-\frac{6\,\mu\,\kappa}{r\,\beta}\right) & \frac{2\,\mu}{r^2}\left[\ell(\ell+1)\left(1+\frac{\lambda}{\beta}\right)-1\right] & -\frac{\lambda}{r\,\beta} & -\frac{3}{r} & \frac{\rho_0}{r} & 0 \\ -4\,\pi\,G\,\rho_0 & 0 & 0 & 0 & -\frac{\ell+1}{r} & 1 \\ -\frac{4\,\pi\,G\,\rho_0\,(\ell+1)}{r} & \frac{4\,\pi\,G\,\rho_0\,\ell(\ell+1)}{r} & 0 & 0 & 0 & \frac{\ell-1}{r} \end{pmatrix} \tag{1.81}$$

with

$$\beta = \lambda + 2\,\mu \tag{1.82}$$

The dishomogeneous term $\boldsymbol{f}$ of the differential system (1.80) accounts for terms related to massive bodies other than the Earth and seismic forces, and is given by

$$\boldsymbol{f}_{\ell m} = \frac{4\,\pi\,r^2}{(2\,\ell+1)}\,\left(\rho^L_{\ell m}\,\boldsymbol{f}^L_\ell + \rho^T_{\ell m}\,\boldsymbol{f}^T_\ell\right) + \boldsymbol{m}_{\ell m} \tag{1.83}$$

with

$$\boldsymbol{f}^L_\ell = \left(0,\,0,\,-\frac{(2\,\ell+1)\,g}{4\,\pi\,r^2},\,0,\,0,\,-\frac{(2\,\ell+1)\,G}{r^2}\right)^T \tag{1.84}$$

$$\boldsymbol{f}^T_\ell = \left(0,\,0,\,0,\,0,\,0,\,-\frac{(2\,\ell+1)\,G}{r^2}\right)^T \tag{1.85}$$

$$\boldsymbol{m}_{\ell m} = \left(0,\,0,\,m^R_{\ell m},\,m^F_{\ell m},\,0,\,0\right)^T \tag{1.86}$$

1.3 Boundary conditions

In order to obtain the solution of the associated elastic problem, the above equations must be solved within each viscoelastic layer of the Earth model and supplemented by proper boundary conditions at the bottom and top interfaces. Each layer is bounded by another viscoelastic layer or by the fluid outer core and the Earth's surface. For each kind of interface we thus need to specify proper boundary conditions.

In the following, we denote the number of layer of the Earth model with N and the radial distance from the Earth centre of the top interface of the j-th layer with r_j. We order the layers in such a way that $r_{j-1} < r_j$ for $j = 2, \cdots N$. Particularly, r_j are interfaces within the viscoelastic mantle for $j = 2, \cdots, N-1$, while r_1 and r_N are the core and Earth radii, also denoted by r_C and a, respectively.

1.3.1 The Earth surface

We begin by considering the Earth surface boundary conditions. We distinguish between massive bodies outside the Earth and loads seated at the Earth surface or its interior. By definition, the density of external bodies ρ^T is zero within a sphere of radius a_T containing the Earth

$$\rho^C(r < a_T) = 0 \tag{1.87}$$

with a_T greater than the Earth radius, $a_T > a$, and the load density ρ^L is zero outside the Earth

$$\rho^L(r > a) = 0 \tag{1.88}$$

Furthermore, we write the load density ρ^L as the sum of the density of internal loads ρ^I and the surface density of loads seated at the Earth surface σ^L

$$\rho^L = \rho^I + \sigma^L \, \delta(r - a) \tag{1.89}$$

where δ is the Dirac delta function.

For internal loading and tidal, centrifugal and seismic forcings, the Earth surface is stress free. For the case of surface loading, instead, the tangential stress $S_{\ell m}$ is still zero while the radial stress $R_{\ell m}$ must compensate the weight of the surface density

$$R_{\ell m}(a^-) = -g(a)\,\sigma^L_{\ell m} \tag{1.90}$$

where $\sigma^L_{\ell m}$ are the spherical harmonic coefficients of the surface density σ^L.

An additional condition can be found for the potential stress $Q_{\ell m}$. By applying the Gauss theorem at the incremental Poisson equation (1.19) within a volume embedded in an infinitesimal pill-box at the Earth surface, we obtain

$$\partial_r \phi^\Delta(a^-) = \partial_r \phi^\Delta(a^+) - 4\,\pi\,G\,\rho_0(a)\,\boldsymbol{u}(a)\cdot\boldsymbol{e}_r - 4\,\pi\,G\,\sigma^L \tag{1.91}$$

where we have assumed that the initial density ρ_0 is zero outside the Earth (i.e., we neglect the atmosphere)

$$\rho_0(r > a) = 0 \tag{1.92}$$

Eq. (1.91) expresses the radial derivative of the potential within the Earth, a^-, in terms of the radial derivative of the potential outside the Earth, a^+, and contributions from perturbations of the Earth's surface topography and surface loading. After spherical harmonic expansion, eq. (1.91) can be arranged as follows

$$Q_{\ell m}(a^-) = \partial_r \Phi^\Delta_{\ell m}(a^+) + \frac{\ell+1}{a}\,\Phi_{\ell m}(a) - 4\,\pi\,G\,\sigma^F_{\ell m} \tag{1.93}$$

where we have used the fact that the potential is continuous across any interface

$$\Phi_{\ell m}(a^+) = \Phi_{\ell m}(a^-) \tag{1.94}$$

The first term in the RHS of eq. (1.93) can be further specified by considering the dependence of the potential on the radial distance from the Earth centre. First, we distinguish between gravitational, tidal and centrifugal potentials as in eq. (1.3). From eqs (1.87)–(1.88), the Poisson equations (1.4)–(1.5) for the gravitational and tidal potentials become Laplace equations outside the Earth and within the sphere of radius a^T containing it, respectively. After spherical harmonic expansion, we thus obtain

$$\nabla_r^2 \Phi_{\ell m}^G = 0 \quad (r > a) \tag{1.95}$$

$$\nabla_r^2 \Phi_{\ell m}^T = 0 \quad (r < a_T) \tag{1.96}$$

where $\Phi_{\ell m}^G$ and $\Phi_{\ell m}^T$ are the spherical harmonic coefficients of the gravitational and tidal potentials, ϕ^G and ϕ^T, respectively. By imposing the regularity conditions at the infinity (in the limit for $r \to \infty$) and the centre of the Earth ($r = 0$), the solutions of the above Laplacian equations read

$$\Phi_{\ell m}^G(r) = \Phi_{\ell m}^G(a) \left(\frac{r}{a}\right)^{-\ell-1} \quad (r > a) \tag{1.97}$$

$$\Phi_{\ell m}^T(r) = \Phi_{\ell m}^T(a) \left(\frac{r}{a}\right)^{\ell} \quad (r < a_T) \tag{1.98}$$

Here $\Phi_{\ell m}^G(a)$ ad $\Phi_{\ell m}^T(a)$ must be intended as constants of integration. The gravitational potential at the Earth surface $\Phi_{\ell m}^G(a)$ will be obtained solving the viscoelastic problem, while the tidal potential $\Phi_{\ell m}^T(a)$ is prescribed by the external bodies for which we are solving the problem

$$\Phi_{\ell m}^T(a) = -\frac{4\,\pi\,G\,a}{2\,\ell+1} \int_{a_T}^{\infty} \rho_{\ell m}^T(r) \left(\frac{a}{r}\right)^{\ell-1} dr \tag{1.99}$$

Furthermore, after expansion in spherical harmonics of eq. (1.6), we obtain for the centrifugal potential ϕ^C

$$\phi^C(r,\theta,\phi) = \Phi^C_{00}(r)\, Y_{00}(\theta,\phi) + \sum_{m=-2}^{2} \Phi^C_{2m}(r)\, Y_{2m}(\theta,\phi) \tag{1.100}$$

where the spherical harmonic coefficients Φ^C_{00} anc Φ^C_{2m} are given by

$$\Phi^C_{00}(r) = -\frac{\omega^2\, r^2}{3} \tag{1.101}$$

$$\Phi^C_{2m}(r) = \frac{\omega^2\, r^2}{3}\, \bar{Y}_{2m}(\theta_C,\varphi_C) \quad (m=-2,\cdots,2) \tag{1.102}$$

while the others are zero, $\Phi^C_{\ell m}=0$ for $\ell = 1,3,\cdots,\infty$. Here, θ_C, φ_C are the colatitude and longitude of the angular velocity $\boldsymbol{\omega}$. Note that the degree–2 spherical harmonics coefficients Φ^T_{2m} and Φ^C_{2m} share the same dependence on r, i.e., r^2. In this respect, the following treatment will be done assuming

$$\Phi^C_{\ell m}(r) = \Phi^C_{\ell m}(a)\, \left(\frac{r}{a}\right)^{\ell} \tag{1.103}$$

that is correct because we do not consider degree–0 perturbations and $\Phi^C_{\ell m}(a)=0$ for $\ell = 1,3,\cdots,\infty$.

By using these results, eq. (1.93) becomes

$$Q_{\ell m}(a^-) = \frac{2\,\ell+1}{a}\, \left(\Phi^T_{\ell m}(a) + \Phi^C_{\ell m}(a)\right) - 4\,\pi\, G\, \sigma^L \tag{1.104}$$

where the terms related to the gravitational potential $\Phi^G_{\ell m}$ in the RHS have cancelled each other using eq. (1.97)

$$\partial_r \Phi^G_{\ell m}(a^+) = -\frac{\ell+1}{a}\, \Phi^G_{\ell m}(a) \tag{1.105}$$

and the radial derivatives of the tidal and centrifugal potentials have been obtained from eqs (1.98) and (1.103)

$$\partial_r \Phi^T_{\ell m}(a^+) = \frac{\ell}{a}\, \Phi^T_{\ell m}(a) \tag{1.106}$$

$$\partial_r \Phi^C_{\ell m}(a^+) = \frac{\ell}{a}\, \Phi^C_{\ell m}(a) \tag{1.107}$$

In summary, for the forcings that we are considering, the tangential stress $S_{\ell m}$ is zero at the Earth surface while the radial, $R_{\ell m}$, and potential, $Q_{\ell m}$, stresses are constrained by eqs (1.90) and (1.104). We collect these findings in the following compact form

$$\mathbf{P}_1\, \boldsymbol{y}(a^-) = \boldsymbol{b} \tag{1.108}$$

where $\mathbf{P}_1$ is the projector for the third, fourth and sixth components of the spheroidal vector solution, and $\boldsymbol{b}$ is the 3–vector

$$\boldsymbol{b} = \frac{4\,\pi\, a^2}{2\,\ell + 1}\, \sigma^L_{\ell m}\, \boldsymbol{b}^L + \left(\Phi^T_{\ell m}(a) + \Phi^C_{\ell m}(a)\right)\, \boldsymbol{b}^T \tag{1.109}$$

with

$$\boldsymbol{b}^L = \begin{pmatrix} -\frac{(2\,\ell+1)\, g(a)}{4\,\pi\, a^2} \\ 0 \\ -\frac{(2\,\ell+1)\, G}{a^2} \end{pmatrix} \tag{1.110}$$

$$\boldsymbol{b}^T = \begin{pmatrix} 0 \\ 0 \\ \frac{2\,\ell+1}{a} \end{pmatrix} \tag{1.111}$$

1.3.2 Chemical boundaries

Between two viscoelastic layers, we assume chemical boundaries where no material crosses the interfaces. Internal interfaces where material does cross, undergoing a phase

change, are instead called phase-change boundaries. Chemical boundaries are adequate for viscoelastic deformation on timescale comparable or smaller than those of age ages, hundreds of thousand years, although some works indicate that the lower-upper mantle interfaces is likely to be partly a chemical and partly a phase-change boundary. However, this possibility is controversial and much of the works about perturbations induced by ice ages neglects it. Phase-change boundary are surely adequate for mantle convection studies if we want obtain the whole mantle circulation. In Chapter 6, we will consider mantle convection as concerns its impact on the rotational stability of Earth. In that case, however, we will use a simple model where compressibility is neglected and the density is constant through the whole mantle. This is a simplified way to obtain the whole mantle circulation without the need of including phase-change boundaries. In this thesis, we thus decided to rely on the chemical boundaries, without further discussion of phase-change boundaries.

At chemical boundaries, there is no cavitation and no slip between two adjacent layers, and the stress components are continuous. By definition, also the potential perturbation is continuous while its radial derivative is discontinuous at interfaces with density contrast. This results applying the Gauss theorem at the incremental Poisson equation (1.19) within a volume embedded in an infinitesimal pill-box at an internal interface

$$\partial_r \phi^{\Delta}(r_j^+) - \partial_r \phi^{\Delta}(r_j^-) = -4\,\pi\, G\, \Delta\rho_j\, \boldsymbol{u}(r_j) \cdot \boldsymbol{e}_r \tag{1.112}$$

where $\Delta\rho_j$ is the density contrast between the two layers (that is positive if the inner layer is denser than the outer layer)

$$\Delta\rho_j = \rho_0(r_j^+) - \rho_0(r_j^-) \tag{1.113}$$

Eq. (1.112) shows that topography perturbations of the internal interfaces affect the local incremental potential in terms of the surface density given by product of the radial displacement and the density contrast. This product describes the local incremental density localized at the internal interfaces. After spherical harmonic expansion, eq. (1.112) can thus be arranged in the continuity condition for the potential stress

$$Q_{\ell m}(r_j^+) = Q_{\ell m}(r_j^-) \tag{1.114}$$

In the light of the above remarks, all the components of the spheroidal vector solution are continuous at chemical boundaries

$$\boldsymbol{y}_{\ell m}(r_j^+) = \boldsymbol{y}_{\ell m}(r_j^-) \tag{1.115}$$

1.3.3 Core-mantle boundary

The conditions at the core-mantle boundary (CMB) have been disputed among geophysicists since the work of Longman (1962, 1963). This controversy focuses on the treatment of the continuity conditions for the radial deformation at the CMB for the case in which the fluid core deviates from the neutral state of equilibirum, i.e., when the core stratification is non-adiabatic and chemically heterogeneous. Indeed, as we are going to show, for such stratifications the solution of the momentum and Poisson equations leads to the conclusion that radial and geoid displacements coincide. This also implies that no isostatic compensation of the mantle bumping into the core would be possible and this is not the case of reality. This problem was named the Longman (1962) paradox. Differently, the Longman (1962) paradox does not subsist if the core is in a neutral state of equilibrium, and the CMB conditions are derived in a straightforward way.

In order to discriminate between the neutral state of equilibrium from departures due to non-adiabatic and chemically heterogeneous stratifications, we consider the density state function ρ as function of the pressure p, entropy s and chemical composition c, and denote with the superscript 0 the respective profiles at the initial state of hydrostatic equilibirum of the Earth model, which only depend on the radial distance from the Earth centre r. By differentiating the density state function with respect to the radial distance from the Earth centre, we obtain the following identity for the initial density gradient

$$\partial_r \rho_0 = -\frac{\rho_0^2\, g}{\kappa} + \gamma \tag{1.116}$$

where we used the definition of the bulk modulus κ and the condition of hydrostatic equilibrium, eqs (1.30) and (1.44), and γ is the compositional coefficient given by

$$\gamma = \left.\frac{\partial\rho}{\partial s}\right|_{p_0,c_0} \partial_r s_0 + \left.\frac{\partial\rho}{\partial c}\right|_{p_0,s_0} \partial_r c_0 \tag{1.117}$$

Eq. (1.116) is named the generalized Williamson–Adams equation (Wolf and Kaufmann, 2000; Cambiotti and Sabadini, 2010). The first term in the RHS shows how compressibility, via the bulk modulus κ, characterizes the initial density profile of the Earth. A finite bulk modulus yields a negative density gradient $\partial_r\rho_0$ and the initial density increases with depth accordingly to compression of the Earth due to its own weight (i.e., self–compression). The second term, the compositional coefficient γ, takes into account the departure from the self–compression due to non-adiabatic and chemically heterogeneous stratifications, i.e., when the gradient of the initial entropy, $\partial_r s_0$, and chemical composition, $\partial_r c_0$, differ from zero. Their contribution does not amount to more than $10-20$ per cent of the actual density gradient of the Earth (Birch, 1952, 1964; Wolf and Kaufmann, 2000) and it occurs likely in the outermost layers of the Earth, like the transition zone and the lithosphere. The core and the lower mantle, instead, deviate marginally from the adiabatic and chemically homogeneous stratification.

Afterwards, we will call compressional stratifications or we will say that a layer of the Earth is in a neutral state of equilibrium if the stratification is adiabatic and chemically homogeneous ($\gamma = 0$). Instead, we will refer to non-adiabatic and chemically heterogeneous stratifications ($\gamma \neq 0$) as compositional stratifications.

We deal with the fluid core as an inviscid body, in which there are no deviatoric stress. The material incremental stress is given by the material incremental hydrostatic stress

$$\boldsymbol{\sigma}^\delta(\boldsymbol{x},t) = -p^\delta\,\mathbf{1} = \kappa\,\Delta\,\mathbf{1} \tag{1.118}$$

and the radial and tangential stresses become

$$R_{\ell m} = \kappa\,\chi_{\ell m} \tag{1.119}$$

$$S_{\ell m} = 0 \tag{1.120}$$

The CMB is a chemical boundary where no material cross. The only difference with respect to the case of solid–solid interfaces, for which all the components of the spheroidal vector solution must be continuous at the interface, consists in the fact that the CMB is a free–slip boundary where the solid mantle can slip over the inviscid core without tangential stress, eq. (1.120). We thus write the spheroidal vector solution at the bottom of the solid mantle as

$$\boldsymbol{y}(r_C^+) = \begin{pmatrix} U_{\ell m}(r_C^-) \\ 0 \\ R_{\ell m}(r_C^-) \\ 0 \\ \Phi_{\ell m}(r_C^-) \\ Q_{\ell m}(r_C^-) \end{pmatrix} + C_2 \begin{pmatrix} 0 \\ 1 \\ 0 \\ 0 \\ 0 \\ 0 \end{pmatrix} \tag{1.121}$$

where the tangential stress is set to zero and we consider the tangential displacement as a constant of integration that we denote with C_2.

The inviscid core can be dealt with either as an elastic body with the shear modulus μ set to zero (Longman, 1963) or as a viscoelastic body in the Laplace domain, with the Laplace variable s set to zero (Wu and Peltier, 1982), since $\hat{\mu}(0) = 0$ from eq. (1.41). We thus obtain the radial and tangential components of the momentum equation for the inviscid body from eqs (1.70)- (1.71) setting $\mu = 0$

$$\frac{\partial_r R_{\ell m}}{\rho_0} - \partial_r (g\, U_{\ell m}) + g\, \chi_{\ell m} - \partial_r \Phi_{\ell m} = 0 \tag{1.122}$$

$$\frac{R_{\ell m}}{\rho_0} - g\, U_{\ell m} - \Phi_{\ell m} = 0 \tag{1.123}$$

Here, we omit the terms related to forcings because we are assuming that they yield zero within the core.

Following the treatment of Longman (1962), we divide both equations by the initial

density ρ_0 and arrange them by subtracting the radial derivative of the second equation to the first equation

$$\frac{\kappa}{\rho_0^2}\left(\partial_r\rho_0 + \frac{\rho_0^2\, g}{\kappa}\right)\chi_{\ell m} = 0 \tag{1.124}$$

Here the quantity within the bracket in the LHS only depends on the material parameter of the Earth model and, after comparison with eq. (1.117), correspons to the compositional coefficient γ. Furthermore, by making use of eqs (1.123)–(1.124) for eliminating the radial displacement and volume changes into the Poisson equation (1.73), the latter becomes a second order differential equation in the only potential $\Phi_{\ell m}$

$$\nabla_r^2\Phi_{\ell m} = 4\,\pi\, G\,\partial_r\rho_0\,\frac{\Phi_{\ell m}}{g} \tag{1.125}$$

The latter differential equation admits only one regular solution at the Earth centre that depends on the harmonic degree ℓ and the density ρ_0 via the ratio between the initial density gradient and gravity, $\partial_r\rho_0/g$. By denoting the regular solution with $\psi_{\ell m}$, such that

$$\lim_{r\to 0} r^{-\ell}\,\psi_\ell(r) = 1 \tag{1.126}$$

we write the potential $\Phi_{\ell m}$ as

$$\Phi_{\ell m}(r) = C_1\,\psi_\ell(r) \tag{1.127}$$

where C_1 is a constant of integration.

Solutions of the radial and tangential components of the momentum equation, eqs (1.122)–(1.123), are perturbed states of hydrostatic equilibrium, where perturbed equipotential, isobaric and equal density surfaces coincide (Chinnery, 1975). For compressional stratifications, eq. (1.124) is identically satisfied for any volume change $\chi_{\ell m}$ because the compositional coefficient is zero, $\gamma = 0$. This means that eqs (1.122)–(1.123) are not linearly independent. We thus restrict our attention only on the tangential component,

eq. (1.123), from which we constrain the radial stress (or the volume change from eq. (1.119)) in terms of the gap between radial displacements and geoid perturbations

$$R_{\ell m} = \rho_0\, g\, \left[U_{\ell m} - \left(-\frac{\Phi_{\ell m}}{g}\right)\right] = \rho_0\, g\, C_3 \tag{1.128}$$

that we consider as a constant of integration, C_3. This allows us to obtain the radial displacement and the potential stress in terms of the constants of integration C_1 and C_3

$$U_{\ell m} = -C_1\, \frac{\psi_\ell}{g} + C_3 \tag{1.129}$$

$$Q_{\ell m} = C_1\, q_\ell + 4\,\pi\, G\, \rho_0\, C_3 \tag{1.130}$$

where q_ℓ is defined by

$$q_\ell = \partial_r \psi_\ell + \frac{\ell+1}{r}\, \psi_\ell - \frac{4\,\pi\, G}{g}\, \psi_\ell \tag{1.131}$$

By making use of eqs (1.127)–(1.130) into the CMB conditions, eq. (1.121), we thus express the spheroidal vector solution at the bottom of the solid mantle as

$$\boldsymbol{y}_{\ell m}(r_C^+) = \mathbf{I}_C\, \mathbf{C} \tag{1.132}$$

where $\mathbf{I}_C$ is the core-mantle boundary (CMB) matrix

$$\mathbf{I}_C = \begin{pmatrix} -\psi_\ell(r_C)/g(r_C) & 0 & 1 \\ 0 & 1 & 0 \\ 0 & 0 & g(r_C)\, \rho_0(r_C^-) \\ 0 & 0 & 0 \\ \psi_\ell(r_C) & 0 & 0 \\ q_\ell(r_C) & 0 & 4\,\pi\, G\, \rho_0(r_C^-) \end{pmatrix} \tag{1.133}$$

and $\mathbf{C}$ is the vector of constants of integration

$$\mathbf{C} = (C_1, C_2, C_3) \tag{1.134}$$

As we will see in section 1.4, these constants of integration must be determined using the boundary condition at the Earth surface for the stress components of the spheroidal vector solution. Once obtained, the perturbed state of the solid mantle is completely determined. Differently, the perturbed state of the core is determined only for some aspects. Indeed, the constants of integrations only determine the potential within the core, and the radial displacement and the radial stress at the CMB. Other information about the core, instead, remain undetermined within the present assumptions. Particularly, below the CMB, we do not know volume changes, displacements and radial stress.

For compositional stratifications ($\gamma \neq 0$) the above boundary conditions must be reconsidered. In this case, eq. (1.124) constrains volume variation χ to be zero

$$\chi_{\ell m} = 0 \tag{1.135}$$

From eq. (1.119), this also constrain the radial stress to zero and, from eq. (1.122), radial displacements and geoid perturbations must coincide

$$U_{\ell m} = -\frac{\Phi_{\ell m}}{g} \tag{1.136}$$

This condition means that all particles located at a given equipotential surface at the initial state of hydrostatic equilibrium (which define a material interface) must displace over the same perturbed equipotential surface (Chinnery, 1975). This constrains to zero the constant of integration C_3 entering the radial stress, eq. (1.128), and one should conclude that isostatic compensation at the CMB is thus impossible for an inviscid core with compositional stratification. This problem was named Longman (1962) paradox and debated in the seventies by many authors, among which Smylie and Mansinha (1971), Pekeris and Accad (1972), and Chinnery (1975).

By considering perturbations of the inviscid core in the frequency ω-domain, Pekeris

and Accad (1972) obtained the static solution as the limit case of the dynamic problem for $\omega \to 0$. They pointed out that static volume variations are indeed zero for compositional stratifications, with the exception for an infinitesimally thin layer just below the CMB where volume variations may occur. Thus, eq. (1.136) does not hold in this thin boundary layer and isostatic compensation of the above solid mantle is obtained by a non-zero gap between radial displacements and geoid perturbations. In light of this, CMB conditions for compressional and compositional stratifications are formally equivalent, although isostatic compensation is achieved in very different ways: for compressional stratifications, perturbations involve the whole core, while, for compositional stratifications, they are confined in a thin boundary layer just below CMB.

Smylie and Mansinha (1971) and Chinnery (1975) obtained CMB conditions for compositional stratifications by assuming that radial displacement can be discontinuous at CMB. This discontinuity, however, should not be intended literally. Indeed, in view of eq. (1.136), these authors considered geoid perturbations within the inviscid core as radial displacements and, thus, the discontinuity actually corresponds to a non-zero gap between radial displacement and geoid perturbations, in agreement with the finding of Pekeris and Accad (1972). In this respect, we also note that the arguments of Denis *et al.* (1998) (see their section 5.3) against CMB conditions of Smylie and Mansinha (1971) and Chinnery (1975) were incorrect. Particularly, we refer to when Denis *et al.* (1998) said that the analogy of the mantle bumping into the core like a boat on a lake is misleading since (i) the boat problem is a local problem, while the static-core problem is a global one, and (ii) water level around the boat can rise by a finite amount, while the fluid core cannot since it is closed by an elastic or viscoelastic membrane, the above solid mantle. Indeed, it is not physically sound thinking that the boat problem cannot be solved as a global problem, where forces acting on and within the lake are also balanced, and, for the simple geometrical reason that Longman (1962) paradox concerns only perturbations of harmonic degrees greater than 0, which do not affect the total volume of the core.

1.4 Elastic and viscoelastic solutions

The general solution of the differential system (1.80) reads

$$\mathbf{y}_{\ell m}(r) = \mathbf{\Pi}_\ell(r, r_0)\mathbf{y}_0 - \int_{r_0}^{r} \mathbf{\Pi}_\ell(r, r')\, \boldsymbol{f}_{\ell m}(r')\, dr' \tag{1.137}$$

where $\mathbf{y}_0$ is the Cauchy datum at the radius r_0

$$\mathbf{y}_{\ell m}(r_0) = \mathbf{y}_0 \tag{1.138}$$

and $\mathbf{\Pi}_\ell$ is the so called propagator matrix. The latter is the 6×6-matrix that solve the following homogeneous differential system

$$\frac{d\mathbf{\Pi}_\ell(r, r')}{dr} = \mathbf{A}_\ell(r)\, \mathbf{\Pi}_\ell(r, r') \tag{1.139}$$

with the Cauchy datum at the radius r' given by the identity matrix $\mathbf{1}$

$$\mathbf{\Pi}_\ell(r', r') = \mathbf{1} \tag{1.140}$$

In this respect, each column of the propagator matrix is one of the six linearly independent solution of the homogeneous differential system

$$\frac{d\mathbf{y}_{\ell m}}{dr} = \mathbf{A}_\ell\, \mathbf{y}_{\ell m} \tag{1.141}$$

When the integration of eq. (1.139) in a viscoelastic layer of the Earth model arrives to an internal chemical boundary, we impose the continuity of the propagator and we continue the integration in the new layer accordingly to eq. (1.115)

$$\mathbf{\Pi}_\ell(r_j^+, r') = \mathbf{\Pi}_\ell(r_j^-, r') \tag{1.142}$$

In this way the spheroidal vector solution $\boldsymbol{y}_{\ell m}$, eq. (1.137), already satisfies the conditions for the chemical boundaries between the viscoelastic layers of the Earth model.

We impose CMB conditions in the general solution (1.137) by choosing the bottom

of the mantle as the radius from which the integration starts, $r_0 = r_C^+$, and equating the Cauchy datum $\mathbf{y}_0$ with the RHS of eq. (1.132)

$$\mathbf{y}_{\ell m}(r_C^+) = \mathbf{y}_0 = \mathbf{I}_C\,\mathbf{C} \tag{1.143}$$

This yields

$$\mathbf{y}_{\ell m}(r) = \mathbf{\Pi}_\ell(r, r_C)\mathbf{I}_C\mathbf{C} - \mathbf{w}(r) \tag{1.144}$$

where, for brevity, we have defined

$$\mathbf{w}(r) = \int_{r_C^+}^{r} \mathbf{\Pi}_\ell(r, r')\,\boldsymbol{f}_{\ell m}(r')\,dr' \tag{1.145}$$

The three constants of integration $\mathbf{C}$ entering the CMB conditions can be estimated by imposing the boundary conditions at the Earth surface (1.108). From eq. (1.144) and by recalling that the spheroidal vector solution in the LHS of eq. (1.108) refers to the solution just below the Earth surface, we write

$$\mathbf{P}_1\mathbf{y}_{\ell m}(a^-) = \mathbf{P}_1\left(\mathbf{\Pi}_\ell(a, r_C)\mathbf{I}_C\mathbf{C} - \mathbf{w}(a^-)\right) = \boldsymbol{b} \tag{1.146}$$

Note that $\mathbf{w}$ is evaluated at a^-, i.e., the integration from the bottom of the mantle entering eq. (1.145) ends just below the Earth surface, a^-. This means that surface loadings do not actually contribute to the integral and this is correct because their effect is already accounted for by the Earth surface boundary condition via the term $\boldsymbol{b}$, eq. (1.109). In other words, the spheroidal vector solution always must be intended as evaluated below the Earth surface a because it refers to perturbations of the Earth, and only the density of internal loads and seismic forces contribute to the vector $\mathbf{w}$. We avoid mistakes in the following physical treatment by omitting those terms entering the dishomogeneous term $\boldsymbol{f}_{\ell m}$ that are zero within the Earth, i.e., the surface density $\sigma_{\ell m}^L$ and the density of external bodies $\rho_{\ell m}^T$

$$\boldsymbol{f}_{\ell m} = \frac{4\,\pi\,r^2}{2\,\ell+1}\,\rho^I_{\ell m}\,\boldsymbol{f}^L + \boldsymbol{m}_{\ell m} \tag{1.147}$$

Then, using eq. (1.146) for obtaining the constants of integration $\mathbf{C}$

$$\mathbf{C} = (\mathbf{P}_1\,\mathbf{\Pi}_\ell(a, r_C)\,\mathbf{I}_C)^{-1}\;(\mathbf{P}_1\,\mathbf{w}(a) + \boldsymbol{b}) \tag{1.148}$$

eq. (1.144) becomes

$$\mathbf{y}_{\ell m}(r) = \mathbf{\Pi}_\ell(r, r_C)\mathbf{I}_C\;(\mathbf{P}_1\,\mathbf{\Pi}_\ell(a, r_C)\,\mathbf{I}_C)^{-1}\;(\mathbf{P}_1\,\mathbf{w}(a) + \boldsymbol{b}) - \mathbf{w}(r) \tag{1.149}$$

This is the solution of the associated elastic problem that uniquely determine the spheroidal deformations and the perturbations of the potential within the Earth, as well as the radial and tangential spheroidal stresses and the potential stress, in response to internal and surface loading, and tidal, centrifugal and seismic forcings.

1.4.1 Load and tidal Love numbers

In the perspective of applications of the present theory to the modelling of geodetic observations, we will consider the solution, denoted with $\mathbf{K}$, for the radial and tangential spheroidal displacements and local incremental potential at the Earth surface

$$\mathbf{K} = \begin{pmatrix} U_{\ell m}(a) \\ V_{\ell m}(a) \\ \Phi_{\ell m}(a) \end{pmatrix} \tag{1.150}$$

From eq. (1.149) we obtain

$$\mathbf{K} = \mathbf{P}_2\,\mathbf{y}_{\ell m}(a) = \mathbf{B}_\ell(a)\;(\mathbf{P}_1\,\mathbf{w}(a) + \boldsymbol{b}) - \mathbf{P}_2\,\mathbf{w}(a) \tag{1.151}$$

where $\mathbf{P}_2$ is the projector for the first, second and fifth components of the spheroidal vector solution and, for brevity, we have defined

$$\mathbf{B}_\ell(r) = \mathbf{P}_1 \mathbf{\Pi}_\ell(r, r_C) \mathbf{I}_C \ (\mathbf{P}_1 \, \mathbf{\Pi}_\ell(a, r_C) \, \mathbf{I}_C)^{-1} \tag{1.152}$$

Seismic forces need a specific treatment of the non-conservative force $\mathbf{M}$ entering the dishomogeneous term $\boldsymbol{f}_{\ell m}$, eq. (1.83), via the vector $\boldsymbol{m}_{\ell m}$. We first deal only with loadings and external potentials and we set the seismic forcing to zero in the dishomogeneous term $\boldsymbol{f}_{\ell m}$, postponing to section 1.7 the discussion of the theory for seismic forces.

We then introduce the so called Love numbers $\boldsymbol{k}$. They are adimensional Green functions that linearly relate the perturbations $\mathbf{K}$ to internal and surface loads, and tidal and centrifugal potentials

$$\mathbf{K}^L = \frac{4\,\pi}{(2\,\ell+1)} \mathbf{N}_L \int_{r_C}^{a} \boldsymbol{k}^L(r) \ \left(\delta(r-a)\,\sigma^L_{\ell m} + \rho^I_{\ell m}(r)\right) r^2 \ dr$$

$$+\mathbf{N}_T \, \boldsymbol{k}^T \ \left(\Phi^T_{\ell m}(a) + \Phi^C_{\ell m}(a)\right) \tag{1.153}$$

where $\mathbf{N}_L$ and $\mathbf{N}_T$ are the dimensional diagonal matrices

$$\mathbf{N}_L = \frac{G}{a} \, \text{Diag}[1/g(a), \, 1/g(a), \, 1] \tag{1.154}$$

$$\mathbf{N}_T = \text{Diag}[1/g(a), \, 1/g(a), \, 1] \tag{1.155}$$

Here, $\boldsymbol{k}^L$ and $\boldsymbol{k}^T$ are load and tidal Love numbers, respectively, that we obtain for comparison between eqs (1.151) and (1.153)

$$\boldsymbol{k}^L(r) = \mathbf{N}_L^{-1} \ (\mathbf{B}_\ell(a) \, \mathbf{P}_1 - \mathbf{P}_2) \, \mathbf{\Pi}_\ell(a, r) \, \boldsymbol{f}^L \tag{1.156}$$

$$\boldsymbol{k}^T = \mathbf{N}_T^{-1}\,\mathbf{B}_\ell(a)\,\boldsymbol{b}^T \tag{1.157}$$

Note that the Love number depends on the material stratification of the Earth models and the harmonic degree ℓ via the propagator matrix $\mathbf{\Pi}_\ell$, but not on the order m. Note also that perturbations due to tidal and centrifgual forces share the same Green functions, the tidal Love numbers, $\boldsymbol{k}^T$, and that the load Love number $\boldsymbol{k}^L$ depend on the radial distance from the Earth centre r where the load is seated. Particularly, from eq. (1.156) evaluated at the Earth surface a, the load Love number for surface loading simplifies into

$$\boldsymbol{k}^L(a) = \mathbf{N}_L^{-1}\,\mathbf{B}_\ell(a)\,\boldsymbol{b}_L \tag{1.158}$$

The components of the load and tidal Love numbers consist of the so called radial, tangential and gravitational Love numbers, that we denote with h, l and k, respectively. They are defined by

$$\boldsymbol{k}^L(r) = \begin{pmatrix} h^L(r) \\ l^L(r) \\ (r/a)^\ell + k^L(r) \end{pmatrix} \tag{1.159}$$

$$\boldsymbol{k}^T = \begin{pmatrix} h^T \\ l^T \\ 1 + k^T \end{pmatrix} \tag{1.160}$$

Due to the term $(r/a)^\ell$ and the unit in the third components, the gravitational Love numbers k^L and k^T only describe the gravitational potential that is due to density perturbations of the Earth, without including the direct contributions from load densities and external potentials.

Eq. (1.153) can be seen as the solution of the static elastic problem or the associated elastic solution, i.e, the solution of the viscoelastic problem in the Laplace domain accordingly to the Correspondence Principle. In the first case, the fields are in the time

domain and the propagator matrix depend on the shear modulus μ. Then eq. (1.153) can readily be used for modelling elastic perturbations at the Earth surface, for which the Love number $\boldsymbol{k}$ are named elastic Love $\boldsymbol{k}_E$, denoted with the subscript E. In the second case, we must intend formulas as in the Laplace domain, where fields are the Laplace transform of fields and the propagator matrix $\mathbf{\Pi}_\ell$ depends on the function $\hat{\mu}(s)$ of the Laplace variable s defined by eq. (1.41), rather than the shear modulus μ. We then define the viscoelastic Love number $\boldsymbol{k}$ in the time domain in terms of their Laplace transforms $\tilde{\boldsymbol{k}}(s)$ that we obtain from eqs (1.156)–(1.157)

$$\tilde{\boldsymbol{k}}^L(r,s) = \mathcal{L}\left[\boldsymbol{k}^L(r,t)\right] = \mathbf{N}_L\ \left(\mathbf{B}_\ell\,\mathbf{P}_1 - \mathbf{P}_2\right)\mathbf{\Pi}_\ell(a,r)\,\boldsymbol{f}^L\big|_{\mu=\hat{\mu}(s)} \tag{1.161}$$

$$\tilde{\boldsymbol{k}}^T(s) = \mathcal{L}\left[\boldsymbol{k}^T(t)\right] = \mathbf{N}_T\,\mathbf{B}_\ell\,\boldsymbol{b}^T\big|_{\mu=\hat{\mu}(s)} \tag{1.162}$$

where we have indicated the dependence on the Laplace variable s via the function $\hat{\mu}(s)$ that substitutes the shear modulus μ. This affects the propagator matrix $\mathbf{\Pi}_\ell$ and also the matrix $\mathbf{B}_\ell$, eq. (1.152). Note that the limit of eqs (1.161)–(1.162) for $|s| \to \infty$ converges to the elastic Love numbers $\boldsymbol{k}_E^L$ and $\boldsymbol{k}_E^T$

$$\lim_{|s|\to\infty} \tilde{\boldsymbol{k}}^L(r,s) = \boldsymbol{k}_E^L(r) \tag{1.163}$$

$$\lim_{|s|\to\infty} \tilde{\boldsymbol{k}}^T(s) = \boldsymbol{k}_E^T \tag{1.164}$$

because the limit of $\hat{\mu}(s)$ for $|s| \to \infty$ converges to the shear modulus μ

$$\lim_{|s|\to\infty} \tilde{\mu}(s) = \mu \tag{1.165}$$

With these definitions, the associated elastic solution in the Laplace domain becomes

$$\tilde{\mathbf{K}}(s) = \frac{4\,\pi}{(2\,\ell+1)}\,\mathbf{N}_L \int_{r_C}^{a} \tilde{\boldsymbol{k}}^L(r,s)\,\left(\delta(r-a)\,\tilde{\sigma}^L_{\ell m}(s) + \tilde{\rho}^I_{\ell m}(r,s)\right) r^2\,dr$$

$$+\mathbf{N}_T\,\tilde{\boldsymbol{k}}^T(s)\,\left(\tilde{\Phi}^T_{\ell m}(a,s) + \tilde{\Phi}^C_{\ell m}(a,s)\right) \tag{1.166}$$

and, after inverse Laplace transform of the product of two functions, eq. (1.35), we obtain the viscoelastic perturbations $\mathbf{K}$ in the time domain as the time convolution of the viscoelastic Love number $\boldsymbol{k}$ and the time histories of the forcing terms

$$\mathbf{K}(t) = \frac{4\,\pi}{2\,\ell+1}\,\mathbf{N}_L \int_{r_C}^{a} \boldsymbol{k}^L(r,t) \star \left(\delta(r-a)\,\sigma^L(r,t) + \rho^I(r,t)\right)\,dr$$

$$+\mathbf{N}_T\,\boldsymbol{k}^T(t) \star \left(\Phi^T_{\ell m}(a,t) + \Phi^C_{\ell m}(a,t)\right) \tag{1.167}$$

Here, the viscoelastic Love numbers must be obtained by inverse Laplace transformation of eqs (1.161)–(1.162). The inverse Laplace transform is formally defined by complex integration along the Bromwich path

$$\boldsymbol{k}(t) = \mathcal{L}^{-1}\left[\tilde{\boldsymbol{k}}(s)\right] = \frac{1}{2\,\pi\,i}\int_{c-i\infty}^{c+i\infty} \tilde{\boldsymbol{k}}(s)\,e^{s\,t}\,ds \tag{1.168}$$

The real constant c is chosen such that singularities of the integrand $\tilde{\boldsymbol{k}}(s)\,e^{s\,t}$ are either all on the left or all on the right side of the vertical line running from $c-i\infty$ to $c+i\infty$. Closing the contour with a half-circle C_R of radius R (either on the left of the line or on the right, depending on where the singularities are situated) leads to the following complex contour integration

$$\boldsymbol{k}(t) = -\frac{1}{2\,\pi\,i}\lim_{R\to\infty}\int_{C_R} \tilde{\boldsymbol{k}}(s)\,e^{s\,t}\,ds + \frac{1}{2\,\pi\,i}\oint_{\Gamma} \tilde{\boldsymbol{k}}(s)\,e^{s\,t}\,ds \tag{1.169}$$

where Γ is an arbitrarily closed contour which contains all the singularities. By considering eqs (1.164)–(1.164) and that the inverse Laplace transform of the unit 1 yields the

Dirac delta $\delta(t)$, we can further specify the first term of the RHS of eq. (1.169), that we write as follows

$$\boldsymbol{k}(t) = \boldsymbol{k}_E\,\delta(t) + \frac{1}{2\,\pi\,i}\oint_\Gamma \tilde{\boldsymbol{k}}(s)\,e^{s\,t}\,ds \tag{1.170}$$

This representation of the viscoelastic Love number separates the instantanteous elastic response of the viscoelastic Earth model to the imposition of loading and external potentials from the following response due to viscoelastic relaxation of the deviatoric stress. We mantain this distinction by defining the viscous Love number $\boldsymbol{k}_V$

$$\boldsymbol{k}_V(t) = \frac{1}{2\,\pi\,i}\oint_\Gamma \tilde{\boldsymbol{k}}(s)\,e^{s\,t}\,ds \tag{1.171}$$

and writing the Love numbers $\boldsymbol{k}$ as

$$\boldsymbol{k}(t) = \boldsymbol{k}_V(t) + \boldsymbol{k}_E\,\delta(t) \tag{1.172}$$

1.5 The relaxation spectrum

The singularities of the integrand $\tilde{\boldsymbol{k}}(s)\,e^{s\,t}$ enclosed in the complex closed contour Γ may arise into different ways. The first source of singularities is when the differential system (1.139) is non–uniformly Lipschitzian. Indeed, this reflects into singularities of the propagator matrix $\boldsymbol{\Pi}_\ell$. The inspection of the function $\hat{\mu}(s)$ and the elements of the matrix $\mathbf{A}_\ell$, defined in eqs (1.41) and (1.81), leads to the conclusion that the differential system is not-uniformly Lipschitzian for $s = 0$, $s = -\tau^{-1}$ and $s = -\varsigma^{-1}$, where ς is the so called compressional transient time (Cambiotti *et al.*, 2009; Cambiotti and Sabadini, 2010) defined by

$$\varsigma = \tau\,\left(1 + \frac{4\,\mu}{3\,\kappa}\right) \tag{1.173}$$

We denote the set of non–uniformly Lipschitzian zones as $\mathcal{N}$

$$\mathcal{N} = \{0\} \cup \mathcal{N}_\tau \cup \mathcal{N}_\varsigma \tag{1.174}$$

with

$$\mathcal{N}_\tau = \left\{ s \in \mathbb{R} \,\middle|\, s = -\frac{1}{\tau(r)} \quad \forall\, r \in [r_C, a] \right\} \tag{1.175}$$

$$\mathcal{N}_\varsigma = \left\{ s \in \mathbb{R} \,\middle|\, s = -\frac{1}{\varsigma(r)} \quad \forall\, r \in [r_C, a] \right\} \tag{1.176}$$

This singularity at the origin of the Laplace domain occurs because $\hat{\mu}(s = 0) = 0$ and the momentum equation becomes the equation for the inviscid body. This demands a specific treatment, like that discussed in section 1.3.3 for the inviscid core. Cambiotti and Sabadini (2010) shown that the origin of the Laplace domain is not a singularity if the stratification of the mantle is compressional ($\gamma = 0$), while it is the cluster point of a infinite denumerable set of roots if the stratification is compositional $(\gamma \neq 0)$. We will return later on this issue in eq. (1.185) and Chapter 2.

The second source of singularities comes from the determination of the constants of integration $\mathbf{C}$ using the boundary conditions at the Earth surface, eq. (1.148). Indeed, the inverse of the 3×3-matrix

$$[\mathbf{P}_1 \mathbf{\Pi}_\ell(a, r)\, \mathbf{I}_C]_{\mu=\hat{\mu}(s)} \tag{1.177}$$

may be singular for some value of the Laplace variable s. In this respect, we recast the matrix $\mathbf{B}_\ell$ as follows

$$\mathbf{B}_\ell\big|_{\mu=\hat{\mu}(s)} = \frac{(\mathbf{P}_1 \mathbf{\Pi}_\ell(a, r_C)\, \mathbf{I}_C)\ (\mathbf{P}_1 \mathbf{\Pi}_\ell(a, r_C)\, \mathbf{I}_C)^\dagger \Big|_{\mu=\hat{\mu}(s)}}{\Delta(s)} \tag{1.178}$$

where $\dagger$ stands for the matrix of complementary minors, and Δ is the so called secular determinant

$$\Delta(s) = \det\left(\mathbf{P}_1 \mathbf{\Pi}_\ell(a,r)\,\mathbf{I}_C\right)|_{\mu=\hat{\mu}(s)} \tag{1.179}$$

The singularities thus occur for the solutions of the so called secular equation

$$\Delta(s) = 0 \tag{1.180}$$

that is the conditions when the secular determinant entering the denominator of eq. (1.178) is zero. Tanaka *et al.* (2006) proved that these solutions must be on the real axis of the Laplace domain, i.e., $\Im s = 0$. We denote the set of these singularities as $\mathcal{S}$

$$\mathcal{S} = \{\, s \in \mathbb{R} |\ \Delta(s) = 0\} \tag{1.181}$$

Experience and analytical proofs have lead to the conclusion that the solution of the secular equation (1.180) are finite or, at the most, infinite denumerable (they may have cluster points belonging to the non–uniformly Lipschitzian zone $\mathcal{N}$). Also, they are first-order roots and, in this respect, the Love numbers in the Laplace domain have first-order poles at these roots. This is the simplest type of singularity that we dealt with by means of the residue theorem (Sabadini and Vermeersen, 2004). Particularly, each root contributes to the complex integration along the closed contour Γ entering eq. (1.171) for

$$\oint_{\Gamma_j} \boldsymbol{k}(s)\, ds = \boldsymbol{k}_j\, e^{s_j\, t} \tag{1.182}$$

where s_j and Γ_j denote the j-th first-order poles and the closed path containing only this root, and $\boldsymbol{k}_j$ is the residue

$$\boldsymbol{k}_j = \lim_{s \to s_j} (s - s_j)\boldsymbol{k}(s) \tag{1.183}$$

This show that each root s_j is associated with a response of the viscoelastic Earth

model due to the imposition of loading and external potentials. These responses are called normal modes and have characteristic relaxation times t_j given by the inverse of the root s_j. They describe the transition from the elastic to fluid behaviours due to viscoelastic relaxation of deviatoric stress. The roots s_j depends generally on the material parameters of all the layers of the viscoelastic Earth model and on the harmonic degree ℓ (and thus must be determined for each harmonic degree). It turns out that the roots s_j are always negative but for density inversion at the internal interfaces between the layers of the model, i.e., when the density of the layers is lower than that of the neighboring layer above (Plag and Jüttner, 1995; Vermeersen and Mitrovica 2000; Cambiotti and Sabadini, 2010), and for unstable compositional stratifications, i.e., for positive compositional coefficients $\gamma > 0$ (see Chapter 2; Cambiotti *et al.* 2009; Cambiotti and Sabadini 2010). Unstable stratifications trigger normal modes with positive roots s_j that, according to eq. (1.182), are responsible for the divergence of the displacements and the potential at large timescales, called Rayleigh-Taylor instabilities. If that is the case, unstable convective motions will be triggered in the Earth model and the theory as developed in this thesis breaks down on timescales comparable with the characteristic relaxation time of Rayleigh-Taylor instabilities, $t_j = 1/s_j$.

For simple layered incompressible models, the total number of normal modes is finite and can be determined by means of the following rules:

- At each boundary between two viscoelastic layers, one buoyancy mode is triggered if the densities on both sides of the boundary are different. Buoyancy modes between two mantle layers are usually labelled Mi, with $i = 1, 2, \cdots$. At the same boundary, two additional relaxation modes are triggered if the Maxwell times of both sides of the boundary are different. These paired modes are called transient viscoelastic modes as they have relatively short relaxation times and therefore usually labelled Ti^+ and Ti^-, with $i = 1, 2, \cdots$.

- If one side of the boundary is elastic and the other is viscoelastic, as the interface between the elastic lithosphere and the viscoelastic mantle, only the two transient viscoelastic modes are triggered, labelled M0 and L0 in this case. No buoyancy mode is instead triggered at such a boundary (even if there is a density contrast).

- If the lithosphere is viscoelastic or we consider the viscoelastic upper mantle as the

outermost layer, the viscoelastic Earth's surface contributes with a buoyancy mode that is also labelled M0, confusingly with one of the two transient viscoelastic modes that are triggered at the interface between the elastic lithosphere and the viscoelastic mantle.

- The core-mantle boundary contributes with one buoyancy mode, labelled C0.

Compressible layered models and the self-compressed compressible sphere share the same normal modes of layered incompressible models, and additional relaxations modes associated to compressibility (Han and Wahr, 1995; Cambiotti et al. 2009; Cambiotti and Sabadini, 2010):

- Each viscoelastic compressible layer triggers two modes. These paired modes are called transient compressible modes as they have relatively short relaxation times and usually labelled Zi^+ and Zi^-, with $i = 1, 2, \cdots$. Within the same layer, also an infinite denumerable set of modes is triggered. They are called dilatational modes, labelled D$_j$, with $j = 1, \cdots, \infty$, and their characteristic times converge to the compressional transient time ς in the limit for $j \to \infty$

$$\lim_{j\to\infty} s_{\mathrm{D}_j} = -\varsigma^{-1} \tag{1.184}$$

These are all normal modes for compressible Earth models with compressional stratifications ($\gamma = 0$), i.e. when the initial density stratification is due to the only self-compression of the Earth. Instead, compositional stratifications ($\gamma \neq 0$) trigger another infinite denumerable set of buoyancy modes with very long characteristic times. They are called compositional modes, labelled C$_j$, with $j = 1, \cdots, \infty$. These modes can be both stable, $s_{\mathrm{C}_j} < 0$, and unstable, $s_{\mathrm{C}_j} > 0$, and their poles s_{C_j} monotonically converge to the origin of the Laplace domain for $j \to \infty$

$$\lim_{j\to\infty} s_{\mathrm{C}_j} = 0 \tag{1.185}$$

The stable case will be carefully discussed in Chapter 2. In the unstable case, instead, the compositional modes describe Rayleigh-Taylor instabilities that occur on timescales of the order of the shortest characteristic time $t_{\mathrm{C}_1} = 1/s_{\mathrm{C}_1}$, with $j = 1$.

The presence of dilatational and compositional modes arises theoretical and computational problems in obtaining all the contributions from normal modes, eq. (1.182), to the viscous Love numbers, eq. (1.171). However, for all intents and purposes, it is sufficient to detect the first few of these modes in order that the Green functions converge to the exact ones. In fact, for $j \to \infty$, the residues $\boldsymbol{k}_{\mathrm{D}_j}$ and $\boldsymbol{k}_{\mathrm{C}_j}$ of dilatational and compressional modes go to zero sufficiently fast so that their summation converges once the first few of them has been taken into account (see Chapter 2; Cambiotti *et al.*, 2009; Cambiotti and Sabadini, 2010).

1.5.1 Modal and non-modal contributions

The Love number $\tilde{\boldsymbol{k}}(s)$ has two different types of not analyticity. The first comes from a denumerable set of poles $s_j \in \mathcal{S}$. The second comes from the continuous set $\mathcal{N}$ of the Maxwell and compressional transient times τ and ς. Accordingly to Fang and Hager (1995), we will refers to these contributions as the "modal" and "non–modal" contributions, respectively. The modal contribution can be explicited in the viscoelastic Love number by making use of the residue theorem as in eq. (1.182)

$$\boldsymbol{k}(t) = \sum_{s_j \in \mathcal{S}_0} \boldsymbol{k}_j \, e^{s_j \, t} + \frac{1}{2 \, \pi \, i} \oint_{\Gamma} \boldsymbol{k}_N(s) \, ds + \boldsymbol{k}_E \, \delta(t) \tag{1.186}$$

Here, $\tilde{\boldsymbol{k}}_N(s)$ stands for the non-modal contribution that we cannot further explicit and must be obtained by complex integration along the closed contour Γ.

The non modal contribution is inherently associated with the continuous variations of the Maxwell and compressional transient times. Indeed, as discussed in Spada *et al.* (1992a), Han and Whar (1995), Vermeersen and Sabadini (1997a) and Cambiotti *et al.* (2009), these singularities do not contribute to the perturbations in the time domain if they are isolated points in the Laplace s-domain. This is the case for layered Earth models, where the elastic parameter and the viscosity are constant within each layer, because the Maxwell and compressional transient times do not vary within each layer. Eq. (1.171) thus becomes

$$\boldsymbol{k}_V(t) = \sum_{s_j \in \mathcal{S}_0} \boldsymbol{k}_j \, e^{s_j \, t} \tag{1.187}$$

On the contrary, we have verified that a not null contribution comes from the set $\mathcal{N}$ when it is continuous (Cambiotti and Sabadini, 2010; Cambiotti *et al.* 2010) and, thus, we must necessarily evaluate the complex contour integration along the contour Γ in eq. (1.186).

1.6 The complex contour integration

For applications of the present theory for modelling perturbations in the time domain, we do not need to investigate any time the relaxation spectrum. We just need to know where the singularities are located in order to choose the closed contour Γ that contains them, and then perform the complex contour integration entering eq. (1.171). This straightforward approach was implemented by Tanaka *et al.* (2006) for modelling post-seismic perturbations due to the December 2004 Sumatran earthquake. In the following we describe some aspects necessary for obtaining stable numerical codes able to compute the viscoelastic response in a wide range of time scales, from the instantaneous elastic response to the billion year time scales.

Fig. 1.1 shows the contour Γ (dashed line) that we use in eq. (1.171) and the contour of Tanaka *et al.* (2006) (solid line). The difference consists in the fact that our contour is situated on the half space with positive real part of the Laplace variable s, $\Re s > 0$, only for the semi–circle of radius R

$$R = \max \left\{ 5 \, s_{C1}, 10^{-5} \, \mathrm{kyr}^{-1} \right\} \tag{1.188}$$

where s_{C1} is the largest positive pole of the first compositional mode due to unstable compositional stratifications. The factor 5 and the lower bound $10^{-5} \, \mathrm{kyr}^{-1}$ in eq. (1.188) have been chosen in order to avoid numerical unstability in the radial Gill-Runge-Kutta integration of the differential system (1.139) near the pole s_{C1} and the origin of the Laplace domain, $s = 0$. This choice reduces the numerical unstability in the numerical evaluation of eq. (1.171) due to the term $e^{\Re s \, t}$, which diverges in the limit $t \to \infty$ if

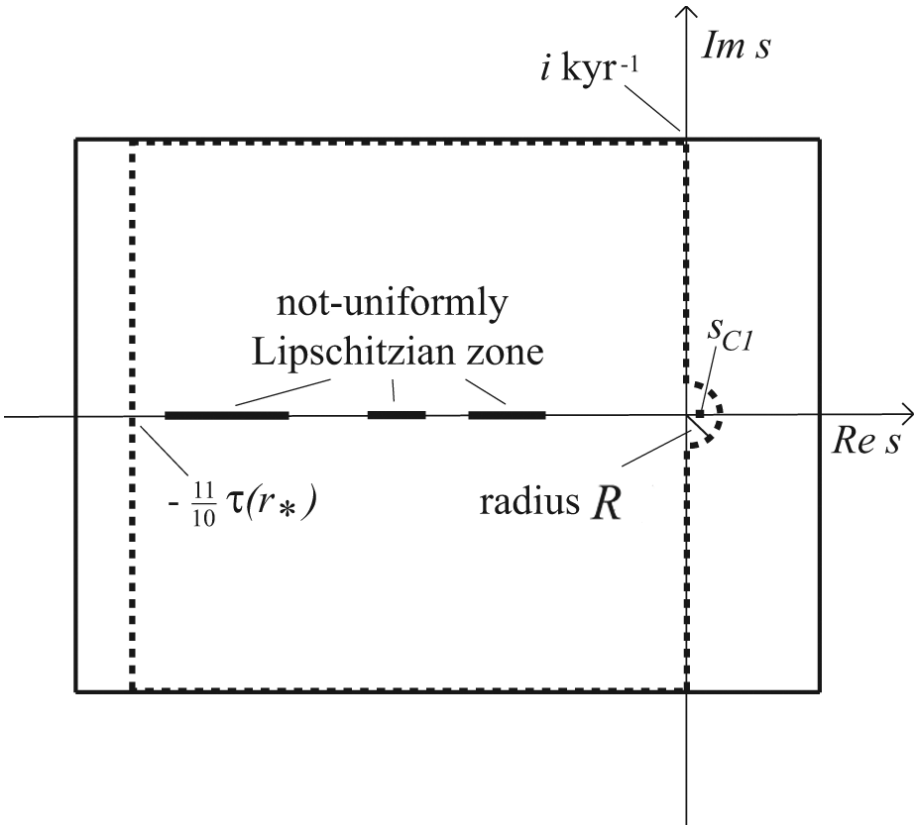

Figure 1.1: The closed contour Γ and that used in Tanaka *et al.* (2006) (dashed and solid lines, respectively).

$\Re s > 0$. The pole s_{C1} is obtained by means of a root-finding algorithm, which can be applied safety in the positive half of the real axis becuse the non–uniformly Lipschitzian zone $\mathcal{N}$ is situated in the negative half, by definition, eq. (1.174).

The value Z defining the lowest $\Re s < 0$ of the contour Γ is chosen as

$$Z = -\frac{11}{10}\frac{1}{\tau(r_*)} \tag{1.189}$$

where r_* is the radius at which the Maxwell relaxation time τ assumes its smallest value. This is due to the fact that the singularities can be composed only of isolated poles $s_j \in \mathcal{S}$ if $\Re s < -\tau(r_*)$, and our experience has shown that there are not poles such that $s_j < -\tau(r_*)$.

We choose $1\,\mathrm{kyr}^{-1}$ for the greatest and lowest $\Im s$ of the contour Γ. Increasing the time t numerical instabilities may happen due to the sign oscillations of $e^{\Im s\, t}$ near the imaginary axis, for small $\Re s$. Indeed, elsewhere the term $e^{\Re s\, t}$ goes rapidly to zero increasing t, since $\Re s < 0$, and this damps the oscillations of $e^{i\,\Im s\, t}$. To avoid the numerical unstability near the the imaginary axis, particularly for those s with $\Re s \geq 0$, we proceed as follows. We adopt an adaptive Cavalieri-Simpson method to evaluate the contour integral entering eq. (1.171) and, at each stage, we increase artfully the sampling of the integrand $\tilde{\boldsymbol{k}}(s)$ by using the same second order interpolating polynomial on which the Cavalieri-Simpson method is based. This way the number of steps at which $\tilde{\boldsymbol{k}}(s)$ is effectively evaluated depends only on the smoothness or stiffness of $\tilde{\boldsymbol{k}}(s)$ along the contour Γ, rather than on the condition $t\,\Im s << 2\,\pi$ proposed by Tanaka *et al.* (2006). The time scale at which the numerical unstability due to the oscillation of $e^{\Im s\, t}$ occurs is increased of about 1–2 orders of magnitude, under the same number of effective evaluations of $\tilde{\boldsymbol{k}}(s)$.

1.7 Fault discontinuities

Earthquakes yield a discontinuity in the displacement across the fault plane, where the rock fractures. By denoting with $d\mathbf{S} = dS\,\boldsymbol{n}$ an infinitesimal surface element of the fault plane of area dS and unit normal vector $\boldsymbol{n}$, we thus impose the following condition for displacements due to earthquakes

$$\delta\boldsymbol{u} = \delta u\,\boldsymbol{v} = \lim_{\epsilon\to 0}\left[\boldsymbol{u}(\boldsymbol{r}_0 + \epsilon\,\boldsymbol{n}) - \boldsymbol{u}(\boldsymbol{r}_0 - \epsilon\,\boldsymbol{n})\right] \tag{1.190}$$

where $\boldsymbol{r}_0$ is the position of the infinitesimal surface element, and $\delta\boldsymbol{u} = \delta u\,\boldsymbol{v}$ is the displacement discontinuity of length δu and direction $\boldsymbol{v}$. Discontinuities which are parallel to the fault plane ($\boldsymbol{v}\cdot\boldsymbol{n} = 0$) are called tangential (or shear) displacement dislocations. Discontinuities which are normal to the fault plane ($\boldsymbol{v}\cdot\boldsymbol{n} = 1$) are called tensile displacement dislocations. Between the two type of dislocations, we will focus only on the former as it is responsible for the main contribution to co- and post-seismic perturbations.

Smylie and Mansinha (1971), Mansinha *et al.* (1979) and Ben–Menahem and Singh

(1981) shown that the effect of displacement dislocations is equivalent to including an extra body force $\mathbf{M}$ in the momentum equation. For shear displacement dislocations, the equivalent body force is the double couple

$$\mathbf{M} = M\ (\boldsymbol{n} \otimes \boldsymbol{v} + \boldsymbol{v} \otimes \boldsymbol{n}) \cdot \boldsymbol{\nabla}_0 \delta(\boldsymbol{r} - \boldsymbol{r}_0) \tag{1.191}$$

where M is the moment of each couple given by

$$M = \mu(r_0)\, \delta u\, dS \tag{1.192}$$

and the gradient operator $\boldsymbol{\nabla}_0$ operates on the coordinates of the seismic source point $\boldsymbol{r}_0 = (r_0, \theta_0, \varphi_0)$. In order to understand the definition of the equivalent body force $\mathbf{M}$, eq. (1.191), we rewrite it as the sum of two single couples $\mathbf{M}_{n,v}$ and $\mathbf{M}_{v,n}$

$$\mathbf{M} = \mathbf{M}_{n,v} + \mathbf{M}_{v,n} \tag{1.193}$$

The single couple $\mathbf{M}_{n,v}$ (and similarly $\mathbf{M}_{v,n}$) is given by two opposite point-like forces of magnitude F and direction $\boldsymbol{v}$ located at points $\boldsymbol{r}_0 \pm \epsilon/2\, \boldsymbol{n}$

$$\mathbf{M}_{n,v} = F\, \boldsymbol{v}\, \delta(\boldsymbol{r} - (\boldsymbol{r}_0 + \epsilon/2\, \boldsymbol{n})) - F\, \boldsymbol{v}\, \delta(\boldsymbol{r} - (\boldsymbol{r}_0 - \epsilon/2\, \boldsymbol{n})) \tag{1.194}$$

and, in the limit for F going to infinity and ϵ going to zero, it yields

$$\mathbf{M}_{n,v} = M\, \boldsymbol{n}\, \boldsymbol{v} \cdot \boldsymbol{\nabla}_0 \delta(\boldsymbol{r} - \boldsymbol{r}_0) \tag{1.195}$$

Here, we have assumed that the product between F and ϵ remains finite and it coincides with the seismic moment M given by eq. (1.192)

$$M = \lim_{F \to \infty, \epsilon \to 0} F\, \epsilon \tag{1.196}$$

In order to obtain the forcing $\boldsymbol{m}_{\ell m}$, eq. (1.86), entering the differential system (1.80) via the dishomogeneous term $\boldsymbol{f}_{\ell m}$, eq. (1.83), we must expand in spherical harmonics the expression for double couple, eq. (1.191). First we recast eq. (1.191) as follows

$$\mathbf{M} = M\,\boldsymbol{n}\cdot[\boldsymbol{v}\cdot\boldsymbol{\nabla}_0\otimes(\delta(\boldsymbol{r}-\boldsymbol{r}_0)\,\mathbf{1})] + M\,\boldsymbol{v}\cdot[\boldsymbol{n}\cdot\boldsymbol{\nabla}_0\otimes(\delta(\boldsymbol{r}-\boldsymbol{r}_0)\,\mathbf{1})] \tag{1.197}$$

where we have utilized $\boldsymbol{\nabla}_0\delta(\boldsymbol{r}-\boldsymbol{r}_0)\otimes\mathbf{1} = \boldsymbol{\nabla}_0\otimes(\delta(\boldsymbol{r}-\boldsymbol{r}_0)\,\mathbf{1})$. The above expression for the double couple is convenient as the spherical harmonic expansion of the three-dimensional Dirac delta $\delta(\boldsymbol{r}-\boldsymbol{r}_0)$ multiplied by the unit diadyc $\mathbf{1}$ yields

$$\delta(\boldsymbol{r}-\boldsymbol{r}_0)\,\mathbf{1} = \frac{\delta(r-r_0)}{r^2}\sum_{\ell=0}^{\infty}\sum_{m=-\ell}^{\ell}\frac{1}{\Omega_{\ell m}}\,\big[\mathbf{R}_{\ell m}(\theta,\varphi)\,\bar{\mathbf{R}}_{\ell m}(\theta_0,\varphi_0)$$

$$+\frac{1}{\ell(\ell+1)}\,\big(\mathbf{S}_{\ell m}(\theta,\varphi)\,\bar{\mathbf{S}}_{\ell m}(\theta_0,\varphi_0)+\mathbf{T}_{\ell m}(\theta,\varphi)\,\bar{\mathbf{T}}_{\ell m}(\theta_0,\varphi_0)\big)\Big] \tag{1.198}$$

where the bar stands for the complex conjugate.

The Green functions for the displacement and the gravitational potential perturbation due to the seismic forcing are obtained by considering the infinitesimal fault plane $d\mathbf{S}$ located along the polar axis, i.e., taking the limit of eq. (1.197) for the colatitude θ_0 and longitude φ_0 of the seismic source going to zero. In view of this, we shall use the following limits

$$\lim_{\theta_0,\varphi_0\to 0}\boldsymbol{e}_\theta(\theta_0,\varphi_0) = \boldsymbol{x}_1 \tag{1.199}$$

$$\lim_{\theta_0,\varphi_0\to 0}\boldsymbol{e}_\varphi(\theta_0,\varphi_0) = \boldsymbol{x}_2 \tag{1.200}$$

$$\lim_{\theta_0,\varphi_0\to 0}\boldsymbol{e}_r(\theta_0,\varphi_0) = \boldsymbol{x}_3 \tag{1.201}$$

where $\boldsymbol{x}_j$ are the Cartesian unit vectors of the geographical reference ($\boldsymbol{x}_1$ points to the equator and the Greenwich meridian, while $\boldsymbol{x}_3$ points to the north pole, i.e., coincides with the present-day rotation axis), and

$$\lim_{\theta_0,\varphi_0\to 0} \bar{Y}_{\ell m}(\theta_0,\varphi_0) = \delta_{m0} \tag{1.202}$$

$$\lim_{\theta_0,\varphi_0\to 0} \frac{\partial \bar{Y}_{\ell m}(\theta_0,\varphi_0)}{\partial \theta_0} = \frac{1}{2}\left[\ell(\ell+1)\,\delta_{m1} - \delta_{m(-1)}\right] \tag{1.203}$$

$$\lim_{\theta_0,\varphi_0\to 0} \frac{1}{\sin\theta_0}\frac{\partial \bar{Y}_{\ell m}(\theta_0,\varphi_0)}{\partial \varphi_0} = \frac{i}{2}\left[\ell(\ell+1)\,\delta_{m1} + \delta_{m(-1)}\right] \tag{1.204}$$

$$\lim_{\theta_0,\varphi_0\to 0} \frac{\partial}{\partial \theta_0}\left(\frac{\partial \bar{Y}_{\ell m}(\theta_0,\varphi_0)}{\partial \varphi_0}\right) = -\frac{i}{4}\left[\frac{(\ell+2)!}{(\ell-2)!}\,\delta_{m2} - \delta_{m(-2)}\right] \tag{1.205}$$

Then, by making use of eq. (1.198) into eq. (1.197) and by considering the limit of the latter for θ_0 and φ_0 going to zero in order to locate the double couple along the polar axis, we obtain

$$\mathbf{M} = M\sum_{\ell=0}^{\infty}\sum_{m=-\ell}^{\ell}\left[m^R_{\ell m}(r)\,\mathbf{R}_{\ell m}(\theta,\varphi) + m^S_{\ell m}(r)\,\mathbf{S}_{\ell m}(\theta,\varphi) + m^T_{\ell m}(r)\,\mathbf{T}_{\ell m}(\theta,\varphi)\right] \tag{1.206}$$

where

$$m^R_{\ell m}(r) = \frac{1}{\Omega_{\ell m}}\lim_{\theta_0,\varphi_0\to 0}\left\{\boldsymbol{n}\cdot\left[\boldsymbol{v}\cdot\boldsymbol{\nabla}_0\left(\frac{\delta(r-r_0)}{r^2}\,\bar{\mathbf{R}}_{\ell m}(\theta_0,\varphi_0)\right)\right]\right.$$
$$\left.+\boldsymbol{v}\cdot\left[\boldsymbol{n}\cdot\boldsymbol{\nabla}_0\left(\frac{\delta(r-r_0)}{r^2}\,\bar{\mathbf{R}}_{\ell m}(\theta_0,\varphi_0)\right)\right]\right\} \tag{1.207}$$

$$m^S_{\ell m}(r) = \frac{1}{\ell(\ell+1)\,\Omega_{\ell m}} \lim_{\theta_0,\varphi_0\to 0} \left\{ \boldsymbol{n} \cdot \left[\boldsymbol{v} \cdot \boldsymbol{\nabla}_0 \left(\frac{\delta(r-r_0)}{r^2}\, \bar{\mathbf{S}}_{\ell m}(\theta_0,\varphi_0) \right) \right] \right.$$

$$\left. + \boldsymbol{v} \cdot \left[\boldsymbol{n} \cdot \boldsymbol{\nabla}_0 \left(\frac{\delta(r-r_0)}{r^2}\, \bar{\mathbf{S}}_{\ell m}(\theta_0,\varphi_0) \right) \right] \right\} \tag{1.208}$$

$$m^T_{\ell m}(r) = \frac{1}{\ell(\ell+1)\,\Omega_{\ell m}} \lim_{\theta_0,\varphi_0\to 0} \left\{ \boldsymbol{n} \cdot \left[\boldsymbol{v} \cdot \boldsymbol{\nabla}_0 \left(\frac{\delta(r-r_0)}{r^2}\, \bar{\mathbf{T}}_{\ell m}(\theta_0,\varphi_0) \right) \right] \right.$$

$$\left. + \boldsymbol{v} \cdot \left[\boldsymbol{n} \cdot \boldsymbol{\nabla}_0 \left(\frac{\delta(r-r_0)}{r^2}\, \bar{\mathbf{T}}_{\ell m}(\theta_0,\varphi_0) \right) \right] \right\} \tag{1.209}$$

with

$$\Omega_{\ell m} = \frac{2\,\ell+1}{4\,\pi}\, \frac{(\ell+m)!}{(\ell-m)!} \tag{1.210}$$

As discussed in section 1.2, in the following we will do not discuss further the toroidal component of the seismic force. By writing the unit direction $\boldsymbol{v}$ of the slip and the unit normal $\boldsymbol{n}$ to the infinitesimal fault plane in terms of dip, α, and slip, γ, angles

$$\boldsymbol{v} = \cos\gamma\, \boldsymbol{x}_1 + \sin\gamma\, \cos\alpha\, \boldsymbol{x}_2 + \sin\gamma\, \sin\delta\, \boldsymbol{x}_3 \tag{1.211}$$

$$\boldsymbol{n} = -\sin\alpha\, \boldsymbol{x}_2 + \cos\alpha\, \boldsymbol{x}_3 \tag{1.212}$$

after some straightforward algebra, eqs (1.207)–(1.208) can be cast as follows

$$m^X_{\ell m}(r) = \frac{\delta(r-r_0)}{r^2\, r_0}\, m^{(0)X}_{\ell m}(r) + \frac{d_r\delta(r-r_0)}{r^2}\, m^{(1)X}_{\ell m}(r) \tag{1.213}$$

Here, X denotes the spheroidal radial, $X = R$, and tangential, $X = S$, components of

the seismic force, and $m_{\ell m}^{(x)X}$, for $x = 0, 1$ and $X = R, S$, is given by

$$m_{\ell 0}^{(0)R} = -\frac{2\,\ell + 1}{4\,\pi}\,\sin 2\delta\,\sin\gamma \tag{1.214}$$

$$m_{\ell 1}^{(0)R} = \frac{2\,\ell + 1}{8\,\pi}\,(\cos\delta\,\cos\gamma - i\,\cos 2\alpha\,\sin\gamma) \tag{1.215}$$

$$m_{\ell 2}^{(0)R} = 0 \tag{1.216}$$

$$m_{\ell 0}^{(1)R} = -\frac{2\,\ell + 1}{4\,\pi}\,\sin 2\alpha\,\cos\gamma \tag{1.217}$$

$$m_{\ell 1}^{(1)R} = 0 \tag{1.218}$$

$$m_{\ell 2}^{(1)R} = 0 \tag{1.219}$$

$$m_{\ell 0}^{(0)S} = \frac{2\,\ell + 1}{8\,\pi}\,\sin 2\delta\,\sin\gamma \tag{1.220}$$

$$m_{\ell 1}^{(0)S} = \frac{2\,\ell + 1}{8\,\pi\,\ell\,(\ell + 1)}\,(-\cos\delta\,\cos\gamma + i\,\cos 2\delta\,\sin\gamma) \tag{1.221}$$

$$m_{\ell 2}^{(0)S} = \frac{2\,\ell + 1}{16\,\pi\,\ell\,(\ell + 1)}\,(2\,i\,\sin\delta\,\cos\gamma + \sin 2\delta\,\sin\gamma) \tag{1.222}$$

$$m_{\ell 0}^{(1)S} = 0 \tag{1.223}$$

$$m_{\ell 1}^{(1)S} = \frac{2\,\ell + 1}{8\,\pi\,\ell\,(\ell + 1)}\,(-\cos\delta\,\cos\gamma + i\,\cos 2\delta\,\sin\gamma) \tag{1.224}$$

$$m_{\ell 2}^{(1)S} = 0 \tag{1.225}$$

with i being the imaginary unit. The scalars $m_{\ell m}^{(0)X}$ and $m_{\ell m}^{(1)X}$ of order $|m| > 2$ are

zero and their expression for $m = -1, -2$ are obtained by the above expressions by considering that

$$m^X_{\ell -m} = (-1)^m \, \frac{(\ell - m)!}{(\ell + m)!} \, \bar{m}^X_{\ell m} \tag{1.226}$$

In view of these results, the vector $\boldsymbol{m}_{\ell m}$, eq. (1.86), which describes the seismic force and enters the differential system (1.80) via the dishomogeneous term $\boldsymbol{f}_{\ell m}$, eq. (1.83), takes the following form

$$\boldsymbol{m}_{\ell m}(r) = \frac{M}{r^2} \left(\frac{\delta(r - r_0)}{r_0} \, \boldsymbol{m}^{(0)}_{\ell m} + \frac{\partial \delta(r - r_0)}{\partial r} \, \boldsymbol{m}^{(1)}_{\ell m} \right) \tag{1.227}$$

where the vectors $\boldsymbol{m}^{(x)}_{\ell m}$, for $x = 0, 1$, are given by

$$\boldsymbol{m}^{(x)}_{\ell m} = \left(0, 0, m^{(x)R}_{\ell m}, m^{(x)S}_{\ell m}, 0, 0 \right)^T \tag{1.228}$$

The differential system (1.80) for the seismic problem thus becomes

$$\frac{\mathbf{y}_{\ell m}}{r} = \mathbf{A}_{\ell m} \, \mathbf{y}_{\ell m} - \frac{M}{r^2} \left(\frac{\delta(r - r_0)}{r_0} \, \boldsymbol{m}^{(0)}_{\ell m} + \frac{\partial \delta(r - r_0)}{\partial r} \, \boldsymbol{m}^{(1)}_{\ell m} \right) \tag{1.229}$$

that is solve by

$$\boldsymbol{y}_{\ell m}(r) = \boldsymbol{\Pi}_\ell(r, r_C) \, \mathbf{I}_C \, \mathbf{C} - \mathbf{w}(r) \tag{1.230}$$

Here, $\mathbf{w}$ is defined by eq. (1.145) and, for the seismic force, yields

$$\mathbf{w}(r) = \frac{M}{r_0^2} \, H(r - r_0) \, \boldsymbol{\Pi}_\ell(r, r_0) \left[\frac{\boldsymbol{m}^{(0)}_{\ell m}}{r_0} + \frac{2 \, \boldsymbol{m}^{(1)}_{\ell m}}{r_0} + \boldsymbol{A}_\ell(r_0) \, \boldsymbol{m}^{(1)}_{\ell m} \right] \tag{1.231}$$

It is important to note the second term within the brackets of the RHS of eq. (1.231). This term results from the fact that the expression for $\boldsymbol{m}_{\ell m}$ obtained above, eq. (1.227), which is similar to that obtained by Smylie and Mansinha (1971) and Mansinha *et al.* (1979) (but for some convection about spherical harmonics), also depends on the radial variable r rather than on the only radius of the seismic source r_0. If this dependence is omitted, the theory for the seismic source of Smylie and Mansinha (1971) and Mansinha *et al.* (1979) yields

$$\mathbf{w}_{\ell m}(r) = \frac{M}{r_0^2}\, H(r - r_0)\, \mathbf{\Pi}_\ell(r, r_0) \left[\frac{\boldsymbol{m}_{\ell m}^{(0)}}{r_0} + \mathbf{A}_\ell(r_0)\, \boldsymbol{m}_{\ell m}^{(1)} \right] \tag{1.232}$$

and it would differ from that discussed in Takeuchi and Saito [1972]. References to Smylie and Mansinha [1971] and Mansinha *et al.* [1979] should not neglect this subtle dependence and use eq. (1.231) rather than eq. (1.232).

Both spheroidal radial, $R_{\ell m}$, and tangetial, $S_{\ell m}$, components of stress must be zero at the Earth surface, as well as the potential stress $Q_{\ell m}$. Then, the Earth surface boundary conditions are those for a free surface

$$\mathbf{P}_1\, \boldsymbol{y}_{\ell m}(a) = \mathbf{0} \tag{1.233}$$

After elimination of the constants of integration $\mathbf{C}$ imposing the free Earth surface boundary conditions (1.233) from eq. (1.230), the solution $\mathbf{K}$ for the radial and tangential spheroidal displacements and local incremental potential at the Earth surface becomes

$$\boldsymbol{K} = (\mathbf{B}_\ell\, \mathbf{P}_1 - \mathbf{P}_2)\ \mathbf{w}(a) \tag{1.234}$$

We do not further specify the seismic perturbations in terms of seismic Love number (Sun and Okubo, 1993) because they have little use in the scientific literature.

Part I

COMPRESSIBLE VISCOELASTODYNAMICS

Abstract

The problem of compressibility in the modelling of viscoelastic perturbations of planetary bodies is still a topic under discussion, on the common agreement that compressibility should be considered in Glacial Isostatic Adjustments (GIA) studies. The main aspects of this discussion are: the identification of instabilities to be physically related to convective instability (Plag and Jüttner, 1995), the discussion of this behaviour by means of instability modes in the spectral Laplace domain (Vermeersen *et al.*, 1996b; Hanyk *et al.*, 1999; Klemann *et al.*, 2003) and the discussion of its relevance for realistic Earth-like structures (Vermeersen and Mitrovica, 2000). The result of this intellectual process was: the instabilities exist, but they are not relevant for the Earth due to the fact that the characteristic times for these instabilities are much larger than the age of the planet, when a realistic Earth structure like PREM (Dziewonski and Anderson, 1981) is considered.

The basic problem when considering material compressibility in GIA is the often neglected compressibility in the definition of the initial state of the viscoelastic Earth model. This means that a perturbation theory is applied to a non-consistently specified initial state and results in an ill-posed problem, evident in denumerable infinite numbers of modes in the spectral representation of the solution (Plag and Jüttner, 1995; Cambiotti and Sabadini, 2010). This focus motivates a review of the Longman (1963) paradox, which treats the boundary condition of a compressible fluid core. A similar problem, indeed, occurs in the case of viscoelastic perturbations due to surface loading, where the fluid limit, which is comprised in Maxwell viscoelasticity due to relaxation of deviatoric stress at large timescales, and the final isostatic equilibrium justify an overview of the mantle at large timescales as an inviscid body (Wu and Peltier, 1982). As already mentioned in Chapter 1, section 1.3, the isostatic compensation of mantle bumping into a fluid core, which deviates from the neutral state of equilibrium, is achieved only by mass redistribution within a thin layer just below the core-mantle boundary (Pekeris and Accad, 1972), whereas elsewhere radial displacement and geoid must coincide. At this point the question is whether we should expect a similar behaviour for the viscoelastic mantle loaded at its surface.

In order to clarify this issue, herein we investigate the effects of the initial stratificaton of the mantle on viscoelastic perturbations at large time scales and, then, on the

final isostatic equilibrium with surface loading. Attempts to establish a consistent theory (Wolf and Kaufmann:, 2000; Martinec *et al.*, 2001; Wolf and Li, 2002) have so far failed also due to the fact that the elastic structure, compressibility and density have to be prescribed for theoretical aspects that neglect compressibility in some features. Recently, we derived the analytical solution in the Laplace domain of an Earth model composed of an inviscid core and a viscoelastic mantle characterized by a specific Darwin-law density profile. This allows us to distinguish between compressional (adiabatic and chemically homogeneous) and compositional (non-adiabatic and chemically heterogeneous) stratifications and to revisit the problem of compressible viscoelasticity where, starting from a neutral initial state, we investigated deviations parameterized similar to the Brunt–Väiäsala frequency in dynamics. Compositional stratifications were shown to result in a new class of spectral modes that we named compositional modes and also describe the instabilities discussed in the previous works.

Whereas the consequences of compositional stratifications were discussed in Cambiotti and Sabadini (2010) for perturbations at the Earth surface, herein we also focus on perturbations within the viscoelastic mantle in order to give a full description of the perturbed state of the Earth. We thus obtain the analytical solution for the compressible viscoelastic problem, present the analytical representation of the compressional modes, discuss their influence for describing the isostatic equilibrium and conclude with the physical meaning and consequences of compositional stratifications.

Chapter 2

The self–compressed compressible sphere

Cambiotti and Sabadini (2010) found the analytical solution of viscoelastic perturbations in the Laplace domain for a specific self-gravitating compressible Maxwell Earth model, called "self-compressed compressible sphere". This model is composed of an incompressible inviscid core and a compressible Maxwell mantle with constant shear modulus, μ, bulk modulus, κ, and viscosity, ν. In order to account for the self-compression of the mantle at the initial state of hydrostatic equilibrium, the initial density profile within the mantle varies with the radial distance from the Earth centre r according to

$$\rho_0(r) = \begin{cases} \frac{3\,\alpha}{2\,r_C} & 0 \leq r \leq r_C \\ \frac{\alpha}{r} & r_C < r \leq a \end{cases} \tag{2.1}$$

where r_C, a and α are the core radius, the Earth radius and a constant related to the total Earth mass M_E by

$$M_E = 2\,\pi\,\alpha\,a^2 \tag{2.2}$$

This choice of the initial density profile fixes the initial gravity acceleration g within the mantle to

$$g = 2\,\pi\,G\,\alpha \tag{2.3}$$

with G being the universal gravitational constant.

Depending on the bulk modulus κ, the self-compressed compressible sphere describes compressional or compositional stratifications of the mantle. Indeed, from the generalized Williamson-Adams equation (1.116) with the compositional coefficient set to zero, $\gamma = 0$, we obtain that compressional stratifications are characterized by a constant bulk modulus to which we will refer as compressional bulk modulus κ_0

$$\kappa_0 = g\,\alpha = 2\,\pi\,G\,\alpha^2 \tag{2.4}$$

Departures from this value result in compositional stratifications. Particularly, the com-

positional coefficient γ yields

$$\gamma = -\frac{\epsilon\,\alpha}{r^2} \tag{2.5}$$

with

$$\epsilon = \frac{\kappa - \kappa_0}{\kappa} \tag{2.6}$$

As it results from the analysis of the relaxation spectrum of the self-compressed compressible sphere, that we will discuss later in section 2.2, the compositional stratification is stable if $\kappa > \kappa_0$ and unstable if $\kappa < \kappa_0$. This also results from the comparison between the generalized Williamson-Adams equation (1.116) and the expression for the square of the Brunt-Väiäsala frequency ω

$$\omega^2 = -\frac{g}{\rho_0}\left(\partial_r \rho_0 + \frac{g\,\rho_0^2}{\kappa}\right) = -\frac{g\,\gamma}{\rho_0} \tag{2.7}$$

The Brunt-Väiäsala frequency ω characterizes the motion of a particle in the ideal fluid that adiabatically moves away from its equilibrium position. The particle will oscillate around its equilibrium position with frequency ω if $\omega^2 > 0$, while it will continue to move away from its equilibrium position if $\omega^2 < 0$. Differently, the particle remains in the new position due to the perturbation if $\omega = 0$. Although the present theoretical framework is based on the assumption of quasi-static deformations (we neglected the inertial forces in the momentum equation), the analysis of the sign of ω^2 allows to establish if the viscoelastic model is stable or instable (Plag and Jüttner, 1995; Vermeersen and Mitrovica, 2000). In view of eq. (2.7), the stability only depends on the sign of the compositional coefficient γ. The model is stable if $\gamma \leq 0$ and instable if $\gamma > 0$. For instance layered compressible models present the instable Rayleigh–Taylor modes (Plag and Jüttner, 1995) and, indeed, their compositional coefficient becomes positive because the radial derivative of the density is zero in this case. An alternative way to describe layered compressible models consists in the assumption that they are incompressible at the initial state of hydrostatic equilibrium, i.e, they have an infinitely large bulk modulus

at the initial state, $\kappa \to \infty$, and a finite bulk modulus during the perturbations. This would imply that $\gamma = 0$ from (2.7), but it is not a self-consistent with compressibility during deformation and so we reject this interpretation, which also contrasts with the presence of Rayleigh–Taylor instabilities.

In view of the way in which we have defined the self-compressed compressible sphere, we have the possibility of studying the effects of the compressional and compositional stratifications on the relaxation process of Maxwell Earth models. Previous analytical solutions were obtained assuming material or local incompressibility and for the case of the "homogeneous compressible sphere" (Gilbert and Backus, 1968). Only the latter model actually accounts for compressibility during perturbations, but all the material parameters, included the initial density, are constant from the centre to the surface of the Earth. Its analytical solution has been widely used, first, in seismology and, after, in viscoelastic modelling (Vermeersen *et al.*, 1996). Nevertheless, it neglects the self-compression at the initial state of hydrostatic equilibrium since it has a constant density profile: in this respect, the homogeneous compressible sphere is always unstable. Instead, our self-compressed compressible sphere (Cambiotti and Sabadini, 2010) takes into account compressibility both during the perturbations and at the initial state, having a depth dependent density profile, eq. (2.1). In addition to this qualitative improvement with respect to the homogeneous compressible sphere, our model also reproduces the density contrast at the core-mantle boundary, although it neglects other density contrasts within the mantle due to the simple Darwin-law used to describe the compressibility at the initial state. This also results into a better reproduction of the actual initial gravity acceleration predicted by PREM, which is indeed almost constant within the mantle as in eq. (2.3). We show this in fig. 2.1 where we compare the initial gravity acceleration predicted by PREM and the self-compressed and homogeneous compressible spheres.

2.1 The analytical solution

In order to solve the spheroidal radial and tangential components of the momentum equation and the Poisson equation, eqs (1.70)-(1.71) and (1.73), for compressible Earth models with constant elastic parameters κ and μ, it is convenient to divide these equations by the initial density ρ_0 and recast them in the following form

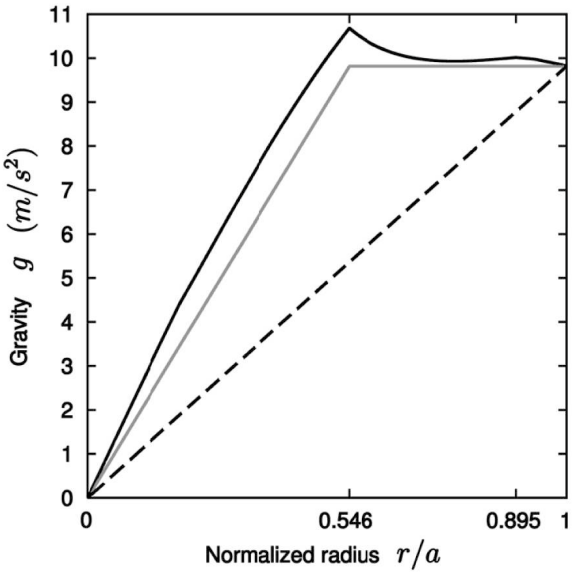

Figure 2.1: Initial gravity acceleration g of PREM (black solid line), the self-compressed compressible sphere (our new model, grey line) and the homogeneous compressible sphere (Gilbert and Backus 1968, black dashed line).

$$\frac{\beta}{\rho_0}\,\partial_r \chi_{\ell m} - \partial_r(g\,U) + g\,\chi_{\ell m} - \partial_r \Phi_{\ell m} + \frac{\mu}{\rho_0}\,\frac{\ell(\ell+1)}{r}\,H_{\ell m} = 0 \tag{2.8}$$

$$\frac{\beta}{\rho_0}\,\chi_{\ell m} - g\,U_{\ell m} - \Phi_{\ell m} + \frac{\mu}{\rho_0}\,\partial_r(r\,H_{\ell m}) = 0 \tag{2.9}$$

where, for brevity, we introduced the quantity $H_{\ell m}$ defined by

$$H_{\ell m} = \partial_r V_{\ell m} + \frac{V_{\ell m} - U_{\ell m}}{r} \tag{2.10}$$

Note that we have omitted the forcing terms because we are interested in the analytical solution for the propagator matrix $\mathbf{\Pi}_\ell$ that solve the homogeneous differential system (1.139). The propagator matrix, indeed, is the only term that we need in order to obtain the Love numbers, i.e., the Green functions of the response of the Earth model to general loading and external forces.

The following step consists in obtaining two differential equations that involve only the radial and tangential displacements. This is possible owing to the specific initial density and gravity of the self-compressed compressible sphere, eqs (2.1)-(2.3). The first differential equation is obtained by subtracting to eq. (2.8) the derivative of eq. (2.9) with respect to the radial variable r

$$\left(\frac{\beta}{\alpha} - g\right)\, \chi_{\ell m} + \frac{\mu}{\alpha}\, \left[r^2 \partial_r^2 H_{\ell m} + 3\, r\, \partial_r H_{\ell m} + (1 - \ell(\ell+1))\, H_{\ell m}\right] = 0 \qquad (2.11)$$

The second differential equation is obtained by applying the operator $\partial_r + 2/r$ to the radial component (2.8) of the momentum equation and subtracting to it the tangential component (2.9) multiplied by $\ell(\ell+1)/r^2$

$$\begin{aligned} &-\nabla_r^2 \Phi_{\ell m} + \nabla^2 \left(\frac{\beta}{\alpha}\, \chi_{\ell m} - g\, U_{\ell m}\right) \\ &+ \left(g - \frac{\beta}{\alpha}\right)\, \frac{1}{r}\, \partial_r \left(r^2 \chi_{\ell m}\right) + \frac{\mu}{\alpha}\, \frac{\ell(\ell+1)}{r}\, H_{\ell m} = 0 \end{aligned} \qquad (2.12)$$

Here, we also substitute the Laplacian of the potential by means of the Poisson equation (1.73) together with eqs (2.1) and (2.3)

$$\nabla_r^2 \Phi_{\ell m} = -\frac{2\, g\, \alpha}{r}\, \left(\chi_{\ell m} - \frac{1}{r}\, U_{\ell m}\right) \qquad (2.13)$$

This yields

$$\begin{aligned} &\frac{2\, g\, \alpha}{r}\, \left(\chi_{\ell m} - \frac{1}{r}\, U_{\ell m}\right) + \nabla^2 \left(\frac{\beta}{\alpha}\, \chi_{\ell m} - g\, U_{\ell m}\right) \\ &+ \left(g - \frac{\beta}{\alpha}\right)\, \frac{1}{r}\, \partial_r \left(r^2 \chi_{\ell m}\right) + \frac{\mu}{\alpha}\, \frac{\ell(\ell+1)}{r}\, H_{\ell m} = 0 \end{aligned} \qquad (2.14)$$

Let us now suppose that the six linearly independent solutions of eqs (2.11) and (2.14) may have the following form

$$U_{\ell m} = u\, r^z \tag{2.15}$$

$$V_{\ell m} = v\, r^z \tag{2.16}$$

with u, v and z as constants, and substitute these trial solutions. From eqs (2.11) and (2.14), we thus obtain

$$\frac{\mu}{\alpha}\, r^{z-1}\, \{u\, [Z - z\,(\zeta+1) - 2\,\zeta] - v\, [Z\, z - \ell(\ell+1)\,(1+\zeta)]\} = 0 \tag{2.17}$$

$$\begin{aligned}\frac{\mu}{\alpha}\, r^{z-2}\, \Bigg\{ & u\, \left[\frac{g\,\alpha}{\mu}\,(Z+2)(z+1) + (Z-2)(z+1)\,\zeta - \ell(\ell+1)(\zeta+1)\right] \\ & -v\,\ell(\ell+1)\left[\frac{g\,\alpha}{\mu}\,(Z+2) + Z\,\zeta - (\zeta+1)(z+1)\right]\Bigg\} = 0\end{aligned} \tag{2.18}$$

Here, Z is the second order polynomial in z

$$Z = z^2 + z - \ell(\ell+1) \tag{2.19}$$

and ζ is given by

$$\zeta = \frac{\beta - g\,\alpha}{\mu} \tag{2.20}$$

Since it has been possible to collect the dependence on the radial variable r in eqs (2.17)-(2.18), the latter can be seen as equations for the constants u, v and z. Solving eq. (2.17) for v, we obtain

$$v = u\,\frac{Z - z\,(\zeta+1) - 2\,\zeta}{Z\,z - \ell(\ell+1)\,(1+\zeta)} \tag{2.21}$$

and, using this in eq. (2.18), after some straightforward algebra, it yields the following polynomial in Z of order three

$$a_0 + a_1\,Z + a_2\,Z^2 + Z^3 = 0 \tag{2.22}$$

with a_0, a_1 and a_2 being constant coefficients, which depend solely on the material parameters and the harmonic degree ℓ

$$a_2 = 4\,\frac{g\,\alpha}{\beta} - 2 \tag{2.23}$$

$$a_1 = \ell(\ell+1)\,\left(\frac{g\,\alpha}{\beta}\,(\zeta+3) - 4\right) \tag{2.24}$$

$$a_0 = 2\,\ell(\ell+1)\,\frac{g\,\alpha}{\beta}\,(\zeta-1) \tag{2.25}$$

In order to satisfy eq. (2.22), Z has to be one of the three roots Z_j, with $j = 1, 2, 3$, of the order three polynomial of the LHS. We do not report here the lengthy expressions for Z_j. However, we note that they only depend on the harmonic degree ℓ and on the material parameters of the self-compressed compressible sphere via $g\,\alpha/\beta$ and ζ. Then, by considering that Z is a second order polynomial in the constant z, the latter can assumes only two values z_j and z_{j+3} for each root Z_j

$$z_j = -\frac{1}{2}\,\left(1 + \sqrt{1 + 4\,(\ell(\ell+1) + Z_j)}\right) \tag{2.26}$$

$$z_{j+3} = -\frac{1}{2}\,\left(1 - \sqrt{1 + 4\,(\ell(\ell+1) + Z_j)}\right) \tag{2.27}$$

We thus have obtained six constants z_j that, once substituted into eqs (2.15)-(2.16)

and (2.21), yield six linearly independent solutions of the two differential equations (2.17)-(2.18)

$$U_{\ell m} = \sum_{j=1}^{6} u_j \, r^{z_j} \tag{2.28}$$

$$V_{\ell m} = \sum_{j=1}^{6} u_j \, v_j r^{z_j} \tag{2.29}$$

where u_j are the constants of integration and, according to eq. (2.21), v_j are given by

$$v_j = \frac{Z_j - z_j \, (\zeta + 1) - 2 \, \zeta}{Z_j \, z_j - \ell(\ell + 1) \, (1 + \zeta)} \tag{2.30}$$

Since Z_j has been defined only for $j = 1, 2, 3$, we impose that Z_4, Z_5 and Z_6 coincide with Z_1, Z_2 and Z_3, respectively.

The solution for the gravitational potential $\Phi_{\ell m}$ is obtained by substituting eqs (2.28)-(2.29) into the Poisson equation (2.13). This yields the following disohomogeneous differential equation of the second order in $\Phi_{\ell m}$

$$\nabla^2 \Phi_{\ell m} = -2 \sum_{j=1}^{6} u_j \, r^{z_j - 2} \, g \, [(z_j + 1) - \ell(\ell + 1) \, v_j] \tag{2.31}$$

It is solved by the particular solution

$$\Phi_{\ell m} = \sum_{j=1}^{6} u_j \, p_j \, r^{z_j} \tag{2.32}$$

with

$$p_j = 2 \, g \, \frac{\ell(\ell + 1)(1 - \zeta) - Z_j^2}{Z_j \, (Z_j \, z_j - \ell(\ell + 1) \, (\zeta + 1))} \tag{2.33}$$

and by the two solutions of the homogenenous differential equation (i.e., the Laplace equation)

$$\Phi_{\ell m} = c\, r^{\ell} + c^{*}\, r^{-(\ell+1)} \tag{2.34}$$

with c and c^{*} being constants of integration. The latter, however, must not be considered. Indeed they solve neither the radial nor the tangential components of the momentum equation (2.8)-(2.9), once set $U_{\ell m}$ and $V_{\ell m}$ to zero. This is due to the fact that we have already used the Poisson equation (2.13) to obtain eq. (2.14) from eq. (2.12).

Within the solid mantle of the self-compressed compressible model, on the basis of eqs (2.28), (2.29), (2.32), the spheroidal vector solution $\boldsymbol{y}$ defined in eq. (1.78) yields

$$\boldsymbol{y}_{\ell m}(r) = \mathbf{Y}_{\ell}(r)\, \mathbf{C} \tag{2.35}$$

where $\mathbf{Y}_{\ell}$ and $\mathbf{C}$ are the so called fundamental matrix for the self-compressed compressible and the vector of constants of integration

$$\mathbf{Y}_{\ell} = \left(\boldsymbol{y}^{(1)}_{\ell m}, \boldsymbol{y}^{(2)}_{\ell m}, \boldsymbol{y}^{(3)}_{\ell m}, \boldsymbol{y}^{(4)}_{\ell m}, \boldsymbol{y}^{(5)}, \boldsymbol{y}^{(6)}_{\ell m} \right) \tag{2.36}$$

$$\mathbf{C} = \left(u_1, u_2, u_3, u_4, u_5, u_6 \right)^{T} \tag{2.37}$$

with $\boldsymbol{y}^{(j)}$ being the six linearly independent solutions

$$\boldsymbol{y}^{(j)}_{\ell m}(r) = \begin{pmatrix} r^{z_j} \\ v_j\, r^{z_j} \\ \left[\beta\, z_j + 2\,\lambda - \ell(\ell+1)\, v_j\, \lambda\right]\, r^{z_j - 1} \\ \mu\, \left[1 + (z_j - 1) v_j\right]\, r^{z_j - 1} \\ p_j\, r^{z_j} \\ \left[2\, g + (z_j + \ell + 1)\, p_j\right]\, r^{z_j - 1} \end{pmatrix} \tag{2.38}$$

Note that the fundamental matrix $\mathbf{Y}_{\ell}$ describe the dependence on the radial distance from the Earth centre r of the propagator matrix $\mathbf{\Pi}_{\ell}$, which solves the homogeneous differential system (1.139). Particularly, we have

$$\mathbf{\Pi}_\ell(r, r') = \mathbf{Y}_\ell(r)\, \mathbf{Y}_\ell^{-1}(r') \tag{2.39}$$

This result can be used to solve more sophisticated models composed of different layers within the mantle, each with different (but constant) shear and bulk moduli, and viscosities. Nevertheless, the density profile must be the same given by (2.1). It is sufficient to use the fundamental matrix $\mathbf{Y}_\ell$ to obtain the propagator matrix $\mathbf{\Pi}_\ell$ in each layer and, then, impose chemical boundary conditions at the internal interfaces for propagating the solution from the inner to the outer layers. In this way, the self-compressed compressible sphere also takes into account the contrasts of the rheological parameters at the main Earth interfaces, but not the density contrasts.

2.2 The relaxation spectrum

Let us now consider the self-compressed compressible spheres with compressional stratification, that we denote with CC_0, where the compositional coefficient is zero, $\gamma = 0$. The viscoelastic mantle is characterized by shear modulus $\mu = 1.45 \times 10^{11}$ Pa and viscosity $\nu = 10^{21}\times$ Pa s. The core radius is 3480 km and the Earth radius is 6371 km. In order to respect the total Earth mass $M_E = 5.97 \times 10^{24}$ kg, the density profile given by eqs (2.1) is characterized by $\alpha = 2.34 \times 10^{10}\,\mathrm{kg/m^2}$ and, from eq. (2.4), the compressional bulk modulus is $\kappa_0 = 2.23 \times 10^{11}$ Pa, which is comparable with the range of PREM bulk modulus in the transition zone, from 1.53×10^{11} Pa to 2.56×10^{11} Pa. The resulting core density is $10096.3\,\mathrm{kg/m^3}$, which differs by 8 per cent from the volume-averaged PREM core density and its density profile within the mantle differs from that of PREM by 9, 6 and 21 per cent at the Moho discontinuity, the 670 km discontinuity and the core-mantle boundary, respectively. Nevertheless, the model density differs from PREM by 41 per cent at the Earth surface, due to the compositional decrease of the Earth density within the crust.

In Fig. 2.2 we compare the relaxation spectra (up to the harmonic degree $\ell = 100$) of the self-compressed compressible sphere with compressional stratification, CC_0, and of a two layered compressible model, that we denote with MC, consisting of homogeneous core and mantle, where the material parameters are constant and obtained from the

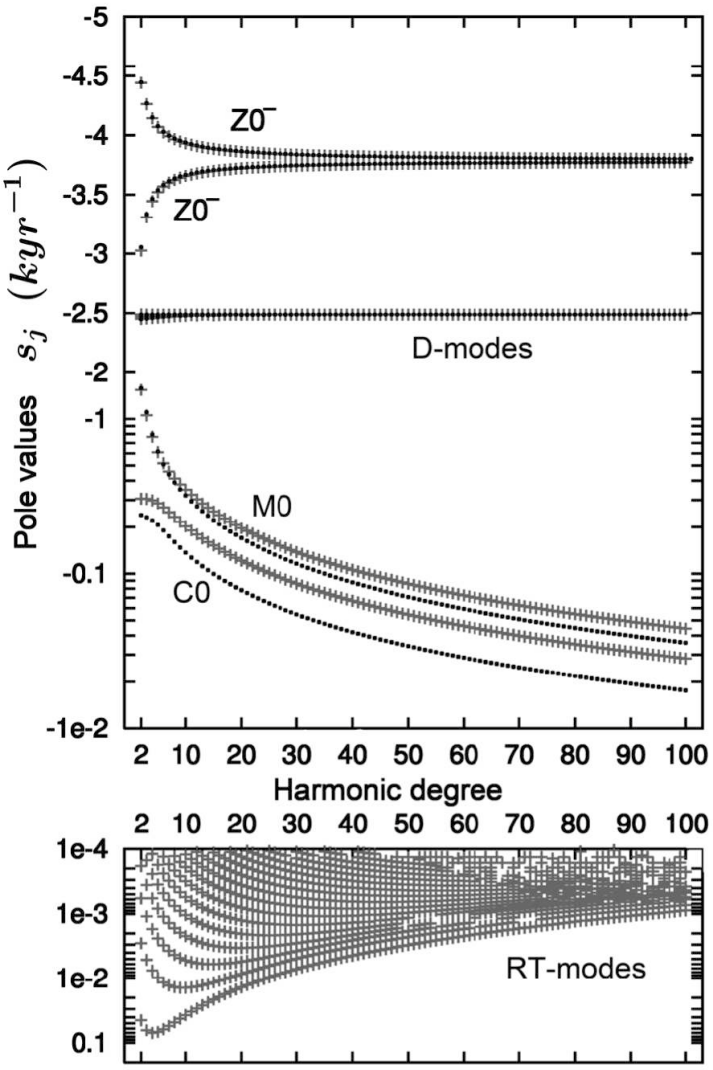

Figure 2.2: Pole values s_j of the relaxation modes of the models CC_0 (dot points) and MC (cruciform points). The inverse Maxwell and compressional transient times of both models are $\tau^{-1} = 4.58\,\mathrm{kyr}^{-1}$ and $\varsigma^{-1} = 2.49\,\mathrm{kyr}^{-1}$

model CC_0 by means of volume averages, with mantle density of $4623\,\mathrm{kg/m^3}$. Note that these two models share the $\mathrm{M}0$ and $\mathrm{C}0$ buoyancy modes, the pair of compressional transient modes, $\mathrm{Z}0^+$ and $\mathrm{Z}0^-$, and the dilatational modes (also abbreviated as D–modes). The pair of compressional transient modes, $\mathrm{Z}0^+$ and $\mathrm{Z}0^-$, have been identified and discussed for the first time in Cambiotti *et al.* (2009) in the case of layered compressible models. Nevertheless, only the layered model MC has the Rayleigh–Taylor modes (also abbreviated as RT–modes) that are, indeed, absent in the relaxation spectrum of the self-compressed model CC_0.

The transient relaxation spectra of the models CC_0 and MC, characterized by the D-modes and the pair of the modes $\mathrm{Z}0^+$ and $\mathrm{Z}0^-$, differ mainly at low harmonic degree, while the differences decrease at high harmonic degrees. Instead, the $\mathrm{C}0$ buoyancy mode presents important differences at all harmonic degrees and the $\mathrm{M}0$ buoyancy mode agrees only at the first 10 harmonic degrees. Such a circumstance is due only to the different density profiles of the two models, since the elastic parameters and the viscosity are the same. We thus safely argue that the differences in the pole values are caused by the different density contrasts of the two models at the core-mantle interface and Earth surface, respectively, which affect mainly the buoyancy modes $\mathrm{C}0$ and $\mathrm{M}0$.

Let us now consider two representative self-compressed compressible spheres with stable and instable compositional stratifications, where the bulk modulus κ differs from the compressional bulk modulus κ_0. In view of the fact that combined contribution of compositional and non-adiabatic stratifications does not amount to more than $10-20\%$ of that of the compressional stratification (Birch, 1952; Birch, 1964; Wolf and Kaufmann, 2000), we assume bulk modulus of 2.62×10^{11} Pa and 1.94×10^{11} Pa to describe stable and instable compositional stratifications, respectively. They correspond to values of -0.15 and 0.15 for the parameter ϵ, eq. (2.6), and, in this respect, we denote these two models with $\mathrm{CC}_{-0.15}$ and $\mathrm{CC}_{0.15}$.

Fig. 2.3 compares the relaxation spectra of the self-compressed compressible spheres with compressional and compositional stratifications. Note that the compositional models $\mathrm{CC}_{-0.15}$ and $\mathrm{CC}_{0.15}$ share the same relaxation modes of the compressional model CC_0, but they have further relaxation modes that are infinite denumerable, with the origin of the Laplace domain as cluster point. The latter relaxation modes are stable for $\epsilon=-0.15$ and instable for $\epsilon=0.15$, in agreement with the analysis of the gravitational stability based on the sign of the Brunt–Väiäsala frequency ω^2, eq. (2.7). They

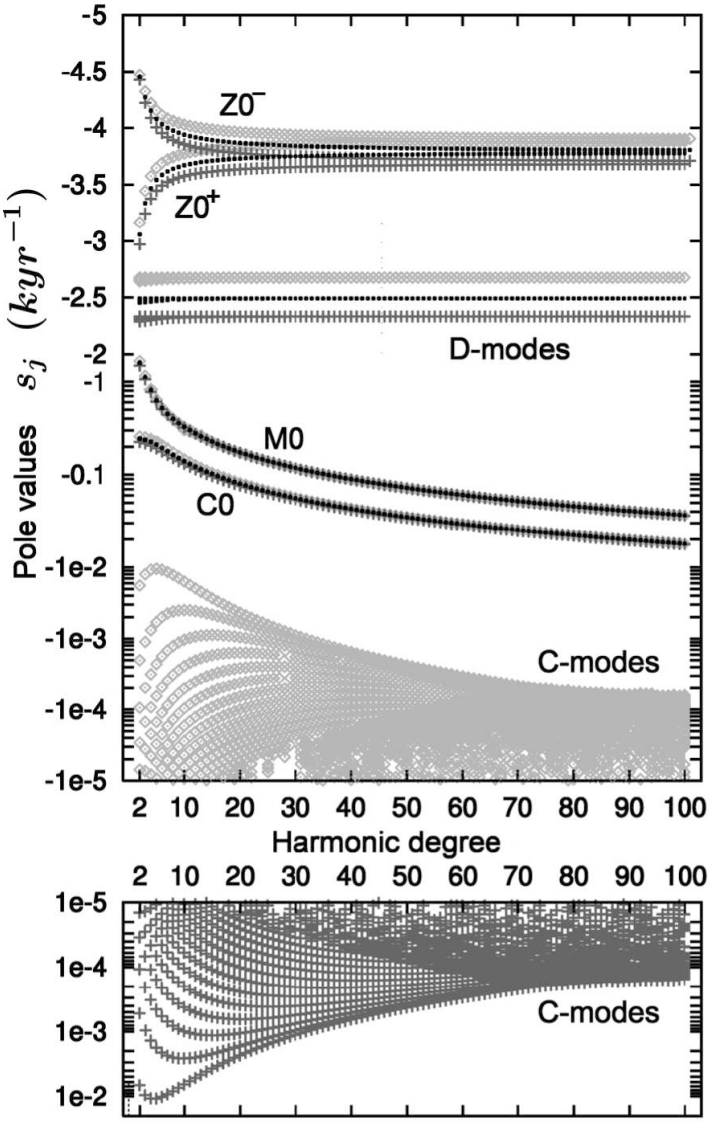

Figure 2.3: Pole values s_j of the relaxation modes of the models CC_0 (dot points), $\mathrm{CC}_{-0.15}$ (diamond points) and $\mathrm{CC}_{0.15}$ (cruciform points). The inverse Maxwell relaxation time of all three models is $\tau^{-1} = 4.58\,\mathrm{kyr}^{-1}$ while the inverse compressional relaxation times are $\varsigma^{-1} = 2.49\,\mathrm{kyr}^{-1}$, $2.67\,\mathrm{kyr}^{-1}$ and $2.33\,\mathrm{kyr}^{-1}$, respectively.

thus describe relaxation processes involved by the compositional stratification and, for this reason, we called them compositional modes (also abbreviated as C–modes). With respect to the common relaxation modes of the three models, we note that they differ mainly in the transient region where the characteristic relaxation times of the D-modes and the pair of transient compressional modes $\mathrm{Z0}^+$ and $\mathrm{Z0}^-$ of the models $\mathrm{CC}_{-0.15}$ and $\mathrm{CC}_{0.15}$ are greater and lower than those of the the model CC_0, respectively. This reflects the different compressional transient times ς, eq. (1.173), that decrease for increasing bulk modulus, 0.43 kyr, 0.40 kyr and 0.37 kyr for $\epsilon = -0.15,\ 0$ and 0.15.

2.2.1 The compositional modes

The denumerable set of C-modes originates from the oscillating behaviour of the secular determinant $\Delta_\ell(s)$ near the origin. It occurs on the positive or negative real axis of the Laplace domain, depending on the sign of the compositional coefficient γ. Such a behaviour is like that of the secular determinant of layered compressible models to which the Rayleigh–Taylor modes are associated, with the exception that the RT-modes are always instable because layered compressible Earth models have always an instable compositional stratification.

Let us now derive an approximated analytical expression for the pole values of the C-modes. After substitution of the analytical expression for the propagator matrix $\mathbf{\Pi}_\ell$ of the self-compressed compressible sphere, eq. (2.39) into the expression for the secular determinant Δ, eq. (1.179), and after expansion in Taylor series of the function $\hat{\mu}(s)$, eq. (1.41), we obtain that the dominant terms of the secular determinant Δ is proportional to

$$\Delta_\ell(s) \propto \left(\frac{a}{r_C}\right)^{i\left(\frac{\kappa_0\,\ell(\ell+1)\,\epsilon}{\hat{\mu}(s)}\right)^{\frac{1}{4}}} - 1 \tag{2.40}$$

By equating to zero the RHS of eq. (2.40), we thus obtain the following approximated analytical expression for the roots of the secular equation (1.180), which are the poles s_{C_m} of the compositional modes

$$s_{C_m} = -\ell(\ell+1)\,\frac{\kappa_0\,\epsilon}{\nu}\,\left(\frac{\log\left(\frac{r_C}{a}\right)}{\pi\,m}\right)^4 + O(m^{-6}) \tag{2.41}$$

for $m = 1, \cdots, \infty$. It confirms that the compositional modes are an infinite denumerable set of relaxation modes and that the origin of the Laplace domain, $s = 0$, is the cluster point of the poles s_{C_m} for $m \to \infty$ since they converge to zero as m^{-4}. Besides this, the dependence of eq. (2.41) on the parameter ϵ gives us the possibility to show analytically that a little deviation from the completely compressional stratification is sufficient to activate the compositional modes. Particularly, they are stable if $\epsilon > 0$ and instable if $\epsilon < 0$. This suggests both that the Rayleigh–Taylor modes are actually a particular case of the compositional modes and that the compositional modes describe buoyancy relaxation processes arising from deviations of the stratification from the neutral state of equilibrium. This interpretation is furthermore supported by the characteristic relaxation times of the compositional and Rayleigh–Taylor modes. As shown in Fig. 2 and Fig. 3 their upper limits are of similar order of magnitude, that is greater than $10 - 10^2$ kyr. This short time scales, however, are due to the use of simplified models. Indeed, more realistic Earth models based on PREM predict much larger characteristic relaxation times of order $1 - 100\,\mathrm{Myr}$ (Plag and Jüttner, 1995; Vermeersen and Mitrovica, 2000).

These findings contrast with the interpretation of Han and Wahr (1995) that a continuous density profile yields a continuous spectrum of buoyancy modes. This interpretation was based on the investigation of the relaxation spectrum of layered compressible models, where each density contrast contributes with a buoyancy mode M*i*. For very fine layered models, where little density contrasts are introduced in order to reproduce better the continuous variations of the PREM density, the number of buoyancy modes M*i* is large. This was interpreted by Han and Wahr (1995) as an evidence that continuous variations of the initial density imply a continuous set of buoyancy modes in the region of small Laplace variable s. In view of the relaxation spectrum of the self-compressed compressible sphere, however, we can already say that this is not the case. Indeed, despite the continuous variations of the initial density described by the Darwin-law profile, eq. (2.1), it is remarkable that no additional buoyancy modes other than the $\mathrm{M}0$ and $\mathrm{C}0$ modes are present in the compressional model CC_0 and that only a discrete, although infinite denumerable, set of compositional modes are triggered by compositional strati-

fications.

Even if Han and Wahr (1995) supported the normal mode approach, we note that their conclusion about the presence of a continuous spectrum in the buoyancy region has weakened the normal mode approach, discouraging further investigations of the relaxation spectrum for not layered Earth models, where the continuous variations of the material parameters within the layers of the Earth are taken into account. On the contrary, our results indicate that such an analysis can be done and interesting physical knowledge of the viscoelastic relaxation processes at large timescales can be obtained as we will show in sections 2.3 and 2.4.

2.3 Viscoelastic perturbations due to surface loading

In order to investigate the role of the definition of the initial state of the viscoelastic Earth model, characterized by compressional or compositional stratifications, in Glacial Isostatic Adjustment (GIA) we only focus on Love numbers $\boldsymbol{k}$ for loads seated at the Earth surface (we will omit the superscript L). Differently from Chapter 1, here we also consider perturbations within the mantle for which the Love numbers for surface loading in the Laplace s-domain read

$$\tilde{\boldsymbol{k}}_{\ell m}(r,s) = \begin{pmatrix} \tilde{h}(r,s) \\ \tilde{l}(r,s) \\ \tilde{k}(r,s) \end{pmatrix} = \mathbf{N}_L^{-1}\,\mathbf{B}_\ell(r)\,\mathbf{b}^L\big|_{\mu=\hat{\mu}(s)} \tag{2.42}$$

with the tilde standing for the Laplace transform and the dimensional matrix $\mathbf{N}_L$ given by eq. (1.154). Here, $\tilde{h}$, $\tilde{l}$, and $\tilde{k}$, are the radial, tangential and gravitational viscoelastic Love numbers in the Laplace domain and their dependence on the radial distance from the Earth centre r refers to where we calculate the perturbations. In this respect, note that the matrix $\mathbf{B}_\ell$ also depend on r.

In view of the study of relaxation spectrum of the self-compressed compressible sphere, the viscoelastic Love numbers can be recast by a spectrum of relaxation modes

$$\tilde{\boldsymbol{k}}(r,s) = \begin{pmatrix} \tilde{h}(r,s) \\ \tilde{l}(r,s) \\ \tilde{k}(r,s) \end{pmatrix} = \boldsymbol{k}_E(r) + \sum_{j\in\mathcal{S}} \frac{\boldsymbol{k}_j(r)}{s - s_j} \tag{2.43}$$

where $\boldsymbol{k}_E = (h_E, l_E, k_E)$ consists of the elastic Love numbers, $\boldsymbol{k}_j = (h_j, l_j, k_j)$ contains the residues of the j–th relaxation mode and s_j is the corresponding pole. Here, $\mathcal{S}$ denotes the whole set of relaxation modes, which is denumerable but infinite (Cambiotti and Sabadini, 2010). The set $\mathcal{S}$ of relaxation modes is split into two types:

$$\mathcal{S} = \mathcal{F} \cup \mathcal{C} \tag{2.44}$$

The set $\mathcal{F}$ of fundamental modes appears both for compressional and compositional stratifications: the $\mathrm{M0}$ and $\mathrm{C0}$ buoyancy modes (associated with the Earth surface and CMB), the pair of transient compressible modes, Z_- and Z_+, and the infinite and denumerable set of dilatational modes, $\mathrm{D_m}$, with $m = 1, \cdots, \infty$. The set $\mathcal{C}$ of compositional modes, $\mathrm{C_m}$, with $m = 1, \cdots, \infty$ is again denumerable and infinite but is triggered only in the case of compositional stratifications.

The fundamental modes describe the transition from the elastic to the Newtonian-fluid behaviour, while the compositional modes control the long time-scale perturbations towards the isostatic equilibrium described by the inviscid fluid. Accordingly, we split the perturbations $\mathbf{K}$ due to a point-like surface load of unit mass with Heaviside time history into contributions describing the elastic response, the transition to the Newtonian fluid and the final transition towards the isostatic equilibrium

$$\begin{pmatrix} U(r,t) \\ V(r,t) \\ \Phi(r,t) \end{pmatrix} =$$

$$\boldsymbol{k}_E(r) - \sum_{j\in\mathcal{F}} \frac{\boldsymbol{k}_j(r)}{s_j} \left(1 - e^{s_j\, t}\right) - \sum_{m\in\mathcal{C}} \frac{\boldsymbol{k}_{\mathrm{C_m}}(r)}{s_{\mathrm{C_m}}} \left(1 - e^{s_{\mathrm{C_m}}\, t}\right) \tag{2.45}$$

where U, V and Φ are the degree-ℓ non-dimensional radial and tangential displace-

ments (normalized by a/M_E), and gravitational potential perturbation (normalized by $a\,g/M_E$). In view of the fact that the poles s_j of the fundamental modes are negative and that their characteristic relaxation times, $|1/s_j|$, are shorter than those of the compositional modes, $|1/s_{\mathrm{Cm}}|$, we can write the final transition towards the isostatic equilibrium as

$$\boldsymbol{K}(r,t) = \boldsymbol{k}_S(r) + \boldsymbol{K}_C(r,t) \tag{2.46}$$

where $\boldsymbol{k}_S$ is the secular perturbation due to the elastic response and the relaxation of the fundamental modes

$$\boldsymbol{k}_S(r) = \begin{pmatrix} h_S(r) \\ l_S(r) \\ k_S(r) \end{pmatrix} = \boldsymbol{k}_E(r) - \sum_{j\in\mathcal{F}} \frac{\boldsymbol{k}_j(r)}{s_j} \tag{2.47}$$

and where $\boldsymbol{K}_C$ is the perturbation due to the only compositional modes

$$\boldsymbol{K}_C(r,t) = \begin{pmatrix} U_C(r,t) \\ V_C(r,t) \\ \Phi_C(r,t) \end{pmatrix} = -\sum_{m=1}^{\infty} \frac{\boldsymbol{k}_{C_m}(r)}{s_{C_m}} \left(1 - e^{s_{C_m}\,t}\right) \tag{2.48}$$

Because compressional stratifications have no compositional modes, the viscoelastic Love number $\tilde{\boldsymbol{k}}(s)$ is an analytic function in a neighbourhood of the origin of the Laplace domain, $s = 0$. Thus, $\tilde{\boldsymbol{k}}(s = 0)$ exists and is finite. From eqs. (2.43) and (2.47), we obtain the following identity

$$\boldsymbol{k}_S(r) = \tilde{\boldsymbol{k}}(r, s = 0) \tag{2.49}$$

This implies that the summation over the strengths $\boldsymbol{k}_j/s_j$ of the fundamental modes entering eq. (2.47) converges to a finite value. Furthermore, the secular perturbations describe the isostatic equilibrium to surface loading (Wu and Peltier, 1982). In this respect, the secular radial displacement and gravitational-potential perturbation satisfy

the isostatic conditions at the Earth surface a

$$\lim_{t\to\infty} U(a,t) = h_S(a) = -\frac{2\,\ell+1}{2} \tag{2.50}$$

$$\lim_{t\to\infty} \Phi(a,t) = k_S(a) = -1 \tag{2.51}$$

Perturbations below the Earth surface, as well as the tangential displacement at the Earth surface are instead unconstrained due to the indeterminateness of static perturbations of the inviscid body discussed by Longman (1962, 1963). They must be obtained solving the whole viscoelastic problem and using eq. (2.47).

2.3.1 The long-period tangential flux of material

Due to the fact that the origin of the Laplace domain is the cluster point of compositional modes, for compositional stratifications, the viscoelastic Love number $\tilde{\boldsymbol{k}}$ is not analytic at $s = 0$ and, so, not well defined. In order to interpret the final transition towards the isostatic equilibrium, we have to consider the perturbation due to compositional modes. For unstable stratifications, the poles s_{C_m} of the compositional modes are positive and eq. (2.48) describes Rayleigh–Taylor unstabilities (Plag and Jüttner, 1995) resulting in divergent displacement and divergent gravitational potential in the limit of $t \to \infty$. In contrast, for stable stratifications, the poles s_{C_m} are negative and eq. (2.48) describes a slow relaxation process. From numerical evaluation of the strengths $\boldsymbol{k}_{C_m}/s_{C_m}$ of the first few compositional modes (at most to $m = 20$ for the harmonic degree $\ell = 2$), Cambiotti and Sabadini (2010) concluded that tangential strengths, $l_{C_m}(a)/s_{C_m}$, at the Earth surface, a, converge to a non zero value L in the limit for $m \to \infty$

$$\lim_{m\to\infty} \frac{l_{C_m}(a)}{s_{C_m}} = L \tag{2.52}$$

Using the representation of eq. (2.48), and eqs. (70) and (72) of Cambiotti and Sabadini (2010), the tangential displacement V_C due to stable compositional modes at large time scale can be approximated by

$$V_C(a,t) = -\sum_{m\in\mathcal{C}} \frac{l_{C_m}}{s_j}\left(1-e^{s_{C_m}\,t}\right) \approx L\left(\ell(\ell+1)\,\frac{\epsilon\,\kappa_0}{\nu}\,t\right)^{1/4} \frac{\log\left(\frac{b}{a}\right)\,\Gamma[3/4]}{\pi} \tag{2.53}$$

with Γ being the gamma function. This tangential displacement of the material away from the load, named 'long period tangential flux of material', diverges as $t^{1/4}$ in the limit of $t \to \infty$. The mathematical proof of eq. (2.52) and a physical interpretation of this peculiar flux will be discussed in the following section, where we will investigate the final transition to the isostatic equilibrium within the solid mantle (not only at the Earth surface), taking into account the whole infinite denumerable set $\mathcal{C}$ of compositional modes.

2.4 The isostatic equilibrium

In order to investigate the final transition towards the isostatic equilibrium for a stable compositional stratification, eq. (2.46), we must compute the summation over compositional modes entering eq. (2.48) without a too low cut-off. Due to numerical complexities, we are interested in an analytical form for the strengths $\boldsymbol{k}_{C_m}(r)/s_{C_m}$ of compositional modes, in addition to the analytical expression for their poles s_{C_m}, eq. (2.41). It can be obtained by neglecting self-gravitation since this greatly facilitate to handle the analytical expression of the viscoelastic Love number $\tilde{\boldsymbol{k}}(r,s)$ in the Laplace s-domain. This simplification does not alter the main issue of the Longman (1962) paradox or the appearance of instability (Klemann *et al.*, 2003). Indeed, the only alteration consists in the fact that gravitational potential perturbation is zero by definition. Particularly, eq. (1.124) still holds in the gravitating case and constrains volume variation to be zero for compositional stratifications. As a consequence, in view of the fact that the radial displacement must coincide with the geoid perturbation, eq. (1.136), the radial displacement yields zero in the simpler case of a gravitating inviscid Earth model.

In Appendix A.3, we obtain the analytical solution of the viscoelastic load Love number $\tilde{\boldsymbol{k}}(r,s)$ in the Laplace s-domain for the self-compressed compressible sphere by neglecting self-gravitation, eq. (A.88), and we use this solution to obtain analytical

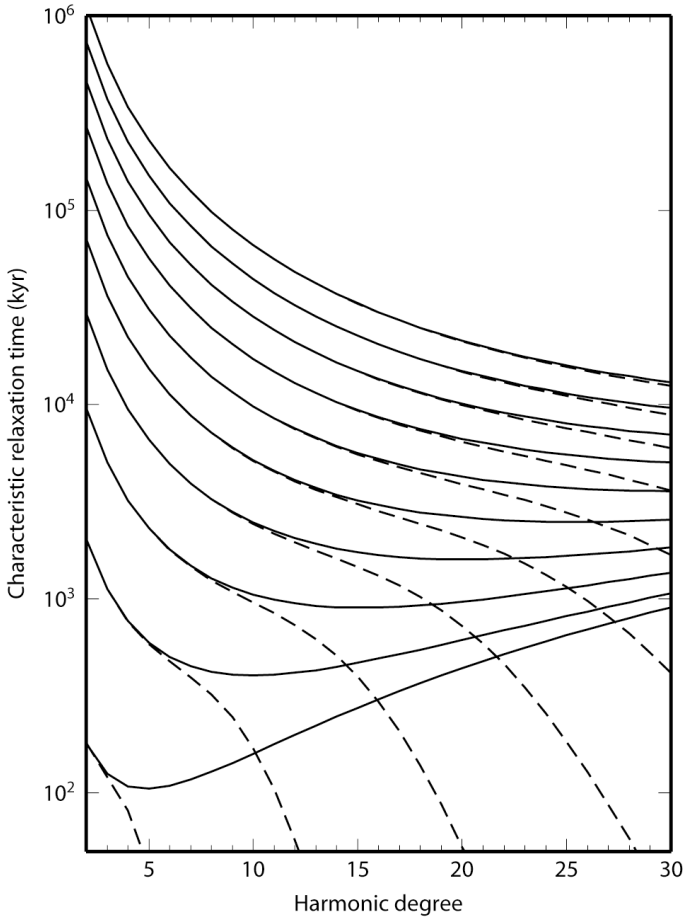

Figure 2.4: Characteristic relaxation times, $t_{C_m} = |1/s_{C_m}|$, of the first ten compositional modes obtained numerically (solid) and using their analytical approximation, eq. (A.100) (dashed).

approximations for poles, s_{C_m}, and strengths, $\boldsymbol{k}_{C_m}(r)/s_{C_m}$, of compositional modes, eqs. (A.100-A.102). Note that the dominant terms of the analytical approximations are the same for the poles, s_{C_m}, obtained accounting for self-gravitation, eq. (2.41), or not accouting for, eq. (A.100). This confirms the small influence of self-gravitation on the final transition from Newtonian-fluid behaviour to isostatic equilibrium.

Figure 2.4 shows for degrees $\ell = 2, \cdots, 30$ the characteristic relaxation times $t_{C_m} = |1/s_{C_m}|$ of the first ten compositional modes obtained numerically without any approximation and using their analytical approximation, eq. (A.100). They were calcu-

lated for the self-compressed compressible sphere $\mathrm{CC}_{-0.15}$ already used in section 2.2, although we now neglect self-gravitation. In particular, we chose the bulk modulus κ to be 15 per cent larger than the compressional bulk modulus κ_0 in order to obtain a stable compositional stratification and to take into account that, for the Earth, the contribution of the compositional stratification does not amount to more than $10 - 20$ per cent of that of the compressional stratification (Birch, 1952; Birch, 1964; Wolf and Kaufmann, 2000). In this respect, fig. 2.4 shows that the analytical approximation fits quite well and deviates only for the first compositional modes and increasing harmonic degrees. Furthermore, the shortest exact characteristic relaxation time is $105\,\mathrm{kyr}$, corresponding to the first compositional mode of degree $\ell = 5$. This short time scale is due to the simplified model; more realistic Earth models based on PREM predict much larger characteristic relaxation times of order $1 - 100\,\mathrm{Myr}$ (Plag and Jüttner, 1995; Vermeersen and Mitrovica, 2000) as already noted for the self-gravitating case, section 2.2..

From eqs. (A.101) and (A.102), we obtain that radial and tangential strengths at the Earth surface, a,

$$\frac{h_{C_m}(a)}{s_{C_m}} = \epsilon\,\frac{(2\,\ell+1)\,\log\left(\frac{b}{a}\right)}{(\pi\,m)^2} + O\left(m^{-3}\right) \tag{2.54}$$

$$\frac{l_{C_m}(a)}{s_{C_m}} = -\frac{(2\,\ell+1)}{\ell(\ell+1)\,\log\left(\frac{b}{a}\right)} + O\left(m^{-2}\right) \tag{2.55}$$

Here, the tangential strengths, $l_{C_m}(a)/s_{C_m}$, converge to a non-zero value in the limit of $m \to \infty$. This finding proves mathematically eq. (2.52), that Cambiotti and Sabadini (2010) obtained numerically in the case of self-gravitation. Also in this simpler case of gravitating Earth models, stable compositional stratification triggers the long-period tangential flux with eq. (2.53),

$$V_C(a,t) \approx \left(\frac{\epsilon\,\kappa_0}{\nu}\,t\right)^{1/4}\,\frac{(2\,\ell+1)\,\Gamma[3/4]}{[\ell(\ell+1)]^{\frac{3}{4}}\,\pi} \tag{2.56}$$

We find a proportionality at the fourth root of ϵ, which describes deviation from the compressional stratification, eq. (2.6), and an inversely proportionality to the fourth root of the viscosity ν. These dependences confirm the findings of Cambiotti and Sabadini

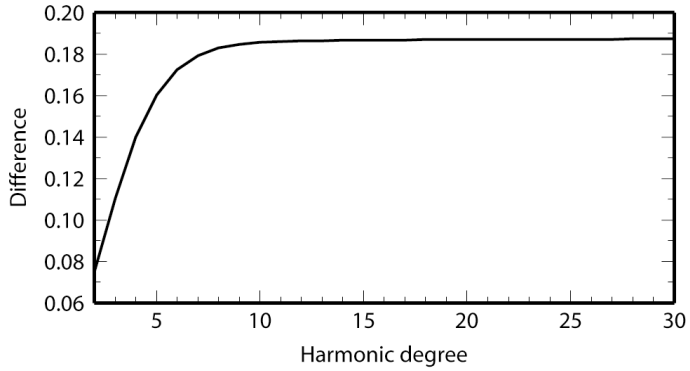

Figure 2.5: Differences between secular, $h_S(a)$, and isostatic, eq. (2.58), radial displacements at the Earth surface a.

(2010), that the long-period tangential flux is a specific process of compositional stratifications when the material behaves like a Newtonian fluid, i.e., after relaxation of the initial elastic stress due to loading.

The radial strengths, $h_{C_m}(a)/s_{C_m}$, at the Earth surface, eq. (2.54), decay as m^{-2} to zero assuring the existence of a finite isostatic equilibrium,

$$\lim_{t\to\infty} U(a,t) = h_S(a) - \sum_{m=1}^{\infty} \frac{h_{C_m}(a)}{s_{C_m}} \tag{2.57}$$

The summation over m can be obtained using the analytical approximations for the strengths of compositional modes, eq. (2.54). Here, the numerical estimates of the first modes are considered in order to avoid inaccuracy of eq. (2.54) at low m and the analytical approximations is used only for m greater than 20. In this way, we confirmed the isostatic equilibrium,

$$\lim_{t\to\infty} U(a,t) = h_S + \lim_{t\to\infty} U_C(a,t) \simeq -\frac{2\,\ell+1}{2} \tag{2.58}$$

for degrees $\ell = 2, \cdots, 30$ with an accuracy of 10^{-5} attributable to numerical precision of the algorithm. In contrast to the compressional stratification, eq. (2.50), the isostatic equilibrium is achieved here only after relaxation of compositional modes which contribute about 0.1–0.2. This is shown in Fig. 2.5, where we plotted the difference between

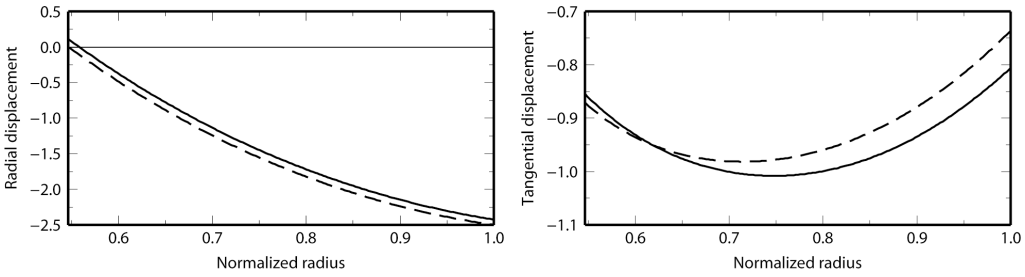

Figure 2.6: Degree-2 secular radial and tangential displacements (left and right panels, respectively) for compressional (dashed) and compositional (solid) stratifications.

secular, $h_S(a)$, and isostatic, eq. (2.58), radial displacements at the Earth surface a for degrees $\ell = 2, \cdots, 30$. For the considered parameterisation, it starts at 0.075 at degree 2 and increases to 0.187 at degrees larger than 15.

Figure 2.6 shows the radial variation from the CMB to the Earth surface for the degree-2 secular radial, h_S, and tangential, l_S, displacements of the considered compressional and compositional stratifications. The secular radial displacements of the compositional stratification have an offset of about 10^{-1} with respect to the compressional stratification. In particular, this means that the secular radial displacement of the compositional stratification is non zero at the CMB, whereas the displacement of the compressional stratification vanishes as it describes consistently an isostatic equilibrium, eq. (2.49). Secular tangential displacements differ mainly in the upper part of mantle by about 10^{-1}, where the compositional stratification predicts smaller values than compressional stratification.

The transition from the secular displacements to the isostatic equilibrium for the case of compositional stratification is shown in Fig. 2.7, at increasing times $t = 10^2$, 10^3, 10^4, 10^6, 10^8, $10^{10}\,\mathrm{kyr}$. According to the momentum equation for a gravitating inviscid body with compositional stratifications, radial and tangential displacements converge to zero in the limit of $t \to \infty$ within the viscoelastic mantle. Thus, compositional modes account for buoyancy forces that bring particles from the deformed secular state described by the fundamental modes back to the initial state of hydrostatic equilibrium. This process starts at the CMB and proceeds towards the Earth surface generating a superficial layer that thins with increasing time. There, the tangential material flow towards and away from the load diverges according to eq. (2.56) in the lower and upper

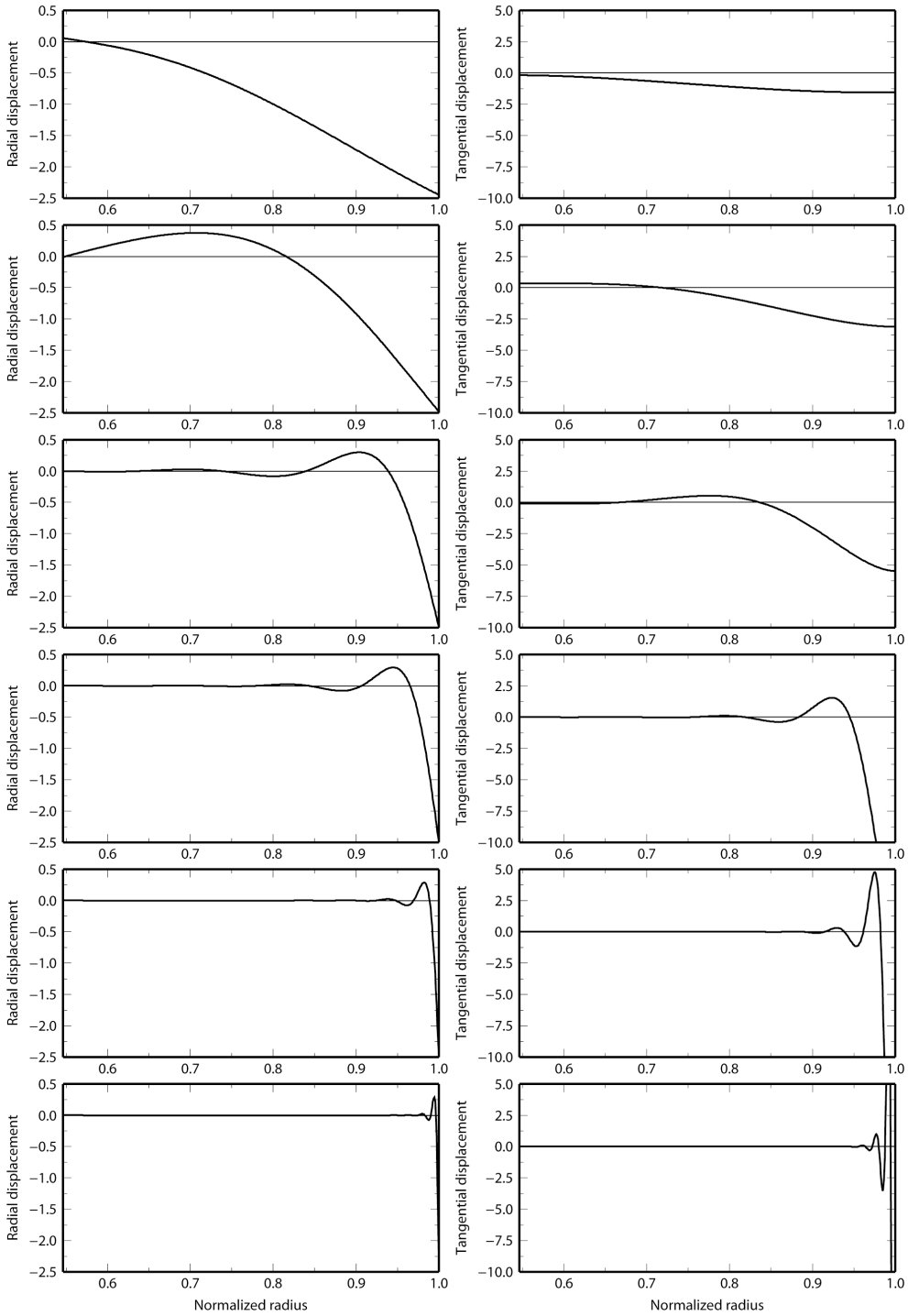

Figure 2.7: Degree-2 radial, $U(t)$ and tangential, $V(t)$, displacements (left and right pannels, respectively) at increasing times $t = 10^2$, 10^3, 10^4, 10^6, 10^8 kyr, 10^{10} kyr (from top to bottom).

parts of this layer.

In view of this and eq. (2.58), compositional stratifications achieve the isostatic equilibrium by means of mass rearrangement confined in an infinitesimally-thin superficial layer that compensates the weight of the load. This behaviour is comparable to the findings of Pekeris and Accad (1972) in the frequency ω-domain for static perturbations of the inviscid core, and corresponds to their findings if the viscosity is reduced to $\nu \to 0$.

2.5 Conclusion

From the analysis of the analytical solution of the self-compressed compressible sphere (Cambiotti and Sabadini, 2010), we have shown that both, compressional and stable compositional stratifications, achieve the isostatic equilibrium with surface loading, although in very different ways. For compressional stratifications, the isostatic equilibrium yields mass rearrangement within the whole mantle, whereas for stable compositional stratifications, buoyancy forces due to relaxation of compositional modes bring particles back to the initial position of hydrostatic equilibrium as prescribed by the momentum equation for an inviscid body (Longman, 1963). Due to the fact, that perturbations within an infinitesimally-thin superficial layer provides isostatic compensation of surface loading, the first-order perturbation theory demands a divergent long-period tangential flux of material at the Earth surface as described in Cambiotti and Sabadini (2010).

Perturbations of the interfaces of the layers of the Earth model yields surface-density perturbations at those interfaces that are dealt with by boundary conditions comparable to those used for surface loading. As a consequence, isostatic compensation of surface loading and of the mantle bumping into the inviscid core do not differ from a physical point of view. This supports our arguments against Denis *et al.* (1998) who criticised the conditions for static perturbations at the CMB proposed by Smylie and Mansinha (1971) and Chinnery (1975), as discussed in section 1.3.3. Furthermore, for stable compositional stratifications, we obtain isostatic perturbations of viscoelastic Earth models due to surface loading similar to those obtained by Pekeris and Accad (1972), where mass rearrangement is confined to an infinitesimally thin layer that compensates the weight of the loading.

Part II

GRAVITATIONAL SEISMOLOGY

Abstract

Mass redistribution caused by giant earthquakes is made visible by its long-wavelength gravity signature, nowadays detectable by the Gravity Recovery And Climate Experiment (GRACE) space mission (Gross and Chao, 2001). The scientific community has used GRACE data for studying the three major seismic events in the past decade, the 2004 Sumatran (Han *et al.*, 2006; de Linage *et al.*, 2009; Cambiotti *et al.*, 2011a; Broerse *et al.*, 2011), 2010 Maule (Heki and Matsuo, 2010; Han *et al.*, 2010) and 2011 Tohoku (Matsuo and Heki, 2011; Zhou *et al.*, 2011) earthquakes. These megathrust earthquakes occur within subduction environments of fast converging oceanic and continental plates, and cause volume changes of rocks in the surrounding of the fault, as well as deformation of the Earth surface and internal layer boundaries with density contrasts. Furthermore, due to the uplift of the ocean floor, they also displace ocean water away from the near field, the gravitational effect of which is comparable with that from mass rearrangement within the solid Earth (de Linage *et al.*, 2009; Cambiotti *et al.*, 2011a; Broerse *et al.*, 2011).

In Chapter 3 we discuss the 2004 Sumatran earthquake on the basis of a novel treatment of the boundary conditions at the Earth surface and of the Poisson equation, aimed to model ocean water redistribution due to earthquakes by means of a thick global ocean layer and separate gravitational potential perturbations due to volume changes from those due to the advection of the initial density field. The analysis of GRACE Level 2 data time series from the Center for Space Research (CSR) and GeoForschungs- Zentrum (GFZ) allows us to estimate the co-seismic gravity signature. It is characterized by a bipolar pattern where the north-eastern negative pole (in the foot-wall side of the fault plane), with minimum gravity anomaly of $-12.7 \pm 0.9\,\mu$Gal, is twice as large as the south-western positive pole (in the hanging-wall side), with maximum gravity anomaly of $+6.1 \pm 1.5\,\mu$Gal.

We demonstrate here that adequate Earth and dislocation models are required to properly interpret GRACE data from comparison between compressible and incompressible self-gravitating Earth models and seismic source models located at different depths, in the crust and uppermost part of the lithospheric mantle. Owing to the novel treatment of the boundary conditions at the Earth surface and of the Poisson equation, we are able to prove that the spatial asymmetry of the co-seismic gravity anomaly towards the nega-

tive pole is not due to a large dilatation of the crust as proposed by Han *et al.* (2006). We show that the large dilatation obtained by Han *et al.* (2006) is actually a dilatation localized at the fault discontinuity, the gravitational effect of which is however compensated by an opposite contribution from topography due to the uplifted crust. We then discuss the importance of discriminating the effects of co-seismic volume changes in the layers of the Earth from the dilatation localized at the fault discontinuity. Otherwise, because the latter dominates over the former, we should conclude that thrust earthquakes cause an overall dilatation of the crust, and this is not physically sound because it does not reflect the pattern of compression and extension induced by the seismic forcing. The overall negative anomaly is rather mainly due to the additional gravitational effects of the ocean water that is displaced away from the near field due to the uplift of the ocean floor, as first indicated by de Linage *et al.* (2009). Furthermore, we discuss the sensitivity of the most robust estimates from GRACE data analysis, consisting of the peak-to-peak gravity anomaly and an asymmetry coefficient given by the ratio of the negative gravity anomaly over the positive anomaly, to seismic source depths and dip angles. This allows us to exploit space gravity data for the first time to help to constrain Centroid Momentum Tensor (CMT) seismic models of the 2004 Sumatran earthquake and to conclude that the seismic moment has been mainly released in the lower crust rather than in the lithospheric mantle.

In Chapter 4 we use this new physics in order to develop a novel procedure for the inversion of the principal seismic source parameters (hypocentre and moment tensor) of large earthquakes relying solely on space gravity data. This procedure, which complements traditional seismology and we name Gravitational Centroid Moment Tensor (GCMT) analysis, is applied for the first time to the 2011 Tohoku earthquake. Rather than analysing the GRACE Level 2 data in the spatial domain as done in previous works, we deal with space gravity data in the spectral domain of Slepian functions. This allow us to spatially localize the long-wavelength gravity anomalies observed by the GRACE space mission and obtain the independent components of the signal in the surrounding of the earthquake. We thus invert this data set and find two distinct seismic solutions. One consistent with previous seismological solutions, with moment magnitude $M_W = 9.1$, dip angle 13° and located in the forearc crust of Japan. The other has a greater moment magnitude, $M_W = 9.2$, a steeper dip angle, 19°, and is located beneath the Japan trench at 37.8N, 143.9E, within the oceanic mantle.

Space gravity data thus help us to gain deep insight into the physics of megathrust earthquakes in terms of huge mass rearrangement within the crust and lithospheric mantle, and ocean water redistribution

Chapter 3

Mass rearrangement caused by the 2004 Sumatran earthquake

Co–seismic gravitational potential perturbations are made visible from GRACE space mission (Gross and Chao, 2001; Mikhailov *et al.*, 2004; Sabadini *et al.*, 2005; Han *et al.* 2006; de Linage *et al.*, 2009). We herein analyze long–wavelength co–seismic geoid and gravity anomalies caused by the 2004 Sumatran earthquake by means of a compressible self–gravitating Earth model, that is fully realistic as it builds on PREM (Dziewonski and Anderson, 1981) and represents the elastic limit of viscoelastic models, recently used for post–glacial rebound studies (Cambiotti *et al.*, 2010) and developed for co–seismic studies by Smylie and Mansinha (1971) and Sun and Okubo (1993). Thus, we overcome the limitation of assuming incompressibility in co–seismic studies (Sabadini *et al.*, 2005; Melini *et al.*, 2010) or the approximation of compressibility based on the Gilbert and Backus (1968) analytical solutions (Cambiotti *et al.*, 2009) used in Sabadini *et al.* (2008) to quantify the effects of the 2004 Sumatran earthquake on the Earth's rotation.

The 2004 Sumatran earthquake was one of the strongest non–periodic gravity variations that occurred at the Earth's surface in the last decade. However, the analysis of the co–seismic signature is quite challenging due to the peculiar noise present in the GRACE data, the so–called stripes, that is particularly strong at equatorial latitudes, and to the contamination that originates from post–seismic perturbations and other phenomena occurring in the Sumatran region, such as hydrological and residual ocean circulation cycles. Then, we devote particular attention to removing those signals other than the co–seismic signature from GRACE data time series in order to provide a realistic comparison between observations and models.

In order to correctly interpret the mass rearrangement caused by the 2004 Sumatran earthquakes, we extend the classic theory for the modelling of co–seismic gravity anomalies. Differently from Smylie and Mansinha (1971) and Sun and Okubo (1993), we decompose the Poisson equation in order to discriminate between gravity anomalies due to volume and topography changes; we can thus address the style of deformation, dilatational versus compressional, without the limitations suffered by plane half–space models, as in Han *et al.* (2006). Furthermore, we refine the approaches used in Han *et al.* (2006) and de Linage *et al.* (2009) for modelling the gravitational effect of ocean water redistribution by developing a self–consistent treatment of the global ocean layer of PREM. This novel theoretical treatment allows us to discuss in detail the different interpretations of the GRACE data proposed in the previous works, which ascribed the

observed pattern of the co–seismic gravity anomaly to the co–seismic dilatation within the crust (Han *et al.*, 2006) or to ocean water redistribution (de Linage *et al.*, 2009). Then, similar to the concept suggested by Gross and Chao (2006) for space–based Earth rotation measurements, we exploit gravity data from the GRACE space mission to help constrain the seismic source model of the 2004 Sumatran earthquake obtained by the multiple Centroid Momentum Tensor (CMT) source analysis of Tsai *et al.* (2005).

3.1 Extension of the classic theory

The perturbation of the gravitational potential ϕ^{Δ} due to an earthquakes is the results of density perturbations of the Earth caused by volume changes of the rock and the advection of the initial density field of the planet, which also includes the contribution from topography perturbations of the internal boundaries and the Earth surface. It satisfies the Poisson equation

$$\nabla^2 \phi^{\Delta} = -C \, (\rho_0 \, \Delta + \boldsymbol{u} \cdot \mathbf{e}_r \, \partial_r \rho_0) \tag{3.1}$$

where ρ_0, Δ, $\mathbf{u}$ and $\mathbf{e}_r$ are the initial density, the volume change, the displacement vector and the radial unit vector, and, for brevity, we have defined $C = 4\,\pi\,G$, with G being the universal gravitational constant.

By solving the momentum and Poisson equations for the elastic mantle and imposing the boundary conditions at the core–mantle boundary and the Earth surface, as described in Chapter 1, we obtain the displacement and the gravitational potential perturbation at the Earth surface that can be compared with geodetic observations. However, we cannot distinguish between the contributions from the density perturbations within the different layer of the Earth model. Also, we cannot separate the contribution due to volume changes from that due to the advection of the initial density field.

To obtain the contribution to the gravitational potential due only to volume changes occuring in a single layer of the Earth, that we denoted with $\phi^{(1)}$, we should make use of the classic definition of the gravitational potential in terms of the volume integral of the ratio of the density distribution over the distance from the observation point $\mathbf{r}$

$$\phi^{(1)}(\mathbf{r}) = C \int_{\mathcal{V}} \frac{\rho_0(\mathbf{r}')\,\Delta(\mathbf{r}')}{|\mathbf{r}-\mathbf{r}'|}\,dV' \tag{3.2}$$

where $\mathcal{V}$ is the 3–D volume of the layer. For an observation point at the Earth surface a, after the expansion in spherical harmonics, eq. (3.2) becomes (Gross and Chao, 2006)

$$\Phi^{(1)}_{\ell m}(a) = \frac{4\,\pi\,G}{a^{\ell+1}\,(2\,\ell+1)} \int_I \rho_0\,\chi_{\ell m}\,r^{\ell+2}\,dr \tag{3.3}$$

where $\Phi^{(1)}_{\ell m}$ and $\chi_{\ell m}$ are the degree–ℓ and order–m spherical harmonic coefficients of the gravitational potential $\phi^{(1)}$ and the volume change Δ, and $I = [r_B, r_T]$ is the radial interval of the layer of which we are considering the contribution from volume changes, with r_B and r_T being the radii of the bottom and top interfaces.

For each harmonic degree and order, this approach require the calculation of volume changes $\chi_{\ell m}$ in the radial interval of the layer of the Earth and their integration entering eq. (3.3). Instead of this classic approach, we propose a novel method that, in addition to computational advantages, allows to point out an important aspect of the way in which the seismic source is taken into account that, if neglected, can lead to erroneous interpretations of the style of deformation (dilatational versus compressional).

We decompose the gravitational potential ϕ^{Δ} into the contribution $\phi^{(1)}$ due only to volume changes within the radial interval I of the layer, and the remaining contribution $\phi^{(2)}$ from all other sources of density perturbations (i.e., volume changes in other layers and the advection of the initial density field)

$$\phi^{\Delta} = \phi^{(1)} + \phi^{(2)} \tag{3.4}$$

Owing to the linearity of the Poisson equation, the two potentials satisfy the following Poisson equations

$$\nabla^2\phi^{(1)} = -C\,\rho_0\,\Delta\,H_I \tag{3.5}$$

$$\nabla^2\phi^{(2)} = -C\,\rho_0\,\Delta\,(1-H_I) - C\,\boldsymbol{u}\cdot\mathbf{e}_r\,\partial_r\rho_0 \tag{3.6}$$

where H_I is the characteristic function of the interval I

$$H_I = \begin{cases} 1 & r \in I \\ 0 & r \notin I \end{cases} \tag{3.7}$$

Note that the RHS of eq. (3.5) describes the density perturbation due only to volume changes within the interval I, whereas the RHS of eq. (3.6) is the remaining density perturbation. This decomposition formally affects the momentum equation, where the gravity perturbation $-\boldsymbol{\nabla}\phi^{\Delta}$ is replaced by the sum of the two gravity perturbations $-\boldsymbol{\nabla}\phi^{(1)} - \boldsymbol{\nabla}\phi^{(2)}$, but this does not mean that we are altering the body forces.

After spherical harmonic expansion, eqs (3.5)–(3.6) become

$$\nabla^2\Phi^{(1)}_{\ell m} = -C\,\rho_0\,\chi_{\ell m}\,H_I \tag{3.8}$$

$$\nabla^2\Phi^{(2)}_{\ell m} = -C\,\rho_0\,\chi_{\ell m}\,(1 - H_I) - C\,U_{\ell m}\,\partial_r\rho_0 \tag{3.9}$$

where $\Phi^{(2)}_{\ell m}$ and $U_{\ell m}$ are the degree–ℓ and order–m spherical harmonic coefficients of the potential $\phi^{(2)}$ and the radial displacement $\mathbf{u}\cdot\mathbf{e}_r$. By applying the Gauss theorem at the Poisson equations (3.8)–(3.9) within a volume embedded in an infinitesimal pill–box at the internal boundaries and at the Earth surface, it can be shown that the potential stresses $Q^{(1)}_{\ell m}$ and $Q^{(2)}_{\ell m}$ for the potentials $\Phi^{(1)}_{\ell m}$ and $\Phi^{(2)}_{\ell m}$ must be defined as follows

$$Q^{(1)}_{\ell m} = \partial_r\Phi^{(1)}_{\ell m} + \frac{\ell+1}{r}\,\Phi^{(1)}_{\ell m} \tag{3.10}$$

$$Q^{(2)}_{\ell m} = \partial_r\Phi^{(2)}_{\ell m} + \frac{\ell+1}{r}\,\Phi^{(2)}_{\ell m} + C\,\rho\,U_{\ell m} \tag{3.11}$$

Note that the total potential stress $Q_{\ell m}$ defined in eq. (1.79) is given by the sum of the two potential stresses

$$Q_{\ell m} = Q^{(1)}_{\ell m} + Q^{(2)}_{\ell m} \tag{3.12}$$

and that both potential stresses must be continuous across the internal boundaries with density contrast and that they are zero at the free Earth surface (we are only considering the seismic forces, not surface loading and external potentials). In this way, indeed, the only potential $\phi^{(2)}$ accounts for the density perturbations associated with topography perturbations of the internal boundaries and the Earth surface.

In order to simultaneously solve the momentum equation and the two Poisson equations (3.8)–(3.9), similarly to the spheroidal 6–vector solution introduced in Chapter 1, eq. (1.78), herein we define the spheroidal 8–vector solution $\mathbf{y}_{\ell m}$

$$\mathbf{y}_{\ell m} = \left(U_{\ell m},\, V_{\ell m},\, R_{\ell m},\, W_{\ell m},\, \Phi^{(1)}_{\ell m},\, Q^{(1)}_{\ell m},\, \Phi^{(2)}_{\ell m},\, Q^{(2)}_{\ell m}\right)^T \tag{3.13}$$

Here T stands for the transpose, and $V_{\ell m}$, $R_{\ell m}$ and $S_{\ell m}$ are the degree–ℓ order–m spherical harmonic coefficients of spheroidal tangential displacements and spheroidal radial and tangential stresses. By definition, the spheroidal solution 8–vector solutions is continuous across the internal boundaries and satisfies the following condition at the free Earth surface

$$\mathbf{P}_1 \mathbf{y}_{\ell m}(a) = \mathbf{0} \tag{3.14}$$

where $\mathbf{P}_1$ is the projector for the 3–rd, 4–th, 6–th and 8–th components. Afterwards, we will however consider different Earth surface boundary conditions in order to account for a thick global ocean layer at the top of the solid Earth.

After spherical harmonic expansion, we cast the spheroidal radial and tangential components of the momentum equation, eqs (1.70)–(1.71), and the two Poisson equations (3.8)–(3.9) into the following linear differential system

$$\partial_r \mathbf{y}_{\ell m} = \mathbf{A}_\ell \, \mathbf{y}_{\ell m} - \mathbf{m}_{\ell m} \tag{3.15}$$

where $\mathbf{A}_\ell$ and $\mathbf{m}_{\ell m}$ are the block 8×8–matrix and the 8–vector describing the seismic forces defined as

$$\mathbf{A}_\ell = \left[\begin{array}{c} \mathbf{A}_\ell^{(U)} \\ \mathbf{A}_\ell^{(L)} \end{array} \right] \tag{3.16}$$

$$\boldsymbol{m}_{\ell m}(r) = \frac{M}{r^2} \left(\frac{\delta(r-r_0)}{r_0}\, \boldsymbol{m}_{\ell m}^{(0)} + \frac{\partial \delta(r-r_0)}{\partial r}\, \boldsymbol{m}_{\ell m}^{(1)} \right) \tag{3.17}$$

with M, r_S and $\delta(r-r_S)$ being the seismic moment, the radial distance from the Earth centre of the point–like seismic source and the Dirac delta. The 4×8–matrices $\mathbf{A}_\ell^{(U)}$ and $\mathbf{A}_\ell^{(L)}$ entering eq. (3.16) are given by

$$\mathbf{A}_\ell^{(U)}(r) = \left(\begin{array}{cccc} -\frac{2\,\lambda}{r\,\beta} & \frac{\ell(\ell+1)\,\lambda}{r\,\beta} & \frac{1}{\beta} & 0 \\ -\frac{1}{r} & \frac{1}{r} & 0 & \frac{1}{\mu} \\ \frac{4}{r^2}\left(\frac{3\,\kappa\,\mu}{\beta} - g\,\rho\,r\right) & \frac{\ell(\ell+1)}{r^2}\left(g\,\rho\,r - \frac{6\,\kappa\,\mu}{\beta}\right) & -\frac{4\,\mu}{r\,\beta} & \frac{\ell(\ell+1)}{r} \\ \frac{1}{r^2}\left(g\,\rho\,r - \frac{6\,\kappa\,\mu}{\beta}\right) & \frac{2\mu}{r^2}\left[2\,\ell(\ell+1)\left(1-\frac{\mu}{\beta}\right)-1\right] & -\frac{\lambda}{r\,\beta} & -\frac{3}{r} \end{array} \right. \quad \cdots$$

$$\left. \begin{array}{cccc} 0 & 0 & 0 & 0 \\ 0 & 0 & 0 & 0 \\ -\frac{(\ell+1)\,\rho}{r} & \rho & -\frac{(\ell+1)\,\rho}{r} & \rho \\ \frac{\rho}{r} & 0 & \frac{\rho}{r} & 0 \end{array} \right) \tag{3.18}$$

$$\mathbf{A}_\ell^{(L)}(r \in I) = \left(\begin{array}{cccc} 0 & 0 & 0 & 0 \\ -\frac{4\,C\,\rho\,\mu}{r\,\beta} & \frac{2\,\ell(\ell+1)\,C\,\rho\,\mu}{r\,\beta} & -\frac{C\,\rho}{\beta} & 0 \\ -C\,\rho & 0 & 0 & 0 \\ -\frac{C\,\rho}{r}\left[\ell+1-\frac{4\,\mu}{\beta}\right] & \frac{\ell(\ell+1)\,C\,\rho\,\lambda}{r\,\beta} & \frac{C\,\rho}{\beta} & 0 \end{array} \right. \quad \cdots$$

$$\left. \begin{array}{cccc} -\frac{\ell+1}{r} & 1 & 0 & 0 \\ 0 & \frac{\ell-1}{r} & 0 & 0 \\ 0 & 0 & -\frac{\ell+1}{r} & 1 \\ 0 & 0 & 0 & \frac{\ell-1}{r} \end{array} \right) \tag{3.19}$$

$$\mathbf{A}_\ell^{(L)}(r \notin I) = \begin{pmatrix} 0 & 0 & 0 & 0 & -\frac{\ell+1}{r} & 1 & 0 & 0 \\ 0 & 0 & 0 & 0 & 0 & \frac{\ell-1}{r} & 0 & 0 \\ -C\,\rho & 0 & 0 & 0 & 0 & 0 & -\frac{\ell+1}{r} & 1 \\ -\frac{(\ell+1)\,C\,\rho}{r} & \frac{\ell(\ell+1)\,C\,\rho}{r} & 0 & 0 & 0 & 0 & 0 & \frac{\ell-1}{r} \end{pmatrix} \tag{3.20}$$

where μ, λ, κ and g are the two parameters of Lamé, the bulk modulus and the initial gravity, respectively, and β is the elastic parameter given by eq. (1.82). Note that the form of the lower matrix $\mathbf{A}_\ell^{(L)}$ depends on whether the radial distance from the Earth's center r is within or outside of the interval I defining the layer of which we are separately considering volume changes, eqs (3.19) and (3.20), respectively. The expressions for $\mathbf{m}_{\ell m}^{(0)}$ and $\mathbf{m}_{\ell m}^{(1)}$ entering eq. (3.17) are similar to those obtained for the classic seismic problem, eq. (1.228), but for the fact they have two extra zero components

$$\mathbf{m}_{\ell m}^{(x)} = \left(0,\, 0,\, m_{\ell m}^{R(x)},\, m_{\ell m}^{S(x)},\, 0,\, 0,\, 0,\, 0\right)^T \tag{3.21}$$

where $m_{\ell m}^{R(x)}$ and $m_{\ell m}^{S(x)}$ are given by eqs (1.214)-(1.225), for $x = 0, 1$.

The solution of the dishomogeneous differential system 3.15) yields

$$\mathbf{y}_{\ell m}(r) = \mathbf{\Pi}_\ell(r, r_C)\mathbf{I}_C\,\mathbf{C} - \mathbf{w}_{\ell m}(r) \tag{3.22}$$

where r_C is the core radius, $\mathbf{\Pi}$ the propagator matrix that solve the homogeneous differential system, and $\mathbf{w}_{\ell m}$ is given by

$$\mathbf{w}_{\ell m}(r) = H(r - r_S)\,\mathbf{\Pi}_\ell(r, r_S)$$

$$\frac{M}{r_S^2}\left[\mathbf{m}_{\ell m}^{(0)}(r_S) + \mathbf{A}_\ell(r_S)\,\mathbf{m}_{\ell m}^{(1)}(r_S) + \frac{2}{r_S}\,\mathbf{m}_{\ell m}^{(1)}(r_S)\right] \tag{3.23}$$

Also, $\mathbf{I}_C$ is the 8×4–matrix that describes the core–mantle boundary conditions and $\mathbf{C}$

is the 4–vector of constants of integration that must determined using the Earth surface boundary conditions. These boundary condition will be discussed in section 3.2.

3.1.1 Volume changes localized at the dip-slip fault discontinuities

Owing to this approach for the study of gravitational potential perturbations due to co-seismic volume changes, it is possible to clearly point out a specific feature of dip-slip faults. Let us consider the different cases of seismic sources located within or outside of the interval I where we evaluate the contribution due to co-seismic volume changes. It is well known from Smylie and Mansinha (1971), Takeuchi and Saito (1972) and eq. (3.22) that the seismic force is equivalently described by the step-like discontinuity of the spheroidal solution vector $\mathbf{y}_{\ell m}$ at the radial distance from the Earth centre r_S where the seismic source is located

$$[\mathbf{y}_{\ell m}(r_S)]^+_- = -\frac{M}{r_S^2}\left[\mathbf{m}^{(0)}_{\ell m}(r_S) + \mathbf{A}_\ell(r_S)\,\mathbf{m}^{(1)}_{\ell m}(r_S) + \frac{2}{r_S}\,\mathbf{m}^{(1)}_{\ell m}(r_S)\right] \tag{3.24}$$

Here, $[f(r)]^+_-$ indicates the discontinuity of the generic field f at r

$$[X(r)]^+_- = X(r^+) - X(r^-) \tag{3.25}$$

If the seismic source is outside of the radial interval I, $r_S \notin I$, the potential stresses $Q^{(1)}_{\ell m}$ and $Q^{(2)}_{\ell m}$ are continuous across r_S in view of eq. (3.20) and of the fact that the only non-zero components of $\mathbf{m}^{(0)}_{\ell m}$ and $\mathbf{m}^{(1)}_{\ell m}$ are the 3–rd and 4–th components, eq. (3.21). In contrast, if the seismic source is within the shell defined by the radial interval I, $r_S \in I$, the potential stresses $Q^{(1)}_{\ell m}$ and $Q^{(2)}_{\ell m}$ are discontinuous across r_S in view of eqs (3.19) and (3.21)

$$\left[Q^{(1)}_{\ell m}(r_S)\right]^+_- = -\delta_{0m}\,M\,\frac{(2\,\ell+1)\,G}{r_S^2}\,\frac{\rho(r_S)}{\beta(r_S)}\,\sin 2\delta\,\sin\gamma \tag{3.26}$$

$$\left[Q^{(2)}_{\ell m}(r_S)\right]^+_- = -\left[Q^{(1)}_{\ell m}(r_S)\right]^+_- \tag{3.27}$$

Here, δ, γ and δ_{0m} are the dip and slip angles of the seismic source and the Kronecker delta selecting only order-0 harmonic coefficients. Note that the discontinuities of $Q^{(1)}_{\ell m}$ and $Q^{(2)}_{\ell m}$ compensate for each other, eq. (3.27), according to the fact that the total potential stress $Q_{\ell m}$, eq. (3.12), must be continuous across r_S (Smylie and Mansinha, 1971).

This peculiar behavior of the potential stresses is explained by considering the discontinuity in the radial displacement due to the seismic source

$$[U_{\ell m}(r_S)]^+_- = \delta_{0m}\, M\, \frac{2\,\ell+1}{4\,\pi\, r_S^2}\, \frac{1}{\beta(r_S)}\, \sin 2\delta\, \sin\gamma \tag{3.28}$$

and the radial derivative of the radial displacement entering the geometric definition of volume changes $\chi_{\ell m}$, eq. (1.60). Indeed, the discontinuity of the radial displacement contributes with a volume change localized at the seismic source that we denote with $\chi^S_{\ell m}$

$$\chi^S_{\ell m} = [U_{\ell m}(r_S)]^+_-\, \delta(r - r_S) \tag{3.29}$$

As reflected by the dependence of eq. (3.28) on the slip angle γ, it should be noted that for reverse and thrust faults, such as that of Sumatran, eq. (3.29) describes a localized dilatation because $\gamma \in [0°, 180°]$. On the contrary, for normal faults, eq. (3.29) describes a localized compression because $\gamma \in [180°, 360°]$.

When the seismic source is within the radial interval I, the localized volume change χ^S also contribute to the gravitational potential perturbation $\Phi^{(1)}_{\ell m}$. By denoting its contribution with $\Phi^{(1S)}_{\ell m}$, from eqs (3.3) and (3.29)-(3.28), we obtain

$$\Phi^{(1S)}_{\ell m}(a) = \delta_{0m}\, M\, \frac{\rho_0(r_S)}{\beta(r_S)}\, \frac{G}{a}\, \sin 2\delta\, \sin\gamma\, \left(\frac{r_S}{a}\right)^\ell \tag{3.30}$$

As we will show in section 3.5, this contribution dominates over the gravitational po-

tential perturbations due to volume changes elsewhere the seismic source and mask the typical style of deformation in the surrounding of the fault that, for reverse and thrust earthquakes like the Sumatran event, is characterized by compression and dilatation in the foot- and hanging-wall sides of the fault plane, respectively. This contribution, if not properly accounted for, causes the local dilatation associated with the seismic source to be erroneously interpreted as dilatation in the surrounding of the fault, thus leading to the unphysical interpretation given by Han *et al.* (2006) that reverse and thrust faults cause an overall dilatation of crust.

It is noteworthy that we can obtain the gravitational perturbation due to volume changes in the surrounding of the fault, without including the effects of the localized volume change $\chi^S_{\ell m}$, by neglecting the discontinuities of the potential stresses $Q^{(1)}_{\ell m}$ and $Q^{(2)}_{\ell m}$, eqs (3.26)-(3.27). This means that eq. (3.20) should be used instead of eq. (3.19) for the matrix $\mathbf{A}_\ell(r_S)$ when we compute eq. (3.23), even if $r_S \in I$. This alteration of $\mathbf{A}_\ell(r_S)$ entering eq. (3.23) only has the effect of removing from the gravitational potential perturbations $\Phi^{(1)}_{\ell m}$ and $\Phi^{(2)}_{\ell m}$ the contributions due to the opposite discontinuities in the relevant potential stresses, eqs (3.26)-(3.27). This does not alter the radial, $U_{\ell m}$, and tangential, $V_{\ell m}$, displacements and the total gravitational potential perturbation $\Phi_{\ell m}$ because the gravitational potential perturbations due to these discontinuities cancel each other out and they then do not involve any effective volume force in the momentum equation.

3.2 Boundary conditions

Let us discuss how to derive the core-mantle boundary conditions for the sheroidal solution 8–vector and modify the Earth surface boundary conditions in order to account for the global ocean layer of PREM in a physical self-consistent way.

3.2.1 Core-mantle boundary

As pointed out by Longman (1962), volume changes are allowed within the inviscid core only for compressional stratifications. On the contrary, volume changes must be zero for compositional stratifications. However, both for compressional and compositional stratifications, the Poisson equation takes the same form as discussed in Chapter 1, eq.

(1.125). Here, for the sake of simplicity and because we are more interested in volume changes within the mantle rather than in the Longman (1962) paradox, we decided not to discriminate the gravitational potential due to volume changes in the core. We thus assume that the layer for which we are separately considering volume changes does not intersect the core, $I \cap [0, r_C] = \emptyset$. In this respect, eqs (3.8)-(3.9) and (3.10)-(3.11) become

$$\nabla_r^2 \Phi_{\ell m}^{(1)} = 0 \tag{3.31}$$

$$\nabla_r^2 \Phi_{\ell m}^{(2)} = \frac{C\,\partial_r \rho_0}{g}\,\left(\Phi_{\ell m}^{(1)} + \Phi_{\ell m}^{(2)}\right) \tag{3.32}$$

$$Q_{\ell m}^{(1)} = \partial_r \Phi_{\ell m}^{(1)} + \frac{\ell+1}{r}\,\Phi_{\ell m}^{(1)} \tag{3.33}$$

$$Q_{\ell m}^{(2)} = \partial_r \Phi_{\ell m}^{(2)} + \frac{\ell+1}{r}\,\Phi_{\ell m}^{(2)} - \frac{C\,\rho_0}{g}\,\left(\Phi_{\ell m}^{(1)} + \Phi_{\ell m}^{(2)}\right) \tag{3.34}$$

In view of the regularity conditions at the center of the Earth, we impose that

$$\lim_{r\to 0} \Phi_{\ell m}^{(1)}\, r^{-\ell} = A \tag{3.35}$$

$$\lim_{r\to 0} \Phi_{\ell m}^{(2)}\, r^{-\ell} = B \tag{3.36}$$

with A and B being two constants of integration. These conditions also reflect into conditions for the potential stresses that, from eqs (3.33)-(3.34), must satisfy the following regularity conditions

$$\lim_{r\to 0} Q_{\ell m}^{(1)}\, r^{-\ell+1} = (2\,\ell+1)\,A \tag{3.37}$$

$$\lim_{r\to 0} Q_{\ell m}^{(2)}\, r^{-\ell+1} = -3\,A + 2\,(\ell-1)\,B \tag{3.38}$$

Here we have utilized

$$\lim_{r\to 0}\frac{C\,\rho_0(r)\,r}{g(r)} = 3 \tag{3.39}$$

that holds for a finite initial density at the Earth centre. From these consideration, following Longman (1962), Smylie and Mansinha (1971) and Chinnery (1975), we thus impose the core-mantle boundary conditions

$$\mathbf{y}_{\ell m}(r_C^+) = \mathbf{I}_C\,\mathbf{C} \tag{3.40}$$

where $\mathbf{I}_C$ is the 8×4–matrix given by

$$\mathbf{I}_C = \begin{pmatrix} -\frac{\Phi_A^{(1)}(r_C)+\Phi_A^{(2)}(r_C)}{g(r_C)} & -\frac{\Phi_B^{(2)}(r_C)}{g(r_C)} & 0 & 1 \\ 0 & 0 & 1 & 0 \\ 0 & 0 & 0 & \rho(r_C^-)\,g(r_C) \\ 0 & 0 & 0 & 0 \\ \Phi_A^{(1)}(r_C) & 0 & 0 & 0 \\ Q_A^{(1)}(r_C) & 0 & 0 & 0 \\ \Phi_A^{(2)}(r_C) & \Phi_B^{(2)}(r_C) & 0 & 0 \\ Q_A^{(2)}(r_C) & Q_B^{(2)}(r_C) & 0 & C\,\rho(r_C^-) \end{pmatrix} \tag{3.41}$$

and $\mathbf{C}$ is the 4–vector of constants of integration that must be determined by means of the Earth surface boundary conditions

$$\mathbf{C} = (A,\,B,\,C,\,D)^T \tag{3.42}$$

The subscripts A and B in eq. (3.41) indicate solutions of the differential equations (3.31)-(3.32) obtained using the regularity conditions (3.35)-(3.38) with $(A=1, B=0)$ and $(A=0, B=1)$, respectively. Furthermore, the constants of integration C and D in eq. (3.42) describe the free slip at the core-mantle boundary and the isostatic compensation of the mantle bumping into the core, similarly to the classic theory for the

core-mantle boundary discussed in Chapter 1, section 1.3.3.

3.2.2 The self-consistent global ocean

We assume that the ocean behaves as an inviscid fluid with constant initial density ρ_w, i.e., $\partial_r \rho_w = 0$. In this respect, the Poisson equations for $\Phi^{(1)}_{\ell m}$ and $\Phi^{(2)}_{\ell m}$ coincide with those for the inviscid core and become the Laplace equations because the initial density is constant

$$\nabla^2_r \Phi^{(1)}_{\ell m} = 0 \tag{3.43}$$

$$\nabla^2_r \Phi^{(2)}_{\ell m} = 0 \tag{3.44}$$

Similarly, the potential stresses $Q^{(1)}_{\ell m}$ and $Q^{(2)}_{\ell m}$ are still given by eqs (3.33)-(3.34), once substituted ρ_w for ρ_0.

The solutions of eqs (3.43)-(3.44) yields

$$\Phi^{(1)}_{\ell m} = A_1\, r^{\ell} + B_1\, r^{-\ell-1} \tag{3.45}$$

$$\Phi^{(2)}_{\ell m} = A_2\, r^{\ell} + B_2\, r^{-\ell-1} \tag{3.46}$$

$$Q^{(1)}_{\ell m} = A_1\, (2\,\ell + 1)\, r^{\ell-1} \tag{3.47}$$

$$Q^{(2)}_{\ell m} = A_2\ (2\,\ell + 1 - Z(r)\, r)\ r^{\ell-1} - A_1\, Z(r)\, r^{\ell} - (B_1 + B_2)\ Z(r)\, r^{-\ell-1} \tag{3.48}$$

where A_j and B_j, with $j = 1, 2$, are four constants of integration and

$$Z(r) = \frac{C\,\rho_w}{g(r)} \tag{3.49}$$

Because, for the seismic problem, the top surface of the ocean is a free surface on which the radial displacement coincides with the geoid, the potential stresses are zero

$$Q_{\ell m}^{(1)}(b) = 0 \tag{3.50}$$

$$Q_{\ell m}^{(2)}(b) = 0 \tag{3.51}$$

with b being the radius of the Earth, including the global ocean layer. From eqs (3.47)-(3.48) evaluated at $r = b$, we thus obtain

$$A_1 = 0 \tag{3.52}$$

$$A_2 = \alpha(b)\ (B_1 + B_2) \tag{3.53}$$

where for brevity we have defined α as

$$\alpha(r) = \frac{Z(r)\, r^{-2\,\ell}}{2\,\ell + 1 - Z(r)\, r} \tag{3.54}$$

Then eqs (3.45)-(3.48) yield

$$\Phi_{\ell m}^{(1)} = B_1\, r^{-\ell-1} \tag{3.55}$$

$$\Phi_{\ell m}^{(2)} = B_1\, \alpha(b)\, r^{\ell} + B_2\, \left(\alpha(b)\, r^{\ell}\, + r^{-\ell-1}\right) \tag{3.56}$$

$$Q_{\ell m}^{(1)} = 0 \tag{3.57}$$

$$Q_{\ell m}^{(2)} = (B_1 + B_2)\ Z(r)\, r^{-\ell-1}\ \left[\frac{\alpha(b)}{\alpha(r)} - 1\right] \tag{3.58}$$

In order to determine B_1 and B_2, we must consider proper boundary conditions at the bottom of the ocean, namely at the solid Earth radius a. Following Longman (1962), Smylie and Mansinha (1971) and Chinnery (1975), we impose

$$\mathbf{y}_{\ell m}(a^-) = \mathbf{I}_O\, \mathbf{O} \tag{3.59}$$

where $\mathbf{I}_O$ is the 8×4–matrix defined as

$$\mathbf{I}_O = \begin{pmatrix} -\frac{\alpha(b)\, a^\ell + a^{-\ell-1}}{g(a)} & -\frac{\alpha(b)\, a^\ell + a^{-\ell-1}}{g(a)} & 0 & 1 \\ 0 & 0 & 1 & 0 \\ 0 & 0 & 0 & \rho_w\, g(a) \\ 0 & 0 & 0 & 0 \\ a^{-(\ell+1)} & 0 & 0 & 0 \\ 0 & 0 & 0 & 0 \\ \alpha(b)\, a^\ell & \alpha(b)\, a^\ell + a^{-\ell-1} & 0 & 0 \\ \frac{Z(a)}{a^{\ell+1}} \left[\frac{\alpha(b)}{\alpha(a)} - 1\right] & \frac{Z(a)}{a^{\ell+1}} \left[\frac{\alpha(b)}{\alpha(a)} - 1\right] & 0 & C\, \rho_w \end{pmatrix} \tag{3.60}$$

and $\mathbf{O}$ is the 4–vector consisting of the constants of integration

$$\mathbf{O} = (B_1,\, B_2,\, B_3,\, B_4)^T \tag{3.61}$$

The two constants B_1 and B_2 describe the gravitational perturbations $\Phi^{(1)}_{\ell m}$ and $\Phi^{(2)}_{\ell m}$ within the ocean via eqs (3.55)-(3.56), while B_3 and B_4 take into account the free slip and loading due to the water redistribution coming from the gap between the geoid and the radial displacement at the solid-fluid interface.

Let us now consider that the spheroidal 8-vector solution $\mathbf{y}_{\ell m}$ is determined with the four constants of integration $\mathbf{C}$ of the core-mantle boundary conditions (3.40). Then, from eqs (3.22) and (3.59), we obtain the following block matrix equations

$$\left[\; \mathbf{\Pi}_\ell(a, r_C)\, \mathbf{I}_C,\; -\mathbf{I}_O \;\right] \left[\begin{array}{c} \mathbf{C} \\ \mathbf{O} \end{array} \right] = \mathbf{w}_{\ell m}(a) \tag{3.62}$$

which allow us to obtain the eight constants of integration $\mathbf{C}$ and $\mathbf{O}$

$$\begin{bmatrix} \mathbf{C} \\ \mathbf{O} \end{bmatrix} = \begin{bmatrix} \mathbf{\Pi}_\ell(a, r_C)\, \mathbf{I}_C,\ -\mathbf{I}_O \end{bmatrix}^{-1} \mathbf{w}_{\ell m}(a) \tag{3.63}$$

The case of perturbations of harmonic degree $\ell = 1$ must also be considered in order to discriminate between gravitational perturbations due to volume, $\Phi^{(1)}_{1m}$, and topography, $\Phi^{(2)}_{1m}$, changes that can be non-zero, though the total degree–1 gravitational perturbations Φ_{1m} must be zero in view of the conservation of the center of mass (Farrell, 1972, pp. 774–777; Sun and Okubo, 1993). In Appendix A.4, we discuss the additional considerations that this case requires.

We have now fully determined the perturbations both within the solid Earth and the inviscid ocean. At the same time, we have accounted for the interaction between the ocean and solid Earth consisting of the ocean water redistribution and its loading effect. It is noteworthy that for an infinitesimally thin ocean layer, in the limit of $b \to a$, our approach reproduces exactly the sea level theory discussed by Farrell and Clark (1976) in the case of a global ocean. Nevertheless, the present approach cannot be extended to a non spherically symmetric ocean; thus, it cannot consider the continents. On the other hand, it allows a correct description of the effect of the thickness of the ocean layer, which instead is neglected by the sea level theory of Farrell and Clark (1976). For all intents and purposes, the effects for the Earth are small, because $b - a \approx 3\,\mathrm{km}$, and can be ignored.

3.3 Ocean water redistribution

We present results for a compressible self–gravitating Earth model based on PREM (Dziewonski and Anderson, 1981) taking into account the ocean water redistribution by means of our modified boundary conditions at the fluid–solid boundary between the solid Earth and the global ocean layer. We will refer to this model as Ocean–PREM (also abbreviated as O–PREM). In order to quntify the impact of the ocean water redistribution on the gravitational potential perturbation, these results will be compared with those obtain for the same Earth model, but without including the effects of the ocean water redistribution, i.e., implementing the classic boundary conditions for a stress free solid

Earth surface, eq. (3.14). We refer to the latter model as Solid–PREM (also abbreviated as S–PREM). We describe the 2004 Sumatran earthquakes using the seismic source model of Tsai *et al.* (2005), which is composed of five point–like sources at the same depth of 25 km, below the Moho discontinuity that is at 21.4 km depth for PREM, and distributed along the strike of the fault. The total seismic moment is $N_S = 1.17 \times 10^{23}$ N m, corresponding to a moment magnitude of 9.3. Although more realistic slip distributions over the fault are typically used to explain seismic waves and ground motions from GPS (Ammon *et al.* 2005), the differences in the gravitational potential perturbations with respect to the use of the simple seismic source model of Tsai *et al.* (2005) are expected to be small at the limited spatial resolution of GRACE data. For this reason, the analysis will concerns only long–wavelength geoid anomalies, that we obtain by applying an isotropic Gaussian filter with half–width of 350 km (Wahr *et al.*, 1998). Slip distribution along dip instead affects the long–wavelength seismic signal, a sensitivity that we will use in section 3.4.2 to obtain information about the depth at which the largest seismic moment has been released.

In order to gain insight into the physics of ocean water redistribution caused by the 2004 Sumatran earthquake, particularly regarding the asymmetry between the negative and positive gravitational anomalies observed in GRACE data (Han *et al.*, 2006; de Linage *et al.*, 2009), we begin by considering geoid anomalies ΔG rather than gravity anomalies δg. This way, we can directly compare geoid anomalies ΔG and radial displacements $\mathbf{u} \cdot \mathbf{e}_r$ in terms of sea level variations ΔS

$$\Delta S = \Delta G - \mathbf{u} \cdot \mathbf{e}_r \tag{3.64}$$

that describes the height of the column of ocean water that loads the Earth with respect to the initial state of hydrostatic equilibrium. To better isolate the main features of the co–seismic phenomenon, we focus on the maximum, ΔG_{max}, and minimum, ΔG_{min}, geoid anomalies and we investigate the main physical processes affecting the asymmetry coefficient AS, that we define as the ratio between the absolute values of the maximum positive and negative geoid anomalies

$$AS = \left| \frac{\Delta G_{min}}{\Delta G_{max}} \right| \tag{3.65}$$

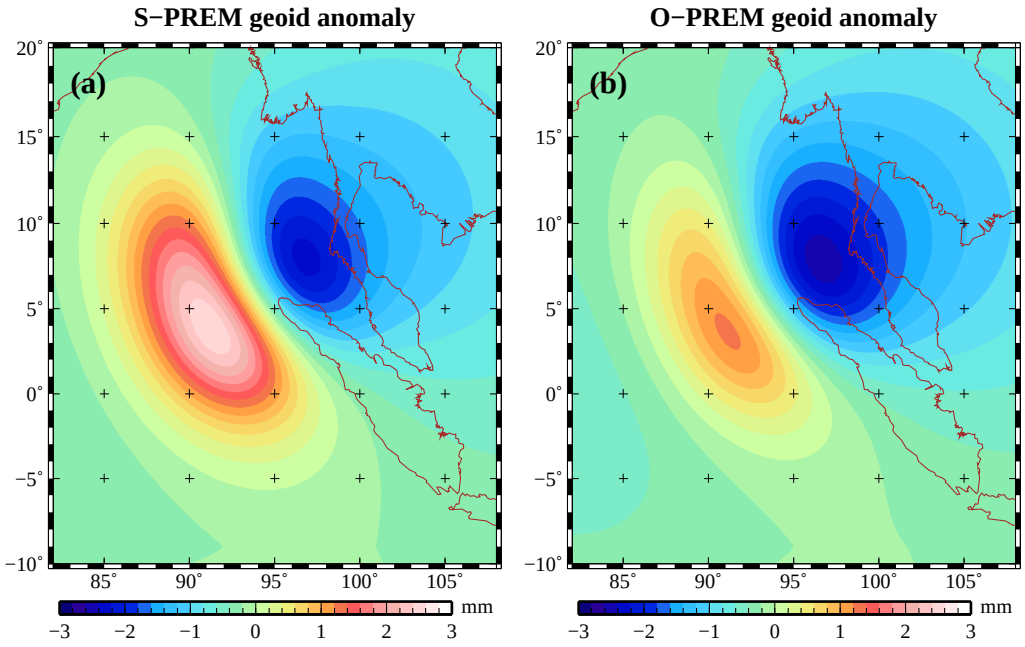

Figure 3.1: Co–seismic geoid anomalies for compressible S–PREM (a) and O–PREM (b), after the 350 km Gaussian filtering.

Fig. 3.1 compares the co–seismic geoid anomalies for the Solid– and Ocean–PREM (pannels a and b, respectively). Both patterns are bipolar, with the positive and negative poles in the hanging– and foot–wall sides of the fault plane, respectively, although the negative pole is more pronounced when we include the gravitational effects of the ocean water redistribution. For Solid–PREM, we obtain maximum and minimum geoid anomalies of $+2.57$ mm and -2.28 mm, respectively, and the asymmetry coefficient is $AS = 0.88$. The positive geoid anomaly results slightly greater in absolute value than the negative one. This indicates that, even if the 2004 Sumatran earthquake caused a large dilatation within the crust, as suggested by Han *et al.* (2006), this dilatation is not sufficiently large to explain the spatial asymmetries observed in GRACE data. On the contrary, for Ocean–PREM, we obtain maximum and minimum geoid anomalies of $+1.24$ mm and -2.52 mm, respectively, and the asymmetry coefficient is $AS = 2.03$. As shown in fig. 3.2, the geoid anomalies due to ocean water redistribution, which we obtain by subtracting the geoid anomalies for Ocean–PREM (fig. 3.1b) from those for Solid–PREM (fig. 3.1a), are comparable in magnitude with the geoid anomalies for

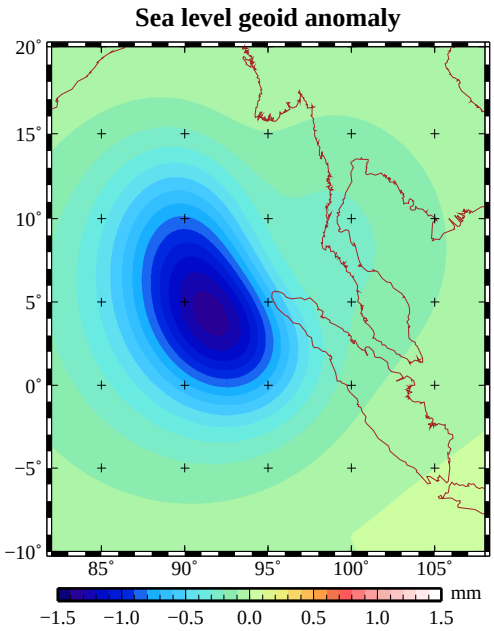

Figure 3.2: Co–seismic geoid anomalies due to ocean water redistribution, obtained subtracting compressible O–PREM and S–PREM geoid anomalies shown in fig. 3.1, after the 350 km Gaussian filtering.

Solid–PREM and negative almost everywhere, with a minimum value of -1.36 mm.

In order to better understand how ocean water redistributes in response to the earthquake, we show in fig. 3.3 the topography perturbations of the solid Earth surface for both Solid– and Ocean–PREM (pannels a and b, respectively), after the 350 km Gaussian filtering for the sake of comparison with the geoid anomalies shown in fig. 3.1. For Solid–PREM, the predicted maximum uplift, $+93.1$ mm, is greater in magnitude by about a factor 5 than the maximum downdrop, -18.3 mm. From the comparison with Ocean–PREM, we also note that the loading due to water redistribution has a negligible effect on the topography perturbations of the ocean floor because the maximum uplift, $+97.0$ mm, and downdrop, -18.6 mm, differ from those for S–PREM by less than 3 per cent. These differences are, however, comparable with the geoid anomalies shown in fig. 3.1. The fact that the radial displacement is larger than the geoid anomaly by almost two order of magnitude indicates that the co–seismic sea level variation, eq. (3.64), is mainly characterized by the variation of the topography rather than that of the geoid. Particularly, the uplift of the ocean floor displaces way ocean water from the near field,

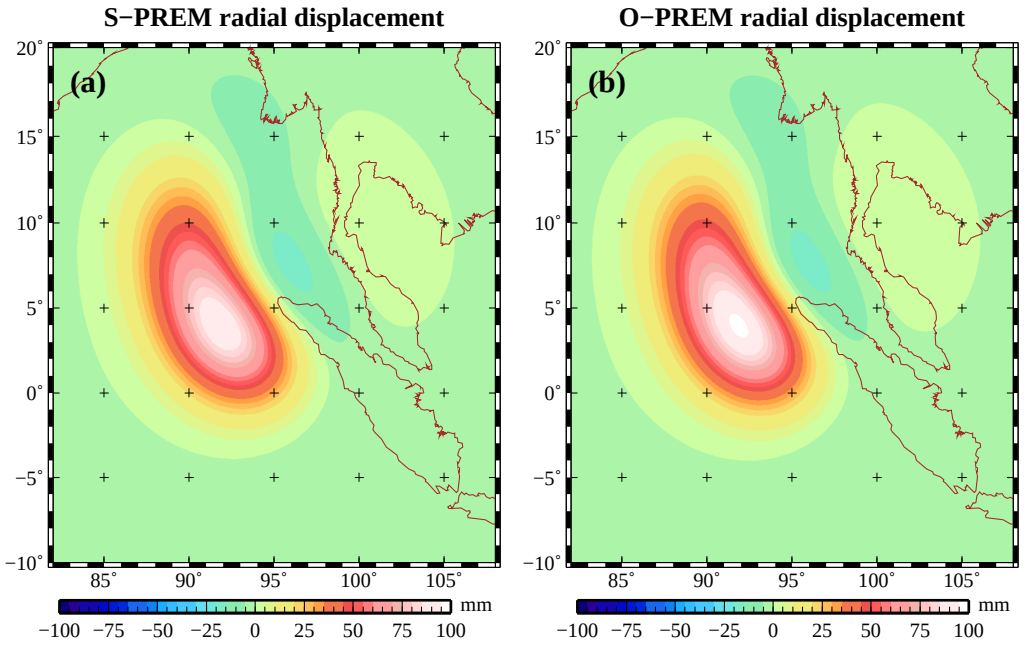

Figure 3.3: Co–seismic radial displacements for compressible S–PREM (a) and O–PREM (b), after the 350 km Gaussian filtering for the sake of comparison with the geoid anomalies shown in fig. 3.1 in terms of sea level variations, eq. (3.64).

causing the reduction of the geoid shown in fig. (3.2).

In the light of these preliminary results, we agree with de Linage *et al.* (2009) in saying that the asymmetry towards the negative pole of the co–seismic gravity anomalies observed in GRACE data is due the ocean water redistribution, rather than the crustal dilatation proposed by Han *et al.* (2006). We will further discuss this issue in sections 3.4 and 3.5 by exploiting our novel approach for the study of gravitational perturbations due to co–seismic volume changes, after the comparison between models and observations from GRACE.

3.4 GRACE data analysis

Let us discuss the main features of the 2004 Sumatran earthquake as recorded in GRACE data. We adopt the representation of GRACE data in gravity anomalies. The other natural choice, the representation in geoid anomalies, is more global and prone to leakage of signals from nearby regions, that are indeed very active from a hydrological point

of view. Hydrology can give strong fluctuations that can be confused with step–like phenomena like the co–seismic perturbation, due to the limited time resolution of the GRACE space mission of one month, and mask the specific slope variation characterizing the time dependence of the post–seismic perturbation. The gravity anomaly representation is instead less sensitive to this form of contamination because is more spatially localized. In this respect, we redefine the asymmetry coefficient AS as the ratio between the absolute values of the maximum positive, δg_{max}, and negative, δg_{min}, gravity anomalies

$$AS = \left| \frac{\delta g_{min}}{\delta g_{max}} \right| \tag{3.66}$$

rather than geoid anomalies, eq. (3.65).

GRACE data are also affected by a peculiar noise, the so called stripes, that is particularly strong at equatorial latitudes and, due to its typical north–south shape, can make the co–seismic signature in the Sumatran region less clear. A good treatment of the stripes is therefore important. Among the various solutions proposed recently, we choose to rely on the anisotropic filtering described in Kusche *et al.* (2007) and Kusche *et al.* (2009). Indeed, at present, this decorrelation filter is the most accurate treatment of the stripe problem, and it does not suffer from the bias present in approaches that are targeted to selected areas or phenomena (Werth *et al.*, 2009) because it is based on the analysis of the orbital characteristics of the GRACE space mission. Kusche *et al.* (2009) provide three anisotropic filters with different spatial resolutions. To better address the main features of the local scale signature of the 2004 Sumatran earthquake, we choose the filter with the highest spatial resolution: the DDK3 filter. Depending on the comparison criterion, this filter is roughly equivalent to an isotropic Gaussian filter of about $240 - 330$ km half width. This spatial resolution is close to the limit of the GRACE nominal resolution, and it can be a risk because some noise can still be present. On the other hand, the earthquake signal is strong at short wavelengths, and, because of the overall improvement in the processing techniques and the effectiveness of the decorrelation, the data are quite clean compared to those used in the early stage of the GRACE space mission.

GRACE Level 2 data are processed and provided to the scientific community by

three official analysis centers: the Center for Space Research (CSR, University of Texas), the GeoForschungsZentrum (GFZ, Potsdam) and the Jet Propulsion Laboratory (JPL, California Institute of Technology). The solutions that they provide are of similar quality, though there are some differences. The CSR data have the longest time series, but some months are affected by serious errors and the Stokes coefficients are available only up to the harmonic degree 60. The GFZ data have Stokes coefficients available up to the harmonic degree 120, but some months are missing. The JPL data have the shortest time series.

In this work, we consider the two official CSR and GFZ solutions. In order to optimize the information that we can gain from different solutions, we perform our analysis on the average of CSR and GFZ data, for each common month of the two time series (i.e. present in the series of both processing centers), although separate usage of the two time series is expected not to impact our conclusions. The average is done after applying the corrections prescribed to the Stokes coefficients of the two data sets and replacing the degree–2 order–0 Stokes coefficient with its more stable estimate from the Satellite Laser Ranging (SLR) constellation satellites, as recommended. The GFZ solution is truncated at the harmonic degree 60 in order to conform to the lower spatial resolution of the CSR solution. The principle at the basis of this average of the solutions is that the two centers work with comparable accuracy, and the possibility of common systematic errors is low. By considering that the unprocessed GRACE data portray a meaningful signal plus errors, the correlation between the data processed from the two centers should be maximized when a strong signal occurs and reduced when errors are dominant. This was first noted by Chambers (2006) and then used in Baur *et al.* (2009) and Barletta *et al.* (2011).

This approach allows us to estimate the uncertainty of GRACE data by considering the spatial distribution of the time–averaged deviation of the DDK3–filtered CSR and GFZ solutions from their mean, which is shown in fig. 3.4(a,b). This uncertainty from different processing is quite small, with values ranging from $0.3\,\mu$Gal to $1.5\,\mu$Gal worldwide. Particularly, it can be estimated to be between $0.4\,\mu$Gal and $0.8\,\mu$Gal in the Sumatran region (fig. 3.4b), with the largest errors north–east of the Sumatra trench, both in the near field and over the Cambodia. This indicates that the main features of the signal are coherent in the official solutions. Clearly, the difference between data from different processing methods could be even larger if one uses data from other processing

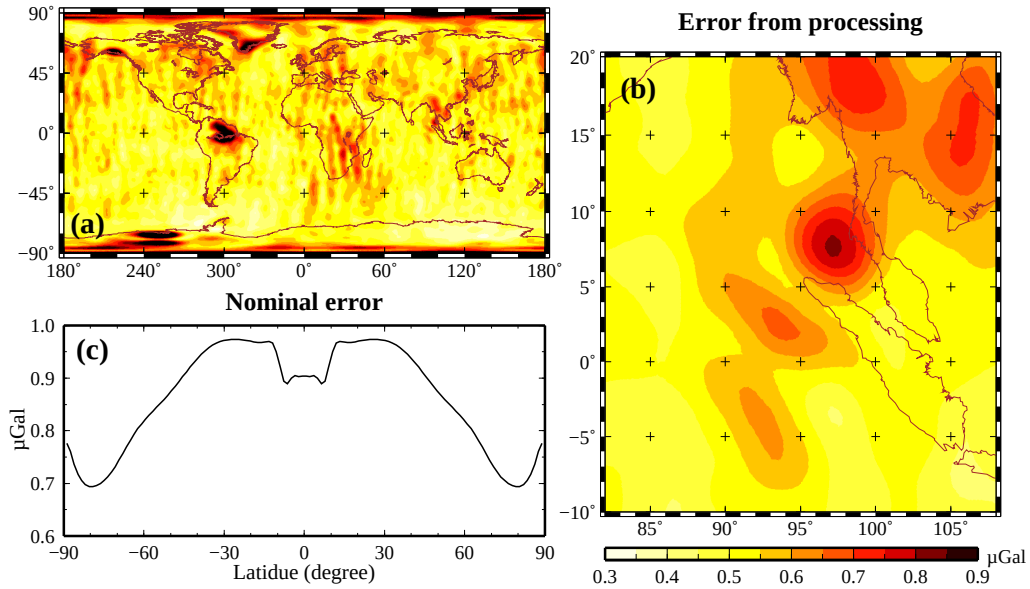

Figure 3.4: Spatial distribution of the time averaged deviation of the DDK3–filtered CSR and GFZ solutions from their mean (a) and its enlargement in the Sumatran region (b). Zonal spatial distribution of the nominal error (c) for the DDK3–filtered CRS solution.

centers (Steffen *et al.*, 2009), but here we decide to consider only the two official releases from CSR and GFZ.

In addition to the uncertainty from different processing, we also take into account the nominal error of GRACE data that we show in fig. 3.4c only for the CSR solution because this error for the GFZ solution is similar. The pattern of the nominal error is zonal, depending mainly on the latitude, and is about $0.9\,\mu$Gal at the equatorial latitudes of the Sumatran region. Then, by combining the uncertainty due to the processing and the nominal error in a conservative way, we assume an error of about $2\,\mu$Gal for GRACE data time series (CSR–GFZ solutions) in the Sumatran region.

3.4.1 Estimate of the co–seismic gravity anomaly

We consider GRACE data time series from August 2002 to November 2009, with June 2003 missing because no estimates are available from either of the two centers (CSR and GFZ) and rejecting December 2004 and January 2005 because the Sumatran earthquake occurred on December 26, 2004. We therefore have 27 and 58 data before and after

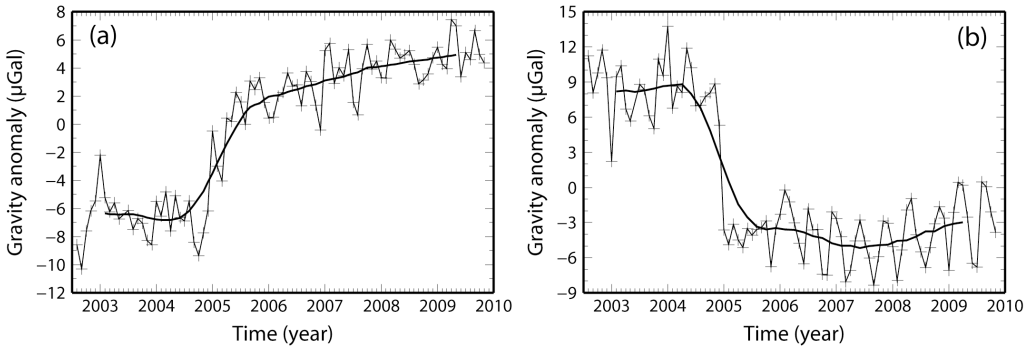

Figure 3.5: Original (thin solid lines, cross–shaped points) and smoothed (thick solid lines) DDK3–filtered GRACE data time series at points 2.1N, 94.2E and 7.7N, 97.0E, in the south–west (a) and north–east (b) near field of the Sumatran trench.

the earthquake, respectively, spanning periods of about 2 and 5 years. Fig. 3.5 shows the GRACE data time series in gravity anomaly representation (thin solid line, cross–shaped points) at the two points 2.1N, 94.2E and 7.7N, 97.0E, in the south–west (a) and north–east (b) near fields of the Sumatra trench, respectively. Because the time resolution of gravity measurements by GRACE space mission is monthly, the estimate of the co–seismic signature is not straightforward. Indeed, as can be seen in fig. 3.5, the upward transition (a) is slow compared to the downward transition (b). This indicates that local phenomena other than the co–seismic jump contribute to the signal. In order to only estimate the seismic signature, particularly the co–seismic gravity anomaly, we avoid the use of fitting schemes for the elimination of seasonal and interannual contributions and the alias at 161 days due to the model error of the S_2 tidal wave (Ray and Luthcke, 2006). Differently, instead of explicitly addressing the different contributions to gravity anomalies, we smooth GRACE data time series δg by means of a Gaussian filter W in the time domain (Barletta *et al.*, 2011)

$$\overline{\delta g}(t) = \int_{-T}^{T} \delta g(t')\, W(t', t)\, dt \tag{3.67}$$

with

$$W(t',t) = \begin{cases} \frac{1}{N}\, e^{-\frac{1}{2}\left(\frac{t'-t}{\sigma_W}\right)^2} & |t'-t| \leq T \\ 0 & |t'-t| > T \end{cases} \tag{3.68}$$

Here, t, N, σ_W and T are the time, the normalizing constant and the half width of the filter, and the truncation constant used to deal with finite time series. We choose $T = \frac{3}{2}\,\sigma_W$ and $\sigma_W = 6$ months. This filter in time reduces by about one order of magnitude the variability due to seasonal and interannual signals due to hydrology from the continent and to the residual ocean circulation component present in the data, together with the alias at 161 days due to the model error of the S_2 tidal wave (Ray and Luthcke, 2006). Permanent co– and post–seismic signatures and signals due to long–period (greater than 2 years) hydrological cycles of periods are preserved.

After the Gaussian smoothing in the time domain, GRACE data time series show evident long–term signals that cannot be considered as the only co–seismic gravity anomaly, as it can be seen in fig. 3.5 (thick solid line). We face this issue by choosing the following interpolating function to describe both co– and post–seismic gravity anomalies

$$f(t) = \begin{cases} -a & t < 0 \\ b + c\,\frac{1-e^{-\frac{t}{\tau}}}{1-e^{-\frac{t_S}{\tau}}} & t \geq 0 \end{cases} \tag{3.69}$$

where $t = 0$ and $t_S = 5$ years are the earthquake time and the end of the GRACE data time series, $a + b$ and c are the co–seismic gravity anomaly and the post–seismic contribution up to the end of the time series, and τ is the characteristic relaxation time. Eq. (3.69) tacitly assumes that the long–period hydrological and residual ocean circulation signals are weak compared to post–seismic perturbations. However, in order to faithfully base on the actual information contained in GRACE data, we do not introduce any prior information about the mean and variance of the interpolating parameters, except for the lower bound of 4 months for the characteristic relaxation time τ that we impose in view of the time resolution of the GRACE data.

Because the Gaussian smoothing in time that we used for removing seasonal and interannual hydrological and ocean circulation cycles from GRACE data also affects the other signals contained in GRACE data, particularly the signal due to the co–seismic gravity anomaly loss its typical step–like signature, we must apply the same filter to the

interpolating function f, eq. (3.69), in order that it has the same physical meaning of the smoothed signals contained in GRACE data time series. This means that we actually fit the smoothed version of eq. (3.69) to the smoothed GRACE data time series

$$\overline{f}(t) = \int_{-T}^{T} f(t')\, W(t,t')\, dt \tag{3.70}$$

Fig. 3.6 compares the estimated co–seismic gravity anomalies and the post–seismic gravity anomalies $t_S = 5$ years after the 2004 Sumatran earthquake at each node of the grid of Gauss for harmonic degree $\ell = 128$, which samples the Sumatran region about every $1.4°$. We find maximum, $+6.1 \pm 1.5\,\mu$Gal, and minimum, $-12.7 \pm 0.9\,\mu$Gal, co–seismic gravity anomalies at points 0.7N, 95.6E and 6.3N, 97.0E, respectively. The peak–to–peak co–seismic gravity anomaly is $+18.8 \pm 1.7\,\mu$Gal, and the asymmetry coefficient is $AS = 2.1 \pm 0.5$. The post–seismic gravity anomalies are comparable in magnitude with the co–seismic estimates and have maximum, $+8.7 \pm 0.7\,\mu$Gal, and minimum, $-7.1 \pm 1.6\,\mu$Gal, values at points 4.9N, 94.2E and 9.1N, 99.8E, respectively. We also find large co– and post–seismic gravity anomalies in the far field that are comparable in absolute value with those in the near field. Particularly, the large estimates north–east of the Sumatran trench, over Cambodia, indicates that phenomena other than the seismic one, likely associated with long–period hydrological and ocean circulation cycles, affect GRACE data.

In order to better understand how the fitting to GRACE data behaves, we compare in fig. 3.7 the smoothed GRACE data time series, eq. (3.67), with the interpolating functions, eq. (3.70), at the points where the maximum (a) and minimum (c) estimates of the co–seismic gravity anomalies are located. The respective original times series and interpolating functions, eq. (3.69), are shown in the right panels (b, d). At the maximum co–seismic gravity anomaly (top), the estimated characteristic relaxation time is short, about 20 months, whereas at the minimum co–seismic gravity anomaly (bottom), the fitting yields large characteristic relaxation times, namely $\tau \to \infty$. These two quite different ways to fit to the data result from the fact that we have not imposed prior information about the mean and variance of the interpolating parameters, thus allowing the non–linear fitting to obtain the best estimate linearly if the post–seismic signature is hidden by other signals. Indeed at the minimum co–seismic gravity anomaly, in addition

to some long–term signal (which could be the post–seismic signature), there are also strong fluctuations of period of about 4 years, likely associated with hydrological and ocean circulation cycles (solid line, fig. 3.7c). Unless the latter signals are carefully removed, looking in this data for post–seismic events with short characteristic relaxation times would not be a good choice. On the other hand, at the maximum co–seismic gravity anomaly (fig. 3.7a), where long–period fluctuations are small compared to the post–seismic signature, the fitting is able to remove the post–seismic signature. These two representative cases show that we should not interpret the results of fig. 3.6b as only post–seismic gravity anomalies because they absorb a number of other phenomena as well.

In light of the characteristic of the data, we must focus our attention only on estimates in the near field. For this reason, in the next section, the comparison with our models will be done only with respect to the maximum, $+6.1 \pm 1.5\,\mu$Gal, and minimum, $-12.7 \pm 0.9\,\mu$Gal, estimates of the co–seismic gravity anomaly from observations, with the warning that the *a–posteriori* one–sigma errors of $1.5\,\mu$Gal and $0.9\,\mu$Gal only simplistically account for the uncertainties due to long–period hydrological and ocean circulation cycles.

3.4.2 Comparison with co–seismic models

In order to make the comparison between estimates from observations with those from models significant, it is important to apply the same spatial filter used to deal with GRACE data to models because the spatial features of the seismic signature make the gravity anomalies very sensitive to the type of filtering. The use of different filters would yield unphysical differences, which would make the comparison less effective. For this reason, we now compare DDK3–filtered CSR–GFZ solutions with equivalently filtered co–seismic models.

Fig. 3.8a shows the co–seismic gravity anomalies modelled using Ocean–PREM (that we introduced in section 3.3) and the seismic source model of Tsai *et al.* (2005), after the DDK3 filtering. We find maximum, $+8.6\,\mu$Gal, and minimum, $-10.0\,\mu$Gal, gravity anomalies at points 2.1N, 92.8E and 6.3N, 97.0E, respectively. The modelled pattern is quite different from that estimated from GRACE data analysis, fig. 3.6a. Indeed, although the peak–to–peak gravity anomaly obtained from the model, $+18.6\,\mu$Gal,

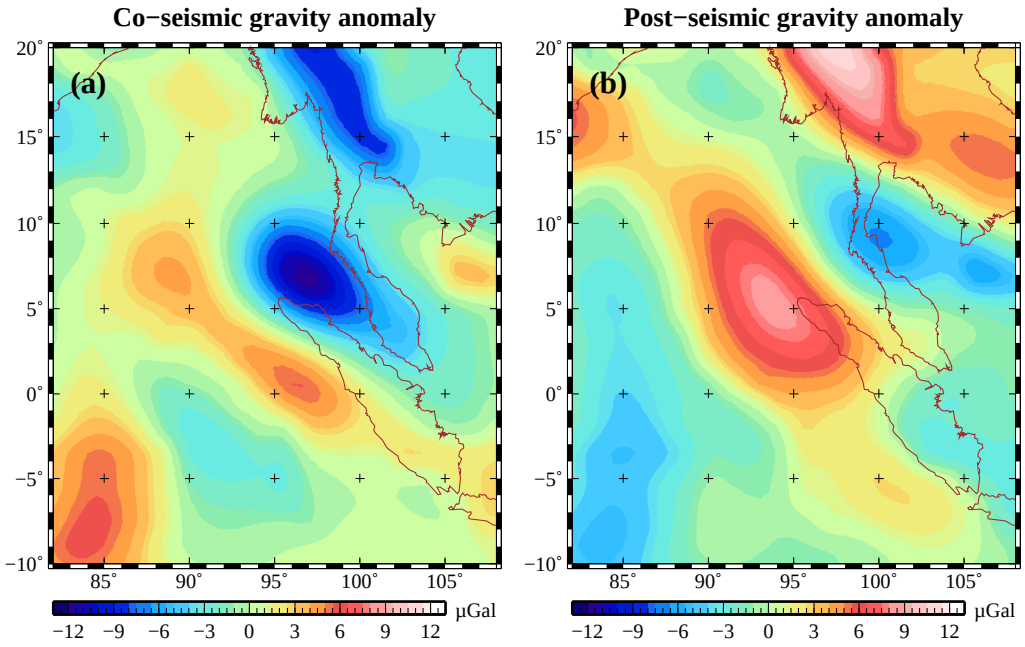

Figure 3.6: Co–seismic gravity anomalies (a) and post–seismic contribution 5 years after the earthquake (b) obtained by the non–linear fitting, eqs (3.69)–(3.70), to the smoothed DDK3–filtered GRACE data time series, eq. (3.67).

is in agreement, within one–sigma error, with the observed one, $+18.8 \pm 1.7\,\mu$Gal, the asymmetry coefficient $AS = 1.2$ differs from the observed one, $AS = 2.1 \pm 0.5$, by about two–sigma error.

As pointed out in section 3.3, in view of the fact that the asymmetry coefficient AS depends mainly on the ocean water redistribution and that the latter is strongly characterized by variations of topography at the bottom of the ocean, we expect AS to be sensitive to the material parameters of the layer of the Earth in which the seismic sources are located, particularly to the elastic parameter β, eq. (1.82). Indeed, from eq. (3.28), the discontinuity of the radial displacement is inversely proportional to the elastic parameter β at the seismic source depth. By considering that β reduces by about a factor 2 at the Moho discontinuity (Dziewonski and Anderson, 1981), from 2.22×10^{11} Pa at the top of the lithospheric mantle to 1.34×10^{11} Pa at the bottom of the crust, we then expect larger radial displacements for earthquakes occurring in the crust than those in the lithospheric mantle. This should cause a larger removal of ocean water from the

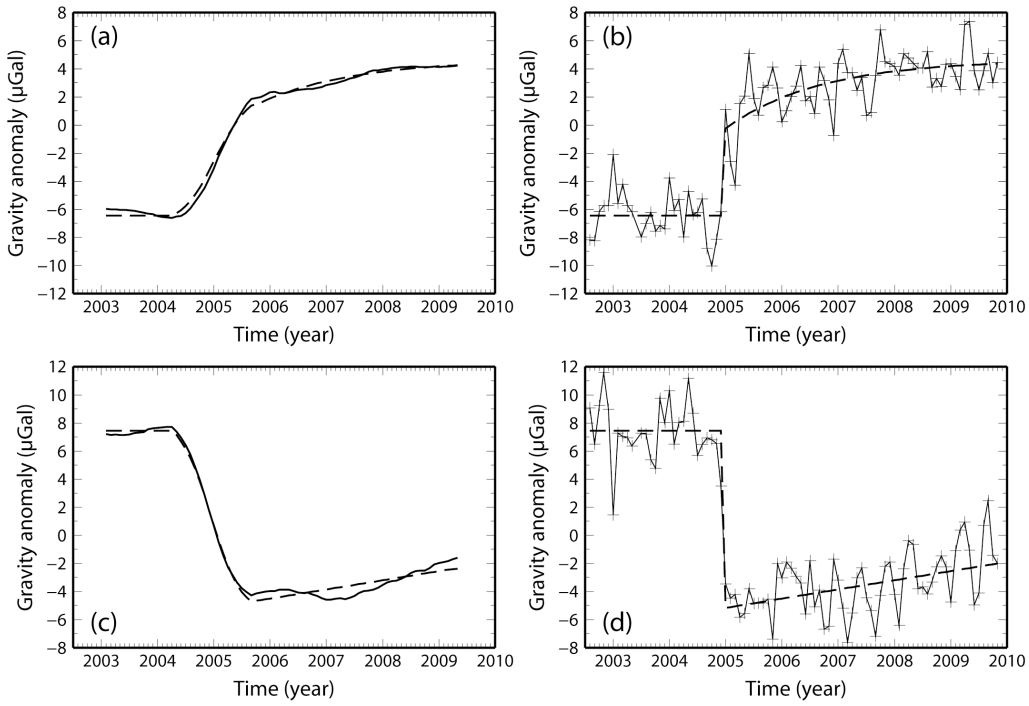

Figure 3.7: Smoothed DDK3–filtered GRACE data time series (solid line), eq. (3.67), and non–linear interpolating functions (dashed line), eqs (3.69)–(3.70), at points 0.7N, 95.6E and 6.3N, 97.0E, where the maximum (a) and minimum (c) estimates of the co–seismic gravity anomaly are located. The respective original time series (thin solid line, cross–shaped point) and non–linear interpolating functions (dashed line), eq. (3.69), are shown in the right panels (b,d).

near field and, thus, a larger asymmetry coefficient AS for seismic sources within the crust than those obtained by using the seismic source model of Tsai *et al.* (2005), which locates all five seismic sources at the depth of 25 km, within the lithospheric mantle.

We investigate this matter in fig. 3.9, where we report the peak–to–peak co–seismic gravity anomaly (thick solid line, a) and the asymmetry coefficient AS (thick solid line, b) obtained for compressible O–PREM and modifying the seismic source model of Tsai *et al.* (2005), varying the source depth d_S from 1 km to 40 km. Both the peak–to–peak gravity anomaly and the asymmetry coefficient AS are quite sensitive to the source depth, with values ranging from 11.7 μGal to 27.8 μGal and from 1.1 to 4.4, respectively. In particular, they have step–like discontinuities at the Moho discontinuity, $d_S = 21.4$ km, and at the lower–upper crust interface, $d_S = 12.0$ km, caused by the step–like variations of PREM material parameters. Three depth intervals, $[6, 9]$ km, $[14, 18]$ km

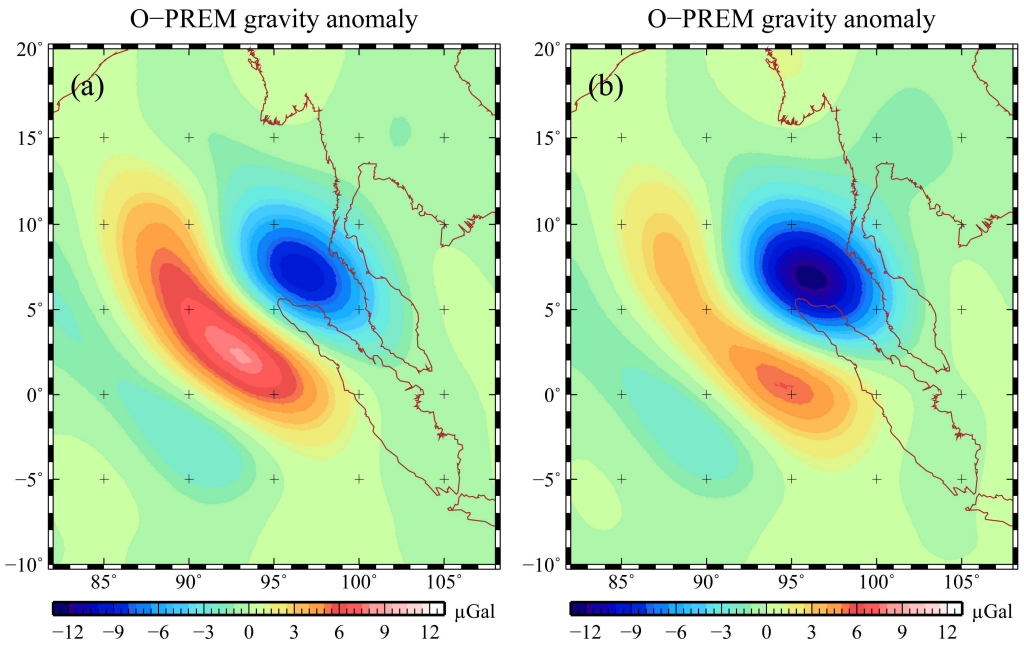

Figure 3.8: DDK3–filtered co–seismic gravity anomalies for compressible O–PREM obtained using the original (a) and modified (b) seismic source models of Tsai *et al.* (2005), with source depths below, 25 km, and above, 15 km, the Moho discontinuity, respectively. The dip angles for the modified seismic source model have been increased by 50 per cent.

and $[22, 28]$ km, within the upper and lower crusts and lithospheric mantle, respectively, agree within one–sigma error (dark gray zone) with the estimate of $+18.8 \pm 1.7\,\mu$Gal from observations. On the contrary, the asymmetry coefficient AS exhibits a monotonic dependence on the source depth and only the depth interval $[11, 21.4]$ km within the lower crust, but for a small portion of the upper crust, agrees within one–sigma error (dark gray zone) with the observed asymmetry $AS = 2.1 \pm 0.5$.

The joint use of these findings, accepting the confidence of one–sigma error (dark gray zones, fig. 3.9), allows us to conclude that the seismic moment of the 2004 Sumatran earthquake has been mainly released within the lower crust. Nevertheless, there is a gap of 4 km between the seismic source depths that match the best estimates of the observed peak–to–peak gravity anomaly and asymmetry coefficient AS (dashed lines, fig. 3.9), 16 km and 12 km, respectively. In order to reduce the misfit between observations and predictions from models, we tried dip angles different from those given by Tsai *et al.* (2005). Fig. 3.8b shows the results that are in best agreement with observations

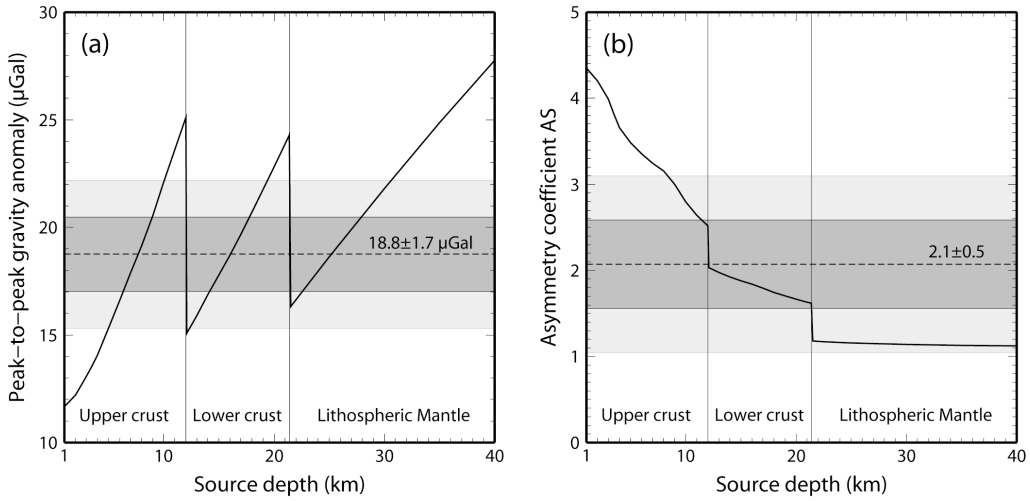

Figure 3.9: Peak–to–peak gravity anomalies (a) and asymmetry coefficient AS (b) for compressible O–PREM (thick solid line) obtained using the seismic source model of Tsai *et al.* (2005) and varying the source depth from 1 km to 40 km, after the DDK3 filtering. The dashed lines indicate the peak–to–peak gravity anomaly, $18 \pm 1.7\,\mu$Gal, and asymmetry coefficient, $AS = 2.1 \pm 0.5$, obtained by the non–linear fitting to the smoothed DDK3–filtered GRACE data time series. The dark and light gray zones indicate values within one– and two–sigma errors, respectively.

obtained for a source depth of $d_S = 15$ km and increasing the dip angles by 50 per cent, such that they become $(9.6°, 9.45°, 8.7°, 12.6°, 12.15°)$ compared to the original values of $(6.4°, 6.3°, 5.8°, 8.4°, 8.1°)$. In this case, both the peak–to–peak gravity anomaly and the asymmetry coefficient AS from modeling match the best estimates from observations, $18.8\,\mu$Gal and 2.1, respectively.

In view of the sharp dependence of the peak–to–peak gravity anomaly and of the asymmetry coefficient on the material parameters of the layer at which the seismic sources are located, we can argue that our results could be affected by lateral heterogeneities of the material parameters in the surrounding of the seismic source. For this reason the so modified seismic source model is intended rather to be an *effective* seismic source model for PREM because the latter does not take into account the variations in depth of the Moho discontinuity, which are large at the subduction trench, or the heterogeneities that are present where the oceanic crust descends into the lithospheric mantle. This warning also holds for the CMT source analysis (Tsai *et al.*, 2005). Indeed, even though this analysis takes into account the long wavelength three–dimensional Earth structure (Ekström *et al.*, 2003), it does not accounts for heterogeneities at small spatial

scales, such as those characterizing the subduction zone.

3.5 Volume changes and compressibility

We now exploit the extension of the classic theory for the study of co–seismic volume changes (section 3.1) in order to address the style of deformation, compressional versus dilatational, due to the 2004 Sumatran earthquake and discuss the findings of Han *et al.* (2006) about the large dilatation of the crust. Rather than the seismic source model of Tsai *et al.* (2005), we will implement the modified seismic source model obtained in section 3.4.2 from the comparison with GRACE data.

Fig. 3.10 shows the DDK3–filtered gravity anomalies for O–PREM due to co–seismic volume changes of the mantle (a) and of the crust (b). We obtain compression within the mantle, evident by the positive pole with maximum gravity anomaly of $19.1\,\mu$Gal. This approximatively agrees with the results of Han *et al.* (2006) (their fig. 3, bottom row), even if their maximum gravity anomaly, about $30\,\mu\mathrm{Gal}$, is larger than ours. In addition to the different spatial filter applied to the model, this difference in magnitude is due to the fact that Han *et al.* (2006) use a simple half–space model (Okubo, 1992), wherein the elastic parameters are those of the crust. This means that they do not account for the realistic stratification of PREM, where the larger bulk modulus of the mantle limits volume changes. As it concerns gravity anomalies due to volume changes of the crust, we obtain a bipolar patter characterized by maximum, $6.6\,\mu\mathrm{Gal}$, and minimum, $-7.0\,\mu\mathrm{Gal}$, gravity anomalies in the foot– and hanging–wall sides of the fault plane, respectively. This shows that there is both compression and dilatation within the crust and invalidates the interpretation of Han *et al.* (2006) that thrust earthquakes, like the Sumatran event, cause an overall crustal dilatation. This difference between our result and that of Han *et al.* (2006) is due to the fact that we have not included in this estimate the contribution due to the volume changes localized at the fault discontinuity, eq. (3.30). We show the latter contribution in fig. 3.10c. In agreement with the physics of dip–slip faults discussed in section 3.1.1, the thrust earthquake causes a large dilatation localized at the fault discontinuity that is responsible for an overall negative gravity anomaly, with a minimum of $-40.7\,\mu\mathrm{Gal}$.

These findings highlight the importance of discriminating the effects of the co–seismic volume changes in the layers of the Earth from the volume change localized

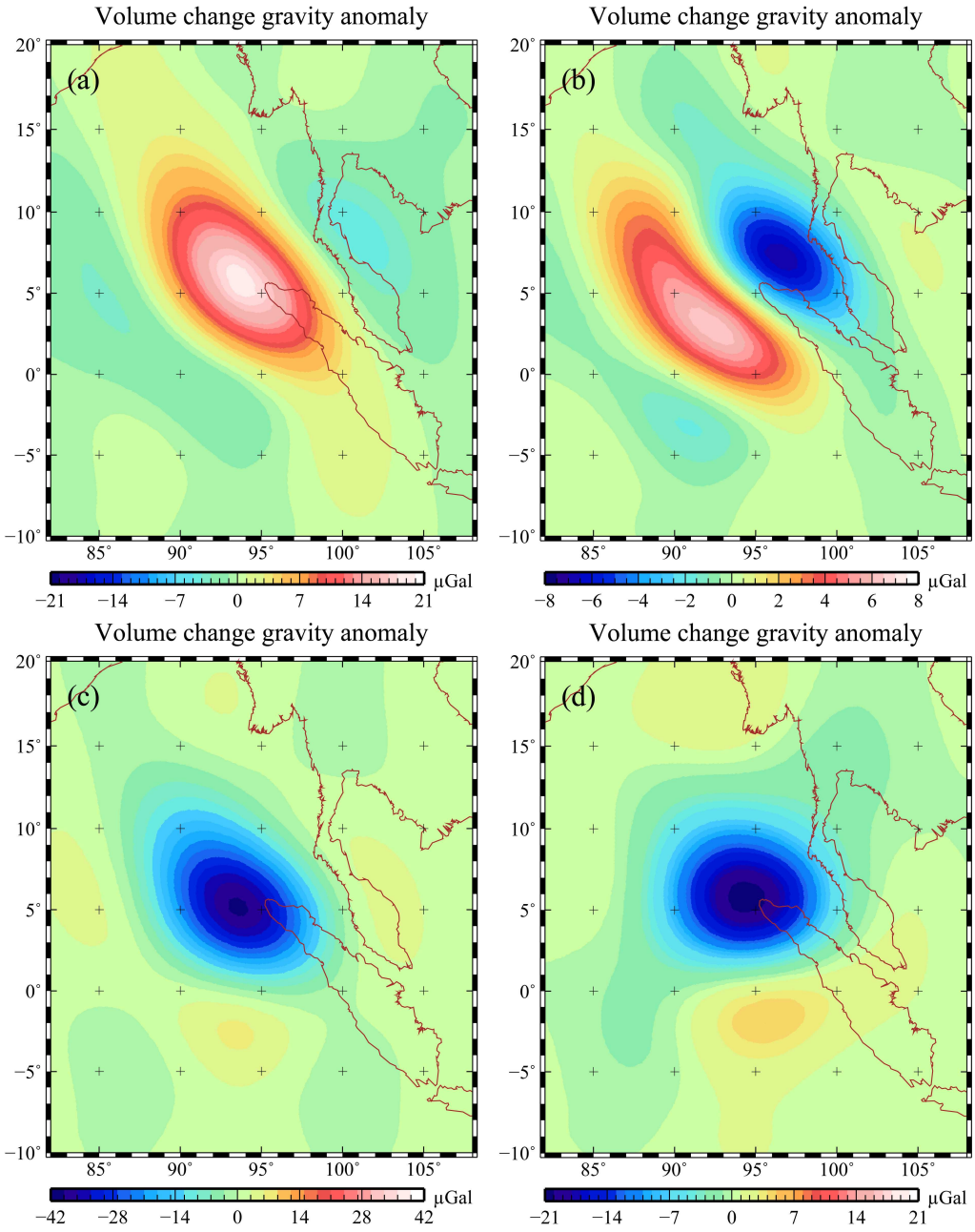

Figure 3.10: DDK3–filtered co–seismic gravity anomalies for compressible O–PREM due to volume changes of the mantle (a), of the crust (b) and localized at the fault discontinuity (c), obtained using the seismic source model of Tsai *et al.* (2005) modified as discussed in section 3.4.2. Panel d is the sum of the previous panels, i.e., the co–seismic gravity anomalies due to the total volume changes within solid Earth.

at the fault discontinuity. Otherwise, because the latter dominates over the former, we should have concluded that thrust earthquakes cause an overall dilatation of the crust, and this is not physically sound because it does not reflect the pattern of compression and extension induced by the seismic forcing. This does not mean that the co–seismic gravity anomalies due to volume changes modelled by Han *et al.* (2006) are incorrect. Indeed, once considered the total gravity anomaly due to all sources of volume changes (within the mantle and the crust, and localized at the fault discontinuity) shown in fig. 3.10d, we obtain results similar to those obtained by Han *et al.* (2006), characterized by a minimum, $-21.5\,\mu\mathrm{Gal}$, in the near field of the Sumatran earthquake and two less pronounced maxima southwards, $5.3\,\mu\mathrm{Gal}$, and northwards, $2.9\,\mu\mathrm{Gal}$.

To gain further insight into this issue, we show in fig. 3.11a the co–seismic gravity anomalies obtained using the compressible Solid–PREM that are due only to mass rearrangement within the solid Earth, without including the gravitational effect of the ocean water redistribution. The peak–to–peak gravity anomaly is $22.8\,\mu$Gal and the pattern is bipolar and asymmetric towards the positive pole, with asymmetry coefficient AS of 0.8. In this respect, the gravity anomaly due to the advection of the initial density field, including the topography perturbations of internal boundaries with density contrast and the solid Earth surface, widely compensates the overall negative anomaly due to volume changes shown in fig. 3.10d. Particularly, the gravitational effect due to the large dilatation localized at the fault discontinuity, eq. (3.30), is compensated by an opposite effect due to the positive perturbations of the solid Earth surface topography. Indeed, it should be remained that the dilatation localized at the fault discontinuity, eq. (3.29), is the result of the step–like discontinuity of the radial displacement, eq. (3.28), which determines the uplift of the portion of the solid Earth above the seismic source.

The above reasoning further invalidates the interpretation of Han *et al.* (2006) that the asymmetry of the co–seismic gravity anomaly towards the negative pole observed in GRACE data is due to a large crustal dilatation, even if we correctly mean for the latter the dilatation localized at the fault discontinuity. Differently, as already discussed in sections 3.3 and 3.4.2, only when the gravitational effect of the ocean water redistribution is included in the modelling, we can explain observations. The reason that the co–seismic model of Han *et al.* (2006) yields a spatial asymmetry similar to that observed is due to the fact that these authors include in an effective, but non–self–consistent, way the contribution from the sea level variation. Particularly, when they compute the co–seismic

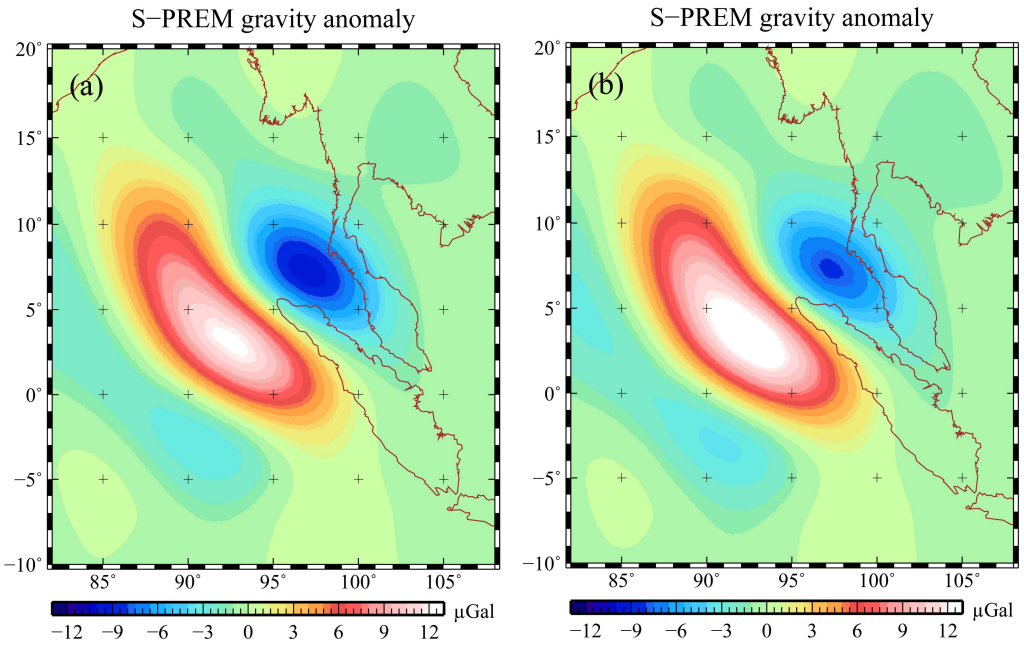

Figure 3.11: DDK3–filtered co–seismic gravity anomalies for compressible (a) and incompressible (b) S–PREM, obtained using the seismic source model of Tsai *et al.* (2005) modified as discussed in section 3.4.2.

gravity anomalies due to the perturbation of the Earth's surface topography, they consider the difference between the density of the crust and of the ocean as density contrast. Thus, they take into account the main gravitational effects of ocean water redistribution, which is affected mainly by radial displacements rather than geoid anomalies, as pointed out in section 3.3.

3.5.1 Compressibility versus Incompressibility

Comparing figs 3.10a and 3.10b with fig. 3.8b, it appears that contributions to co–seismic gravity anomalies due to volume changes of the mantle and of the crust are comparable with the full co–seismic gravity anomaly. This indicates that compressibility is an important feature of co–seismic perturbations. Then, we now compare compressible and incompressible Earth models in order to analyse in detail the role of compressibility in co–seismic studies.

In fig. 3.11 we compare DDK3–filtered co–seismic gravity anomalies for compressible (a) and incompressible (b) S–PREM by using the modified seismic source model

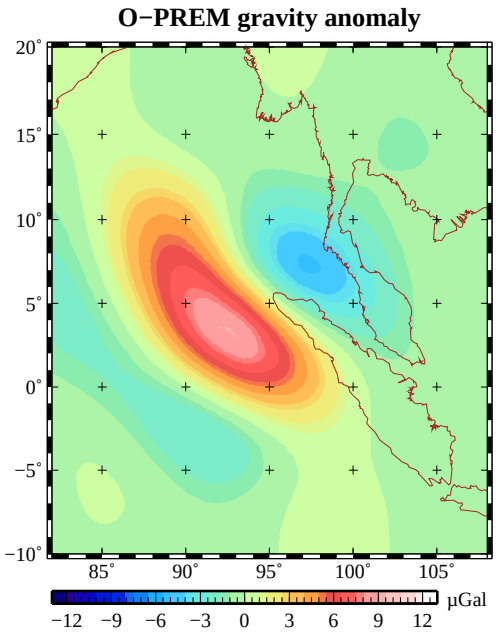

Figure 3.12: DDK3–filtered co–seismic gravity anomalies for incompressible O–PREM, obtained using the seismic source model of Tsai *et al.* (2005) modified as discussed in section 3.4.2.

obtained in section 3.4.2. The peak–to–peak gravity anomalies are 22.8 and $23.4\,\mu\mathrm{Gal}$, and the asymmetry coefficients AS are 0.8 and 0.6, for compressible (a) and incompressible (b) S–PREM, respectively. The two bipolar patterns are asymmetric towards the positive pole, particularly in the incompressible case. To be compared with fig. 3.8b, we show in fig. 3.12 the co–seismic gravity anomalies for incompressible O–PREM. The peak–to–peak gravity anomaly for incompressible O–PREM, $14.8\,\mu\mathrm{Gal}$, is smaller than that for compressible O–PREM, $18.7\,\mu\mathrm{Gal}$, by about 20 per cent. Furthermore, in contrast to the compressible case, the modeled pattern is not asymmetric towards the negative pole, with an asymmetry coefficient of less than one, $AS = 0.6$. This means that compressible and incompressible materials mainly differ for the way in which they model ocean water redistribution.

Let us further analysis this issue in fig. 3.13 where we compare the co–seismic gravity anomalies due only ocean water redistribution for the compressible (a) and incompressible (b) cases. Indeed, for the compressible Ocean–PREM, the ocean water redistribution is responsible for a large negative gravity anomaly in the near field, with

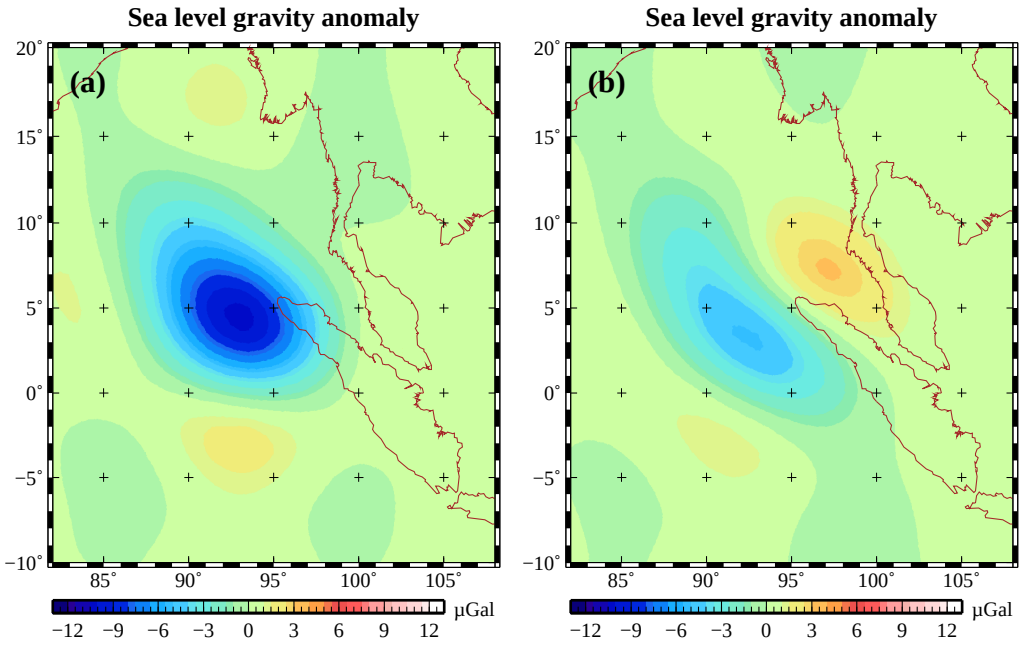

Figure 3.13: DDK3–filtered co–seismic gravity anomalies due to ocean water redistribution obtained subtracting compressible (a) and incompressible (b) O–PREM and S–PREM co–seismic gravity anomalies and using the seismic source model of Tsai *et al.* (2005) modified as discussed in section 3.4.2.

a minimum of $-10.7\,\mu\mathrm{Gal}$. Instead, for the incompressible Ocean–PREM, the ocean water redistribution causes co–seismic gravity anomalies characterized by a bipolar pattern, with maximum and minimum of 3.3 and $-5.3\,\mu\mathrm{Gal}$, respectively. Note that the latter pattern is opposite to that of the co–seismic gravity anomalies of incompressible S–PREM (fig. 3.11b). This means that, in the incompressible case, the ocean water redistribution reduces the magnitude of maximum and minimum co–seismic gravity anomalies. In this respect, it does affect the peak–to–peak gravity anomaly but cannot explain the spatial asymmetry observed in GRACE data.

This difference between compressible and incompressible Earth models is mainly due to the fact that within incompressible materials, seismic forcing does not cause any discontinuity of the radial displacement at the seismic source depth, eq. (3.28), as it does within compressible materials. Indeed, in the limit of the bulk modulus κ going to infinity, also the elastic parameter β goes to infinity and the RHS of eq. (3.28) is zero. This is consistent with the assumption of incompressibility because otherwise, there would

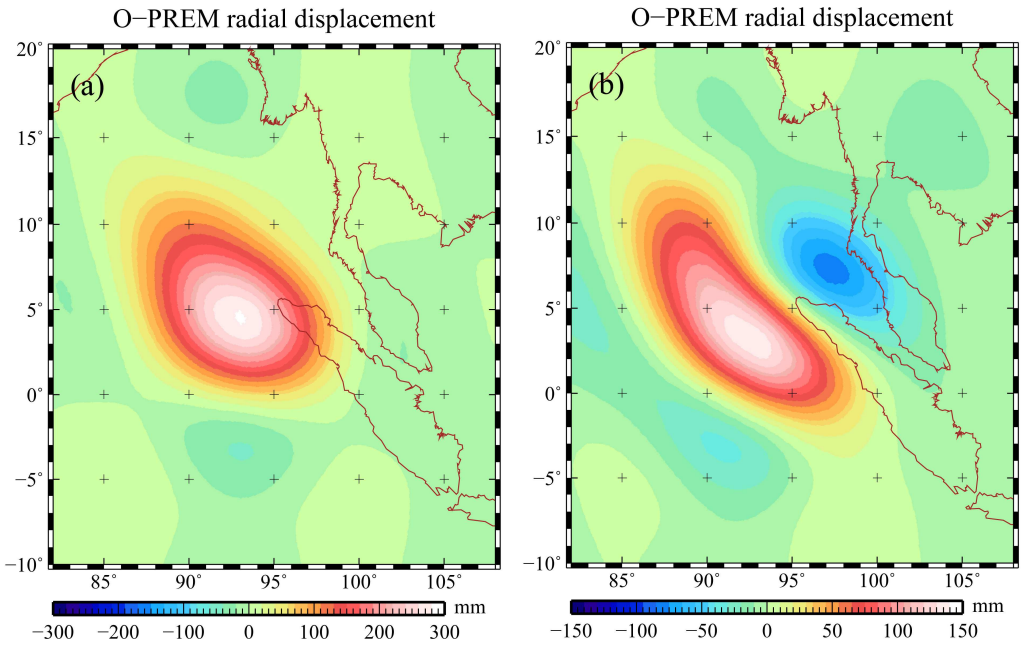

Figure 3.14: Co–seismic radial displacements at the bottom of the ocean for compressible (a) and incompressible (b) O–PREM, after the DDK3–filtering, obtained using the seismic source model of Tsai *et al.* (2005) modified as discussed in section 3.4.2.

be the volume change localized at the fault discontinuity, eq. (3.29). This shortcoming of incompressible models yields a very different pattern of topography perturbations. This is shown in fig. 3.14 where we compare long wavelength (DDK3–filtered) radial displacements at the bottom of the ocean for compressible (a) and incompressible (b) Ocean–PREM. The incompressible model is characterized by a maximum downdrop, $-85\,\mathrm{mm}$, northeastward with respect to the subduction trench, which is absent in the compressible case, and by a maximum uplift, $143\,\mathrm{mm}$, southwestward that is two times smaller than that for the compressible model, $291\,\mathrm{mm}$. Thus, in the compressible case, a large amount of water is displaced away to the far field and causes the gravity reduction in the near field shown in fig. 3.13a. In the incompressible case, instead, the ocean water displaced away from the uplifted foot–wall side accumulates in the downdrop of the hanging–wall side and causes the bipolar pattern shown in fig. 3.13b. These findings clearly point out that the assumption of incompressibility is inappropriate for modeling co–seismic perturbations for reverse and normal faults. This is not due to the fact that incompressible models do not consider volume changes localized at the fault disconti-

nuity, eq. (3.29), because the long–wavelength gravitational effect of the latter actually does not appear in compressible models as discussed before. Instead, this is due to the different ocean water redistribution caused by the reduction of the uplift of the crust, reflecting the fact that the step–like discontinuity of radial displacement at the seismic source, eq. (3.28), must be zero for incompressible models.

3.6 Conclusion

Gravity space missions provide an important opportunity to gain deep insights into the physics of large earthquake co–seismic deformation, due to huge mass redistribution and related gravitational perturbations. We have demonstrated here that adequate Earth and dislocation models are required to properly interpret GRACE data time series for comparison with a new compressible self–gravitating Earth model, applied to the 2004 Sumatran co–seismic gravity anomalies for the first time. A self–consistent treatment of the Poisson equation has allowed us to extract the correct pattern of crustal compression and dilatation in the foot (south–west) and hanging (north–east) walls of the fault plane for a thrust earthquake like the 2004 Sumatran event. Furthermore, we have showed that the previously modeled dilatation pattern of Han *et al.* (2006) is mainly due to a large dilatation localized at the fault discontinuity, the gravitational effect of which is compensated by an opposite contribution from topography due to the uplifted crust. The asymmetry between negative and positive gravity anomalies cannot be caused by crustal dilatation (Han *et al.*, 2006), but rather, it is caused by the gravitational effects of the ocean after water removal from the uplifted crust, which is responsible for the gravity reduction due to the thinned water layer. This is in agreement with the findings of de Linage *et al.* (2009). Furthermore, we have implemented the new mathematics and the physics which are necessary to explain the results of the latter work. Indeed, compressible materials provide a more accurate physical representation of faulting than incompressible materials mainly because the latter do not account for the discontinuity of radial displacements at the fault. This yields a reduction of the crustal uplift that alters the redistribution of ocean water after the earthquake. Thus, incompressible models should not be applied for co–seismic calculations, as they have been in the past (Sabadini *et al.*, 2005; Melini *et al.*, 2010).

After the Gaussian smoothing in the time domain in order to remove short period

hydrological and residual ocean circulation signals, we fitted the DDK3–filtered (Kusche *et al.*, 2009) GRACE data time series (CSR–GFZ solutions) to the co–seismic gravity anomaly and the post–seismic contribution without introducing any *a–priori* information about the mean and variance of the interpolating parameters. We found a peak–to–peak co–seismic gravity anomaly of $+18.8 \pm 1.7\,\mu$Gal and an asymmetry coefficient of $AS = 2.1 \pm 0.5$. Then, modeled gravity anomalies were checked against GRACE data by applying the same spatial filter, the DDK3 filter designed by Kusche *et al.* (2009). We have shown that the seismic source model of Tsai *et al.* (2005) does not adequately explain the observed asymmetry in the data. By discussing the sensitivity of the modeled co–seismic gravity anomalies to the source depth and dip angles, we found that the agreement between data and models is obtained locating the seismic sources above the Moho discontinuity, particularly at the source depth of 15 km and for dip angles of about $10°$.

These findings show that we can obtain a few, but important, constraints from GRACE data that complement the CMT source analyses (Dziewonski *et al.*, 1981; Ekström *et al.*, 2003; Tsai *et al.*, 2005) of the 2004 Sumatran earthquake.

Chapter 4

Two seismic solutions of the 2011 Tohoku earthquake based on space gravity data

Compressible, self–gravitating Earth models (Sun and Okubo, 1993; Cambiotti *et al.*, 2011a) have been used in the past to simulate the long–wavelength gravity anomalies due to mass rearrangement and ocean water redistribution caused by megathrust submarine earthquakes, as discussed in Chapter 3. On the basis of this modelling, we present a novel procedure to estimate the principal seismic source parameters (hypocentre and moment tensor) of giant earthquakes from inversion of GRACE gravity data, applied herein to the 2011 Tohoku event. Our procedure could become an important tool in seismic studies as it complements the well established Centroid Moment Tensor (CMT) analysis from inversion of teleseismic wave observations (Gilbert and Dziewonski, 1975; Dziewonski *et al.*, 1981). In this respect, we name this novel procedure the Gravitational Centroid Moment Tensor (GCMT) analysis.

This novel procedure is accompanied by new efforts in the treatment of the GRACE data that is aimed at optimizing the estimate of the co–seismic gravity anomaly of the 2011 Tohoku earthquake. Differently from previous GRACE data analyses, we make use of the Slepian functions (Simons *et al.*, 2006) in order to spatially localize the time series of Stokes coefficients in the surrounding of the earthquake.

4.1 GRACE data analysis using Slepian function

To estimate the co–seismic gravity signature due to the March 2011 Tohoku earthquake, we consider GRACE Level 2 data provided by GeoForschungsZentrum (GFZ, Potsdam) from January 2009 to September 2011, with September 2010 and January and June 2011 missing and rejecting March 2011, that total 24 and 5 data before and after the earthquake. We reduce the peculiar noise of GRACE data, the so–called stripes, by making use of the anisotropic DDK3–filter (Kusche, 2007; Kusche *et al.*, 2009) that is roughly equivalent to an isotropic Gaussian filter of about 240–330 km half–width. Because the GRACE data consist of Stokes coefficients describing the time dependent gravity field over the whole Earth surface, we also need to spatially localize GRACE data in the surrounding region of the earthquake. We do this by using Slepian functions (Simons *et al.*, 2006), bandlimited to harmonic degree 60 and optimally concentrated within the circular cup of half–width 8° and centred at the USGS mainshock, 38.22N, 134.22E. Larger half–widths of the circular cup would yield the leakage of signals from nearby regions likely associated to geophysical phenomena other than the earthquake,

making harder the discrimination of the seismic signature in GRACE data.

Given an arbitrary region $\mathcal{A}$ of the unit sphere, the Slepian functions are an orthogonal set of strictly bandlimited functions that are defined in such a way that a subset of them is optimally concentrated within the region (Simons *et al.*, 2006). The expansion in Slepian functions of the bandlimited gravity anomaly δg reads

$$\delta g(\theta, \phi) = \sum_{\alpha=1}^{(L+1)^2} S_\alpha(\theta, \phi)\, \delta g_\alpha \tag{4.1}$$

with L being the bandlimit. Here S_α and δg_α are real–valued Slepian functions and coefficients, and θ and ϕ are the colatitude and longitude. The number N of Slepian functions that are optimally concentrated within the region $\mathcal{A}$ is about the spherical analogue of the Shannon number N_S in Slepian's one–dimensional concentration problem

$$N \approx N_S = \sum_{\alpha=1}^{(L+1)^2} \lambda_\alpha = (L+1)^2\, \frac{A}{4\,\pi} \tag{4.2}$$

where A is the solid angle of the region and $\lambda_\alpha \in (0, 1)$ are the eigenvalues quantifying the spatial concentration: Slepian functions that are well ($\lambda_\alpha > 1/2$) or poorly ($\lambda_\alpha \leq 1/2$) concentrated within the region will have eigenvalues near unity or zero, respectively (Simons *et al.*, 2006). The gravity anomaly within the region can thus be approximated by keeping in the right–hand side of eq. (4.1) only those terms associated to the optimally concentrated Slepian functions

$$\delta g(\theta, \phi) \approx \sum_{\alpha=1}^{N} S_\alpha(\theta, \phi)\, \delta g_\alpha \tag{4.3}$$

where we ordered the Slepian functions for decreasing eigenvalues (i.e., $\lambda_\alpha > \lambda_{\alpha'}$ for $\alpha < \alpha'$) in such a way that the first N Slepian functions are those optimally concentrated.

In view of eqs (4.2)–(4.3), the bandlimit L and the region $\mathcal{A}$ determine the number of components that we use in order to describe the gravity anomaly, i.e, the Slepian coefficients δg_α for $\alpha = 1, \ldots, N$. In this respect, the choice of the bandlimit and the region for this spectral domain approach is roughly equivalent to the choice of the

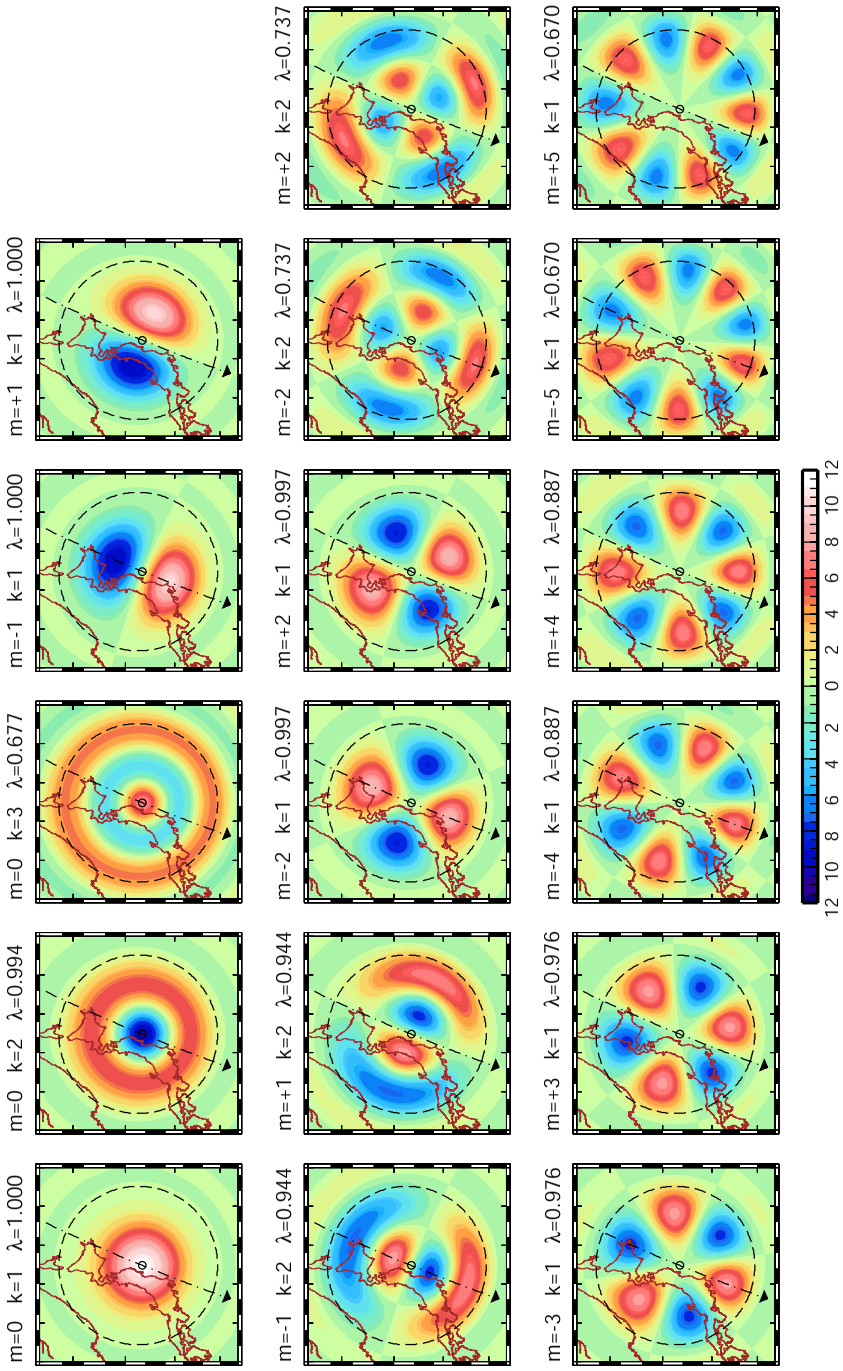

Figure 4.1: The $N = 17$ Slepian functions bandlimited to harmonic degree 60, and optimally concentrated within the circular cup (dashed circle) of half–width 8° and centred at the USGS mainshock, 38.22N, 134.22E.

sampling of the gravity anomaly in the spatial domain.

When the region $\mathcal{A}$ is a circular cup (like we have assumed for dealing with GRACE data), the Slepian functions S_α take the following form

$$S_{\alpha(m,k)}(\theta,\phi) = \begin{cases} h_{mk}(\theta)\,\cos(m\,\phi) & m \leq 0 \\ h_{mk}(\theta)\,\sin(m\,\phi) & m > 0 \end{cases} \tag{4.4}$$

where $m = -L, \ldots, L$ and $k = 1, \ldots, L - |m| + 1$, and h_{mk} are linear combinations of Legendre polynomials $P_{\ell m}$ of the same order m and degrees $\ell = m, \ldots, L$. Here, θ and ϕ must be intended as the colatitude and longitude in the spherical frame with polar axis crossing the center of the cup (Simons *et al.*, 2006), and the index α, as function of the indexes m and k, orders the couple (m, k) accordingly to the order of Slepian functions for decreasing eigenvalues.

For the bandlimit to the harmonic degree $L = 60$ and the circular cup of half–width 8° that we have chosen in order to spatially localize the GRACE gravity data in the surrounding of the 2011 Tohoku earthquake, there are $N = 17$ Slepian functions which are optimally concentrated (we takes only those Slepian functions which have eigenvalues grater than an half, $\lambda_\alpha > 1/2$). The pattern of these Slepian functions is shown in fig. 4.1.

In order to estimate the co–seismic gravity signature of the earthquake, we transform the time series of Stokes coefficients of GRACE Level 2 data into time series of Slepian coefficients, of which we only consider the first N time series. Then, we estimate the co–seismic gravity anomaly in terms of $N = 17$ Slepian coefficients that we obtain by fitting to each time series the step like discontinuity at the earthquake time, together with the reference constant value and a linear trend that accounts for eventual geophysical processes of longer time scales. The interpolating function f_α for the α–th time series thus reads

$$f_\alpha(t) = \delta g_\alpha\, H(t - t_0) + a_\alpha + b_\alpha(t - t_0) \tag{4.5}$$

where t, t_0 and H are the time, the earthquake time and the Heaviside function, and a_α and b_α are the reference constant value and the linear trend, and δg_α is the Slepian

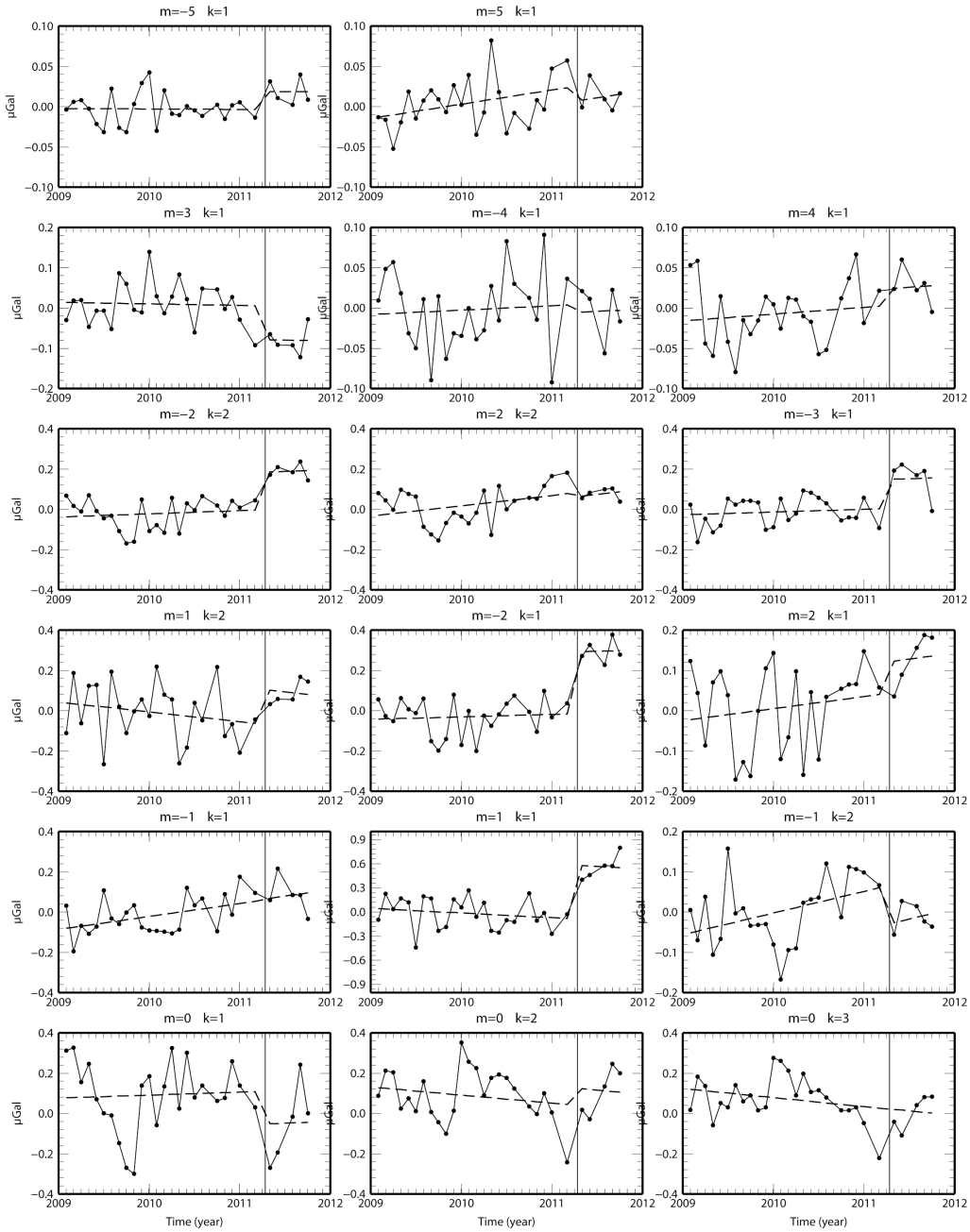

Figure 4.2: The $N = 17$ Time series of Slepian coefficients (solid line and dots) and the interpolating functions (dashed line) defined in eq. (4.5).

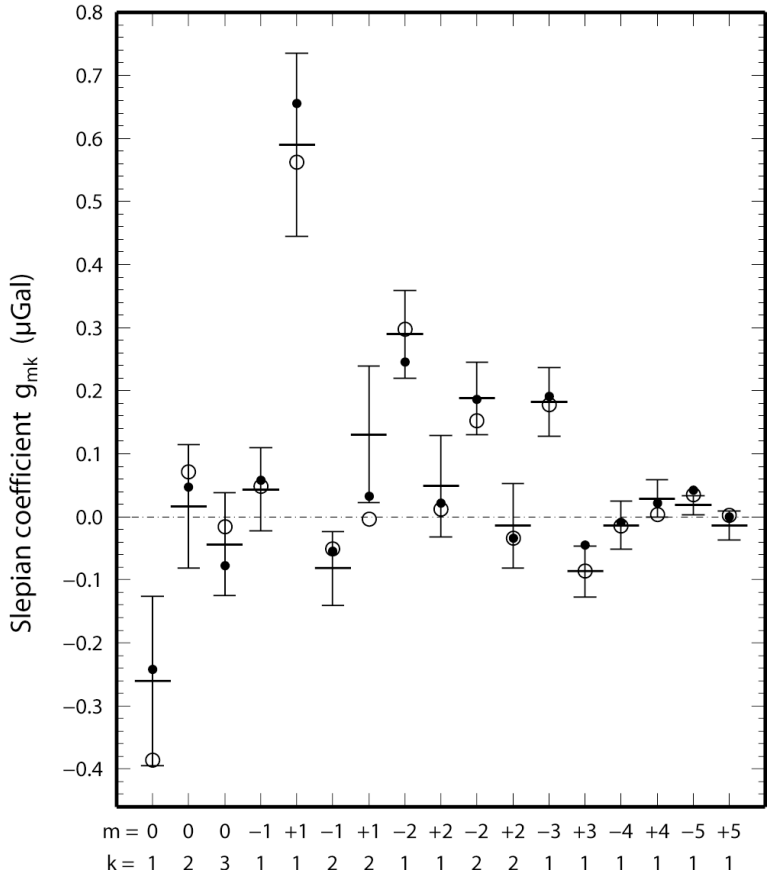

Figure 4.3: Slepian coefficients $g_{\alpha(m,k)}$ of the co-seismic gravity anomaly estimated from GRACE data analysis (horizontal segments, error bars show one-sigma errors inferred *a posteriori* from GRACE data analysis) and modelled using the LC and LM gravitational seismic solutions (open circles and dots) from GCMT analysis discussed in section 4.5.

coefficient of the estimated co–seismic gravity anomaly, which enters eq. (4.3). We do not specifically look for the post–seismic signature due to the few data after the earthquake (only 5 months). Furthermore, differently from the case of the 2004 Sumatran earthquake where clear semi–annual and annual hydrological cycles, the residual ocean circulation cycles and the alias from S_2 tidal wave model errors can be removed fitting sine and cosine functions to the time series (de Linage *et al.*, 2009), this does not substantially improve the fitting for the 2011 Tohoku earthquake.

Fig. 4.2 shows the time series of Slepian coefficients and the estimated interpolating functions. The Slepian coefficients δg_α of the estimated co–seismic gravity anomaly

and their *a posteriori* one–sigma errors are shown in fig. 4.3 and compared with the Slepian coefficients modelled using the seismic solutions that we obtain from GRACE data inversion as described in the next sections of this chapter.

Fig. 4.4 shows the co–seismic gravity change δg^{co} estimated from GRACE data, after DDK3 filtering and spatial localization in the surrounding of the earthquake, eq. (4.3). The patterns is bipolar: the negative pole in the hanging–wall side, with minimum gravity anomaly of $8.6 \pm 1.6\,\mu$Gal at point 39.0N, 137.3E, and the positive pole in the foot–wall side that is characterized by two maxima of $+3.6 \pm 1.5$ and $+3.4 \pm 1.1\,\mu$Gal at points 38.3N, 147.9E and 33.3N, 141.0E.

4.2 Seismic source models

Seismic models belong to two families: point–like sources, which are used in CMT analysis, and finite fault models, which account for realistic co–seismic slip distributions over the fault plane. The latter, however, require prior information on the fault plane (usually inferred from geological information and early inversion of teleseismic waves). In order to use as much as possible only space gravity data, we decide to closely follow the simplifying assumptions of the CMT analysis (Gilbert and Dziewonski, 1975; Dziewonski *et al.*, 1981) and we describe the earthquake as a simple point–like sources. Then, we determine from inversion of GRACE data only the principal seismic source parameters, the hypocentre $\mathbf{r}$ and the moment tensor $\mathbf{m}$, from which we can infer the source mechanism, including the fault plane geometry. This means that we neglect the finite extension of the rupture. While the along–strike extension is not important for the modelling of long–wavelength gravity anomalies, the neglection of the along–dip extension introduces a bias due to the sensitivity of the surface gravity pattern on the seismic source depth, mainly due to the stratification of elastic parameters of the Earth model (Cambiotti *et al.*, 2011a). A similar bias also affects the CMT solution and, in this respect, seismic source depths estimated both from CMT and GCMT analysis should be intended as effective depths.

We model co–seismic gravity changes due to point–like seismic sources by means of a previously developed first–order theory (Sun and Okubo, 1993) implemented in a self–gravitating, compressible 1–D Earth model based on PREM (Dziewonski and Anderson:1981), where the crust and the lithospheric mantle are substituted with CRUST2.0

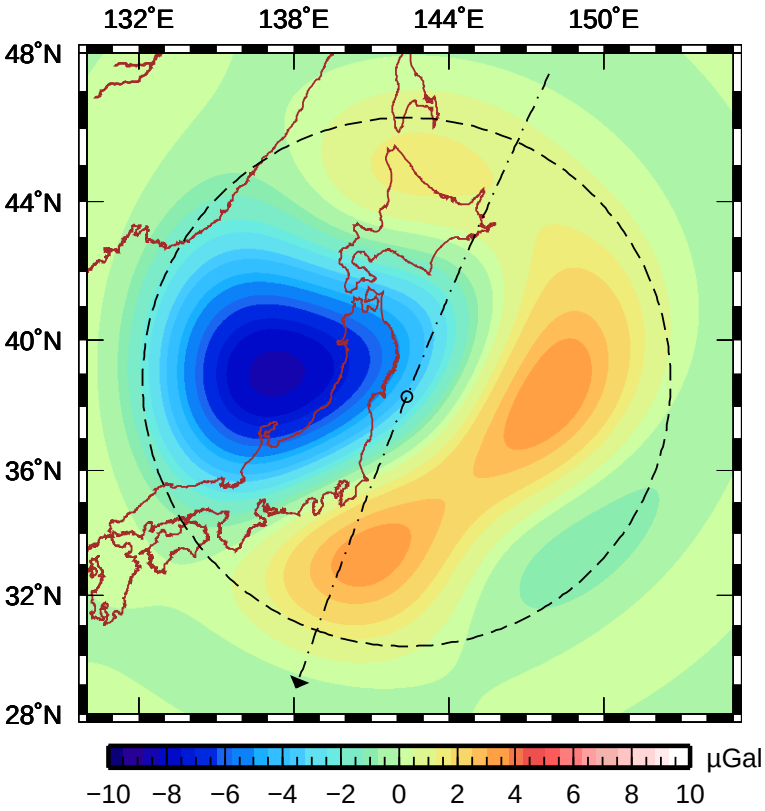

Figure 4.4: Co–seismic gravity anomaly estimated from GRACE gravity data, after DDK3 filtering and spatial localization within a circular cup (dashed circle) of half–width 8° and centred at the USGS epicenter.

Layer	Thickness (km)	S–wave velocity (m/s)	P–wave velocity (m/s)	Density ($\mathrm{kg/m^3}$)
Sediments	0.72	1144.7	2346.0	2130.3
Upper crust	4.94	3237.3	5808.8	2692.7
Middle Crust	5.19	3679.6	6587.2	2896.8
Lower crust	5.28	3856.4	7143.8	3063.9
Upper mantle	203.86	5655.3	8146.9	3358.3

Table 4.1: Material parameters of five outer layers of the Earth based on CRUST2.0 (Bassin *et al.*, 2000). The soft and hard sediment layers have been joined in a single layer and the material parameters of the mantle have been used for the whole upper mantle, above the 220 km discontinuity.

(Bassin *et al.*, 2000) as indicated in Table 4.2. We also account for the gravitational effect of ocean water redistribution including a global ocean layer (Cambiotti *et al.*, 2011a). Within this framework, the relation between co–seismic gravity change $\mathbf{y}$ and the moment tensor $\mathbf{m}$ is linear

$$\mathbf{y} = \mathbf{G}(\mathbf{r})\mathbf{m} \tag{4.6}$$

where $\mathbf{y}$ consists of the $N = 17$ Slepian coefficients of the co–seismic gravity anomaly

$$\mathbf{y} = (\delta g_1, \cdots, \delta g_N) \in \mathcal{Y} \tag{4.7}$$

and $\mathbf{G}$ is the data kernel which non–linearly depends on the hypocentre $\mathbf{r}$. Particularly, the data kernel also depends on the elastic parameters at the depth of the hypocentre and, thus, is discontinuous across the internal interfaces of the Earth model where these parameters have step–like discontinuities (Cambiotti *et al.*, 2011a).

Preliminary tests have yielded seismic solutions characterized by large centers of compression. Rather than to be an indication of the peculiar source mechanism, this indicates that space gravity data that cannot discriminate between the center of compression and the double–couple system of forces equivalent to the tangential dislocation at the fault plane (Ben–Menahem and Singh, 1981). To improve the reliability of our inversion, we remove *a priori* the center of compression from the moment tensor by supplementing the six components of the tensor by a linear constrain, requiring that its trace is zero. Within this scheme, the moment tensor can be decomposed in terms of the balance double–couple and residual dipoles. Removing *a priori* also the residual dipoles would require a non–linear constrain on the moment tensor that increases the complexity of the inverse problem. However, the estimated residual dipoles are weak compared to the balanced double–couple for the 2011 Tohoku earthquake.

4.3 Non–linear inverse problem

Let us consider the model and data spaces, $\mathcal{X}$ and $\mathcal{Y}$, and denote models and data with $\mathbf{x}$ and $\mathbf{y}$, respectively. We also assume that both spaces are linear and finite dimensional

and that it is possible the choice of the parametrization (the system of coordinates for the spaces) such that the metrics are constants. The square of the differential length ds and the volume density v of the $\mathcal{X} \times \mathcal{Y}$ space yield

$$ds^2 = d\mathbf{x}^T \mathbf{g}_X d\mathbf{x} + d\mathbf{y}^T \mathbf{g}_Y d\mathbf{y} \tag{4.8}$$

$$v(\mathbf{x}, \mathbf{y}) = v_X(\mathbf{x})\, v_Y(\mathbf{y}) \tag{4.9}$$

where $\mathbf{g}_X$ and $\mathbf{g}_X$ are the constant metrics of the model and data spaces, and v_X and v_Y are the volume densities

$$v_X = \sqrt{\det \mathbf{g}_X} \tag{4.10}$$

$$v_Y = \sqrt{\det \mathbf{g}_Y} \tag{4.11}$$

Note that also the volume densities are constants. This mens that the probability density (which depends on the specific system of coordinates) and the probability distribution only differ for a constant factor.

Following Mosengard and Tarantola (2002), we consider the probability densities f_X and f_Y that describe prior information on model and data spaces, and we define the joint probability density f in the $\mathcal{X} \times \mathcal{Y}$ space

$$f(\mathbf{x}, \mathbf{y}) = f_X(\mathbf{x})\, f_Y(\mathbf{y}) \tag{4.12}$$

Given the explicit relation between models and data

$$\mathbf{y} = \mathbf{f}(\mathbf{x}) \tag{4.13}$$

the natural way of obtaining posteriori information on the models consists in deriving, from the joint probability density f, the conditional probability on the hypersurface in

the $\mathcal{X} \times \mathcal{Y}$ space defined by eq. (4.13). This yields the posteriori probability density p on the model space $\mathcal{X}$

$$p(\mathbf{x}) = k\, f\, \sqrt{\det \mathbf{A}}\,\Big|_{\mathbf{y}=\mathbf{f}(\mathbf{x})} \tag{4.14}$$

that constitutes the solution of the non–linear inverse problem. Here k is the normalization constant and the matrix $\mathbf{A}$ is given by

$$\mathbf{A} = \mathbf{g}_X + \mathbf{F}\, \mathbf{g}_Y\, \mathbf{F}^T \tag{4.15}$$

where $\mathbf{F}$ is the matrix of partial derivatives

$$\mathbf{F} = \frac{\partial \mathbf{f}}{\partial \mathbf{x}} \tag{4.16}$$

The factor $\sqrt{\det \mathbf{A}}$ in the RHS of eq. (4.14) is because we are not assuming theoretical uncertainties in the modelling (Mosengaard and Tarantola, 2002).

Because the metrics $\mathbf{g}_X$ and $\mathbf{g}_Y$ are constant, the posteriori probability distribution P on the model space $\mathcal{X}$ takes the same form of eq. (4.14)

$$P(\mathbf{x}) = k\, f\, \sqrt{\det \mathbf{A}}\,\Big|_{\mathbf{y}=\mathbf{f}(\mathbf{x})} \tag{4.17}$$

although the normalization constant k differs from that used in eq. (4.14) since it adsorbs the constant term $1/v_X$. From now on k may indicate different normalization constants.

Let us specify the posteriori probability distribution for the general non–linear inverse problem, eq. (4.17), to the case of the principal seismic source parameters (hypocenter and moment tensor) from GRACE data inversion. The data $\mathbf{y}$ are the $N = 17$ Slepian coefficients δg_α of the co–seismic gravity anomaly that we have discussed in sections 4.1 and 4.2, eq. (4.7). We thus keep the data space $\mathcal{Y}$ as the N–dimensional linear space composed by the N Slepian coefficients δg_α associated to Slepian functions that are optimally concentrated within the surrounding of the earthquake. The models $\mathbf{x}$ are instead constituted by the hypocentre $\mathbf{r}$ and the moment tensor $\mathbf{m}$ of the point–like seis-

mic source. The model space $\mathcal{X}$ is thus given by the Cartesian product between the 3–D space restricted to the Earth body $\mathcal{V} \subset \mathbb{R}^3$ for the hypocentre and the 5–D space $\mathcal{M}$ for the moment tensor

$$\mathbf{x} = (\mathbf{r}, \mathbf{m}) \in \mathcal{X} = \mathcal{V} \times \mathcal{M} \tag{4.18}$$

Note that the moment tensor space has only 5 dimensions, rather than 6, because we *a priori* remove the centre of compression as discussed in section 4.2. We parametrize the model space using Cartesian components both for the hypocentre (in the geographycal reference frame) and for the moment tensor (in the epicentral reference system, Ben–Menahmen and Singh, 1981).

We begin assuming the Gaussian probability density f to describe prior information on models and data

$$f(\mathbf{r}, \mathbf{m}, \mathbf{y}) = k \, \exp\left(-S_R - S_M - S_Y\right) \tag{4.19}$$

where

$$2\, S_R = (\mathbf{r} - \mathbf{r}_{pr})^T \mathbf{C}_R^{-1} (\mathbf{r} - \mathbf{r}_{pr}) \tag{4.20}$$

$$2\, S_M = (\mathbf{m} - \mathbf{m}_{pr})^T \mathbf{C}_M^{-1} (\mathbf{m} - \mathbf{m}_{pr}) \tag{4.21}$$

$$2\, S_Y = (\mathbf{y} - \mathbf{y}_{ob})^T \mathbf{C}_Y^{-1} (\mathbf{y} - \mathbf{y}_{ob}) \tag{4.22}$$

Here, $\mathbf{r}_{pr}$, $\mathbf{m}_{pr}$ and $\mathbf{y}_{ob}$ are prior information on the hypocentre, the moment tensor and the observed datum, with uncertainties described by the covariance matrices, $\mathbf{C}_R$, $\mathbf{C}_M$ and $\mathbf{C}_Y$. As suggested by Mosengard and Tarantola (2002), we use these covariances to define the constant metrics $\mathbf{g}_R$, $\mathbf{g}_M$ and $\mathbf{g}_Y$ over the model, $\mathcal{X} = \mathcal{V} \times \mathcal{M}$, and data, $\mathcal{Y}$, spaces

$$\mathbf{g}_R = \mathbf{C}_R^{-1} \tag{4.23}$$

$$\mathbf{g}_M = \mathbf{C}_M^{-1} \tag{4.24}$$

$$\mathbf{g}_Y = \mathbf{C}_Y^{-1} \tag{4.25}$$

This gives the following definition of differential length

$$ds^2 = d\mathbf{r}^T \mathbf{C}_R^{-1} d\mathbf{r} + d\mathbf{m}^T \mathbf{C}_M^{-1} d\mathbf{m} + d\mathbf{y}^T \mathbf{C}_Y^{-1} d\mathbf{y} \tag{4.26}$$

Within this framework and by making use of the relation between models and data, eq. (4.6), into eq. (4.17)), we thus specify the posteriori probability distribution P on the model space $\mathcal{X} = \mathcal{V} \times \mathcal{M}$

$$P(\mathbf{r}, \mathbf{m}) = k \, \exp\left(-S_R - S_M - S_Y\right) \sqrt{\det \mathbf{A}} \Big|_{\mathbf{y}=\mathbf{G}(\mathbf{r})\mathbf{m}} \tag{4.27}$$

where the matrix $\mathbf{A}$ takes the form of the following block matrix

$$\mathbf{A} = \begin{pmatrix} \mathbf{C}_R^{-1} + \mathbf{F}_R \mathbf{C}_Y^{-1} \mathbf{F}_R^T & \mathbf{F}_R \mathbf{C}_Y^{-1} \mathbf{G} \\ \mathbf{G}^T \mathbf{C}_Y^{-1} \mathbf{F}_R^T & \mathbf{G}^T \mathbf{C}_Y^{-1} \mathbf{G} \end{pmatrix} \tag{4.28}$$

and $\mathbf{F}_R$ is the matrix of the partial derivatives with respect to the hypocentre $\mathbf{r}$

$$\mathbf{F}_R = \boldsymbol{\nabla} \left(\mathbf{G}\mathbf{x}\right)^T \tag{4.29}$$

with $\boldsymbol{\nabla}$ being the gradient operator in the 3–D space.

4.4 Gravitational Centroid Moment Tensor solution

Eq. (4.27) constitutes the solution of the inverse problem. Due to the quite large number of variables, 8, it is difficult giving a full description of this solution. However, as we are going to show, it can be further simplified after some straightforward algebra taking advantage of the linear relation between tensor moment $\mathbf{m}$ and data $\mathbf{y}$, eq. (4.6).

We formally define the mean moment tensor $\tilde{\mathbf{m}}$ and covariance matrix $\tilde{\mathbf{C}}_M$ that one would obtain using the least–square method (Tarantola, 2005) when the data kernel $\mathbf{G}$ is constant

$$\tilde{\mathbf{m}} = \mathbf{m}_{pr} + \delta\tilde{\mathbf{m}} \tag{4.30}$$

$$\tilde{\mathbf{C}}_M = \left(\mathbf{C}_M^{-1} + \mathbf{G}^T\mathbf{C}_Y^{-1}\mathbf{G}\right)^{-1} \tag{4.31}$$

with

$$\delta\tilde{\mathbf{m}} = \tilde{\mathbf{C}}_M\, \mathbf{G}^T\, \mathbf{C}_Y^{-1}\, \delta\mathbf{y}_{obs} \tag{4.32}$$

$$\delta\mathbf{y}_{obs} = \mathbf{y}_{obs} - \mathbf{G}\,\mathbf{m}_{pr} \tag{4.33}$$

Because the data kernel $\mathbf{G}$ actually depends on the hypocentre, the above expressions are not the solution of the non–linear inverse problem but they shed light on it. We will also use the data resolution matrix $\tilde{\mathbf{N}}_M$ defined by

$$\mathbf{G}\,\delta\mathbf{m} = \tilde{\mathbf{N}}_M\,\delta\mathbf{y}_{obs} \tag{4.34}$$

that takes the following form

$$\tilde{\mathbf{N}}_M = \mathbf{G}\,\tilde{\mathbf{C}}_M\mathbf{G}^T\,\mathbf{C}_Y^{-1} \tag{4.35}$$

By definition, the formal mean moment tensor $\tilde{\mathbf{m}}$ minimizes the misfit $S_M + S_Y$, eqs (4.21)–(4.22). Also, after some straightforward algebra, $S_M + S_Y$ can be arranged as follows

$$S_M + S_Y = \tilde{S}_M + \tilde{S}_Y \tag{4.36}$$

where

$$2\,\tilde{S}_M = (\mathbf{m} - \tilde{\mathbf{m}})^T\,\tilde{\mathbf{C}}_M^{-1}\,(\mathbf{m} - \tilde{\mathbf{m}}) \tag{4.37}$$

$$2\,\tilde{S}_Y = \delta\mathbf{d}_{obs}\mathbf{C}_Y^{-1}\left(\mathbf{1} - \tilde{\mathbf{N}}_M\right)\delta\mathbf{d}_{obs} \tag{4.38}$$

and $\mathbf{1}$ is the identity matrix. Particularly, $\tilde{S}_Y$ is the minimum of $S_M + S_Y$ at fixed hypocentre. Furthermore, we decompose the matrix $\mathbf{A}$ into the product of block matrices

$$\mathbf{A} = \begin{pmatrix} \mathbf{1} & \mathbf{F}_R\mathbf{C}_Y^{-1}\mathbf{G}_R \\ \mathbf{0} & \tilde{\mathbf{C}}_M^{-1} \end{pmatrix} \begin{pmatrix} \mathbf{C}_R^{-1} + \mathbf{Q} & \mathbf{0} \\ \tilde{\mathbf{C}}_M\mathbf{G}^T\mathbf{C}_Y^{-1}\mathbf{F}_R^T & \mathbf{1} \end{pmatrix} \tag{4.39}$$

where

$$\mathbf{Q} = \mathbf{F}_R\mathbf{C}_Y^{-1}\left(\mathbf{1} - \tilde{\mathbf{N}}_M\right)\mathbf{F}_R^T \tag{4.40}$$

The determinant of the matrix $\mathbf{A}$, eq. (4.28), thus yields

$$\det\mathbf{A} = \frac{\det\left(\mathbf{C}_R^{-1} + \mathbf{Q}\right)}{\det\tilde{\mathbf{C}}_M} \tag{4.41}$$

Note that, in view of eqs (4.29) and (4.35), the components Q_{ij} of the matrix $\mathbf{Q}$ can be expressed as

$$Q_{ij} = \mathbf{m}^T\mathbf{W}_{ij}\mathbf{m} \tag{4.42}$$

where $\mathbf{W}_{ij}$ are bilinear form on the moment tensor space that depend on the hypocentre via the data kernel $\mathbf{G}$ and its gradient $\boldsymbol{\nabla}\mathbf{G}$

$$\mathbf{W}_{ij} = \frac{\partial\mathbf{G}^T}{\partial r_i}\mathbf{C}_Y^{-1}\left(\mathbf{1} - \tilde{\mathbf{N}}_M\right)\frac{\partial\mathbf{G}}{\partial r_j} \tag{4.43}$$

with r_i being the Cartesian components of the hypocentre $\mathbf{r} = (r_1, r_2, r_3)$. In this respect, $\det\mathbf{A}$ is a six–order polynomial in the components of the moment tensor $\mathbf{m}$.

By substituting eqs (4.36) and (4.41) into eq. (4.27), we thus arrange the probability distribution P as follows

$$P(\mathbf{r}, \mathbf{m}) = K(\mathbf{r}, \mathbf{m})\, H(\mathbf{r}) \tag{4.44}$$

where K is the conditional probability distribution for the moment tensor at fixed hypocentre and H is the marginal probability for the hypocentre

$$K(\mathbf{r}, \mathbf{m}) = G(\mathbf{r}, \mathbf{m})\, \frac{\Delta(\mathbf{r}, \mathbf{m})}{\tilde{\Delta}(\mathbf{r})} \tag{4.45}$$

$$H(\mathbf{r}) = k\, \exp\left(-S_R(\mathbf{r}) - \tilde{S}_Y(\mathbf{r})\right)\, Q(\mathbf{r}) \tag{4.46}$$

Here, G is the Gaussian distribution of the formal solution obtained using the least–square method

$$G(\mathbf{r}, \mathbf{m}) = \frac{\exp\left(-\tilde{S}_M(\mathbf{r}, \mathbf{m})\right)}{\sqrt{(2\,\pi)^5 \det \tilde{\mathbf{C}}_M(\mathbf{r})}} \tag{4.47}$$

and

$$\Delta(\mathbf{r}, \mathbf{m}) = \sqrt{\det\left(\mathbf{C}_R^{-1} + \mathbf{Q}(\mathbf{r}, \mathbf{m})\right)} \tag{4.48}$$

$$\tilde{\Delta}(\mathbf{r}) = \int_{\mathcal{M}} G(\mathbf{r}, \mathbf{m})\, \Delta(\mathbf{r}, \mathbf{m})\, d\mathbf{m} \tag{4.49}$$

The calculations of the posteriori probability distribution P, eq. (4.44), does not require numerical efforts because it is based on the analytical expressions for the least square solution, except for the 5–dimensional integration over the moment tensor space involved by the term $\tilde{\Delta}$, eq. (4.49). However, by considering the Gaussian distribution G entering eq. (4.49), we can preliminary estimate the region of the moment tensor space with significant probabilities and optimize the numerical evaluation of this integration.

4.4.1 Model estimators

Owing to the rearrangement of the probability distribution P given by eq. (4.44), we can obtain model estimators as the mean model and its covariance as follows. First, we obtain the mean moment tensor $\mathbf{m}^*$ and covariance matrix $\mathbf{C}_M^*$, over the moment tensor space $\mathcal{M}$ and at fixed hypocentre $\mathbf{r}$, by means of the only conditional probability distribution K for the moment tensor

$$\mathbf{m}^*(\mathbf{r}) = \int_{\mathcal{M}} K(\mathbf{r}, \mathbf{m})\, \mathbf{m}\, d\mathbf{m} \tag{4.50}$$

$$\mathbf{C}_M^*(\mathbf{r}) = \int_{\mathcal{M}} K(\mathbf{r}, \mathbf{m})\ (\mathbf{m} - \hat{\mathbf{m}})^T\, (\mathbf{m} - \hat{\mathbf{m}})\ d\mathbf{m} \tag{4.51}$$

Then, the mean moment tensor $< \mathbf{m} >$ and covariance matrix $< \mathbf{C}_M >$ over a subset $\mathcal{S} \subseteq \mathcal{V}$ of the Earth body yield

$$< \mathbf{m} >= \int_{\mathcal{S}} H(\mathbf{r})\, \mathbf{m}^*(\mathbf{r})\, d\mathbf{r} \tag{4.52}$$

$$< \mathbf{C}_M >= \int_{\mathcal{S}} H(\mathbf{r})\, \mathbf{C}_M^*(\mathbf{r})\, d\mathbf{r} + \int_{\mathcal{S}} H(\mathbf{r})\ (\mathbf{m}^* - < \mathbf{m} >)\, (\mathbf{m}^* - < \mathbf{m} >)\ d\mathbf{r} \tag{4.53}$$

Differently, owing to the linear relation between moment tensor $\mathbf{m}$ and data $\mathbf{y}$, the mean hypocentre $< \mathbf{r} >$ and covariance matrix $< \mathbf{C}_R >$ over a subset $\mathcal{S} \subseteq \mathcal{V}$ of the Earth body do not involve integration over the moment tensor space $\mathcal{M}$

$$< \mathbf{r} >= \int_{\mathcal{S}} H(\mathbf{r})\, \mathbf{r}\, d\mathbf{r} \tag{4.54}$$

$$< \mathbf{C}_R >= \int_{\mathcal{S}} H(\mathbf{r})\, (\mathbf{r} - < \mathbf{r} >)\, (\mathbf{r} - < \mathbf{r} >)\ d\mathbf{r} \tag{4.55}$$

4.4.2 Best models

By making use of the step descend algorithm (Tarantola, 2005), we can easily estimate the maximum likelihood moment tensor $\mathbf{m}_{\rm best}$ at fixed hypocentre $\mathbf{r}$, i.e., the moment tensor for which the conditional probability K is maximum at the fixed hypocentre. Rather than maximize the conditional probability K, we minimize the negative of the logarithmic volumetric probability $\ln K_V$

$$-\ln K_V(\mathbf{r},\mathbf{m}) = \tilde{S}_M(\mathbf{r},\mathbf{m}) + \frac{1}{2}\ln\Big[(2\,\pi)^5\,\det\tilde{\mathbf{C}}_M(\mathbf{r})\Big] + \ln\tilde{\Delta}(\mathbf{r}) - \ln\Delta(\mathbf{r},\mathbf{m}) \tag{4.56}$$

Particularly, choosing the formal covariance $\tilde{\mathbf{C}}_M$ obtained using the least–square method as metric for the moment tensor space, the step ascent vector $\boldsymbol{\gamma}$ is given by

$$\boldsymbol{\gamma} = -\tilde{\mathbf{C}}_M\,\frac{\partial\ln K_V}{\partial\mathbf{m}} = \mathbf{m} - \tilde{\mathbf{m}} - \tilde{\mathbf{C}}_M\,\frac{\partial\Delta}{\partial\mathbf{m}} \tag{4.57}$$

where the partial derivative of Δ with respect to the moment tensor $\mathbf{m}$ takes the following form

$$\frac{\partial\Delta}{\partial\mathbf{m}} = \sum_{i,j,k=1}^{3}\epsilon_{ijk}\,\big[\big(\mathbf{W}_{1i}+\mathbf{W}_{i1}^T\big)\;B_{2j}\,B_{3k}+ B_{1i}\;\big(\mathbf{W}_{2j}+\mathbf{W}_{j2}^T\big)\;B_{3k} + B_{1i}\,B_{2j}\;\big(\mathbf{W}_{3k}+\mathbf{W}_{k3}^T\big)\big]\;\mathbf{m} \tag{4.58}$$

where ϵ_{ijk} and B_{ij} are the Levi–Civita symbol and the components of the matrix $\mathbf{C}_R + \mathbf{Q}$.

Then, we obtain the maximum likelihood seismic model by maximizing the posteriori probability distribution P evaluated at the best moment tensor $\mathbf{m}_{\rm best}$ for the hypocentre. We do this by sampling the Earth body $\mathcal{V}$ every 0.2° degree over the Earth surface and 0.5 km along depth. In this way we also find the maximum likelihood hypocentre $\mathbf{r}_{\rm best}$

$$P(\mathbf{r}_{\rm best},\mathbf{m}_{\rm best}(\mathbf{r}_{\rm best})) = \max_{\mathbf{r}\in\mathcal{S}} H(\mathbf{r})\,K(\mathbf{r},\mathbf{m}_{\rm best}(\mathbf{r})) \tag{4.59}$$

4.5 Gravitational Centroid Moment Tensor analysis

For this first application of the GCMT analysis to the 2011 Tohoku earthquake, we do not assume prior information on models in order to investigate the resolving power of space gravity data from GRACE. We only assume prior information on the epicenter to be consistent with the spatial localization of the gravity anomaly used to estimate the co–seismic gravity anomaly from GRACE data analysis. Particularly, the prior epicenter is the center of the circular cup, i.e., the epicenter of the USGS mainshock, 38.22N, 134.22E, and the prior uncertainties correspond to the half–width of 8°, i.e., about 800 km. Because prior information on model space determines the metrics $\mathbf{g}_R$ and $\mathbf{g}_M$ of the model spaces, eqs (4.23)–(4.24), this choice of prior information also affects the probability distribution P as pointed out by eqs (4.15) and (4.17). In view of eqs (4.31) and (4.41), this is the case only if

$$\mathbf{C}_R^{-1} \gtrsim \mathbf{Q} \tag{4.60}$$

$$\mathbf{C}_M^{-1} \gtrsim \mathbf{G}^T \mathbf{C}_Y^{-1} \mathbf{G} \tag{4.61}$$

Numerical tests for the 2011 Tohoku earthquake have shown that the above constrains require prior information with accuracy comparable or smaller than 10^{22} N m for the moment tensor and than 50 km and 300 km for the depth of hypocentre and the epicentre, respectively.

Note that the posteriori probability distribution P, eq. (4.44), has step–like discontinuities at the internal interfaces of the Earth model due to the discontinuity of the data kernel $\mathbf{G}$ at these interfaces. For this reason, in the following, we will focus on model estimators as function of depths and we will search best models in each layer of the Earth model.

Fig. 4.5 shows the marginal probability for the depth of the hypocentre. The probabilities within the upper, middle and lower crusts and the lithospheric mantle are 4, 6, 30 and 60 per cent, respectively. The largest probabilities are from 11 km to 23 km depths, which total to 75 per cent of the probability distribution, and the maximum marginal probability is just below the Moho discontinuity. GCMT analysis thus contrasts with

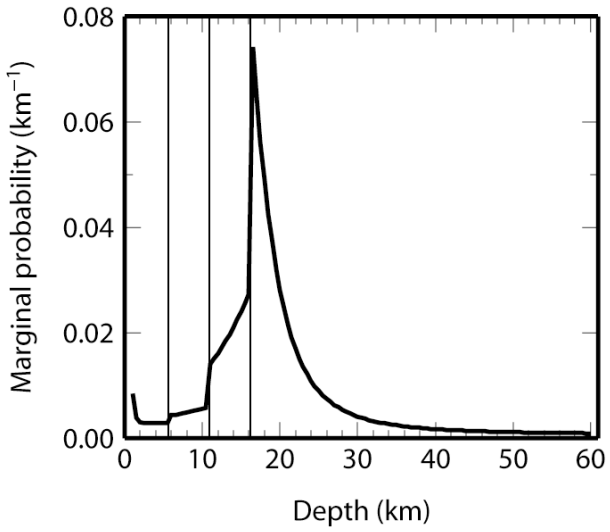

Figure 4.5: Marginal probability for the depth of the hypocentre.

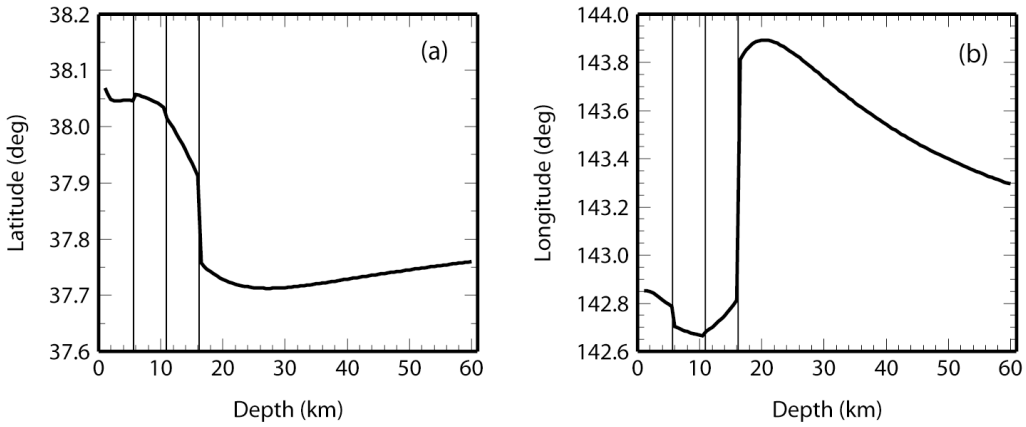

Figure 4.6: Mean (b) latitude and (c) longitude of the epicenter.

the possibility of significant up–dip slip within the shallower crustal layers (Lay *et al.*, 2011a).

Figs 4.6 show the mean epicenter as function of depth. It varies slightly within the crustal layers around the point 38N, 142.8E. Just below the Moho discontinuity the epicenter is shifted seaward at point 37.8N, 133.9E and gradually moves landward to the point 37.8N, 133.3E for increasing depths. By comparing these findings with the geological structure of the Pacific plate subducting beneath the northeastern Japan arc

inferred from seismic experiments (Takahaski *et al.*, 2004), we note a dichotomy between gravitational seismic solutions within the crustal layers and the lithospheric mantle. Indeed, the mean epicenters within the crust indicate that the earthquake occurred within the continental plate or at contact zone between the forearc crust and the uppermost mantle wedge. In contrast, the mean epicenters within the lithospheric mantle indicate an intraplate earthquake occurred beneath the trench and within the oceanic mantle. Both cases are contemplated by the shallower seismic zones inferred from locations of microearthquake hypocentres (Takahaski *et al.*, 2004). However, by considering the marginal probability for the source depth shown in fig. 4.4a, the GCMT analysis mainly support the conclusion that the 2011 Tohoku earthquake occurred within the oceanic mantle. This contrasts with the Global CTM Project and USGS solutions and with previous giant earthquakes occurred in same region, except for the 1933 Sanriku earthquake (Kanamori, 1971), which occurred seaward of the trench with the mechanism of a normal fault type.

Once removed the centre of compression from the moment tensor, the mean models are mainly characterized by the system of double–couples. This is shown in figs 4.7a,b by the comparison of the mean moment magnitudes of the double couple (M_W^{DC}) and of the residual dipoles (M_W^{RD}): the former varies from 9.7 to 8.8 increasing depth, while the latter is always less than 8.6 and, particularly, less than 8 within the lower crust and in a narrow depth interval of the lithospheric mantle, from 22 to 25 km depths. It is noteworthy that M_W^{DC} has step–like discontinuities at the internal interfaces, which are mainly due to discontinuities in the elastic material parameters, and varies almost as the negative of the logarithm of depth within each layer. This suggests testing the following empirical law for the mean seismic moment of the double couple (M^{DC}) of the 2011 Tohoku earthquake

$$M^{DC}(z) \approx \alpha\, z^{-1} \tag{4.62}$$

where z and α are the depth and a constant that only depends on the layer of the Earth model and can be estimated from fig. 4.7c. This empirical law reflects the fact that, for thrust earthquakes of given seismic moment, the peak–to–peak gravity anomaly increases with depth within each layer of the Earth, as it has been pointed out for the case

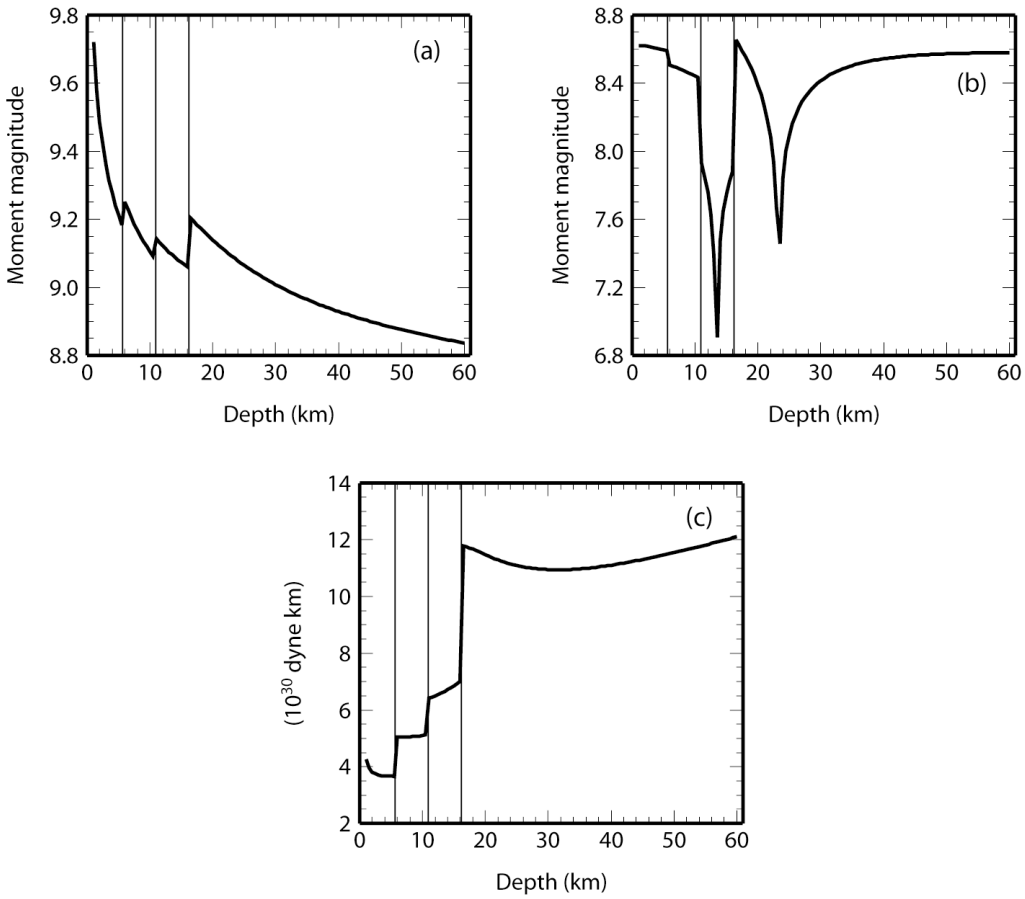

Figure 4.7: (a) Mean moment magnitude M_W^{DC} of the double couple, (b) mean moment magnitude M_W^{RD} of the residual dipoles and (c) the parameter α entering eq. (4.62)

of the 2004 Sumatran earthquake (Cambiotti *et al*, 2011a). Indeed, in order that the modelled peak–to–peak gravity anomaly agrees with observations, fig. 4.4a, the seismic moment must decrease with depth. The estimate of the moment magnitude M_W^{DC} is thus affected by the along depth resolving power of space gravity data. By focusing on the depth interval with the largest probability (the lower crust and the uppermost lithospheric mantle), the moment magnitude M_W^{DC} is within the range $9.0 - 9.2$. These estimates agree with Global CMT Project and USGS solutions and with several finite fault models (Lay *et al.*; 2011a, Ammon *et al.*, 2011; Lay *et al.*, 2011b) from inversion of teleseismic and geodetic data (which range from 9.0 to 9.1), although we do not exclude higher

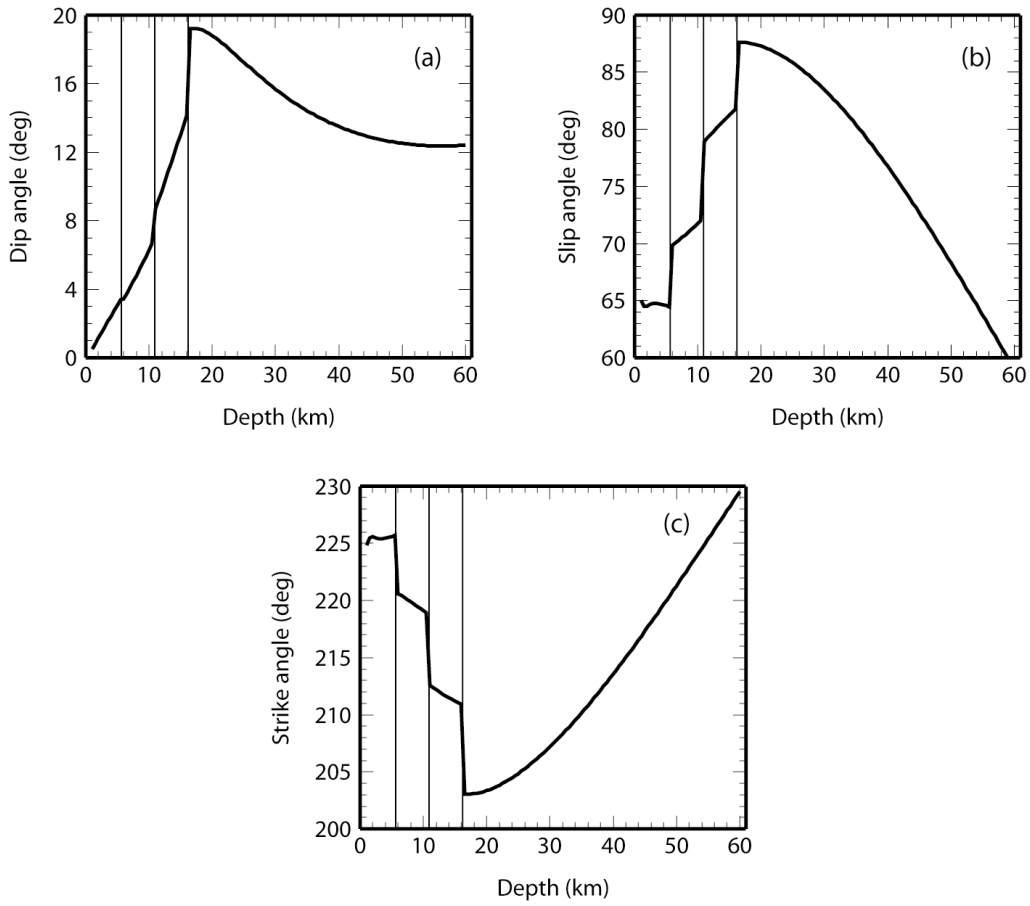

Figure 4.8: Mean (a) dip, (b) slip and (c) strike angles.

magnitudes, 9.2.

Fig. 4.8 shows the geometry of the fault discontinuity in terms of the mean dip, strike and slip angles as function of depth. Within the crust the dip angle grows almost linearly with depth, from $0.5°$ (at 1km depth) to $14°$ (at the Moho). Then, it jumps to $19°$ just below the Moho and decrease to $12.5°$ at 50 km depth. Because we are not using prior information on the fault plane, we can asses the reliability of these results by comparison with geological information of the subduction zone. The increase of the dip angle within the crust is consistent with the subduction angle of the Pacific plate beneath the northeastern Japan arc that becomes gradually steeper from east to west (Takahaski *et al.*, 2004), from $3°$ to $11°$. The dip angle just below the Moho is instead larger by about a

Solution	LC	LM	Global CMT Project	USGS
M^{DC} (10^{29} dyne)	4.6	7.4	5.3	4.5
M_W^{DC}	9.07	9.21	9.12	9.07
M^{RD} (10^{27} dyne)	-0.9	102.4	1.4	-5.0
M_W^{RD}	7.26	8.64	7.40	7.77
Depth (km)	16.5	16.5	20.0	10
Latitude	38.0N	37.8N	37.5N	38.5N
Longitude	142.9E	143.9E	143.1E	142.6E
Dip	13°	19°	10°	14°
Slip	81°	87°	88°	68°
Strike	210°	203°	203°	187°

Table 4.2: Best seismic model parameters of the LC, LM, Global CMT Project and USGS solutions for the 2011 Tohoku earthquake.

factor 2 or greater. This further supports the dichotomy between seismic solutions within the forearc crust and the oceanic lithospheric mantle, where the latter is less constrained to follow the subduction angle. Also, the estimates of strike and slip angles, which ranges from 202° to 225° and from 65° to 88°, respectively, are in agreement with the local trench and the expectation of a thrust earthquake, particularly within the lower crust and the uppermost lithospheric mantle.

The linear dependence of the mean dip angle on depth within the crust, fig. 4.8a, can be explained in terms of the gravitational effect of the ocean water redistribution. Indeed, shallow thrust earthquakes induce an uplift of the ocean floor in the foot–wall side which is greater in magnitude than the downdrop in the hanging–wall side (Cambiotti *et al.*, 2011a). This causes a greater gravity reduction due to ocean water removal from the near field that potentially could hide the positive pole of the co–seismic gravity anomaly observed in GRACE data, fig. 4.4a. However, a smaller dip angle reduces the uplift of the ocean floor, thus causing a less asymmetric pattern of the ocean floor topography. This limits the ocean water removal from the near field because ocean water displaced away from the uplift of hanging wall side partially accumulates in the downdrop of the foot–wall side. In light of this, the smaller dip angles that we obtain for shallower seismic sources from GRACE data inversion compensate for the greater gravity reduction and, particularly, the modelled gravity anomalies keep the bipolar pattern observed in GRACE data.

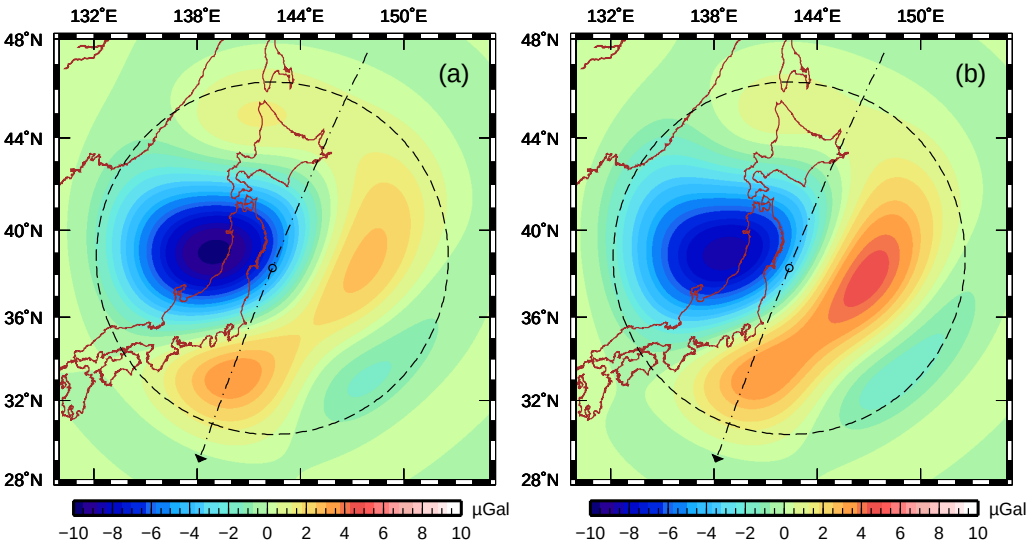

Figure 4.9: Co–seismic gravity anomaly modelled using the LC and LM gravitational seismic solutions, after DDK3 filtering and spatial localization within a circular cup (dashed circle) of half–width 8° and centred at the USGS epicenter.

In order to account for the dichotomy between gravitational seismic solutions within the crust and the lithospheric mantle resulting from the above analysis, we propose two different seismic solutions. They are the maximum likelihood seismic models within the lower crust (LC solution) and the lithospheric mantle (LM solution), the seismic parameters of which are listed in Table 4.1 and compared with the Global CMT Project and USGS solutions. The LC solution well agrees with the two traditional seismological solutions, but for the discrepancy between the depths of the hypocentres likely due to different data set and Earth structures used to model the earthquake. However, the present analysis mainly support the LM solution, which is about two or three times more likely than the LC solution. On the other hand, the source mechanism of the LC solution better agrees with a tangential dislocation, being characterized by a moment magnitude of the residual dipoles smaller than that of the LM solution, 7.3 compared to 8.6. We thus consider both solutions as plausible solutions for the 2011 Tohoku earthquake.

The LM solution mainly differs from the LC solution for the larger moment magnitude (9.2 instead of 9.1), the steeper dip angle (19° instead of 13°) and the hypocentre (at 37.7N, 143.9E just below the Moho instead of 38.0N, 142.8E just above the Moho). Because point–like seismic sources neglect the finite extension of the co–seismic slip

distribution, the estimated depths are actually effective depths. Particularly, the fact that the LC and LM solutions are located just above and below the Moho must be intended as indication of the type of the earthquake: the former occurs within the continental crust just above the contact zone between the forearc crust and the uppermost mantle wedge, while the latter occurs within the oceanic mantle, just below the oceanic crust.

Figs 4.9 compare the co–seismic gravity anomalies obtained implementing the two GCMT solutions, after DDK3 filtering and spatial localization using Slepian functions. Both synthetic data well agree with observations, fig. 4.4, with confidence levels of 38 and 36 per cent for LC and LM solutions, respectively.

4.6 Conclusion

We have developed the Gravitational Centroid Moment Tensor (GCMT) method, based on the inversion of space gravity data, for modelling giant earthquakes in terms of the principal seismic source parameters (hypocentre and moment tensor). Applying this method to GRACE data of the 2011 Tohoku earthquake, we find two distinct gravitational seismic solutions which are both consistent with a megathrust earthquake. The LC solution well agrees with Global CMT Project and USGS solutions based on inversion of teleseismic wave observations and is located within the forearc crust. The LM solution, instead, differs for the steeper dip angle and the larger moment magnitudes of the double–couple and of the residual dipoles, 9.2 and 8.6, respectively. Furthermore, it is located further off–shore and within the oceanic mantle, just below the oceanic crust. In view of this, it could be a candidate solution for explaining the huge tsunami caused by the earthquake.

Our new gravitational seismological method complements the traditional approaches to seismic studies, including those based on the seismic, GPS and tsunami observations.

Part III

TRUE POLAR WANDER

Abstract

Issues related to long time scale instabilities in the Earth's rotation have continuously been debated, after the pioneering works of the sixties by Munk, MacDonald and Gold. The Earth's rotation axis is constantly tracking the main inertia axis of the planet that evolves due to internal and surface mass rearrangements. This motion called True Polar Wander (TPW) is due to mantle convection on the million years time scale. On smaller timescales, hundreds of thousand years, ice ages also cause polar excursion, although their contribution to the Earth's inertia tensor remains negligible compared to that of the mantle 3–D structure.

In Chapter 5 we show TPW simulations driven by ice ages obtained using compressible Maxwell Earth models, based on the numerical integration in the radial variable of the momentum and Poisson equations and on the contour integration in the Laplace domain which allows us to deal with the non–modal contribution from continuous radial rheological variations. We thus discuss the so called "traditional approach" to the Earth's rotation developed during the eighties and nineties and we explain within this approach the sensitivity of TWP predictions to the elastic and viscoelastic rheologies of the lithosphere. We agree on the necessity to include the effects of the non hydrostatic bulge from mantle convection to obtain realistic ice age TPW rates in the lower mantle viscosity range from 10^{21} Pa s to 10^{22} Pa s, as first indicated by Mitrovica *et al.* (2005). We show that their analysis represents a first attempt to couple the effects on TPW from mantle convection and glacial forcing, by including the non hydrostatic bulge due to mantle convection but not the other time–dependent driving terms. This partial coupling freezes in space the non hydrostatic contribution due to mantle convection, thus damping the present–day ice age TPW and forcing the axis of instantaneous rotation to come back to its initial position when ice ages started. We argue that a viscoelastic (with high viscosity) rather than elastic lithosphere should be adopted in the modelling of TPW although it is difficult to disentangle the effects of lithospheric rheology and mantle convection on the time of ice ages. Within this framework, the maximum ice age TPW rates, which is obtained for lower mantle viscosities of about 10^{22} Pa s, do not account for more than 77 per cent of the observation, $0.925^{\circ}\,\mathrm{Myr}^{-1}$ (McCarthy and Luzum, 1996). Mantle convection must therefore contribute to TPW.

We also discuss the implication of self–consistent mantle convection calculations of

the non hydrostatic contribution and its impact on the long–term Earth's rotation stability during ice ages, as well as the effects of the compressible rheology compared to the widely used incompressible one.

In Chapter 6 we face the problem of TPW driven by mantle convection on the million years time scale. Most studies have assumed that on this long time scale the planet readjusts without delay and that the Earth's rotation axis and the Maximum Inertia Direction of Mantle Convection (MID–MC) coincide. We herein overcome this approximation that leads to inaccurate TPW predictions and we provide a new treatment of Earth's rotation discussing both analytical and numerical solutions. We first obtain a linearized theory for modelling finite polar excursions due to slow evolving mantle density heterogeneities. The novel theoretical framework allows to deeply understand the interaction between mantle convection and rotational bulge readjustments, and provides the physical laws for the characteristic times controlling the polar motion in the directions of the intermediate and minimum principal axes of the mantle convection inertia tensor. By solving the non–linearized Liouville equation for the past 100 million years and taking into account the delay of the rotational bulge readjustments, we obtain an average TPW rate in the range from $0.5^\circ\,\mathrm{Myr}^{-1}$ to $1.5^\circ\,\mathrm{Myr}^{-1}$ and a sizeable offset of several degrees between the rotation axis and the MID–MC. This is in distinct contrast with the general belief that these two axes should coincide or that the delay of the readjustment of the rotational bulge can be neglected in TPW studies. We thus clarify a fundamental issue related to mantle mass heterogeneities and to TPW dynamics.

Chapter 5

Ice Age True Polar Wander in a compressible and non hydrostatic Earth

Starting from the works by Munk, MacDonald and Gold, issues related to the secular change of the Earth's rotation axis named True Polar Wander (TPW), never ceased to be discussed or questioned. Progresses have been made since the sixties, on two major aspects: the first deals with the improvement in the modelling of the Earth, in terms of rheological stratifications, and the second is related to the new insights on surface and deep seated density anomalies originating from ice ages and mantle convection as major sources of polar wander. After decades, we are however still in the situation in which it is necessary to come back to some basic TPW issues to dig out deeper insights into the physics of this aspect of the dynamics of our planet, focussing, in particular, on the nature, elastic or viscoelastic, of the outermost part of our planet.

Ricard *et al.* (1993a) first exploited the rotational behaviour of elastic versus viscoelastic outermost part of the Earth, introducing the T time scale characterizing the readjustment of the equatorial bulge, based on realistically stratified viscoelastic Earth models. Vermeersen and Sabadini (1999) pointed out the reduction in the TPW displacements for Maxwell Earth models carrying a viscoelastic lithosphere compared to those with an elastic lithosphere. Nakada (2002) went thoroughly into the issue related to the rheology of the lithosphere by considering high viscous viscoelastic lithospheres. He showed as the TPW rates for the lower mantle viscosity ranging from 10^{21} Pa s to 10^{22} Pa s are extremely sensitive to the choice of the rheology of the lithosphere, elastic or viscoelastic with high viscosity. This might be seen as surprising since the high viscous viscoelastic lithosphere is expected to behave as an elastic body for time scales of 1 Myr comparable to that of post glacial rebound. Mitrovica *et al.* (2005) named this sensitivity of TPW predictions the "Nakada paradox" and (as cited by Nakada) "has suggested that this paradox originates from an inaccuracy in the traditional rotation theory associated with the treatment of the background equilibrium rotating form upon which any load–and rotation–induced perturbations are superimposed (e.g., Wu and Peltier, 1984)".

Starting from these preliminary remarks, Mitrovica *et al.* (2005) suggest a new treatment of the rotational dynamics where the observed fluid Love number is used in the linearized Euler dynamic equation, rather than the tidal fluid limit deduced self–consistently from the Maxwell Earth model which is used to evaluate the load– and rotation–induced perturbations of the inertia tensor. This apparently minor change (the discrepancy between the observed and tidal fluid limits is about 1 per cent) has a potentially large impact on TPW predictions and would solve the "Nakada paradox".

In this chapter, we will restate the mathematical framework of the linearized Earth's rotation theory in order to enlighten the differences between the so called "traditional approach" (Sabadini and Peltier, 1981; Sabadini *et al.*, 1982; Wu and Peltier, 1984) and the treatment indicated by Mitrovica *et al.* (2005). We show results from a newly developed compressible Earth model, including the methodology to transform the results from the Laplace domain into the time domain. This clarifies some issues related to the use of the normal mode relaxation approach within rotational problems. Then, in order to make our TPW simulations as realistic as possible, we explore the roles of the rheology of the lithosphere, elastic or viscoelastic, and the non hydrostatic contribution to the fluid Love number from mantle convection calculations.

5.1 The rotation theory for Maxwell Earth models

The equation of motion of a rotating body in a rotating frame is the well known Euler dynamic equation. When no external torque is applied, it reads

$$\frac{d\left(\boldsymbol{\mathcal{J}}\cdot\boldsymbol{\omega}\right)}{dt}+\boldsymbol{\omega}\times\left(\boldsymbol{\mathcal{J}}\cdot\boldsymbol{\omega}\right)=\mathbf{0} \tag{5.1}$$

where $\boldsymbol{\mathcal{J}}$ and $\boldsymbol{\omega}$ are the inertia tensor and the angular velocity. We adopt the geographical reference frame with unit vectors $\boldsymbol{x}_1$, $\boldsymbol{x}_2$ and $\boldsymbol{x}_3$ ($\boldsymbol{x}_1$ points to the equator and the Greenwich meridian, while $\boldsymbol{x}_3$ points to the north pole) and, before any perturbation occurs, we consider the Earth rotating with constant angular rate ω_0 around $\boldsymbol{x}_3$

$$\boldsymbol{\omega}(t<0)=\boldsymbol{\omega}_0=\omega_0\,\boldsymbol{x}_3 \tag{5.2}$$

Let us subdivide the inertia tensor into three parts

$$\boldsymbol{\mathcal{J}}=I\,\mathbf{1}+\boldsymbol{\mathcal{B}}+\boldsymbol{\mathcal{C}} \tag{5.3}$$

The first term is the inertia of the spherically symmetric Earth model, with I and $\mathbf{1}$ being the inertia moment and the identity matrix. The second term, $\boldsymbol{\mathcal{B}}$, is the inertia tensor

describing the effects of the centrifugal potential, i.e., the rotational bulge. The third term, $\boldsymbol{\mathcal{C}}$, is the inertia tensor due to other contributions, like ice age loading and mantle convection.

The difference between the approach used in a series of papers (Sabadini and Peltier, 1981; Sabadini *et al.*, 1982; Wu and Peltier, 1984) and the newly proposed by Mitrovica *et al.* (2005) can be appreciated starting from the MacCullagh's formula (Jeffreys, 1952; eq. (5.2.3) of Munk and MacDonald, 1960)

$$\boldsymbol{\mathcal{B}} = \frac{a^5}{3\,G}\, k^T \star \left(\boldsymbol{\omega} \otimes \boldsymbol{\omega} - \frac{\omega^2}{3}\, \mathbf{1} \right) \tag{5.4}$$

where k^T and $\omega = |\boldsymbol{\omega}|$ are the degree–2 tidal gravitational Love number in the time t–domain and the angular rate. Here, $\star$ and $\otimes$ stand for the convolution operator and the algebraic product, and a and G are the Earth radius and the universal gravitational constant. As it results from the MacCullagh's formula (5.4), by assuming that the Earth has reached its rotating equilibrium state with the constant angular velocity before the beginning of the ice ages, eq. (5.2), we get

$$\boldsymbol{\mathcal{B}}(t<0) = \boldsymbol{\mathcal{B}}_0 = A\, \boldsymbol{x}_1 \otimes \boldsymbol{x}_1 + A\, \boldsymbol{x}_2 \otimes \boldsymbol{x}_2 + C\, \boldsymbol{x}_3 \otimes \boldsymbol{x}_3 \tag{5.5}$$

where C and A are the equilibrium polar and equatorial inertia moments given by

$$C = \frac{2}{3}\frac{a^5\,\omega_0^2}{3\,G}\, k_F^T \qquad A = -\frac{1}{3}\frac{a^5\,\omega_0^2}{3\,G}\, k_F^T \tag{5.6}$$

Here, k_F^T is the tidal gravitational fluid limit of the Maxwell model that is defined as the limit for $t \to \infty$ of the convolution of the degree–2 tidal gravitational Love number k^T with the Heaviside time history $H(t)$

$$k_F^T = \lim_{t\to\infty}\, k^T(t) \star H(t) \tag{5.7}$$

Notice that the word "fluid" is poorly chosen when some layers are purely elastic and cannot relax their stresses. It would be less confusing to use the expression tidal "equi-

librium" limit. It is only to be in agreement with all our predecessors that we keep the inaccurate but widely used term of tidal "fluid" limit.

Eqs (5.5)–(5.7) implies that before the ice load perturbation, the Earth was submitted to a constant rotation for a time scale greater than the longest characteristic relaxation time of all the viscoelastic layers. Particularly, in the case of a viscoelastic lithosphere, this time scale is greater than the ice age time scale of 1 Myr for a 120 km thick viscoelastic lithosphere with viscosity higher than 10^{24} Pa s and rigidity volume averaged from PREM (Dziewonski and Anderson, 1981). This shows that the theory, based on eq. (5.5) to estimate the initial state of rotational equilibrium, with C and A given by eq. (5.6), is used also on a time scale in which the elastic and the high viscous viscoelastic lithosphere are distinguishable. See for instance fig. 1(1a) in Wu and Peltier (1982).

In the perspective of studying the ice age TPW by means of compressible Maxwell Earth models based on PREM, some remarks on the tidal fluid limit k_F^T are required. Indeed PREM has an unstable compositional stratification above the 670 km discontinuity (Plag and Jüttner, 1995) corresponding to an imaginary Brunt–Väiäsala frequency (i.e., the radial density increases with depth less than what should be expected from the self–compression of the mantle). This unstable stratification generates growing modes which do not converge for $t \to \infty$ in eq. (5.7). These modes similar to Rayleigh Taylor instabilities are discussed in various papers (Plag and Jüttner, 1995; Vermeersen *et al.*, 1996; Vermeersen and Mitrovica, 2000) and included in the wider class of compositional in Cambiotti and Sabadini (2010). As shown in Vermeersen and Mitrovica (2000) these modes are characterized by long relaxation times of $10^2 - 10^3$ Myr and thus their effects are negligible on the time scale of the ice ages. In order to avoid these modes, following Chinnery (1975), we compute the tidal fluid limit k_F^T by considering the viscoelastic layers of the Maxwell Earth model as inviscid, with the exception of the layers properly elastic. This approach is in agreement with the theory of the equilibrium figure of a rotating Earth at first order accuracy and it does not differ from the assumption that Maxwell Earth models are in hydrostatic equilibrium before the loading of the last ice age, as usually done in post glacial rebound studies.

Having clarified this issue related to the tidal fluid limit k_F^T, we can write the MacCullagh's formula (5.4) in the perturbed state as

$$\boldsymbol{\mathcal{B}}(t \geq 0) = \boldsymbol{\mathcal{B}}_0 + \boldsymbol{\Delta\mathcal{B}}(t) \tag{5.8}$$

where $\boldsymbol{\Delta\mathcal{B}}$ describes the perturbations of the rotational bulge

$$\boldsymbol{\Delta\mathcal{B}} = \frac{a^5}{3\,G}\, k^T \star \left(\boldsymbol{\omega} \otimes \boldsymbol{\omega} - \boldsymbol{\omega}_0 \otimes \boldsymbol{\omega}_0 - \frac{\omega^2 - \omega_0^2}{3}\, \mathbf{1} \right) \tag{5.9}$$

Particularly, by writing the angular velocity in the perturbed state in terms of its direction cosines m_1 and m_2 with respect to the equatorial axes $\boldsymbol{x}_1$ and $\boldsymbol{x}_2$, and the relative variation of the diurnal rotation rate m_3

$$\boldsymbol{\omega}(t \geq 0) = \omega_0\, \left[m_1\, \boldsymbol{x}_1 + m_2\, \boldsymbol{x}_2 + (1 + m_3)\, \boldsymbol{x}_3 \right] \tag{5.10}$$

the perturbation in the off–diagonal components $\Delta\mathcal{B}_{13}$ and $\Delta\mathcal{B}_{23}$ yield

$$\Delta\mathcal{B}_{j3} = \frac{a^5\, \omega_0^2}{3\,G} k^T(t) \star\, m_j(t)\, (1 + m_3(t)) \qquad j = 1, 2 \tag{5.11}$$

In addition to this perturbation of the inertia tensor, one must add the driving perturbations due to the direct effect of the ice load, $\boldsymbol{\Delta\mathcal{I}}^{ice}$, and the relevant response of the Earth, controlled by the degree–2 load gravitational Love number $k^L(t)$

$$\boldsymbol{\mathcal{C}}(t \geq 0) = \left(\delta(t) + k^L(t) \right) \star \boldsymbol{\Delta\mathcal{I}}^{ice}(t) \tag{5.12}$$

with $\delta(t)$ being the Dirac distribution.

Within the assumption of infinitesimal perturbations of Earth's rotation and in view of eqs (5.3) and (5.8)–(5.12), the Euler dynamic equation (5.1) can be linearized for $m_j \ll 1$ as in eqs (3.12)–(3.13) of Sabadini and Vermeersen (2004)

$$A\, \omega_0\, \partial_t m_1 + (C - A)\, \omega_0^2\, m_2 = \omega^2\, \Delta\mathcal{B}_{23}^{\omega} + \omega_0^2\, \left(\delta(t) + k_L \right) \star \Delta\mathcal{I}_{23}^{ice} \tag{5.13}$$

$$A\, \Omega\, \partial_t m_2 - (C - A)\, \Omega^2\, m_1 = -\Omega^2\, \Delta\mathcal{B}_{13}^{\omega} - \Omega^2\, \left(\delta(t) + k_L \right) \star \Delta\mathcal{I}_{13}^{ice} \tag{5.14}$$

For the sake of simplicity, in eqs (5.13)–(5.14) we have neglected the time derivative of the off–diagonal perturbations of the inertia tensor in view of their negligible impact on the ice age TPW. Furthermore, in the present work we do not consider the third component of the Euler dynamic equation (5.1), pertaining to the relative variation of the diurnal rate m_3.

At this stage, by dividing each member of eqs (5.13)–(5.14) by $(C - A)\,\Omega^2$, we obtain

$$\frac{\partial_t m_1}{\sigma_r} + m_2 = \frac{k^T \star m_2}{k_F^T} + \frac{(\delta(t) + k_L) \star \Delta\mathcal{I}_{23}^{ice}}{C - A} \tag{5.15}$$

$$\frac{\partial_t m_2}{\sigma_r} - m_1 = -\frac{k^T \star m_1}{k_F^T} - \frac{(\delta(t) + k_L) \star \Delta\mathcal{I}_{13}^{ice}}{C - A} \tag{5.16}$$

where σ_r is the Eulerian free precession frequency

$$\sigma_r = \Omega\,\frac{C - A}{A} \tag{5.17}$$

and, from eq. (5.6), we utilized the following identity

$$k_F^T = \frac{3\,G\,(C - A)}{a^5\,\Omega^2} \tag{5.18}$$

Eqs (5.15)–(5.16) can be recast in the widely used and more compact form

$$\frac{i}{\sigma_r}\,\partial_t \mathbf{m}(t) + \left(\delta(t) - \frac{k^T(t)}{k_F^T}\right) \star \mathbf{m}(t) = \left(\delta(t) + \tilde{k}_L(t)\right)\,\boldsymbol{\phi}(t) \tag{5.19}$$

that, after the Laplace transformation, becomes

$$\frac{i\,s}{\sigma_r}\,\tilde{\mathbf{m}}(s) + \left(1 - \frac{\tilde{k}^T(s)}{k_F^T}\right)\,\tilde{\mathbf{m}}(s) = \left(1 + \tilde{k}_L(s)\right)\,\tilde{\boldsymbol{\phi}}(s) \tag{5.20}$$

Here, the tilde stands for the Laplace transform, i is the imaginary number and we have

made use of the complex notation

$$\mathbf{m} = m_1 + i\, m_2 \qquad \phi = \frac{\Delta \mathcal{I}_{13}^{ice} + i\, \Delta \mathcal{I}_{23}^{ice}}{C - A} \tag{5.21}$$

This demonstrates that the theory (Sabadini and Peltier, 1981; Sabadini *et al.*, 1982; Wu and Peltier, 1984), built on the work of Munk and MacDonald (1960), provides a mathematically sound treatment of ice age TPW under the assumption that the load– and rotation–induced perturbations and the equilibrium background form must be computed using the same Earth model. In this regard, different tidal fluid limits k_f^T are used in eq. (5.20) for models with an elastic or viscoelastic lithosphere since the first carries a finite strength after the initial rotational spin–up of the model, while the second is fully relaxed. For models sharing the same reference density profile, this results in a smaller initial rotational bulge for the elastic case (E) than for the viscoelastic case (V)

$$k_{F,E}^T < k_{F,V}^T \tag{5.22}$$

Two rheological models of the Earth will only predict the same ice age TPW if their behaviours agree both on the time scale of the ice ages ($\lesssim 1$ Myr) and at infinite time, since the latter controls the initial rotational bulge within the traditional approach, as shown in eq. (5.18). The behaviour of elastic and high viscous viscoelastic lithospheres are indistinguishable on short time scale but not at infinite time. This issue was discussed in detail by Mitrovica *et al.* (2005), though we believe their use of the term "Nakada paradox" was an overstatement. Indeed, the findings of Nakada (2002) consist in the understanding that the dependence of ice age TPW predictions on the lithospheric rheology can be very important for lower mantle viscosities lesser than 10^{22} Pa s, as we will show in detail in sections 5.2, 5.3 and 5.4.

The new treatment made by Mitrovica *et al.* (2005) consists in noticing that the inertia tensor of the real Earth is not only that of a homogeneous rotating planet plus an ice load perturbation as implied by (5.3), but that perturbations due to the mantle 3–D structure are also present. Coming back to the stage before the linearization of the Euler dynamic equation (5.1), this is equivalent to adding to the equilibrium inertia tensor obtained by the rotational spin–up of the model, eq. (5.5), the perturbations ΔI_{11}^C, ΔI_{22}^C

and ΔI_{33}^C in the diagonal components due to mantle convection. This choice implies that mantle convection does not directly drive polar motion, since the off–diagonal components ΔI_{13}^C and ΔI_{23}^C due to mantle convection are not added, or, alternatively, that the axis of rotation has already readjusted to the slowly evolving convection forcing so that the off–diagonal inertia perturbations are only those arising from post glacial rebound. This assumption implies that the evolution of the convective mantle is so slow that it appears frozen during the glaciation–deglaciation phases. Since the series of eight ice age cycles occurs over 800 kyr, this remains probably a reasonable approximation but not necessarily so and convection may also have contributed to the TPW during this period. According to Besse and Courtillot (1991), over geological times the TPW occurs indeed at rates not much slower than those due to glacial readjustments. This suggests that the two processes of mantle driven and surface driven TPW may be intermingled. Before Mitrovica *et al.* (2005), in all studies of glaciation induced TPW, the diagonal components ΔI_{11}^C, ΔI_{22}^C and ΔI_{33}^C were not introduced, and the mantle was considered without lateral density variations. The role of mantle convection was studied separately from the ice age TPW, as done by Ricard *et al.* (1993a,b).

By keeping the assumption of symmetry around the polar axis, $\Delta I_{11}^C = \Delta I_{22}^C$, we therefore perform the change of variables

$$C \to C + \Delta I_{33}^C \qquad A \to A + \frac{\Delta I_{11}^C + \Delta I_{22}^C}{2} \tag{5.23}$$

Particularly, eq. (5.18) has to be written as

$$k_{F,obs}^T = k_F^T + \beta = \frac{3\,G\,(C-A)}{a^5\,\Omega^2} \tag{5.24}$$

where $k_{F,obs}^T$ is the observed fluid Love number and β is given by

$$\beta = \frac{3\,G}{a^5\,\Omega^2}\left(\Delta I_{33}^C - \frac{\Delta I_{11}^C + \Delta I_{22}^C}{2}\right) \tag{5.25}$$

We will refer to eq. (5.24) as the "β correction" to the tidal fluid limit k_F^T following eq. (16) in Mitrovica *et al.* (2005). The $k_{F,obs}^T$ is thus an observation and k_F^T a predic-

tion from viscoelastic modelling, while β is the contribution from mantle convection, assumed frozen during the period of ice ages. In view of this, eq. (5.20) becomes

$$\frac{i\,s}{\sigma_r}\,\tilde{\mathbf{m}}(s) + \left(1 - \frac{\tilde{k}^T(s)}{k_F^T + \beta}\right)\tilde{\mathbf{m}}(s) = \left(1 + \tilde{k}_L(s)\right)\,\tilde{\boldsymbol{\phi}}(s) \tag{5.26}$$

Making use of $k^T_{F,obs} = k^T_F + \beta$, rather than k^T_F, has thus the meaning of coupling, in a simplified fashion and within a linearized scheme, the effects of the ice age TPW with those from mantle convection, but assuming for the latter only its contribution to the non hydrostatic ellipsoidal shape of the Earth (ΔI^C_{11}, ΔI^C_{22} and ΔI^C_{33} differing from zero) and not its active driving effect (ΔI^C_{13}, ΔI^C_{23} assumed equal to zero).

5.1.1 Layered compressible Earth models

For layered incompressible models it is possible to show analytically how the β correction impacts the linearized equations for the ice age TPW. The normal mode expansions of the gravitational Love number k in the Laplace s–domain, both for loading and tidal forcing (denoted with the superscripts L and T, respectively), is

$$\tilde{k}(s) = k_E + \sum \frac{k_j}{s - s_j} \tag{5.27}$$

where k_E, k_j and s_j are the elastic gravitational Love number, the residue and the pole of the j–th relaxation mode. The long term behavior, when $s = 0$, is controlled by

$$k_F = k_E - \sum \frac{k_j}{s_j} \tag{5.28}$$

and therefore $\tilde{k}(s)$ can be rearranged as follows

$$\tilde{k}(s) = k_F + s \sum \frac{k_j}{s_j\ (s - s_j)} \tag{5.29}$$

This allows us to collect in eq. (5.20) (i.e. in the case where the initial flattening is only due to rotation without contribution from mantle dynamics, $\beta = 0$) a term linear in the

Laplace variable s

$$s\left(\frac{i}{\sigma_r}-\frac{1}{k_F^T}\sum\frac{k_j^T}{s_j\ (s-s_j)}\right)\tilde{\mathbf{m}}(s)=\left(1+k_F^L+s\sum\frac{k_j^L}{s_j\ (s-s_j)}\right)\tilde{\phi}(s) \tag{5.30}$$

as in eq. (3.47) in Sabadini and Vermeersen (2004). By solving this equation for $\tilde{\mathbf{m}}(s)$, we get

$$\tilde{\mathbf{m}}(s)=\frac{1+k_F^L+s\sum\frac{k_j^L}{s_j(s-s_j)}}{s\left(\frac{i}{\sigma_r}-\frac{1}{k_F^T}\sum\frac{k_j^T}{s_j(s-s_j)}\right)}\tilde{\phi}(s) \tag{5.31}$$

where the factor s collected at the denominator is responsible for the so–called secular term, which characterizes the ice age TPW in such a way that it gains a net displacement at the end of each ice age cycle.

If now we want to account for the contribution of mantle convection to the inertia tensor by applying the β correction, eq. (5.31) becomes

$$\tilde{\mathbf{m}}(s)=\frac{1+k_F^L+s\sum\frac{k_j^L}{s_j(s-s_j)}}{\frac{\beta}{k_F^T+\beta}+s\left(\frac{i}{\sigma_r}-\frac{1}{k_F^T+\beta}\sum\frac{k_j^T}{s_j(s-s_j)}\right)}\tilde{\phi}(s) \tag{5.32}$$

The secular term is, in this case, substituted by an extra exponential decaying term, which drags the equatorial bulge and forces the ice age TPW to return to the initial position of the rotation axis, after a sufficiently long time. This can be explained in the following way. While the hydrostatic flattening readjusts during the ice age TPW, the mantle density anomalies act as a counterweight that limits the polar excursion and ultimately control the position of the pole. In section 5.4, we will show that these considerations are not restricted to the simple layered incompressible models, but they extend also to the case of more realistic compressible Earth models which take into account the continuous variations of the material parameters. It is noteworthy that our advanced Earth model has a continuous relaxation spectrum (Fang and Hager, 1995; Tanaka *et al.*, 2006; Cambiotti

and Sabadini, 2010), which does not allow the analytical derivation of eqs (5.31)–(5.32) based on the discretized normal mode expansion given by eq. (5.27).

5.1.2 The compressible Maxwell Earth model

We thus consider a self–gravitating, compressible Maxwell Earth model, with the initial density ρ_0, shear modulus μ and bulk modulus κ of PREM. We consider these material parameters as given in Table 1 of Dziewonski and Anderson (1981), in terms of polynomials of the radial distance from the Earth centre r in each of the main layers of the Earth. In this way we take into account the continuous variations of the material parameters, without introducing any fine layered stratification. As concerns the viscosity ν, even though we could consider continuous variations, in the present work we adopt a simple stepwise profile characterized by the lower, $\nu_{\rm LM}$, and upper, $\nu_{\rm UM}$, mantle viscosities and the lithospheric viscosity $\nu_{\rm L}$. The thickness of the lithosphere is of 120 km and we choose the lithospheric viscosity $\nu_{\rm L} = 10^{26}$ Pa s in order to discuss the issues raised by Nakada (2002) and Mitrovica *et al.* (2005). Besides this, we consider the lower mantle viscosity $\nu_{\rm LM}$ as free parameter, ranging from 10^{21} Pa s to 10^{23} Pa s, while the upper mantle viscosity $\nu_{\rm UM}$ is fixed at 10^{21} Pa s. The outer oceanic layer of PREM is replaced by extending the upper crust to the Earth's radius a. The tidal fluid limit k_F^T for this model with viscoelastic lithosphere agrees with the value of 0.934 given in Mitrovica *et al.* (2005).

In order to get the degree–2 load, $\tilde{k}^L(s)$, and tidal, $\tilde{k}^T(s)$, gravitational Love numbers in the Laplace s–domain, we integrate the differential system describing the conservation of the momentum and the self–gravitation, after expansion in spherical harmonics and Laplace transformation. The radial integration, from the core–mantle boundary (CMB) to the Earth surface, is based on the Gill–Runge–Kutta fourth order method. We consider the core as inviscid and we impose the fluid–solid boundary conditions (Chinnery, 1975) as Cauchy data for the differential system at the core radius. This implies that we have to get the perturbation of the equipotential surface of the inviscid core at the CMB and we do it as described in Smylie and Manshina (1971). At the interfaces at which the material parameters of PREM have stepwise discontinuities, we impose the chemical boundary conditions, while at the Earth surface a we impose the boundary conditions describing the surface loading and the tidal forcing. This algorithm thus strictly

follows the theory outlined in Chapter 1.

In this way we have a numerical algorithm able to provide load, $\tilde{k}^L(s)$, and tidal, $\tilde{k}^T(s)$, gravitational Love numbers at fixed Laplace variable s. As pointed out in a series of papers (Fang and Hager, 1995; Tanaka *et al.*, 2006; Cambiotti and Sabadini, 2010), the continuous variations of the rheological parameters (not those of the initial density ρ_0 as pointed out in Cambiotti and Sabadini, 2010) lead to a continuous relaxation spectrum. In this respect, we cannot resort to the normal mode approach (Wu and Peltier, 1982; Han and Wahr, 1995) in order to get the perturbations in the time domain. Then, following the Bromwich path approach described in Tanaka *et al.* (2006), we get the degree–2 non–dimensional perturbation $K(f;t)$ due to a forcing with time history $f(t)$ by evaluating the inverse Laplace transform of the product $\tilde{k}(s)\,\tilde{f}(s)$

$$K(f;t) = \mathcal{L}^{-1}\left[\tilde{k}(s)\,f(s)\right] = k_E\,f(t) + \frac{1}{2\,\pi\,i}\int_\Gamma \tilde{k}(s)\,\tilde{f}(s)\,e^{s\,t}\,ds \tag{5.33}$$

where k_E and $\tilde{f}(s)$ are the elastic gravitational Love number and the Laplace transform of the forcing time history $f(t)$, and Γ is the contour in the Laplace s–domain enclosing the sets in which $\tilde{k}(s)$ and $f(s)$ are not analytic as discussed in Chapter 1, sections 1.5 and 1.6.

The same algorithm is used to evaluate the direction cosines m_1 and m_2 describing the ice age TPW, eq. (5.10). We solve eq. (5.26) for $\tilde{\mathbf{m}}(s)$ and we evaluate the complex contour integral entering the solution in the time t–domain

$$\mathbf{m}(t) = \frac{1+k_E^L}{1-\frac{k_E^T}{k_F^T+\beta}}\,\boldsymbol{\phi}(t) + \frac{1}{2\,\pi\,i}\int_\Gamma \frac{1+\tilde{k}^L(s)}{1-\frac{\tilde{k}^T(s)}{k_F^T+\beta}}\,\tilde{\boldsymbol{\phi}}(s)\,e^{s\,t}\,ds \tag{5.34}$$

Note that we have made use of the approximation proposed in Wu and Peltier (1984), which consists in neglecting in eq. (5.26) the term associated with the Eulerian free precession frequency σ_r. As pointed out in Mitrovica and Milne (1998), this replaces the Chandler wobble by an instantaneous elastic response, representing the time average of the Chandler Wobble. In this way, we can maintain the same contour Γ as in eq. (5.33) since the rotation pole associated with the Chandler Wobble is avoided (this pole

with a large imaginary part does not lie within the contour Γ). Furthermore, we note that this approximation neglects the coupling between the direction cosines m_1 and m_2. Nevertheless, such a coupling, in addition to the 14 month Chandler wobble, results in a long term wobble around the initial rotation axis, characterized by time scale much longer than the ice age time scale of 1 Myr (Mitrovica and Milne, 1998; Sabadini and Vermeersen, 2004). In the following sections we consider the TPW displacement $m(t)$ defined as

$$m(t) = p\sqrt{m_1^2(t) + m_2^2(t)} \tag{5.35}$$

with p being $+1$ or -1 respectively whether the instantaneous rotation pole is farther away or closer from the position of the surface load than its initial position. A zero value $m(t) = 0$ means that the instantaneous rotation pole is crossing the initial north pole position.

5.2 Readjustment of the rotational bulge

The numerical algorithm described in section 5.1.2 is now used to elucidate the role of the rheology of the lithosphere, elastic or viscoelastic. We assume that the viscoelastic lithosphere has a very high viscosity $\nu_{\rm L} = 10^{26}$ Pa s. The lower and upper mantle viscosities are $\nu_{\rm LM} = 10^{22}$ and $\nu_{\rm UM} = 10^{21}$ Pa s, respectively.

In fig. 5.1 (a) we compare the time evolution of the Green function $k_F^T - K^T$, with K^T being the convolution of the tidal gravitational Love number k^T with the Heaviside time history H, for the models with the elastic (E, solid line) and viscoelastic (V, dashed line) lithospheres

$$K^T(t) = k^T(t) \star H(t) \tag{5.36}$$

It expresses how fast the rotational equatorial bulge readjusts to a new rotation axis, where the total readjustment is obtained when $k_F^T - K^T = 0$. As discussed in section 5.1, we obtain the tidal fluid limit k_F^T from the tidal isostatic response (Chinnery, 1975), which is $k_{F,E}^T = 0.920$ and $k_{F,V}^T = 0.934$ for the cases of elastic and viscoelastic lithosphere, respectively. The difference between the tidal fluid limits $k_{F,V}^T - k_{F,E}^T = 0.014$

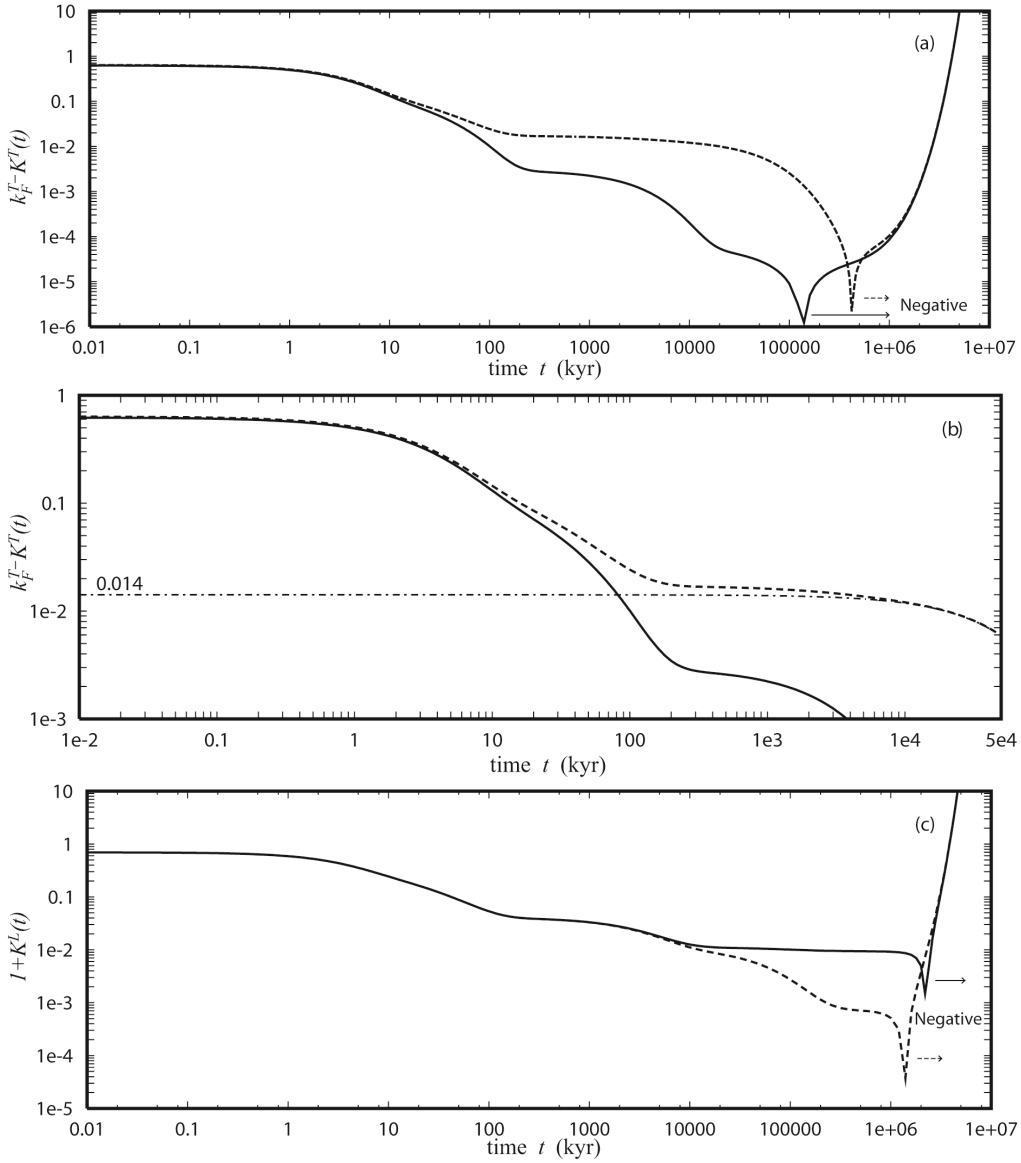

Figure 5.1: (a, b) Readjustment of the equatorial bulge, $k_T^F - K_T$, and (c) load response, $1 + K_L$, for compressible PREM with elastic (solid) and high viscous viscoelastic (dashed) lithosphere and lower mantle viscosity $\nu_{\rm LM} = 10^{22}$ Pa s. In the panel (b) the difference between the reajustments of the equatorial bulge of the model with the elastic (E) and viscoelastic (V) lithosphere is also shown, $k^T_{F,V} - K^T_V - (k^T_{F,E} - K^T_E)$ (dashed–dot line).

reflects a difference in the equilibrium flattening. The elastic lithosphere carries a finite strength that, instead, the model with the viscoelastic lithosphere does not have, being fully relaxed at large time (i.e., the elastic lithosphere is pre–stressed while the viscoelastic lithosphere is in hydrostatic equilibrium). Note that the Green function $k^T_{F,E} - K^T_E$ for the elastic lithosphere case (solid line) is always smaller than the Green function $k^T_{F,V} - K^T_V$ for the viscoelastic case (dashed line). Within 10 Myr, $k^T_{F,E} - K^T_E$ approaches zero, namely the equatorial bulge readjusts completely to a new rotation axis. On the contrary $k^T_{F,V} - K^T_V$ is 0.014 at 10 Myr, which is precisely the difference between the tidal fluid limits $k^T_{F,V}$ and $k^T_{F,E}$. This indicates that the accumulated stresses during the displacement of the equatorial bulge are almost completely relaxed within the viscoelastic mantle, but they are still present in the viscoelastic lithosphere with high viscosity. Indeed the viscoelastic lithosphere behaves as an elastic body at time scale lower than the lithospheric Maxwell time, 50 Myr. We show this in fig. 5.1 (b) for the time window of 50 Myr where, in addition to the previous Green functions, we plot also their difference $k^T_{F,V} - K^T_V - \left(k^T_{F,E} - K^T_E\right)$ (dash–dotted line). Before 10 Myr, the Green functions K^T_V and K^T_E coincide and the only difference between $k^T_{F,V} - K^T_V$ and $k^T_{F,E} - K^T_E$ is due to the difference in tidal fluid limits $k^T_{F,V} - k^T_{F,E} = 0.014$. After 10 Myr this difference reduces since the viscoelastic lithosphere relaxes and the rotational bulge readjusts completely to the new rotation axis. Nevertheless, as shown in fig. 5.1 (a), this process is intermingled with the gravitational overturning due to the unstable compositional stratification of PREM above the 670 km discontinuity (Plag and Jüttner, 1995). The unstable compositional modes (Cambiotti and Sabadini, 2010) make K^T change sign. The cuspidal point at $t = 400$ Myr represents, in the logarithmic scale, this change of sign, from positive to negative, of the Green function $k^T_{F,V} - K^T_V$ for the case of viscoelastic lithosphere. For the elastic lithosphere case, the change of sign of the Green function $k^T_{F,E} - K^T_E$ occurs at 130 Myr. This overturn is a mathematical consequence of the unstable PREM stratification but has little physical consequence because TPW is anyway dominated by mantle convection on this long time scale (Spada *et al.*, 1992b).

In fig. 5.1 (c) we compare the time evolution of the Green function $1 + K^L$, with K^L being the convolution of the load gravitational Love number k^L with the Heaviside time history H, for models with elastic (E, solid line) and viscoelastic (V, dashed line) lithospheres

$$K^L(t) = k^L(t) \star H(t) \tag{5.37}$$

It expresses the return to isostatic compensation of a surface point–like load, that is obtained when $1 + K^L = 0$. The two load Green functions agree up to 10 Myr, but after this time $1 + K^L_V$ goes to zero for the viscoelastic lithosphere case as the load becomes fully compensated. Instead, $1 + K^L_E$ for the elastic lithosphere case converges to the value of 0.01, which is the gravitational anomaly $1 + k^L_{F,E}$ remaining because of the elastic support. In the end, starting from 1 Gyr, the gravitational overturn breaks the final equilibrium with the load, the cuspidal points at 2.3 and 1.3 Gyr for the elastic and viscoelastic lithosphere cases, respectively, having the same meaning as in fig. 5.1 (a).

These findings show that over the time scale of post glacial rebound and until 10 Myr as well, there are no significant differences between the tidal, K^T, and load, K^L, Green functions computed with an elastic lithosphere or with a viscoelastic lithosphere with high viscosity, $\nu_{\rm L} = 10^{26}$ Pa s. However the TPW involves not only the Love numbers K^T and K^L at short time period but also the limit at infinite time of the tidal Green function K^T, which is the so called tidal fluid limit k^T_F as seen in eq. 5.20. Particularly, the rheology of the lithosphere, elastic or viscoelastic (i.e., fluid at infinite time) does affect the TPW because it controls the equilibrium figure of the Earth because $k^T_{F,V} \geq k^T_{F,E}$, eq. (5.22) (see also fig. 1 in Mitrovica *et al.*, 2005). The equilibrium figures are different for the two cases and the rotation of the model with the high viscous viscoelastic lithosphere is more stable since its equatorial bulge is not able to readjust to a new rotation axis on the ice age time scale (Mitrovica *et al.*, 2005). From fig. 1(a,b), we can understand that the sensitivity on the lithospheric rheology, pointed out by Nakada (2002), actually is due to the stabilizing effects of delay of the readjustment of the rotational bulge. Classically, the lower mantle viscosity $\nu_{\rm LM}$ was considered as the main parameter controlling this delay. Instead, adopting Earth models with the high viscous viscoelastic lithosphere allows to take into account also the delay associated with the high lithospheric viscosity $\nu_{\rm L}$, in addition to that associated with the lower mantle viscosity $\nu_{\rm LM}$. In view of this, models with elastic and viscoelastic lithospheres are not expected do lead to the same TPW.

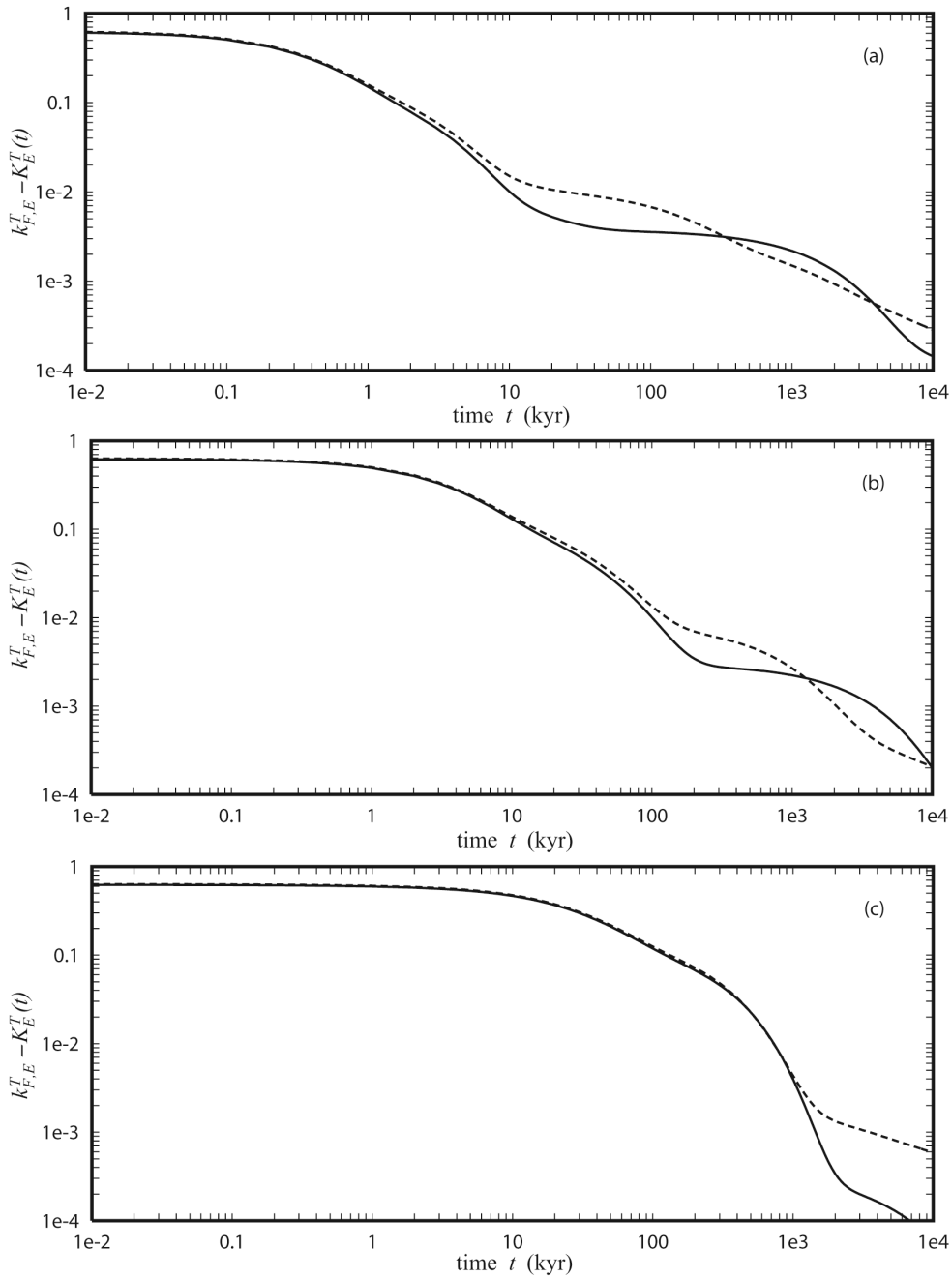

Figure 5.2: Readjustment of the equatorial bulge, $k^T_{F,E} - K^T_E$, for compressible (solid) and incompressible (dashed) PREM with elastic lithosphere. The lower mantle viscosity $\nu_{\rm LM}$ is (a) 10^{21} Pa s, (b) 10^{22} Pa s and (c) 10^{23} Pa s.

5.3 Compressible and incompressible True Polar Wander

Incompressible Maxwell Earth models have been widely used in the last two decades for TPW simulations. For this reason we now compare these models with the compressible Maxwell Earth models. At the same time, we quantify the effects of the different rheologies of the lithosphere, elastic or viscoelastic.

Fig. 5.2 shows the comparison between the compressible (solid line) and incompressible (dashed line) Green functions $k^T_{F,E} - K^T_E$ in the case of an elastic (E) lithosphere, 120 km thick. The lower mantle viscosity $\nu_{\rm LM}$ is increased by one order of magnitude from 10^{21} Pa s to 10^{23} Pa s from top to bottom panel. The time window considered is 10 Myr, much longer than the ice age time scale of 1 Myr. In general the compressible rotational bulge readjusts faster than the incompressible one. Indeed, the Green function $k^T_{F,E} - K^T_E$ for the compressible model is lower than that for the incompressible model, with the exception of the time intervals $[3 \times 10^2, 4 \times 10^3]$ kyr (panel a) and $[10^3, 10^4]$ kyr (panel b) for the lower mantle viscosities $\nu_{\rm LM} = 10^{21}$ and 10^{22} Pa s, respectively. For $\nu_{\rm LM} = 10^{23}$ Pa s (panel c) the two models predict very similar values until 1 Myr, where the compressible rotational bulge begins to readjust faster to the new rotation axis than the incompressible rotational bulge.

In fig. 5.3, the elastic (E) lithosphere has been replaced by the viscoelastic (V) lithosphere, with viscosity $\nu_{\rm L} = 10^{26}$ Pa s. In this case, the Green function $k^T_{F,V} - K^T_V$ for the compressible model is always lower than that for the incompressible model. The vertical scale has been reduced compared to fig. 5.2. Indeed, at 10 kyr, all the layers have significantly relaxed except for the high viscous viscoelastic lithosphere, which behaves as an elastic body as shown in fig. 5.1 (b). This results in the fact that at 10 Myr both the compressible and incompressible Green functions $k^T_{F,V} - K^T_V$ differ from zero by the discrepancy $k^T_{F,V} - k^T_{F,E}$. Since $k^T_{F,E}$ depends on the rheology of the elastic lithosphere, compressible, 0.920, or incompressible, 0.918, the discrepancy $k^T_{F,V} - k^T_{F,E}$ for the compressible model, 0.014, is smaller than that for the incompressible model, 0.016. Thus, before 10 Myr, the viscoelastic compressible lithosphere is more deformable than the incompressible lithosphere and this explains the fact that the compressible bulge readjust faster than the incompressible bulge.

Fig. 5.4 shows the comparison between the compressible (solid line) and incom-

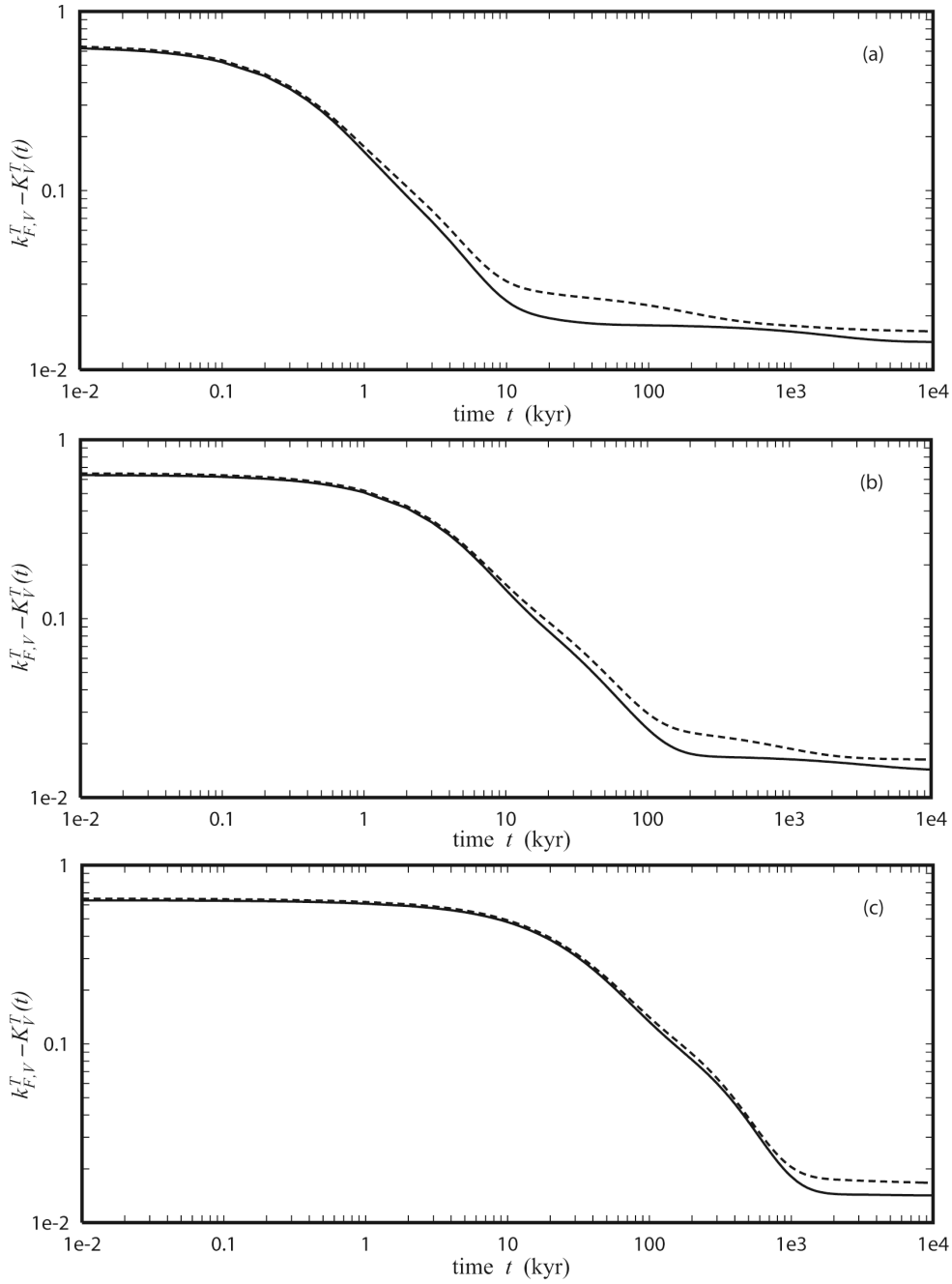

Figure 5.3: Readjustment of the equatorial bulge, $k^T_{F,V} - K^T_V$, for compressible (solid) and incompressible (dashed) PREM with viscoelastic lithosphere. The lower mantle viscosity $\nu_{\rm LM}$ is (a) 10^{21} Pa s, (b) 10^{22} Pa s and (c) 10^{23} Pa s, and the lithosphere viscosity $\nu_{\rm L}$ is always 10^{26} Pa s.

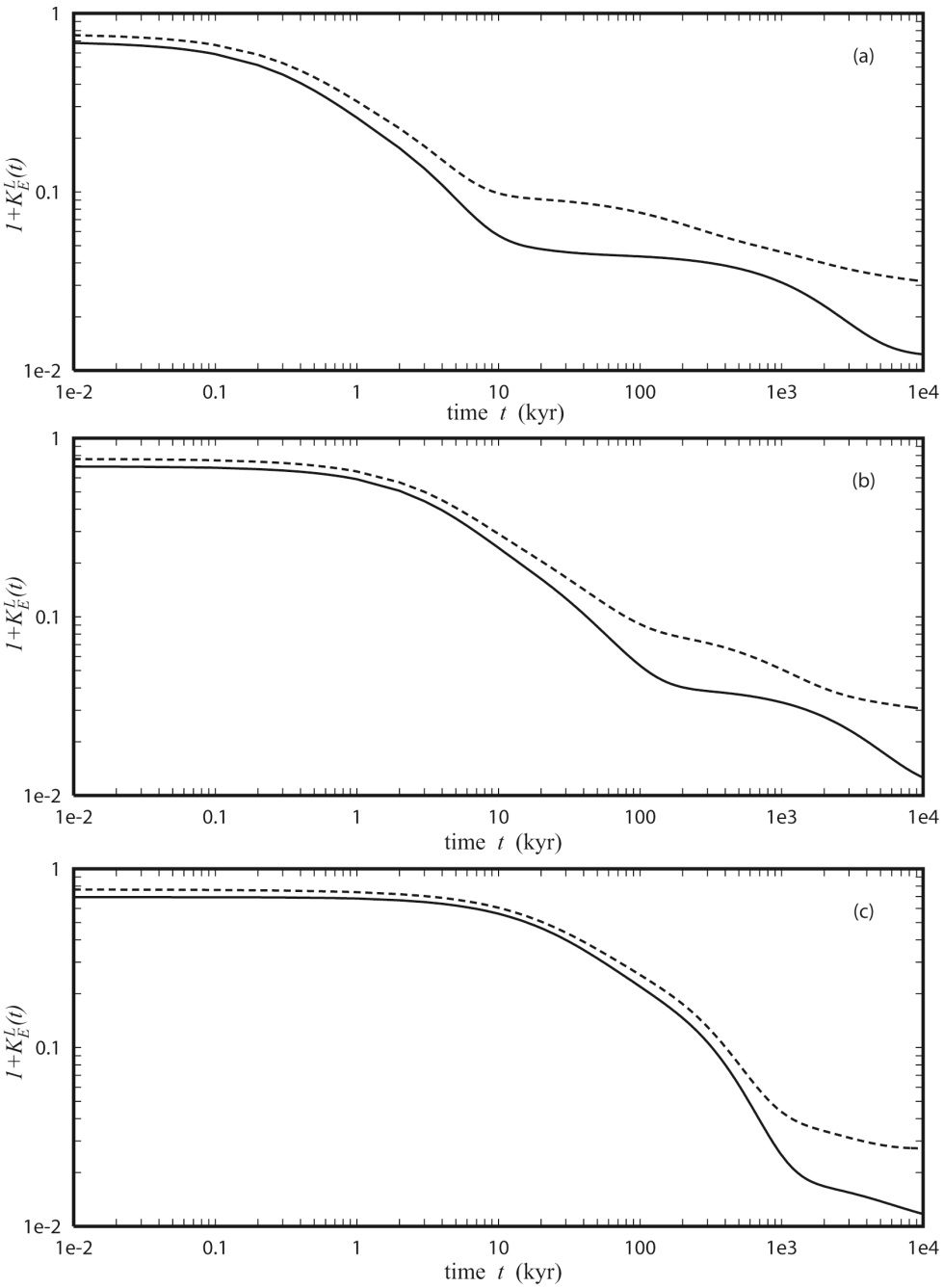

Figure 5.4: Load response $1 + K_E^L$ of the compressible (solid) and incompressible (dashed) PREM with the elastic lithosphere. The lower mantle viscosity $\nu_{\rm LM}$ is (a) 10^{21} Pa s, (b) 10^{22} Pa s and (c) 10^{23} Pa s.

pressible (dashed line) Green function $1 + K_E^L$ for the elastic (E) lithosphere case. As in figs 5.2 and 5.3, the lower mantle viscosity $\nu_{\rm LM}$ is increased of one order of magnitude from 10^{21} Pa s to 10^{23} Pa s in each panel and we consider a time window of 10 Myr. The Green function $1 + K_E^L$ for the compressible model is always lower than for the incompressible models, indicating that compressible models are more deformable. The difference between the compressible and the incompressible cases is larger for the load response than for the equatorial bulge readjustment (compare fig. 5.4 with figs 5.2 and 5.3). Particularly, in the elastic limit $t \to 0$, the readjustment of the equatorial bulge is marginally affected by the different rheologies (see fig. 5.2 and 5.3), while compressible and incompressible cases differ by 10 per cent for loading, fig. 5.4. We do not show the results for the model with the viscoelastic lithosphere since, on the time scale of 10 Myr, they are very similar to those shown in fig. 5.4 for the elastic lithosphere case.

By comparing the Green functions between the panels of figs 5.2, 5.3 and 5.4, we note that the increase of the lower mantle viscosity $\nu_{\rm LM}$ by one order of magnitude, from 10^{21} to 10^{23} Pa s, delays by about one order of magnitude the time at which compressibility becomes effective during the transient, from 10 kyr to 10^3 kyr, both for loading and equatorial bulge readjustments. Particularly, for the high lower mantle viscosity $\nu_{\rm LM} = 10^{23}$ Pa s (panel c), the compressibility is almost undistinguishable from incompressibility on time scale of the ice ages, 1 Myr.

We now consider TPW simulations driven by ice ages. For the ice loading, we begin by consider only the last ice age, characterized by linear glaciation and deglaciation phases of 90 kyr and 10 kyr, respectively, and the same maximum ice sheet inertia perturbations as in Mitrovica *et al.* (2005), $\Delta\mathcal{I}_{13}^{ice} = -6.67\,10^{31}\,\mathrm{kg\,m^2}$ and $\Delta\mathcal{I}_{23}^{ice} = 2.31\,10^{32}\,\mathrm{kg\,m^2}$. Fig. 5.5 compare the TWP displacements, eq. (5.35), for compressible (solid line) and incompressible (dashed line) PREM with elastic lithosphere, without considering any non hydrostatic contribution from mantle convection, $\beta = 0$. Fig. 5.6 is the same but for the case of viscoelastic lithosphere, with viscosity $\nu_{\rm L} = 10^{26}$ Pa s. As for figs 5.2, 5.3 and 5.4, the TPW displacements are computed for increasing lower mantle viscosities $\nu_{\rm LM}$, from 10^{21} Pa s to 10^{23} Pa s from top to bottom.

The shape of TPW displacement curves is characterized by an increasing displacement during the glaciation phase, from 10 to 90 kyr, away from Hudson bay followed by a still ongoing displacement toward Hudson Bay. Starting from the elastic lithosphere results, fig. 5.5, the TPW displacements for the compressible models are always smaller

than those for the incompressible models, except when $\nu_{\rm LM} = 10^{21}$ Pa s (panel a) in the time interval $[120, 200]$ kyr. This finding is in agreement with the Green functions $1 + K_E^L$ of fig. 5.4. Indeed, the incompressible lithosphere does not readjust to a load as fast as the more deformable compressible lithosphere, and thus the ice age loading drives more efficiently the polar wander for the incompressible rheology.

As already observed from the Green functions, an increase of the lower mantle viscosity $\nu_{\rm LM}$ reduces the differences between the compressible and incompressible models, as clearly shown in fig. 5.5 (c). The TPW displacements are always positive, meaning that the rotation pole does not cross the initial north pole while it moves back towards Hudson bay. Indeed the displacements m at $t = 1$ Myr differ significantly from the initial north pole position at zero, particularly for lower mantle viscosities 10^{21} and 10^{22} Pa s, fig. 5.5 (a, b), and for the incompressible rheology. This shows that each glaciation cycle moves the pole by a finite amount away from Hudson bay not only for the layered incompressible models as the secular term of eq. (5.31) implies, but also for continuous, compressible or incompressible, models.

The models with the viscoelastic lithosphere are depicted in fig. 5.6. The TPW displacements resemble those shown in fig. 5.5 for the case of the elastic lithosphere, although with some reduction in amplitudes. This behaviour is more effective for the lower mantle viscosity $\nu_{\rm LM} = 10^{21}$ Pa s, characterized by almost a factor of 2 reduction (compare panels (a) of figs 5.5 and 5.6). This indicates that the difference between viscoelastic and elastic lithospheres is the largest for a soft lower mantle. Differently from fig. 5.5, now the rotation pole crosses the initial north pole at about 200 kyr, fig. 5.6 (a), and at 700 kyr, fig. 5.6 (b), both for compressible and incompressible models, while for the lower mantle with high viscosity, fig. 5.6 (c), the crossing occurs at 500 kyr only for the compressible model. Thus the TPW displacement of models with a viscoelastic lithosphere does not end up with any finite displacement away from Hudson bay (Mitrovica *et al.*, 2005). This drastic reduction of the TPW displacement is due to the increased delay in the readjustment of the hydrostatic equatorial bulge due to the high viscous viscoelastic rheology of the lithosphere which stabilizes rotationally the planet, as discussed in section 5.2.

The drastic reduction of the TPW displacement when the viscosity of the viscoelastic lithosphere is reduced to that of the upper mantle, $\nu_{\rm L} = 10^{21}$ Pa s, compared to the elastic case, has been shown first by Vermeersen and Sabadini (1999) in their fig. 8,

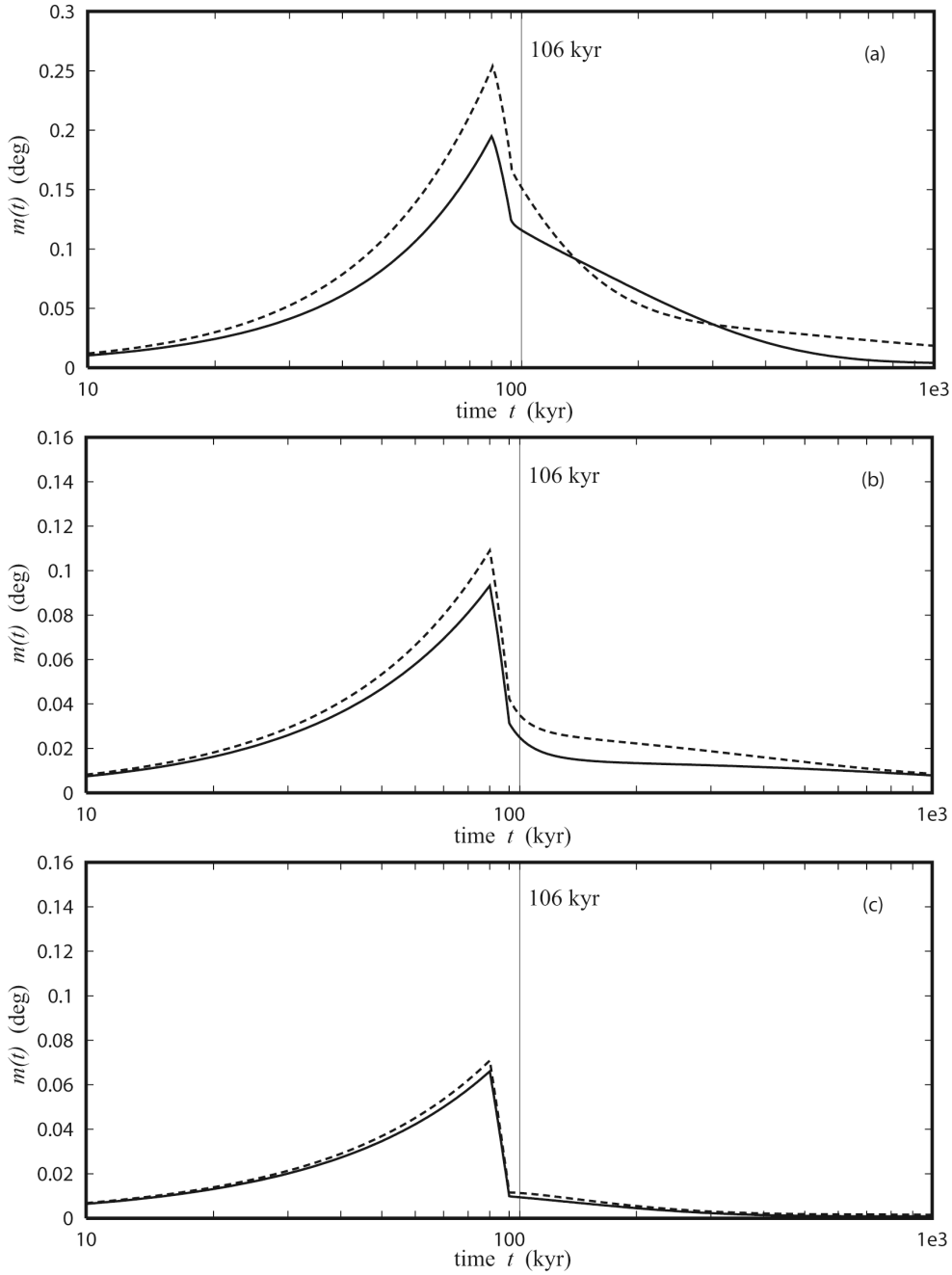

Figure 5.5: The TPW displacement m due only to the last ice age for the compressible (solid) and incompressible (dashed) PREM with the elastic lithosphere. The lower mantle viscosity is $\nu_{\rm LM} = 10^{21}$ (a), $\nu_{\rm LM} = 10^{22}$ (b) and $\nu_{\rm LM} = 10^{23}$ (c) Pa s.

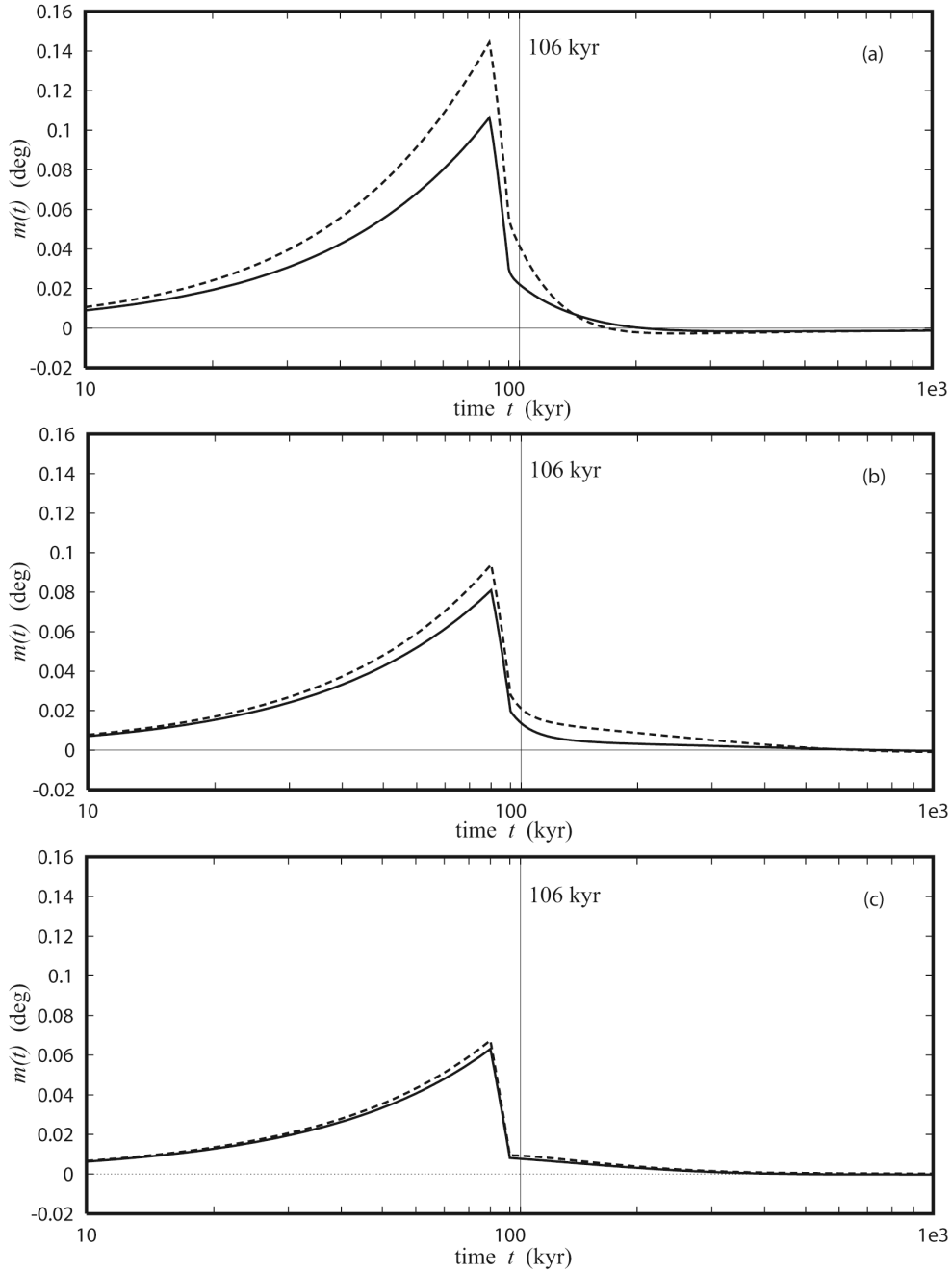

Figure 5.6: The TPW displacement m due only to the last ice age for the compressible (solid) and incompressible (dashed) PREM with the viscoelastic lithosphere, $\nu_{\rm L} = 10^{26}\,{\rm Pa\,s}$. The lower mantle viscosity is $\nu_{\rm LM} = 10^{21}$ (a), $\nu_{\rm LM} = 10^{22}$ (b) and $\nu_{\rm LM} = 10^{23}$ (c) Pa s. The negative values of m indicate that the rotation pole has already crossed its initial position.

for the full series of ice age cycles. In this case, two counteracting effects are involved. First, the easier relaxation of the lithospheric stresses accumulated during the polar excursion allows the equatorial bulge to readjust faster, as pointed in fig. 3 of Ricard *et al.* (1993). Second, the full isosatic compensation on the ice age time scale reduces the perturbation of the inertia tensor due to the ice age loading, eq. (5.12). Between the two effects, which respectively reduces and increases the rotational stability of the Earth, the stabilizing one due to isostatic compensation is dominant as indicated by the reduction of the TPW displacement. The importance of the full isostatic compensation in TPW predictions can be understood by considering that the viscoelastic lithosphere nullifies the secular term responsible of a net shift of the rotation axis away from Hudson bay after the end of each ice age cycle. Indeed, the load fluid love number is $k_L^F = 1$ for the viscoelastic lithosphere and, then, the factor s can be simplified from the numerator and the denominator of eq. (5.31).

Although carried out with different values for the lithospheric viscosity $\nu_{\rm L}$, the TPW simulations of Vermeersen and Sabadini (1999), Nakada (2002), Mitrovica *et al.* (2005) and those given in fig. 5.6 behave as expected on the basis of the underlying physical hypotheses. Particularly, the "Nakada paradox" is explained within the "traditional approach" in terms of an increase in the delay of the readjustment of the hydrostatic equatorial bulge due to the high lithospheric viscosity $\nu_{\rm L}$.

5.4 The role of mantle heterogeneities

In order to estimate the correction β, eq. (5.25), Mitrovica *et al.* (2005) considers the difference between the observed fluid Love number $k^T_{F,obs}$ and the tidal fluid limit $k^T_{F,\rm II}$ coming from the second–order theory of the hydrostatic equilibrium figure of the rotating Earth (Nakiboglu, 1982). These authors found that $\beta = k^T_{F,obs} - k^T_{F,\rm II} = 0.008$. This difference represents the non–hydrostatic contribution due to the lateral density variations and dynamic topography sustained by convection.

Nakiboglu's hydrostatic flattening is close to the values given by other authors (Denis, 1989; Alessandrini, 1989). However as the β parameter is the small difference between two large numbers (observed fluid Love number and tidal fluid limit), the β deduced from these different authors only agree within 10 per cent. Notice also that all these papers were using PREM (Dziewonski and Anderson, 1981) which was in agree-

ment with an Earth's mass and inertia that have been sligthly reevaluated since. The hydrostatic flattening according to Clairaut's first order theory is essentially controlled by I/Ma^2 (Radau's result, where I, M and a are the Earth's, inertia, mass and radius), a parameter equal to 0.3308 in PREM while the most recent estimate is 0.33069 (Chambat and Valette, 2001). This reevaluation should reduce the predicted hydrostatic flattening and, by consequence, increase β. Clearly a more rigorous estimate of the hydrostatic flattening is needed but is beyond the goal of this paper (see Chambat *et al.*, 2010). It seems qualitatively that the β parameter chosen by Mitrovica *et al.* (2005) might be a conservative value that could be increased up to $\beta = 0.01$. Mitrovica *et al.* (2005) were aware of the possible uncertainity on the β parameter and indeed they consider the reasonable range $0.006 < \beta < 0.01$ in their fig. 10.

We now quantify the effects of the slow mantle convection for models with a high viscous viscoelastic lithosphere, $\nu_{\rm L} = 10^{26}$ Pa s, by making use of the same β correction as in Mitrovica *et al.* (2005), namely $\beta = 0.008$ in eq. (5.24). Fig. 5.7 shows the effects of this non hydrostatic contribution to the equatorial bulge, to be compared with fig. 5.6. For the soft lower mantle $\nu_{\rm LM} = 10^{21}$ Pa s (panels a of figs 5.6 and 5.7), the minor differences during the active loading glaciation–deglaciation phase, from 10 to 100 kyr, are accompanied by large deviations at the end of the unloading. At 100 kyr, the displacement is reduced by a factor of 3 with respect to the compressible rheology and almost by a factor of 2 with respect to the incompressible one. For the higher lower mantle viscosities $\nu_{\rm LM} = 10^{22}$ Pa s (panel b) and $\nu_{\rm LM} = 10^{23}$ Pa s (panel c). Differently, the effects of the non hydrostatic contribution are not as important. The TPW displacement for $\nu_{\rm LM} = 10^{21}$ Pa s is so inhibited by the non hydrostatic contribution that both compressible and incompressible models predict a change of sign in the displacement m at about 15 kyr after the end of deglaciation, fig. 5.7 (a), with the axis of rotation being displaced toward the deglaciated region with respect to the initial north pole. Zero crossings occur earlier in time also for the higher viscosity cases, fig. 5.7 (b, c), but not as dramatically as for the models with the soft lower mantle of $\nu_{\rm LM} = 10^{21}$ Pa s.

This behaviour of the TPW displacement, like a dampened pendulum crossing the initial north pole, occurs both for the high viscosity lithosphere and in the presence of a non hydrostatic correction β. It is a completely different process than that due to the coupling in the linearized rotation equations of the direction cosines m_1 and m_2 involved by the first term of the right side of eqs (5.20) and (5.26), neglected in the present work

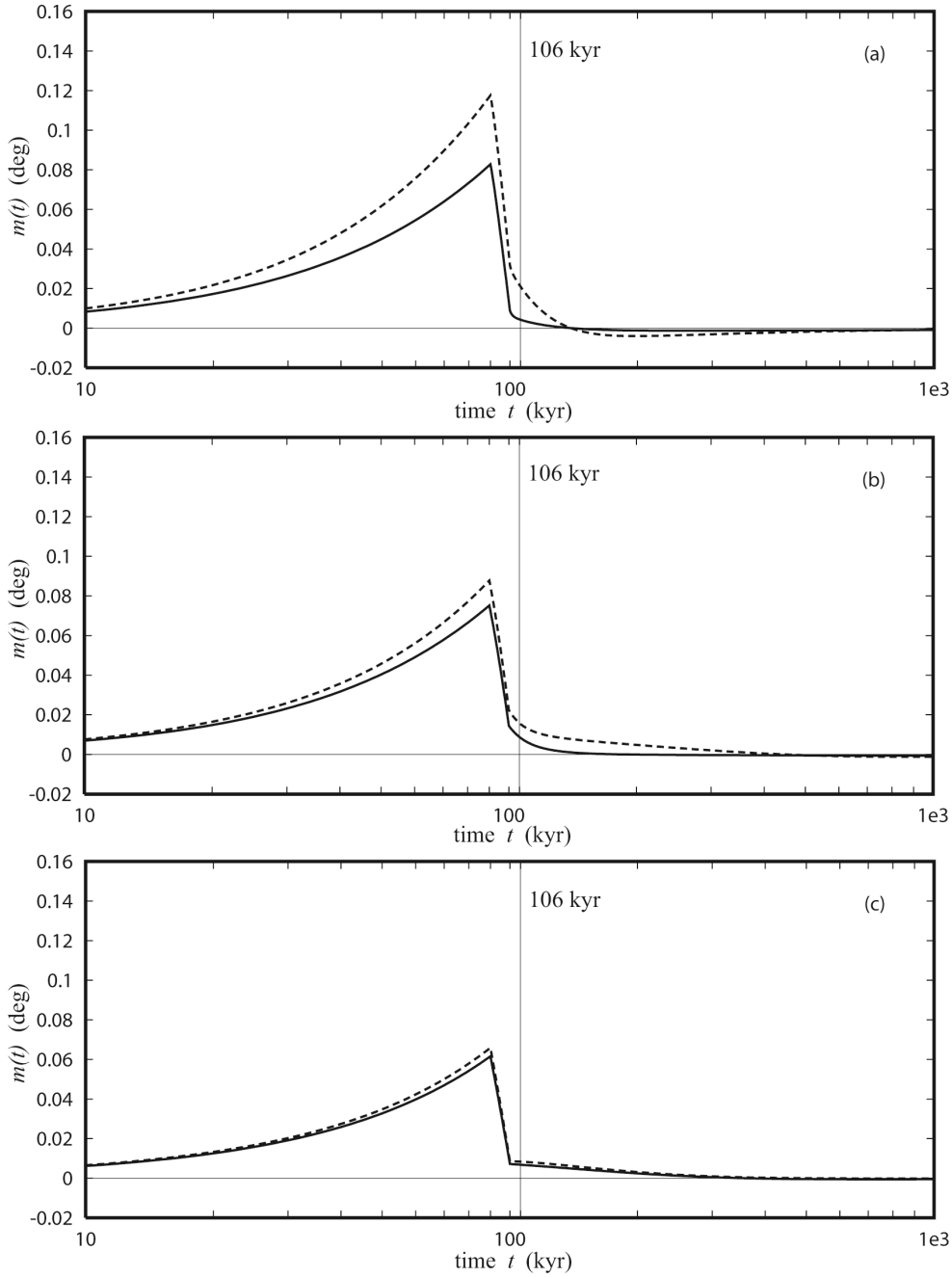

Figure 5.7: The TPW displacement m due to the last ice age only of the compressible (solid) and incompressible (dashed) PREM with the viscoelastic lithosphere, $\nu_{\rm L} = 10^{26}$ Pa s, and the non–hydrostatic correction $\beta = 0.008$. The lower mantle viscosity is $\nu_{\rm LM} = 10^{21}$ Pa s (a), $\nu_{\rm LM} = 10^{22}$ Pa s (b) and $\nu_{\rm LM} = 10^{23}$ Pa s (c). The negative values of m indicate that the rotation pole has already crossed its initial position.

following Mitrovica and Milne (1998). This coupling explains the 14 month Chandler wobble and a small amplitude wobble with a period much larger than the 1 Myr considered in figs 5.6 and 5.7.

We now investigate the sensitivity of the present–day TPW predictions to the rheology of the lithosphere and to the β correction. Fig. 5.8 shows the present–day TPW rate, namely the time derivative of the displacements of figs 5.5, 5.6 and 5.7 evaluated at 6 kyr after the end of unloading, as a function of the lower mantle viscosity $\nu_{\rm LM}$. We use the compressible model with a viscoelastic lithosphere (dashed line) and we vary the β correction (thin solid lines) by steps of 0.002 from 0.002 to 0.016, around the value of 0.008 (dash–dotted line) used in Mitrovica *et al.* (2005). The case with an elastic lithosphere is indicated by the thick solid line. In this figure, only one ice cycle is considered. The largest sensitivity of TPW rates to lithospheric rheology and β correction occurs for lower mantle viscosities $\nu_{\rm LM}$ smaller than 10^{22} Pa s. At $\nu_{\rm LM} = 10^{21}$ Pa s the predicted rates vary from -0.91 deg/Myr, for the model with the elastic lithosphere (thick solid line), to -0.29 deg/Myr, for the model with the viscoelastic lithosphere and the correction $\beta = 0.008$ (dash–dotted line). As first shown by Mitrovica *et al.* (2005), the effects of the non hydrostatic bulge is to dampen TPW rates when the lower mantle viscosity $\nu_{\rm LM}$ is in the range from 10^{21} Pa s to 10^{22} Pa s. For very large β corrections, 0.014 and 0.016, the damping effect of the non hydrostatic bulge is made evident by the change of sign of the TPW rate, indicating that the rotation pole crosses its initial position and is going now away from Hudson bay once again. The non hydrostatic contribution from convection is so effective in fixing the rotation axis that the pole of rotation comes back to its initial position without any finite displacement of the pole.

A better comparison with Mitrovica *et al.* (2005) results, and a more realistic estimate of present–day TPW rates, is obtained by considering the full series of eight ice age cycles, as shown in fig. 5.9. For the elastic lithosphere case and when $\nu_{\rm LM} = 10^{21}$ Pa s, adding the seven previous ice age cycles to the single cycle considered in fig. 5.8, increases the TPW rates by a factor of 2, while for $\nu_{\rm LM}$ greater than 10^{22} Pa s the increase is only of 10% or less. On the contrary, for the model with the viscoelastic lithosphere, both with or without the non hydrostatic contribution, the previous seven ice ages have a negligible effect, the differences being lesser than 5% for the whole range of lower mantle viscosity. This shows that the TPW rate remains mostly sensitive to only the last ice age.

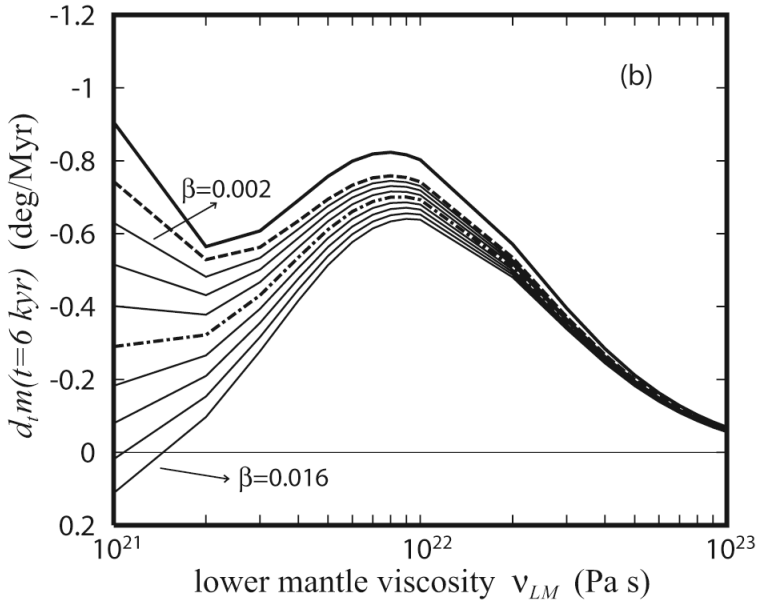

Figure 5.8: The present TPW rate $\partial_t m$ due only to one ice age, evaluated at 6 kyr after the end of the deglaciation, as function of the lower mantle viscosity $\nu_{\rm LM}$, for PREM with the elastic lithosphere (thick solid line), the high viscosity viscoelastic lithosphere, (dashed line), $\nu_{\rm L} = 10^{26}$ Pa s, and with the non–hydrostatic contribution $\beta = 0.008$ (dashed–dot line). The thin solid lines refer to the PREM with the hard viscoelastic lithosphere and the non hydrostatic correction β varying from 0.002 to 0.016 by steps of 0.002, from top to bottom. The sign of $\partial_t m$ indicates whether the rotation pole moves forward to, negative, or go away from, positive, the Hudson bay.

This latter remark explains also why, with the elastic lithospheric rheology, the TPW rate versus lower mantle viscosity $\nu_{\rm LM}$ does not have the same bell shape as the geopotential changes due to PGR. In this case, the TPW predictions are sensitive also to the previous seven ice ages mainly for lower mantle viscosity in the range from 10^{21} Pa s to 10^{22} Pa s as it results from the comparison of figs 5.8 and 5.9 for the model with the elastic lithosphere (thick solid line). This is due to the fact that, without a high viscosity viscoelastic lithosphere or a non hydrostatic contribution from mantle convection, the only stabilizing effect is the delay in the readjustment of the hydrostatic equatorial bulge to the axis of instantaneous rotation controlled by the lower mantle viscosity $\nu_{\rm LM}$, which becomes smaller and smaller decreasing $\nu_{\rm LM}$.

The damping effect due to the high viscosity of the lithosphere and to the non hydrostatic contribution is more evident in the displacement of the rotation axis than in the TPW rate, as we show in fig. 5.10. After the eight ice age cycles, in the case of

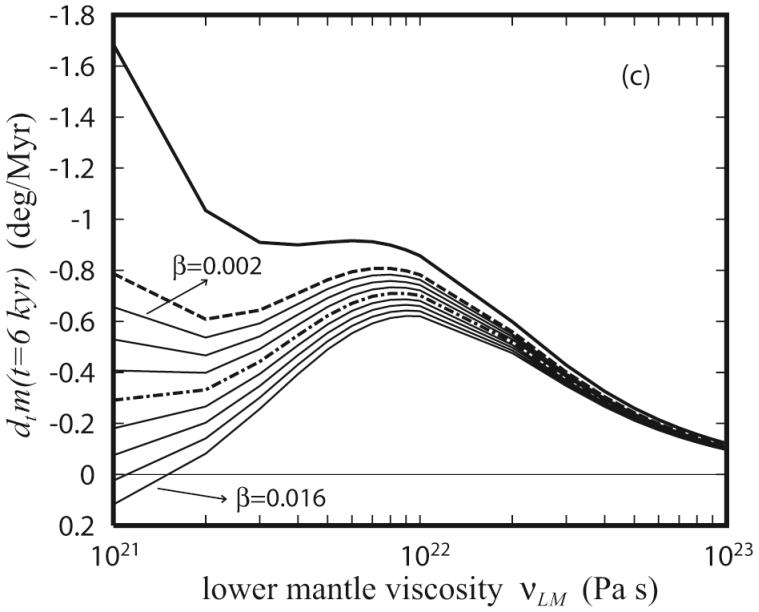

Figure 5.9: The same as fig. 5.8, but for the full series of eight ice ages.

the elastic lithosphere (thick solid line), the axis of rotation is displaced from its initial position by 0.27 deg, at $\nu_{\rm LM} = 10^{21}$ Pa s, and this value diminishes gradually with the lower mantle viscosity to about 0.02 deg/Myr at $\nu_{\rm LM} = 10^{23}$ Pa s. The rheology change from elastic (thick solid line) to viscoelastic (dashed line) lithosphere causes reductions in the TPW displacements by factors ranging from 20, at $\nu_{\rm LM} = 10^{21}$ Pa s, to 2, at $\nu_{\rm LM} = 10^{23}$ Pa s. The value obtained for our compressible model with the elastic lithosphere and the low lower mantle viscosity of $\nu_{\rm LM} = 10^{21}$ Pa s is very similar to what is obtained in Vermeersen and Sabadini (1999) for a simpler 5–incompressible model. The TPW displacements are subjected to further reductions when a β correction is added. Particularly, for $\beta = 0.008$ (dash–dotted line), the rotation pole crosses the initial north position. Generally, as shown in fig. 5.10 (b), the TPW displacements for the viscoelastic lithosphere range in a narrow interval for any values of the lower mantle viscosity $\nu_{\rm LM}$, from -0.011 deg to 0.022 deg even without the β correction.

The present–day TPW rates obtained using the correction $\beta = 0.008$ reaches at most -0.71 deg/Myr for a lower mantle viscosity $\nu_{\rm LM} = 8 \times 10^{21}$ Pa s. This is -0.215

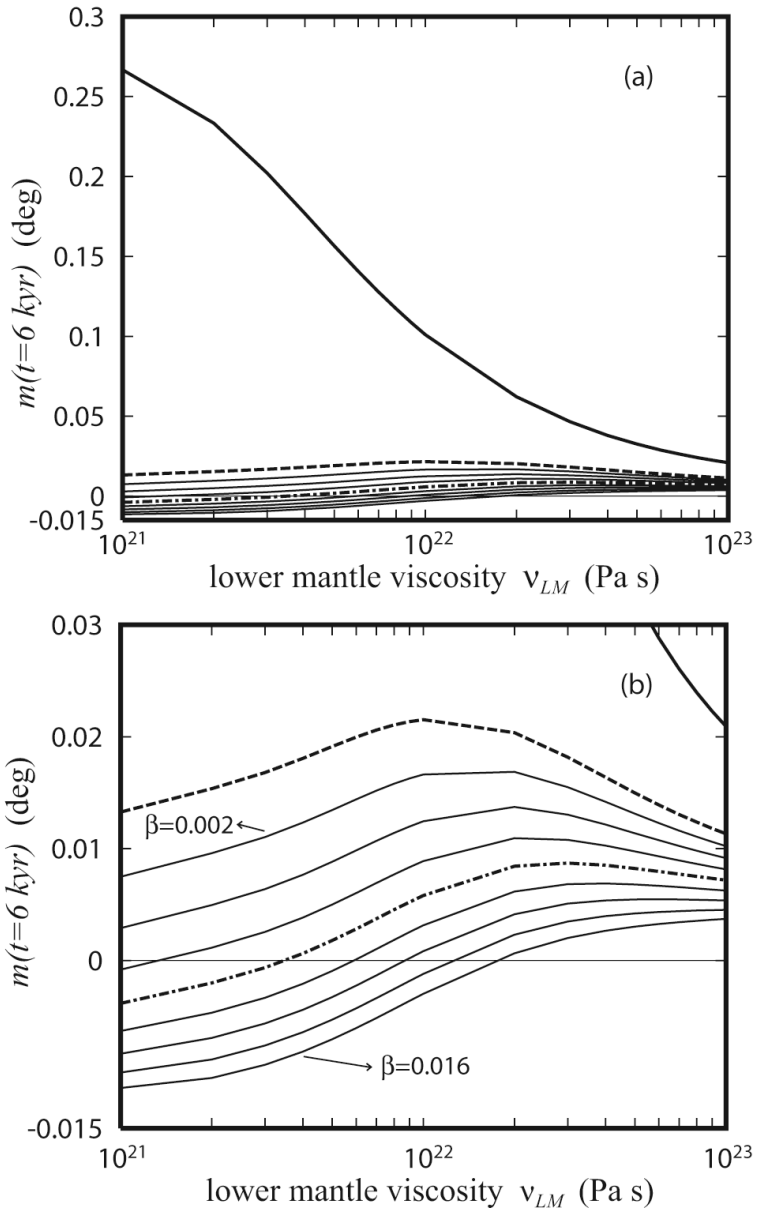

Figure 5.10: The present TPW displacement m due to the full series of eight ice ages, evaluated at 6 kyr after the end of the deglaciation, as function of the lower mantle viscosity $\nu_{\rm LM}$, for PREM with the elastic lithosphere (thick solid line), the high viscosity viscoelastic lithosphere, (dashed line), $\nu_{\rm L} = 10^{26}$ Pa s, and with the non hydrostatic correction $\beta = 0.008$ (dashed–dot line). The thin lines refer to PREM with the viscoelastic lithosphere and the non hydrostatic correction β varying from 0.002 to 0.016 by steps of 0.002, from top to bottom. The negative values of m indicates that the rotation pole has already crossed its initial position. The panel (b) shows the enlargement of the panel (a) in the range of $[-0.015, 0.03]$ deg.

deg/Myr lower than the observed rate of -0.925 deg/Myr (McCarthy and Luzum, 1996). Our findings fully support the results obtained by Mitrovica *et al.* (2005) and, having been obtained on the basis of compressible Earth models which take into account continuous variations of the material parameters, and thus relying on the contour integration rather than on normal mode summation, they provide an independent confirmation. Even if we consider models with elastic lithosphere we obtain the same TPW predictions once the tidal fluid limit $K^T_{F,E} = 0.920$ from modelling is replaced by the estimate $k^T_{F,obs} = 0.942$ of Mitrovica *et al.* (2005), their eq. (16). Indeed the stabilizing effect of the larger non hydrostatic bulge for models with elastic lithosphere, $\beta = k^T_{F,obs} - K^T_{F,E} = 0.022$, would be quantitatively the same of the two stabilizing effect acting in the case of models with the high viscous viscoelastic lithosphere: the delayed readjustment of the equatorial bulge together with the smaller non hydrostatic bulge, $\beta = k^T_{F,obs} - K^T_{F,V} = 0.008$. This means that TPW studies cannot discriminate between the effects of the lithospheric rheology and of the lateral density variations and dynamic topography sustained by convection. In any case, the parameter β has to be consistent with mantle convection models.

5.5 Conclusions

We have compared ice age TPW predictions using the traditional approach where the equilibrium flattening is self consistently computed (Sabadini and Peltier, 1981; Sabadini *et al.*, 1982; Wu and Peltier, 1984) and the scheme proposed by Mitrovica *et al.* (2005) where the observed tidal fluid number is considered. The motion of the rotation axis, given by the linearized Liouville equation (5.20), depends on the load–induced perturbation, $1 + \tilde{k}^L(s)$, and on the readjustment of the equatorial bulge, $k^T_F - \tilde{k}^T(s)$. Over the time of ice age, the load, $\tilde{k}^L(s)$, and tidal, $\tilde{k}^T(s)$, Love numbers, computed for models with an elastic and high viscous viscoelastic lithosphere are the same. Nevertheless, the traditional approach leads to different TPW predictions due to the fact that the high viscous viscoelastic lithosphere implies an extra delay of the readjustment of the equatorial bulge, compared to the elastic lithosphere (see fig. 1). The elastic and viscoelastic lithospheres are indeed associated with different stress patters. Frozen stresses are present in the elastic lithosphere before and after the glaciation, while the viscoelastic lithosphere is initially stress free and it builds up stress that cannot relax during the

polar motion for high lithospheric viscosities.

In order to take into account the difference between observed and modelled tidal fluid numbers, Mitrovica *et al.* (2005) introduce the β–correction, eq. (5.25). This scheme represents a first attempt to couple mantle convection with ice age TPW within a linear rotation theory. As first enlightened by Mitrovica *et al.* (2005), this ice age–convection coupling dampens present–day ice age TPW rates since the non hydrostatic extra bulge, frozen within the planet, stabilizes the planet by slowing down the displacement of the axis of rotation away from this fixed orientation so effectively that the rotation pole goes back to its initial position at large time. We show that self–consistent non hydrostatic bulge resulting from convection calculations plays a fundamental role in obtaining realistic estimates of this non hydrostatic contribution, due to its major impact in TPW simulations in the lower mantle viscosity range from 10^{21} Pa s to 10^{22} Pa s.

With the extra degree of freedom given by the parameter β, models with elastic and high viscous elastic lithosphere lead to the same ice age TPW prediction. It is therefore difficult to choose the most appropriate lithospheric rheology when the distinction is made between the actual shape of the Earth and its equilibrium shape. We agree however with Mitrovica *et al.* (2005) that using a viscoelastic lithosphere in the framework of the traditional theory seems reasonable because it is simpler (but not necessary true) to start from a relaxed lithospheric stress and because the tidal fluid limit from the viscoelastic modelling is closer to observation and thus a smaller mantle contribution β needs to be introduced.

The present–day value of β, related to the excess flattening due to mantle convection, cannot be best evaluated than by subtracting the computed hydrostatic tidal fluid limit to the observed fluid Love number, eq. (5.25). On geological time scale, as the Earth is constantly reorienting to maximize its equatorial inertia, i.e., to be more flattened than the hydrostatic estimate, β should always remain positive except maybe during exceptional inertial interchange polar excursion (Richards *et al.*, 1999). The value of the non hydrostatic contribution β due to convection can be estimated by means of convection models or, for the last hundred million years, from paleoreconstruction of plate tectonics (Ricard *et al.*, 1993b). The difference between the time dependent inertia terms remains of the same order than Mitrovica *et al.* (2005) estimate of 0.008 within a factor 2. This means that the Earth's rotation axis is always very stable with respect to short term forcings like glaciations: as soon as the forcing vanishes, the mantle density anomalies force

the rotation axis to come back to its initial position. Only mantle convection, can drive large TPW displacements (Spada *et al.*, 1992b).

Once the Mitrovica *et al.* (2005) estimate of the correction $\beta = 0.008$ is taken into account, the highest present–day TPW rate of 0.71 deg/Myr from glacial forcing is obtained for a lower mantle viscosity of 10^{22} Pa s, which means that at least 23 per cent of the observed value of 0.925 deg/Myr (McCarthy and Luzum, 1996) remains unexplained. This implies that mantle convection must drive polar motion to be compliant with observations. Recent mantle circulation models by Schaber *et al.* (2009), characterized by a large heat flux at the core–mantle boundary, require a lower mantle viscosity of 10^{23} Pa s to stabilize the planet rotation, leading to TPW rates of about 0.5 deg/Myr in rough agreement with the direction towards Newfoundland in the last 100 Myr. The first self–consistent TPW calculations from mantle convection have been obtained by Ricard *et al.* (1993b) and already required a substantial increase in the lower mantle viscosity, 10^{22} Pa s at least, to rotationally stabilize the planet. The ice age TPW, coupled with the stabilizing effect of the excess flattening due to mantle convection, in addition to the TPW driven by mantle convection are thus both needed to fulfill observations, requiring lower mantle viscosity ranging from 10^{22} to 10^{23} Pa s. If this is the case, the β–correction proposed by Mitrovica *et al.* (2005) would only impact marginally the estimate of ice age TPW rates, as it would be the high viscosity of the lower mantle that would control the TPW. It is notable that an inconsistency for lower mantle viscosity predictions between glacial and convection forcing continues to exist. Indeed, for the Schaber *et al.* (2009) estimate of 10^{23} Pa s lower mantle viscosity, glacial forcing would provide at most TPW rates of 0.1 deg/Myr that, summed to the convection TPW rate of 0.5 deg/Myr, would not explain the observation of 1 deg/Myr. The exact balance of the TPW, between deglaciation and convection forcings, is therefore not yet well understood.

Chapter 6

New insights into Mantle Convection True Polar Wander

True Polar Wander, the slow motion of Earth's rotation axis with respect to the mantle is generally taken as evidence of mantle convection (Spada *et al.*, 1992) and Pleistocene ice sheet melting (Sabadini and Peltier, 1981; Mitrovica *et al.*, 2005; Cambiotti *et al.*, 2010). Owing to the ability of the rotational bulge to relax and readjust to perturbations of the rotation axis on a time scale T that ranges from 1 to $100\,\mathrm{kyr}$, depending on the internal viscoelastic stratification (Ricard *et al.*, 1993a), Earth's rotation axis constantly tracks the Maximum Inertia Direction of Mantle Convection (MID–MC) on the million year time scale of mantle convection. On this long time scale, however, it is often assumed that the planet readjusts without delay and that the rotation axis and the MID–MC coincide (Jurdy, 1978; Steinberger and O'Connell, 1997; Rouby *et al.*, 2010).

This coincidence, however, cannot be taken as a general rule. Using mantle density anomalies observed by seismic tomography, Ricard and Sabadini (1990) showed out that the present–day rotation axis lags behind the MID–MC by some degrees. Ricard *et al.* (1993a) pointed out that the planet, submitted to a change of inertia of order E attributable to mantle convection, will wander with a characteristic time of order $T\,(C - A)/E$, with C and A being the polar and equatorial inertia moments. In view of this, the Earth can shift its rotation pole from a starting position to a new position in a time larger than a few $100\,\mathrm{kyr}$ or a few million years. On the basis of similar arguments, Steinberger and O'Connell (1997) estimated that the offset between the rotation axis and the MID–MC should be less than 1°, even for an high viscous mantle with lower mantle viscosity of $10^{23}\,\mathrm{Pa\,s}$. This estimate, however, was obtained assuming a MID–MC rate less than $0.2^\circ/\mathrm{Myr}$ during the past $50\,\mathrm{Myr}$. Accounting for the delay of the readjustment of the rotational bulge and allowing for an offset between the geographic north pole and the present–day MID–MC, Richards *et al.* (1997) estimated TPW paths for different viscosity profiles of the mantle. Nevertheless, they did not quantify the offset and concluded that the influence of the delay on TPW is small.

In light of this, although Ricard *et al.* (1993a), Richards *et al.* (1997) and Steinberger and O'Connell (1997) provided some insights into the long time scale rotational behaviour of the Earth, a concise and complete picture of the problem is still lacking at the moment. We herein overcome these limitations and discuss a new treatment of the non–linear Liouville equation that allows to describe the long time scale rotational behaviour of the Earth via a simple linear theory. Thus, we clarifies this long debated issue and its connections with seismic tomography.

6.1 Linearized rotation theory for finite polar excursions

To clarify the long time scale rotational behaviour of the Earth, we must start with the basic laws governing the relative motion of the rotation axis with respect to the MID–MC. It can be appropriately dealt with in the reference frame defined by the three eigenvectors $\boldsymbol{e}_k$ of mantle convection inertia tensor $\boldsymbol{\mathcal{C}}$

$$\boldsymbol{\mathcal{C}} = \sum_{k=1}^{3} C_k \, \boldsymbol{e}_k \otimes \boldsymbol{e}_k \tag{6.1}$$

where $\otimes$ stands for the algebraic product and where C_k are the inertia moments. Here C_3 is the maximum inertia moment ($C_3 \geq C_2$ and $C_3 \geq C_1$) and $\boldsymbol{e}_3$ is the MID–MC. This is a time dependent reference frame and, from geometric considerations (Ben–Menahem and Singh, 1981), the time derivatives of the eigenvectors $\boldsymbol{e}_k$ yield

$$\frac{d\boldsymbol{e}_k}{dt} = \boldsymbol{\xi} \times \boldsymbol{e}_k \tag{6.2}$$

Here, $\boldsymbol{\xi}$ is the angular velocity of the mantle convection inertia that we write as follows

$$\boldsymbol{\xi} = -V_2 \, \boldsymbol{e}_1 + V_1 \, \boldsymbol{e}_2 + V_3 \, \boldsymbol{e}_3 \tag{6.3}$$

in such a way that V_1 and V_2 are the components of the MID–MC velocity $d\boldsymbol{e}_3/dt$ along the equatorial axes $\boldsymbol{e}_1$ and $\boldsymbol{e}_2$, respectively. V_3 describes the counterclockwise rotation rate of the equatorial axes around the MID–MC.

We write Earth's angular velocity $\boldsymbol{\omega}$ as $\boldsymbol{\omega} = \omega \, \boldsymbol{n}$, where ω and $\boldsymbol{n}$ are the rotation rate and axis. Within the reasonable assumption that the angle between rotation axis and MID–MC is small, the rotation axis $\boldsymbol{n}$ can be expressed in terms of direction cosines m_1 and m_2 along the equatorial axes $\boldsymbol{e}_1$ and $\boldsymbol{e}_2$,

$$\boldsymbol{n} = m_1 \, \boldsymbol{e}_1 + m_2 \, \boldsymbol{e}_2 + \boldsymbol{e}_3 \tag{6.4}$$

The time variation of Earth's angular velocity $\boldsymbol{\omega}$ is therefore

$$\frac{d\boldsymbol{\omega}}{dt} = \boldsymbol{n}\frac{d\omega}{dt} + \omega\frac{d\boldsymbol{n}}{dt} \tag{6.5}$$

where the first term on the right is related to the change of the length of the day and the second term to the TPW velocity $\boldsymbol{v} = d\boldsymbol{n}/dt$, which, assuming that the time evolution of mantle convection is slow, becomes

$$\boldsymbol{v} = \left(\frac{dm_1}{dt} + V_1\right)\boldsymbol{e}_1 + \left(\frac{dm_2}{dt} + V_2\right)\boldsymbol{e}_2 \tag{6.6}$$

The expressions (6.4) and (6.6) are correct to first order, for small m_1, m_2 and $\boldsymbol{\xi}$ (i.e., neglecting terms of order $m_i\, m_j$ or $m_i\, V_j$).

The rotation axis, averaged over a few Chandler periods, is aligned with the direction of maximum total inertia (Munk and MacDonald, 1960), i.e., is the eigenvector of the sum of the inertia tensors due to the rotational bulge, $\boldsymbol{\mathcal{B}}$, and the mantle convection, $\boldsymbol{\mathcal{C}}$,

$$\boldsymbol{n} \times (\boldsymbol{\mathcal{B}} + \boldsymbol{\mathcal{C}}) \cdot \boldsymbol{n} = 0 \tag{6.7}$$

We take into account the relaxation of rotational bulge by means of the long–term approximation (Spada *et al.*, 1992; Ricard *et al.*, 1993a) of the MacCullagh's formula for centrifugal deformation (Munk and MacDonald, 1960). As shown in Appendix A of Cambiotti *et al.* (2011b), it can be cast as follows

$$\boldsymbol{\mathcal{B}} = \beta\,\omega^2\left[\left(1 - \frac{2\,T}{\omega}\,\frac{d\omega}{dt}\right)\left(\boldsymbol{n}\otimes\boldsymbol{n} - \frac{1}{3}\,\mathbf{1}\right) - T\,(\boldsymbol{n}\otimes\boldsymbol{v} + \boldsymbol{v}\otimes\boldsymbol{n})\right] \tag{6.8}$$

where $\mathbf{1}$ is the identity matrix, T the time scale of readjustment of rotational bulge and $\beta\,\omega^2$ the difference between polar and equatorial inertia moments of the hydrostatic rotational bulge. The time scale T can easily be computed for any spherically symmetric viscoelastic Earth's model and should be of the order of $30\,\mathrm{kyr}$ (Ricard *et al.*, 1993a).

Eq. (6.8) accounts for the readjustment of the rotational bulge due to variations of the length of day via the term proportional to $d\omega/dt$. However, as we have neglected the time derivative of the angular momentum in the Liouville equation averaged over a few

Chandler periods (see eq. (6.7)), the length of day remains constant and the minute term $(2T/\omega)(d\omega/dt)$ can also be neglected.

Thus, by solving eq. (6.7) using eqs (6.1), (6.4), (6.6) and (6.8), we obtain a first order differential equation for each direction cosine m_i

$$\frac{dm_i}{dt} + \frac{m_i}{T_i} = -V_i \qquad (i = 1, 2) \tag{6.9}$$

where T_i are time scales defined by

$$T_i = \frac{\beta\,\omega^2}{C_3 - C_i}\,T \qquad (i = 1, 2) \tag{6.10}$$

Eqs (6.9) and (6.10) show that V_i are the forcings of the relative motion of rotation axis and that the actual time scales T_i controlling this relative motion are not simply the time scale T of the rotational bulge readjustment, but are increased by the factor $\beta\,\omega^2/(C_3 - C_i)$.

The difference between polar and equatorial inertia moments of the hydrostatic rotational bulge $\beta\,\omega^2$ has been recently estimated (Chambat *et al.*, 2010)

$$\beta\,\omega^2 \approx 1.0712 \times 10^{-3}\,Ma^2 \tag{6.11}$$

with M and a being the Earth's mass and mean radius. The differences between the inertia moments of mantle convection, $C_3 - C_i$, is typically of order of the differences between the observed total inertia moments of the Earth (usually defined as A, B and C), minus the hydrostatic contribution $\beta\,\omega^2$ (Chambat and Valette, 2001)

$$\begin{aligned} C_3 - C_1 &\approx (C - A) - \beta\,\omega^2 = 1.48 \times 10^{-5}\,Ma^2 \\ C_3 - C_2 &\approx (C - B) - \beta\,\omega^2 = 0.78 \times 10^{-5}\,Ma^2 \end{aligned} \tag{6.12}$$

Thus, as already argued in Ricard *et al.* (1993a), the time scales T_i are greater than T by a factor of about 100. Assuming $T = 30\,\mathrm{ky}$, the relative motion of rotation axis is con-

trolled by time scales $T_i \approx 3\,\mathrm{Myr}$, that are comparable with those of mantle convection, say greater than $1\,\mathrm{Myr}$. These findings show that the previous approximation based on the assumption that the rotational bulge readjusts instantaneously to perturbations of the rotation axis is not accurate. Particularly, it missed a fundamental aspect of TPW dynamics: the inertia perturbations due to mantle convection are two orders of magnitude smaller than those of the rotational bulge. Such a smallness increases the time scales for viscoelastic readjustment of the rotational bulge during the TPW to values comparable to those of mantle convection. Notice also that the two direction cosines m_1 and m_2 behave differently as T_1 and T_2 are likely to differ due to dependence in eq. (6.10) on the differences $C_3 - C_1$ and $C_3 - C_2$ (they differ by a factor of 2 at the present–day). Furthermore, since the time scales T_i are evolving with time, they could potentially become infinite during inertial interchanges (Richards *et al.*, 1999), a case that would invalidate our linearized approach.

The role of the time scales T_i becomes clear by assuming them constant. In this case, the solution of the linearized Earth's rotation differential equations, eq. (6.9), yields

$$m_i(t) = -e^{-t/T_i} \star V_i(t) \qquad (i = 1, 2) \tag{6.13}$$

with $\star$ standing for time convolution. This means that the time scales T_i are the relaxation times for the relative motion of the rotation pole forced by the MID–MC velocity components V_i. In this respect, eq. (6.9) and its particular solution, eq. (6.13), allow us to discerns the effects on TPW dynamics due to the delay of the readjustment of the rotational bulge and to the time evolution of mantle convection. A MID–MC velocity, constant for a time greater than T_i, drives the pole at the same velocity, $dm_i/dt = 0$, but with the pole lagging behind the MID–MC by the angle

$$m_i = -T_i\, V_i \qquad (i = 1, 2) \tag{6.14}$$

This result has the same physical meaning as eq. (1) of Steinberger and O'Connell (1993). Furthermore, from eq. (6.13), it is also clear that variations of the MID–MC velocity, occuring on times comparable or smaller than T_i, break the equilibrium of the relative position of the rotation axis with respect to the MID–MC given by eq. (6.14).

Particularly, they yield different TPW and MID–MC velocity amplitudes and directions. Such a result cannot be inferred within the previous framework (Ricard *et al.*, 1993a; Richards *et al.*, 1997; Steinberger and O'Connell, 1997) and shows that estimates of TPW rates must account both for fluctuations of Earth's inertia tensor and the delay of readjustment of rotational bulge.

6.2 Time–dependent inertia due to mantle convection

Let us consider the components $\mathcal{C}_{ij} = \boldsymbol{x}_i \cdot \boldsymbol{\mathcal{C}} \cdot \boldsymbol{x}_j$ and $\mathcal{B}_{ij} = \boldsymbol{x}_i \cdot \boldsymbol{\mathcal{B}} \cdot \boldsymbol{x}_j$ of the mantle convection and rotational bulge inertia tensors in the geographical reference frame with unit vectors $\boldsymbol{x}_1$, $\boldsymbol{x}_2$ and $\boldsymbol{x}_3$ ($\boldsymbol{x}_1$ points to the equator and the Greenwich meridian, while $\boldsymbol{x}_3$ points to the north pole, i.e., coincides with the present–day rotation axis). In view of eq. (6.7), at present time $t = 0$, the total inertia tensor (mantle convection plus rotational bulge) has zero off–diagonal components along $\boldsymbol{x}_3$

$$\mathcal{C}_{i3}(0) + \mathcal{B}_{i3}(0) = 0 \qquad (i = 1, 2) \tag{6.15}$$

and, by making use of eqs (6.8), we obtain

$$\mathcal{C}_{i3}(0) = \beta\, \omega^2\, T\, \boldsymbol{x}_i \cdot \boldsymbol{v}(0) \qquad (i = 1, 2) \tag{6.16}$$

which corresponds to eqs (8)–(9) of Ricard *et al.* (1993b) or eq. (3) of Steinberger *et al.* (1997). Thus, the off–diagonal components $\mathcal{C}_{13}(0)$ and $\mathcal{C}_{23}(0)$ of the mantle convection inertia tensor are non–zero in a wandering planet (i.e., when $\boldsymbol{v}(0) \neq \mathbf{0}$) and cannot be estimated from observations of the total inertia of the Earth as they are compensated by the rotational bulge not yet readjusted to the north pole. They must be estimated from 3–D models of Earth's density anomalies, accounting for the effect of dynamic topography (Ricard *et al.*, 1993b), or by solving the rotational problem as we are going to show.

We compute the mantle convection inertia tensor by means of our previously developed modelling strategy (Ricard *et al.*, 1993b; Richards *et al.*, 1997), assuming that largest changes in mantle density heterogeneities are likely caused by subduction. We use reconstructions of global plate motions for Cenozoic and late Mesozoic (Lithgow–

Bertelloni *et al.*, 1993), to inject cold slabs into the mantle where plates converge. In order to account for present–day geoid, for much of the observed seismic heterogeneities of the mantle and for the long term rotational stability of the Earth indicated by paleomagnetic data (Richards *et al.*, 1997), we consider lower/upper mantle and lithosphere/upper mantle viscosity ratios of $\eta_1 = 30$ and $\eta_2 = 10$, respectively. The sinking velocity of slabs when they enter the lower mantle is reduced by a factor of 4.4 (the velocity decrease is expected to scale roughly with the logarithm of the viscosity increase). This relation between viscosity increase and velocity reduction is a crude estimate that neglects the complexity of thermal exchanges between the slabs and the transition zone (Ohta, 2010), but it is validated by the good fit to the geoid and to the lower mantle tomography provided by the sinking slab model (Ricard *et al.*, 1993b). Our kinematic approach is independent of any assumed absolute mantle viscosity and yields an average sinking velocity of slabs in the lower mantle of order 1.6 cm yr^{-1}. This typical sinking velocity has been confirmed by other studies (e.g., van der Meer *et al.*, 2010).

This kinematic model of the mantle time–dependent density anomalies is certainly simple but it provides a robust estimate of the inertia tensor which is related to a radial integral of the longest wavelengths of the density anomalies (degree 2). Therefore, the details of paleo–reconstructions do not impact this model. This model should provide a better estimate of the time dependent evolution of Earth's inertia than complex dynamic models (e.g., Steinberger, 2000) that require many questionable assumptions (a backward in time advection of the present density anomalies that requires the choice of an absolute viscosity and assumes a depth dependent rheology in contradiction with the very existence of plates).

The kinematic slab model provides a time–dependent inertia tensor $\boldsymbol{\mathcal{C}}^{slab}(t)$. At present time, this model, $\boldsymbol{\mathcal{C}}^{slab}(0)$, maximizes the correlation with the observed inertia deduced from the geoid, $\boldsymbol{\mathcal{C}}^{obs}$, and is in good agreement with seismic tomography. As discussed previously, the mantle inertia tensor $\boldsymbol{\mathcal{C}}^{obs}$ observed from geoid does not account for the two off–diagonal components along $\boldsymbol{x}_3$ that, according to eq. (6.16), are related to the history of TPW. As a consequence we consider that Earth's rotation is forced by

$$\boldsymbol{\mathcal{C}}(t) = \boldsymbol{\mathcal{C}}^{slab}(t) + \boldsymbol{\mathcal{C}}^{obs} - \boldsymbol{\mathcal{C}}^{slab}(0) + \boldsymbol{\delta\mathcal{C}} \tag{6.17}$$

where $\boldsymbol{\delta\mathcal{C}}$ stands for the two present–day off–diagonal terms $\mathcal{C}_{13}(0)$ and $\mathcal{C}_{23}(0)$

$$\boldsymbol{\delta\mathcal{C}} = \mathcal{C}_{13}(0)\ (\boldsymbol{x}_1 \otimes \boldsymbol{x}_3 + \boldsymbol{x}_3 \otimes \boldsymbol{x}_1) + \mathcal{C}_{23}(0)\ (\boldsymbol{x}_2 \otimes \boldsymbol{x}_3 + \boldsymbol{x}_3 \otimes \boldsymbol{x}_2) \tag{6.18}$$

In this way, the inertia tensor $\boldsymbol{\mathcal{C}}(t)$ is in agreement with that observed and has a time dependence estimated from slab paleo–positions. We then constrain the two unknown terms $\mathcal{C}_{13}(0)$ and $\mathcal{C}_{23}(0)$ by solving the non–linear Liouville equation (6.7) for a given time scale T and by requiring that the present–day rotation axis $\boldsymbol{n}(0)$ coincides with the geographical north pole. In this way, the present–day total inertia $\boldsymbol{\mathcal{C}}(0) + \boldsymbol{\mathcal{B}}(0)$ has zero off–diagonal components along $\boldsymbol{x}_3$, as required by eq. (6.15). Note also that the term $\boldsymbol{\mathcal{C}}^{obs} - \boldsymbol{\mathcal{C}}^{slab}(0)$ entering eq. (6.17) accounts for any contribution other than slab subduction that can be assumed to remain constant with time, as large–scale upwellings (Rouby *et al.*, 2010) and the two large low shear velocity provinces (LLSVPs) in Earth's lowermost mantle (Torsvik *et al.*, 2006; Steinberger and Torsvik, 2010). This term is small as the slabs by themselves explain most of the geoid, which suggests that the LLSVPs should not affect significantly the inertia tensor.

This approach is somewhat similar to the method used in Richards *et al.*(1997) (see their note 26). However, it does not arbitrarily assume that the present–day mantle inertia terms $\mathcal{C}_{13}(0)$ and $\mathcal{C}_{23}(0)$ are zero. The latter assumption has been made in Steinberger and O'Connell (1997) or Schaber *et al.* (2009). It implies the coincidence between the present–day rotation axis and the MID–MC which is in contradiction with the observation of ongoing TPW as shown in eq. (6.16). Instead, by solving for the two unknown terms, $\mathcal{C}_{13}$ and $\mathcal{C}_{23}$, we respect the correct physics of the problem. Notice also that we solve the Liouville equations from past (starting $\sim 100\,\mathrm{Myr}$ ago) to present. It is incorrect to try to solve the Liouville equation backward in time as was done in Schaber *et al.* (2009) which results in rotation axis apparently preceding the MID–MC rather than lagging behind the MID–MC as it should (see their fig. 5).

In the following, we will express the off–diagonal terms $\mathcal{C}_{13}$ and $\mathcal{C}_{23}$ of the mantle convection inertia tensor in terms of the C_{21} and S_{21} geoid coefficients in meters, that are due to mantle convection alone and would be observed in the absence rotation. They are related to each other as follows

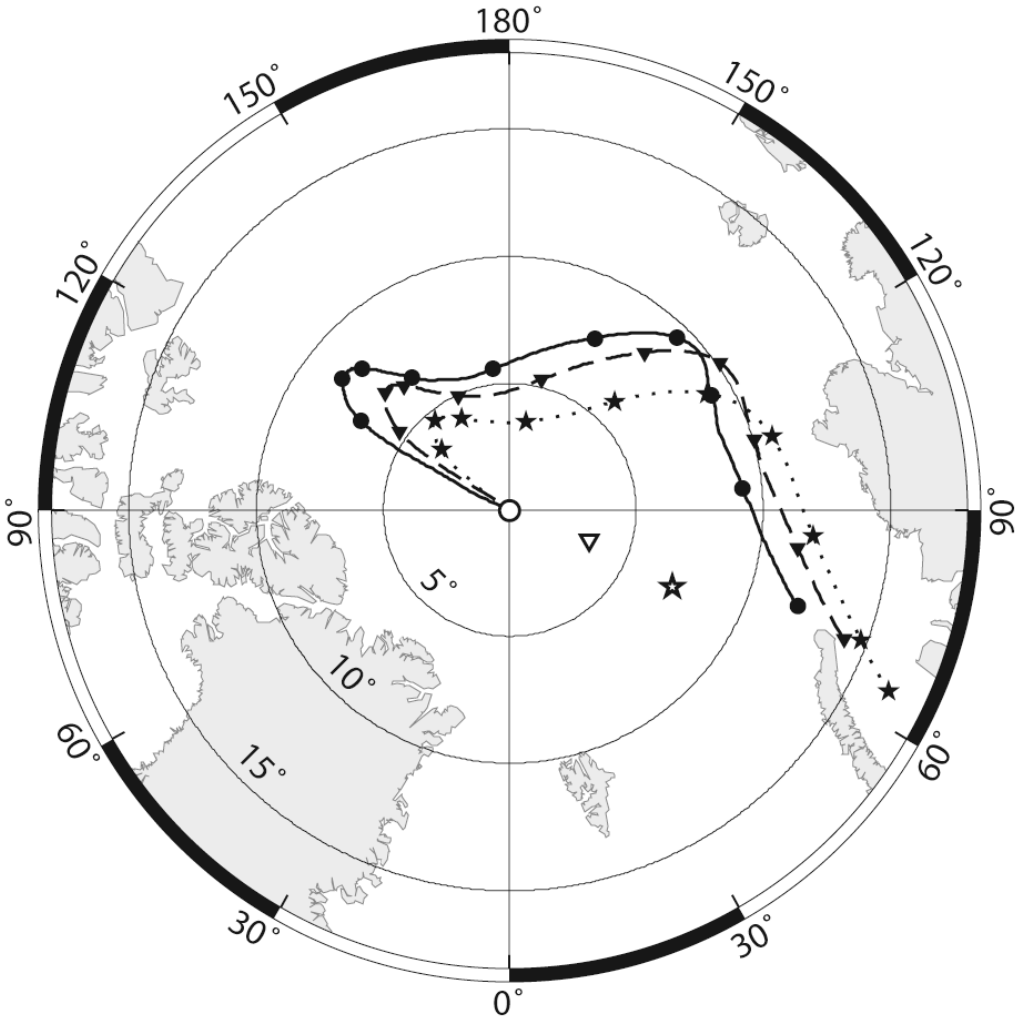

Figure 6.1: TPW paths for three time scales $T = 0$, 30 and $100\,\mathrm{kyr}$ (solid, dashed and dot lines with circles, triangles and stars, respectively). The symbols are given at intervals of $10\,\mathrm{Myr}$. The present–day MID–MC positions for three time scales $T = 0$, 30 and $100\,\mathrm{kyr}$ are also shown (open circles, triangles and stars, respectively). Only when the rotational bulge readjusts instantaneously ($T = 0$), the MID–MC coincides with the north pole.

$$\begin{aligned} \mathcal{C}_{13} &= -M\,a^2\,\sqrt{\frac{5}{3}}\,\frac{C_{21}}{a} \\ \mathcal{C}_{23} &= -M\,a^2\,\sqrt{\frac{5}{3}}\,\frac{S_{21}}{a} \end{aligned} \tag{6.19}$$

6.3 True Polar Wander simulations

Fig. 6.1 compares TPW paths obtained for three time scales $T = 0$, 30 and $100\,\mathrm{kyr}$. The case of $T = 0$ corresponds to the readjustment of the rotational bulge without delay. For viscosity ratios of $\eta_1 = 30$ (lower to upper mantle) and $\eta_2 = 10$ (lithosphere to upper mantle), the time scales $T = 30$ and $100\,\mathrm{kyr}$ correspond to upper mantle viscosities of about 10^{21} and $3.3 \times 10^{21}\,\mathrm{Pa\,s}$, respectively (the time scale T is proportional to the upper mantle viscosity ν_M, as discussed in Ricard *et al.*, 1993a,b). As initial condition for the Liouville equation, we assume that the rotation axis coincides with the MID–MC at $100\,\mathrm{Myr}$ before present. However, in view of eq. (6.13), it should be noticed that the TPW path is affected by the initial condition only for a time of order T_i (fig. 6.2), about 3 and $9\,\mathrm{Myr}$ for $T = 30$ and $100\,\mathrm{Kyr}$.

Due to the differences in the relaxation of the rotational bulge, TPW paths differ from each other. Particularly, the polar excursion in the past $10\,\mathrm{Myr}$ reduces from $6.9°$ for $T = 0$ to $5.3°$ and $3.6°$ for $T = 30$ and $100\,\mathrm{kyr}$, respectively. Furthermore, the present–day MID–MC occupies different positions, reflecting the estimated C_{21} and S_{21} geoid coefficients due to mantle convection driven by slab subduction (Table 1). Particularly, for $T = 0$, the present–day MID–MC is at the north pole since the rotational bulge readjusts instantaneously. On the contrary, for $T = 30$ and $100\,\mathrm{kyr}$, the present–day MID–MC are displaced by $3.4°$ and $7.1°$ towards $68.9°\,E$ and $64.6°\,E$, respectively.

A reduction of the polar excursion by increasing the time scale T is expected on physical grounds, once the herein developed linearized differential equations, eqs (6.9) and (6.13), are considered to reinterpret the non–linear calculations. For the three time scales $T = 0$, 30 and $100\,\mathrm{kyr}$, fig. 6.3 compares the MID–MC and TPW rates. For $T = 0$, the rotational bulge readjusts instantaneously and, thus, the MID–MC and TPW

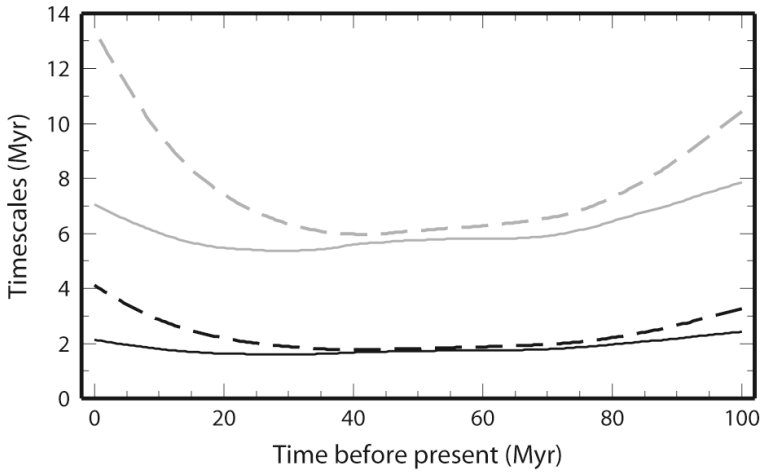

Figure 6.2: Time scales T_1 and T_2 (solid and dashed lines, respectively) controlling the relative motion of the rotation axis with respect to the MID–MC, eq. (6.10), for the time scale $T = 30$ and $100\,\mathrm{kyr}$ (black and gray lines, respectively).

GEOID COEFFICIENTS (m)	C_{21}	S_{21}
Seismic tomography	-1.00	0.53
TPW dynamics ($T = 0$)	0	0
TPW dynamics ($T = 30\,\mathrm{kyr}$)	-1.05	-2.07
TPW dynamics ($T = 100\,\mathrm{kyr}$)	-2.87	-4.19

Table 6.1: Present–day C_{21} and S_{21} geoid coefficients due to mantle convection estimated from seismic tomography (top line, coefficients obtained using the tomographic model Smean of Becker and Boschi (2002) as described in Ricard *et al.*, 1993b) or self–consistently estimated from TPW dynamics driven by the model of subduction, for the three time scales $T = 0,\ 30$ and $100\,\mathrm{kyr}$ (bottom lines).

rates and paths coincide. Particularly, the TPW rate is affected by every short–term fluctuation of Earth's inertia tensor. Instead, for $T = 30$ and $100\,\mathrm{kyr}$, the inhibition of the bulge relaxation filters out in time the short–term fluctuations of Earth's inertia, thus smoothing TPW rates. Furthermore, accordingly to eq. (6.13), variations of TPW rates are delayed with respect to those of MID–MC by a time comparable to the time scales T_i (fig. 6.2). Particularly, this yields a reduction of the present–day TPW rate since the MID–MC rate increases by about $1^\circ\,\mathrm{Myr}^{-1}$ in the past $10\,\mathrm{Myr}$. Compared to the present–day TPW rate of $1.24^\circ\,\mathrm{Myr}^{-1}$ for $T = 0$, the present–day TPW rates of $0.85^\circ\,\mathrm{Myr}^{-1}$ and $0.55^\circ\,\mathrm{Myr}^{-1}$ for $T = 30$ and $100\,\mathrm{kyr}$, respectively, are reduced by 32 and 56 per cent.

Together with the TPW rate decrease, the offset angle between the rotation axis and the MID–MC increases, see fig. 6.4. For $T = 30$ and $100\,\mathrm{kyr}$, they are about $0.8°$ and $2.2°$ in the past $100\,\mathrm{Myr}$ and they increase to $3.4°$ and $7.1°$ at the present–day due to the acceleration of the MID–MC in the past $10\,\mathrm{Myr}$. Differently, the present–day TPW directions are only slightly affected by the readjustment of rotational bulge (fig. 6.1) and they point towards $66.7°\,E$, $61.5°\,E$ and $55.7°\,E$ for $T = 0,\ 30$ and $100\,\mathrm{kyr}$, respectively. Even though the estimated TPW rates are in rough agreement with the observation of $0.925 \pm 0.022°\,\mathrm{Myr}^{-1}$ (McCarthy and Luzum, 1996), these results are in contrast with the observed direction towards Newfoundland ($75.0 \pm 1.1°\,W$). The general motion since the early Tertiary (50 to 60 Myr) of about $4°$–$9°$ toward Greenland is however in agreement with paleomagnetic data (Besse and Courtillot, 2002), althought we do not obtain the period of (quasi) standstill at 10–$50\,\mathrm{Myr}$.

6.4 Conclusion

We have reinterpreted TPW simulations on the basis of the linearization of the Liouville equation provided in eq. (6.9). Discerning between the effects of the delay of the readjustment of the rotational bulge from those of the specific mantle convection models used in TPW simulations, we have pointed out when the former can affect significantly both TPW path and rates. By implementing a previously developed mantle circulation model (Ricard *et al.*, 1993b; Richards *et al.*, 1997), we have shown that the delay of the readjustment of the rotational bulge can shift the TPW and MID–MC paths by several degrees and affects present–day TPW rates by about 50 per cent.

The slow change of the mantle convection inertia tensor remains the main factor explaining the long–term rotational stability of the Earth (Richards *et al.*, 1997). However, as clearly indicated by eqs (6.9) and (6.13), the relaxation of the rotational bulge introduces a further stabilizing effect. Indeed, it filters out every short–term fluctuations of the Earth's inertia tensor and delays variations of TPW rates by the time scales T_i, eq. (6.10), with respect to MID–MC rates. This yields significant differences between TPW and MID–MC rates, particularly during the past $10\,\mathrm{Myr}$ for our mantle convection model.

In addition to slab subduction, we have accounted also for any other contributions to mantle density anomalies that can be assumed to remain constant with time. Further-

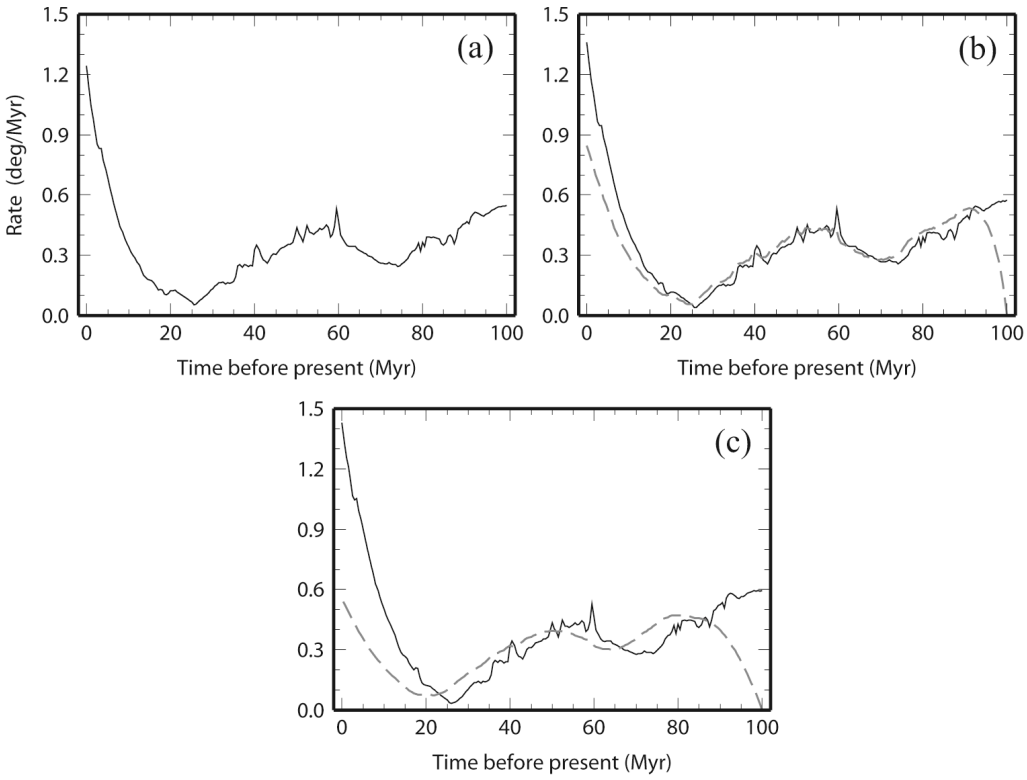

Figure 6.3: MID–MC, $|d\boldsymbol{e}_3/dt|$, and TPW, $|\boldsymbol{v}|$, rates (solid and dashed lines, respectively) for the three time scales $T = 0,\ 30$ and $100\,\mathrm{kyr}$ (panels a, b and c, respectively). The MID–MC and TPW rates coincide for $T = 0$. The TPW rates for $T = 30$ and $100\,\mathrm{kyr}$ are zero at $100\,\mathrm{Myr}$ before present since we have imposed as initial condition that the rotation axis and the MID–MC coincide at that time. The TPW simulations do no longer depend on the initial condition after a time comparable with the time scales T_i (fig. 6.2).

more, the present–day C_{21} and S_{21} geoid coefficients due to mantle density anomalies alone, which cannot be observed since they are compensated by the rotational bulge not yet readjusted to the north pole, have been estimated self–consistently with TPW dynamics. Within our framework, it is possible to check if TPW simulations are in agreement with seismic tomography. By using in eqs (6.16) and (6.19) the C_{21} and S_{21} geoid coefficients obtained from the tomographic model Smean of Becker and Boschi (2002) (see Table 1) which is an average of various recent models, we obtain a present–day TPW direction of $28^\circ\,W$, in rough agreement with the observed direction towards Newfoundland, and a present–day TPW rate of $0.0123^\circ/T$, inversely proportional to the time scale T (the observed TPW rate of $0.925 \pm 0.22^\circ\,\mathrm{Myr}^{-1}$ is explained when $T = 13\,\mathrm{kyr}$).

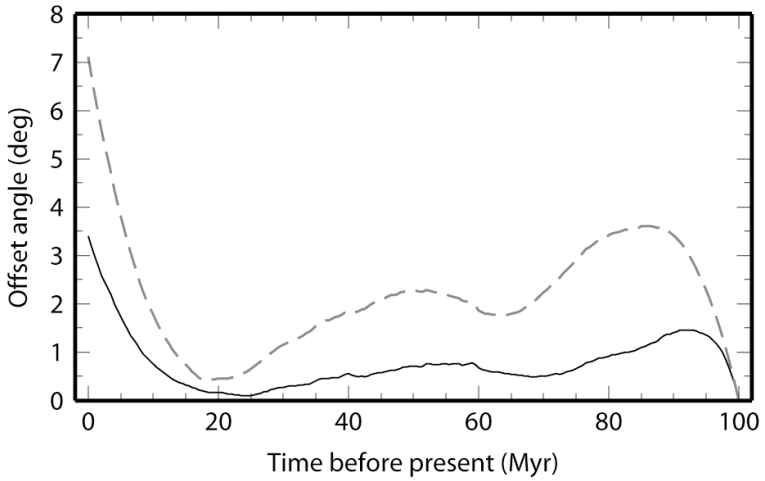

Figure 6.4: Offset angle, $\arccos(\boldsymbol{n} \cdot \boldsymbol{e}_3)$, between the rotation axis and the MID–MC for the time scales $T = 30$ and $100\,\mathrm{kyr}$ (solid and dashed lines, respectively). For $T = 0$ the offset angle is zero at any time since the rotational bulge readjusts instantaneously.

Nevertheless, these estimates concern only the present–day and are not consistent with TPW simulations obtained using the time evolution of mantle convection inferred from global plate motions (Ricard *et al.*, 1993b; Lithgow–Bertelloni, 1993).

The combined use of seismic tomography and reconstructions of global plate motions could greatly improve our understanding of both past and present–day TPW driven by mantle convection. However, these two data sets cannot be used contemporarily to simulate TPW if the delay of the rotational bulge is accounted for. Furthermore, in order to fulfill observations, the contribution to TPW from Pleistocene ice sheet melting must be also considered, being comparable in magnitude with that from mantle convection and pointing towards Newfoundland (Mitrovica *et al.*, 2005; Cambiotti *et al.*, 2010). Because it occurs on a much shorter period than mantle convection, the deglaciation affects the TPW, but its contribution to Earth's inertia tensor remains negligible compared to that of the mantle 3–D structure.

Appendix A

Appendix

A.1 Curilinear orthonormal coordinates

Let us identify the points P of the 3–D space by means of curvilinear orthogonal coordinates (q_1, q_2, q_3) and consider the associated position vector $\boldsymbol{r}$ as function of (q_1, q_2, q_3)

$$\boldsymbol{r} = \boldsymbol{r}(q_1, q_2, q_3) \tag{A.1}$$

At a given point P, we define the unit vectors $\boldsymbol{e}_\alpha$, with $\alpha = 1, 2, 3$, as the unit tangent to the α-th coordinate line passing at P (i.e., the line obtained varying the only α-th coordinate q_α while the remaining coordinates are fixed and those of P) and oriented in the direction of increasing q_α, that is

$$\boldsymbol{e}_\alpha = \frac{1}{h_\alpha} \frac{\partial \boldsymbol{r}}{\partial q_\alpha} \tag{A.2}$$

where h_α are normalizing constants, also called scale factors, which are given by

$$h_\alpha = \sqrt{\frac{\partial \boldsymbol{r}}{\partial q_\alpha} \cdot \frac{\partial \boldsymbol{r}}{\partial q_\alpha}} \tag{A.3}$$

in order that $\boldsymbol{e}_\alpha \cdot \boldsymbol{e}_\alpha = 1$. By definition, if the unit vectors $\boldsymbol{e}_\alpha$ define an orthonormal right-hand base, they also have to satisfy the following conditions

$$\boldsymbol{e}_\alpha \cdot \boldsymbol{e}_\beta = \delta_{\alpha\beta} \tag{A.4}$$

$$\boldsymbol{e}_\alpha \times \boldsymbol{e}_\beta = \sum_\gamma \epsilon_{\gamma\alpha\beta}\, \boldsymbol{e}_\gamma \tag{A.5}$$

with $\delta_{\alpha\beta}$ and $\epsilon_{\gamma\alpha\beta}$ being the Kronecker delta and the Levi-Civita symbol.

The expression for the gradient operator $\boldsymbol{\nabla}$ in curvilinear orthogonal coordinates is obtained by writing the differential df of a scalar function f in two ways

$$df = \sum_\alpha \frac{\partial f}{\partial q_\alpha}\, dq_\alpha \tag{A.6}$$

$$df = \boldsymbol{\nabla} f \cdot d\boldsymbol{r} \tag{A.7}$$

with $d\boldsymbol{r}$ being the differential

$$d\boldsymbol{r} = \sum_{\alpha} \frac{\partial \boldsymbol{r}}{\partial q_\alpha} dq_\alpha = \sum_{\alpha} h_\alpha \, \boldsymbol{e}_\alpha \, dq_\alpha \tag{A.8}$$

Indeed, comparing eqs (A.6)–(A.7) and using eqs (A.4) and (A.8), we obtain that the gradient of a scalar function yields

$$\boldsymbol{\nabla} f = \sum_{\alpha} \boldsymbol{e}_\alpha \frac{1}{h_\alpha} \frac{\partial f}{\partial q_\alpha} \tag{A.9}$$

where the gradient operator $\boldsymbol{\nabla}$ is defined by

$$\boldsymbol{\nabla} = \sum_{\alpha} \boldsymbol{e}_\alpha \frac{1}{h_\alpha} \frac{\partial}{\partial q_\alpha} \tag{A.10}$$

A.1.1 The unit vectors

The unit vectors $\boldsymbol{e}_\alpha$ of curvilinear coordinates can be expressed in terms of the three Cartesian unit vectors $\boldsymbol{x}_1$, $\boldsymbol{x}_2$ and $\boldsymbol{x}_3$, that have fixed orientations in space. Let us consider the position vector $\boldsymbol{r}$ in the Cartesian frame

$$\boldsymbol{r}(q_1, q_2, q_3) = \sum_{j} r_j(q_1, q_2, q_3) \, \boldsymbol{x}_j \tag{A.11}$$

where (r_1, r_2, r_3) are the Cartesian coordinates that we consider as functions of the curviliear coordinates (q_1, q_2, q_3)

$$r_j = r_j(q_1, q_2, q_3) \tag{A.12}$$

Then, by using eq. (A.2) and eqs. (A.11)–(A.12), we obtain the following expression for the unit vectors $\boldsymbol{e}_\alpha$

$$\boldsymbol{e}_\alpha = \frac{1}{h_\alpha} \sum_j \boldsymbol{x}_j \frac{\partial r_j}{\partial q_\alpha} \tag{A.13}$$

with

$$h_\alpha = \sqrt{\sum_j \frac{\partial r_j}{\partial q_\alpha} \frac{\partial r_j}{\partial q_\alpha}} \tag{A.14}$$

In the particular case of spherical coordinates $(q_1, q_2, q_3) = (\theta, \varphi, r)$, eq. (A.12) takes the following form

$$r_1(\theta, \varphi, r) = r \, \sin\theta \, \cos\varphi \tag{A.15}$$

$$r_2(\theta, \varphi, r) = r \, \sin\theta \, \sin\varphi \tag{A.16}$$

$$r_3(\theta, \varphi, r) = r \, \cos\theta \tag{A.17}$$

and, from eqs (A.13)-(A.14), the unit vectors $\boldsymbol{e}_\alpha$ and scale factors h_α yield

$$\boldsymbol{e}_\theta = \cos\theta \, \cos\varphi \, \boldsymbol{x}_1 + \cos\theta \, \sin\varphi \, \boldsymbol{x}_2 - \sin\theta \, \boldsymbol{x}_3 \tag{A.18}$$

$$\boldsymbol{e}_\varphi = -\sin\varphi \, \boldsymbol{x}_1 + \cos\varphi \, \boldsymbol{x}_2 \tag{A.19}$$

$$\boldsymbol{e}_r = \sin\theta \, \cos\varphi \, \boldsymbol{x}_1 + \sin\theta \, \sin\varphi \, \boldsymbol{x}_2 + \cos\theta \, \boldsymbol{x}_3 \tag{A.20}$$

and

$$h_\theta = r \qquad h_\varphi = r \, \sin\theta \qquad h_r = 1 \tag{A.21}$$

From eq. (A.10), the gradient $\boldsymbol{\nabla}$ becomes

$$\nabla = \boldsymbol{e}_r \frac{\partial}{\partial r} + \boldsymbol{e}_\theta \frac{1}{r} \frac{\partial}{\partial \theta} + \boldsymbol{e}_\varphi \frac{1}{r \sin\theta} \frac{\partial}{\partial \varphi} \tag{A.22}$$

A.1.2 Christoffel symbol

Afterwards, we shall evaluate partial derivatives of the unit vectors $\boldsymbol{e}_\alpha$ with respect to the curvilinear coordinates q_β. These are vector quantities and, thus, they can be expressed as a linear combination of the unit vectors $\boldsymbol{e}_\gamma$

$$\frac{\partial \boldsymbol{e}_\alpha}{\partial q_\beta} = \sum_\gamma \Gamma^\gamma_{\alpha\beta} \boldsymbol{e}_\gamma \tag{A.23}$$

Here, $\Gamma^\gamma_{\alpha\beta}$ is the Christoffel symbol of the second kind representing the component of the derivatives $\partial \boldsymbol{e}_\alpha / \partial q_\beta$ along $\boldsymbol{e}_\gamma$

$$\Gamma^\gamma_{\alpha\beta} = \boldsymbol{e}_\gamma \cdot \frac{\partial \boldsymbol{e}_\alpha}{\partial q_\beta} = -\frac{1}{h_\alpha} \frac{\partial h_\alpha}{\partial q_\beta} \delta_{\alpha\gamma} + \frac{1}{h_\gamma h_\alpha} \frac{\partial \boldsymbol{r}}{\partial q_\gamma} \cdot \frac{\partial^2 \boldsymbol{r}}{\partial q_\beta \partial q_\alpha} \tag{A.24}$$

Despite this lengthly expression, the Christoffel symbol satisfies some identities that make simple their use. By differentiating eq. (A.4) with respect to the coordinate q_γ and using eq. (A.23), it can be shown that

$$\Gamma^\beta_{\alpha\gamma} + \Gamma^\alpha_{\beta\gamma} = 0 \tag{A.25}$$

from which the following identities hold

$$\Gamma^\alpha_{\alpha\gamma} = 0 \qquad \Gamma^\alpha_{\alpha\alpha} = 0 \tag{A.26}$$

Furthermore, by making use of eqs (A.24)-(A.25) and (A.27), we can prove that

$$h_\alpha \Gamma^\gamma_{\alpha\beta} = h_\beta \Gamma^\gamma_{\beta\alpha} \qquad \gamma \neq \alpha \neq \beta \tag{A.27}$$

$$\Gamma^{\gamma}_{\alpha\beta} = 0 \qquad \gamma \neq \alpha \neq \beta \tag{A.28}$$

In view of eqs (A.26) and (A.28), the Christoffel symbol $\Gamma^{\gamma}_{\alpha\beta}$ is different from zero only for $\alpha \neq \beta = \gamma$ and $\alpha = \beta \neq \gamma$. Particularly, by using eqs (A.24)-(A.25), it can be shown that

$$\Gamma^{\gamma}_{\alpha\gamma} = \frac{1}{2\,h_\gamma\,h_\alpha}\,\frac{\partial}{\partial q_\alpha}\left(\frac{\partial \boldsymbol{r}}{\partial q_\gamma}\cdot\frac{\partial \boldsymbol{r}}{\partial q_\gamma}\right) = \frac{1}{h_\alpha}\,\frac{\partial h_\gamma}{\partial q_\alpha} \qquad \gamma \neq \alpha \tag{A.29}$$

$$\Gamma^{\alpha}_{\gamma\gamma} = -\Gamma^{\gamma}_{\alpha\gamma} = -\frac{1}{h_\alpha}\,\frac{\partial h_\gamma}{\partial q_\alpha} \qquad \gamma \neq \alpha \tag{A.30}$$

Having defined the components of the partial derivatives of the unit vectors $\boldsymbol{e}_\alpha$ with respect to the coordinates q_β in terms of the Christoffel symbol $\Gamma^{\gamma}_{\alpha\beta}$, eq. (A.23), we can now consider divergence and curl of a vector field $\boldsymbol{a}$ in curvilinear coordinates

$$\boldsymbol{a} = \sum_\alpha a_\alpha\,\boldsymbol{e}_\beta \tag{A.31}$$

They are given by the scalar and cross products, respectively, between the gradient operator $\boldsymbol{\nabla}$ and the vector field $\boldsymbol{a}$

$$\boldsymbol{\nabla}\cdot\boldsymbol{a} = \sum_{\alpha,\beta}\frac{1}{h_\alpha}\,\boldsymbol{e}_\alpha\cdot\frac{\partial(a_\beta\,\boldsymbol{e}_\beta)}{\partial q^\alpha} = \sum_\alpha\frac{1}{h_\alpha}\left(\frac{\partial a_\alpha}{\partial q_\alpha} + \sum_\beta a_\beta\,\Gamma^{\alpha}_{\beta\alpha}\right) =$$

$$= \sum_\alpha\frac{1}{h_\alpha}\left(\frac{\partial a_\alpha}{\partial q_\alpha} + \sum_{\beta\neq\alpha}\frac{a_\beta}{h_\alpha}\,\frac{\partial h_\beta}{\partial q_\alpha}\right) \tag{A.32}$$

$$\boldsymbol{\nabla}\times\boldsymbol{a} = \sum_{\alpha,\beta}\frac{1}{h_\alpha}\,\boldsymbol{e}_\alpha\times\frac{\partial(a_\beta\,\boldsymbol{e}_\beta)}{\partial q^\alpha} = \sum_{\alpha,\beta}\frac{1}{h_\alpha}\,\left(\frac{\partial a_\beta}{\partial q^\alpha} + \sum_\gamma a_\gamma\,\Gamma^{\beta}_{\gamma\alpha}\right)\,\boldsymbol{e}_\alpha\times\boldsymbol{e}_\beta =$$

$$= \sum_{\alpha,\beta} \frac{1}{h_\alpha} \left(\frac{\partial a_\beta}{\partial q^\alpha} - \frac{a_\alpha}{h_\beta} \frac{\partial h_\alpha}{\partial q_\beta} \right) \boldsymbol{e}_\alpha \times \boldsymbol{e}_\beta \tag{A.33}$$

The Laplacian operator ∇^2, which is defined as the scalar product of the gradient operator $\boldsymbol{\nabla}$ by itself, yields

$$\nabla^2 = \boldsymbol{\nabla} \cdot \boldsymbol{\nabla} = \sum_{\alpha,\,\beta} \frac{1}{h_\alpha} \boldsymbol{e}_\alpha \cdot \frac{\partial}{\partial q_\alpha} \left(\frac{1}{h_\beta} \boldsymbol{e}_\beta \frac{\partial}{\partial q_\beta} \right) =$$

$$= \sum_{\alpha} \left[\frac{1}{h_\alpha} \frac{\partial}{\partial q_\alpha} \left(\frac{1}{h_\alpha} \frac{\partial}{\partial q_\alpha} \right) + \sum_{\beta \neq \alpha} \frac{1}{h_\beta^2} \frac{\partial h_\alpha}{\partial q_\beta} \frac{\partial}{\partial q_\beta} \right] \tag{A.34}$$

and, in spherical coordinates, it reads

$$\nabla^2 = \frac{\partial^2}{\partial r^2} + \frac{2}{r} \frac{\partial}{\partial r} + \frac{1}{r^2} \left(\frac{\partial^2}{\partial \theta^2} + \cot\theta \frac{\partial}{\partial \theta} + \frac{1}{\sin^2\theta} \frac{\partial^2}{\partial \varphi^2} \right) \tag{A.35}$$

A.2 Dyadics

Tensor fields as the material incremental stress, $\boldsymbol{\sigma}^\delta$, and strain, $\boldsymbol{\epsilon}$, tensors can be dealt with in general coordinate systems by means of the dyadic formulation. The general expression for a dyadic $\mathcal{B}$ is given in terms of the unit vectors $\boldsymbol{e}_\alpha$

$$\mathcal{B} = \sum_{\alpha,\,\beta} B_{\alpha\beta} \, \boldsymbol{e}_\alpha \otimes \boldsymbol{e}_\beta \tag{A.36}$$

where $\otimes$ stands for the algebraic product. Each of its element $B_{\alpha\beta} \, \boldsymbol{e}_\alpha \otimes \boldsymbol{e}_\beta$ is known as a dyad, and $B_{\alpha\beta}$ are the components of the dyadic. We may write $B_{\alpha\beta} \, \boldsymbol{e}_\alpha \otimes \boldsymbol{e}_\beta = \boldsymbol{e}_\alpha \otimes \boldsymbol{e}_\beta \, B_{\alpha\beta}$, but the order of the vectors cannot be changed. If we reverse the order of the vectors in each dyads of a dyadic, we get transpose of the dyadic

$$\mathcal{B}^T = \sum_{\alpha,\,\beta} B_{\alpha\beta} \, \boldsymbol{e}_\beta \otimes \boldsymbol{e}_\alpha = \sum_{\alpha,\,\beta} B_{\beta\alpha} \, \boldsymbol{e}_\alpha \otimes \boldsymbol{e}_\beta \tag{A.37}$$

denoted with the subscript T.

The most general dyad is the juxtaposition of any two vector $\boldsymbol{a}$ and $\boldsymbol{b}$ and it is written as $\boldsymbol{a} \otimes \boldsymbol{b}$. It is defined as a particular case of eq. (A.36)

$$\boldsymbol{a} \otimes \boldsymbol{b} = \sum_{\alpha,\,\beta} a_\alpha \, b_\beta \, \boldsymbol{e}_\alpha \otimes \boldsymbol{e}_\beta \tag{A.38}$$

and it is known as the algebaric product between $\boldsymbol{a}$ and $\boldsymbol{b}$, in contradistinction to the scalar, $\boldsymbol{a} \cdot \boldsymbol{b}$, and cross, $\boldsymbol{a} \times \boldsymbol{b}$, products. It can be shown that any dyadic $\boldsymbol{\mathcal{B}}$ can be reduced to the sum of three dyads

$$\boldsymbol{\mathcal{B}} = \boldsymbol{a} \otimes \boldsymbol{u} + \boldsymbol{b} \otimes \mathbf{v} + \boldsymbol{c} \otimes \mathbf{w} \tag{A.39}$$

where $(\boldsymbol{a}, \boldsymbol{b}, \boldsymbol{c})$ or $(\boldsymbol{u}, \mathbf{v}, \mathbf{w})$, but not both, are arbitarily chosen non-coplanar vectors (as the unit vectors $\boldsymbol{e}_\alpha$ which compose an orthonormal right-hand base).

The left and right, scalar and cross products between dyadics $\boldsymbol{\mathcal{B}}$ and vectors $\boldsymbol{c}$ are defined by those between dyads $\boldsymbol{a} \otimes \boldsymbol{b}$ and vectors $\boldsymbol{c}$

$$\boldsymbol{c} \cdot \boldsymbol{a} \otimes \boldsymbol{b} = \boldsymbol{b} \, (\boldsymbol{c} \cdot \boldsymbol{a}) \qquad\qquad \boldsymbol{a} \otimes \boldsymbol{b} \cdot \boldsymbol{c} = \boldsymbol{a} \, (\boldsymbol{b} \cdot \boldsymbol{c}) \tag{A.40}$$

$$\boldsymbol{c} \times \boldsymbol{a} \otimes \boldsymbol{b} = \boldsymbol{b} \, (\boldsymbol{a} \times \boldsymbol{c}) \qquad\qquad \boldsymbol{a} \otimes \boldsymbol{b} \times \boldsymbol{c} = \boldsymbol{a} \, (\boldsymbol{b} \times \boldsymbol{c}) \tag{A.41}$$

Note that the left scalar and cross products between a vector and a dyadic yield the right scalar and cross products between the vector and the transpose of the dyadic, respectively

$$\boldsymbol{a} \cdot \boldsymbol{\mathcal{B}} = \boldsymbol{\mathcal{B}}^T \cdot \boldsymbol{a} \tag{A.42}$$

$$\boldsymbol{a} \times \boldsymbol{\mathcal{B}} = \boldsymbol{\mathcal{B}}^T \times \boldsymbol{a} \tag{A.43}$$

The divergence of a dyadic is obtained by considering the scalar product between the gradient operator and the dyadic. It yields the following vector

$$\boldsymbol{\nabla}\cdot\boldsymbol{\mathcal{B}}=\sum_{\gamma,\alpha,\beta}\frac{1}{h_\gamma}\,\boldsymbol{e}_\gamma\cdot\frac{\partial\left(B_{\alpha\beta}\,\boldsymbol{e}_\alpha\boldsymbol{e}_\beta\right)}{\partial q_\gamma}=$$

$$=\sum_{\alpha,\beta}\left[\frac{1}{h_\alpha}\,\frac{\partial B_{\alpha\beta}}{\partial q_\alpha}+\sum_{\gamma}\frac{1}{h_\gamma}\,\left(B_{\alpha\beta}\,\Gamma^{\gamma}_{\alpha\gamma}+B_{\gamma\alpha}\,\Gamma^{\beta}_{\alpha\gamma}\right)\right]\boldsymbol{e}_\beta=$$

$$=\sum_{\beta}\left\{\sum_{\alpha}\frac{1}{h_\alpha}\,\frac{\partial B_{\alpha\beta}}{\partial q_\alpha}+\sum_{\alpha\neq\beta}\frac{1}{h_\alpha\,h_\beta}\left(\frac{\partial h_\beta}{\partial q_\alpha}\,B_{\beta\alpha}-\frac{\partial h_\alpha}{\partial q_\beta}\,B_{\alpha\alpha}\right)\right.$$

$$\left.+\sum_{\alpha}\sum_{\gamma\neq\alpha}\frac{B_{\alpha\beta}}{h_\gamma\,h_\alpha}\,\frac{\partial h_\gamma}{\partial q_\alpha}\right\}\boldsymbol{e}_\beta \tag{A.44}$$

We can also consider the gradient of a vector. It is defined as the algebraic product between the gradient operator and the vector, and it yields the following dyadic

$$\boldsymbol{\nabla}\otimes\boldsymbol{a}=\sum_{\alpha,\,\beta}\boldsymbol{e}_\alpha\otimes\left[\frac{1}{h_\alpha}\,\frac{\partial\left(a_\beta\,\boldsymbol{e}_\beta\right)}{\partial q_\alpha}\right]=\sum_{\alpha,\,\beta}\frac{1}{h_\alpha}\,\left(\frac{\partial a_\beta}{\partial q_\alpha}+\sum_{\gamma}a_\gamma\,\Gamma^{\beta}_{\gamma\alpha}\right)\boldsymbol{e}_\alpha\otimes\boldsymbol{e}_\beta=$$

$$=\sum_{\alpha}\frac{1}{h_\alpha}\,\left[\left(\frac{\partial a_\alpha}{\partial q_\alpha}+\sum_{\gamma\neq\alpha}\frac{a_\gamma}{h_\gamma}\,\frac{\partial h_\alpha}{\partial q_\gamma}\right)\,\boldsymbol{e}_\alpha\otimes\boldsymbol{e}_\alpha+\sum_{\beta\neq\alpha}\left(\frac{\partial u_\beta}{\partial q_\alpha}-\frac{a_\alpha}{h_\beta}\,\frac{\partial h_\alpha}{\partial q_\beta}\right)\,\boldsymbol{e}_\alpha\otimes\boldsymbol{e}_\beta\right] \tag{A.45}$$

It can be easily shown that the following identities hold

$$\boldsymbol{b}\cdot(\boldsymbol{\nabla}\otimes\boldsymbol{a})=(\boldsymbol{b}\cdot\boldsymbol{\nabla})\,\boldsymbol{a} \tag{A.46}$$

$$\boldsymbol{\nabla}\otimes(\boldsymbol{a}\cdot\boldsymbol{b})=(\boldsymbol{\nabla}\otimes\boldsymbol{a})\cdot\boldsymbol{b}+(\boldsymbol{\nabla}\otimes\boldsymbol{b})\cdot\boldsymbol{a} \tag{A.47}$$

$$\boldsymbol{\nabla}\cdot(\boldsymbol{\nabla}\boldsymbol{a})=\nabla^2\boldsymbol{a} \tag{A.48}$$

$$\boldsymbol{\nabla} \cdot (\boldsymbol{\nabla} \otimes \boldsymbol{a})^T = \boldsymbol{\nabla} \otimes (\boldsymbol{\nabla} \cdot \boldsymbol{a}) \tag{A.49}$$

A.2.1 Stress and strain in spherical coordinates

The above results, after substitution of the scale factors h_α for spherical coordinates given by eq. (A.21), allow us to obtain the expression for the divergence of the material incremental stress tensor $\boldsymbol{\sigma}^\delta$ entering the momentum equation (1.46)

$$\begin{aligned}
\boldsymbol{\nabla} \cdot \boldsymbol{\sigma}^\delta = & \left[\partial_r \sigma^\delta_{rr} + \frac{1}{r}\left(\partial_\theta \sigma^\delta_{\theta r} + \frac{1}{\sin\theta}\,\partial_\varphi \sigma^\delta_{\varphi r} + 2\,\sigma^\delta_{rr} - \sigma^\delta_{\theta\theta} - \sigma^\delta_{\varphi\varphi} + \sigma^\delta_{\theta r}\,\cot\theta\right)\right]\boldsymbol{e}_r \\
& + \left[\partial_r \sigma^\delta_{r\theta} + \frac{1}{r}\left(\partial_\theta \sigma^\delta_{\theta\theta} + \frac{1}{\sin\theta}\,\partial_\varphi \sigma^\delta_{\varphi\theta} + 3\,\sigma^\delta_{r\theta} + \left(\sigma^\delta_{\theta\theta} - \sigma^\delta_{\varphi\varphi}\right)\cot\theta\right)\right]\boldsymbol{e}_\varphi \\
& + \left[\partial_r \sigma^\delta_{r\varphi} + \frac{1}{r}\left(\partial_\theta \sigma^\delta_{\theta\varphi} + \frac{1}{\sin\theta}\,\partial_\varphi \sigma^\delta_{\varphi\varphi} + 3\,\sigma^\delta_{r\varphi} + 2\,\sigma^\delta_{\theta\varphi}\,\cot\theta\right)\right]\boldsymbol{e}_\varphi
\end{aligned} \tag{A.50}$$

where we have utilized that fact the stress tensor is symmetric, i.e., $\sigma^\delta_{\alpha\beta} = \sigma^\delta_{\beta\alpha}$.

Furthermore, by making use of eqs (A.37) and (A.45), the strain tensor $\boldsymbol{\epsilon}$ defined in eq. (1.24) reads

$$\begin{aligned}
\boldsymbol{\epsilon} = \frac{1}{2}\left[\boldsymbol{\nabla}\,\boldsymbol{u} + (\boldsymbol{u}\,\boldsymbol{\nabla})^T\right] = & \sum_\alpha \frac{1}{h_\alpha}\left(\frac{\partial u_\alpha}{\partial q_\alpha} + \sum_{\gamma\neq\alpha}\frac{u_\gamma}{h_\gamma}\frac{\partial h_\alpha}{\partial q_\gamma}\right)\boldsymbol{e}_\alpha\,\boldsymbol{e}_\alpha \\
& + \sum_\alpha \sum_{\beta\neq\alpha} \frac{1}{2}\left(\frac{h_\beta}{h_\alpha}\frac{\partial\left(u_\beta/h_\beta\right)}{\partial q_\alpha} + \frac{h_\alpha}{h_\beta}\frac{\partial\left(u_\alpha/h_\alpha\right)}{\partial q_\beta}\right)\boldsymbol{e}_\alpha\,\boldsymbol{e}_\beta
\end{aligned} \tag{A.51}$$

where u_α are the component of the displacement $\boldsymbol{u}$

$$\boldsymbol{u} = \sum_{\alpha} u_{\alpha}\, \boldsymbol{e}_{\alpha} \tag{A.52}$$

By considering the trace of the strain tensor $\boldsymbol{\epsilon}$, i.e., the sum of its diagonal components $\epsilon_{\alpha\alpha}$

$$\mathrm{Tr}\left[\boldsymbol{\epsilon}\right] = \sum_{\alpha} \epsilon_{\alpha\alpha} = \sum_{\alpha} \frac{1}{h_{\alpha}} \left(\frac{\partial u_{\alpha}}{\partial q_{\alpha}} + \sum_{\gamma \neq \alpha} \frac{u_{\gamma}}{h_{\gamma}} \frac{\partial h_{\alpha}}{\partial q_{\gamma}} \right) \tag{A.53}$$

we note that it coincides with the divergence of the displacement $\boldsymbol{\nabla} \cdot \boldsymbol{u}$, that corresponds to the volume change Δ defined in eq. (1.22) and that one can also obtain by means of eq. (A.32). Thus, we have that the trace of the strain tensor coincides with the volume change

$$\Delta = \boldsymbol{\nabla} \cdot \boldsymbol{u} = \mathrm{Tr}\left[\boldsymbol{\epsilon}\right] \tag{A.54}$$

After substitution of eq. (A.21) into eqs (A.51)-(A.53), we obtain the components $\epsilon_{\alpha\beta}$ of the strain tensor $\boldsymbol{\epsilon}$ and the volume change Δ in spherical coordinates

$$\epsilon_{rr} = \frac{\partial u_r}{\partial r} \tag{A.55}$$

$$\epsilon_{\theta\theta} = \frac{1}{r} \left[\frac{\partial u_{\theta}}{\partial \theta} + u_r \right] \tag{A.56}$$

$$\epsilon_{\varphi\varphi} = \frac{1}{r} \left[\frac{1}{\sin\theta} \frac{\partial u_{\varphi}}{\partial \varphi} + u_r + u_{\theta}\, \cot\theta \right] \tag{A.57}$$

$$\epsilon_{r\theta} = \frac{1}{2} \left[\frac{\partial u_{\theta}}{\partial r} + \frac{1}{r} \left(\frac{\partial u_r}{\partial \theta} - u_{\theta} \right) \right] \tag{A.58}$$

$$\epsilon_{r\varphi} = \frac{1}{2} \left[\frac{\partial u_{\varphi}}{\partial r} + \frac{1}{r} \left(\frac{1}{\sin\theta} \frac{\partial u_r}{\partial \varphi} - u_{\varphi} \right) \right] \tag{A.59}$$

$$\epsilon_{\theta\varphi} = \frac{1}{2\,r}\,\left[\left(\frac{\partial u_\varphi}{\partial\theta} - u_\varphi\,\cot\theta\right) + \frac{1}{\sin\theta}\,\frac{\partial u_\theta}{\partial\varphi}\right] \tag{A.60}$$

and

$$\Delta = \frac{\partial u_r}{\partial r} + \frac{1}{r}\,\left[\frac{\partial u_\theta}{\partial\theta} + \frac{1}{\sin\theta}\,\frac{\partial u_\varphi}{\partial\varphi} + 2\,u_r + u_\theta\,\cot\theta\right] \tag{A.61}$$

A.3 Gravitating self-compressed compressible sphere

Here we derive the analytical solution of the momentum equation for the gravitating self-compressed compressible sphere, that we discuss in Chapter 2, section 2.4. After expansion in spherical harmonics and Laplace transform, the radial and tangential components of the momentum equation within the mantle of the gravitating self-compressed compressible sphere can be cast as follows,

$$\frac{\beta}{\alpha}\,r\,\partial_r\chi_{\ell m} - g\,\partial_r U_{\ell m} + g\,\chi_{\ell m} + \frac{\mu}{\alpha}\,\ell(\ell+1)\,H_{\ell m} = 0 \tag{A.62}$$

$$\frac{\beta}{\alpha}\,r\,\chi_{\ell m} - g\,U_{\ell m} + \frac{\mu}{\alpha}\,r\,\partial_r(r\,H_{\ell m}) = 0 \tag{A.63}$$

We consider the representations

$$U_{\ell m} = \sum_{j=1}^{4} C_j\,U_j \tag{A.64}$$

$$V_{\ell m} = \sum_{j=1}^{4} C_j\,V_j \tag{A.65}$$

where U_j and V_j are four independent solutions of eqs (A.62)-(A.63) that we assume of the following form

$$U_j = r^{x_j} \tag{A.66}$$

$$V_j = v_j\, r^{x_j} \tag{A.67}$$

Here, v_j and x_j are scalars to be determined in the following and C_j are constants of integration. We then subtract the radial derivative of eq. (A.62) and eq. (A.63)

$$\frac{\beta}{\alpha}\,\partial_r \chi_{\ell m} + g\,\chi_{\ell m} + \frac{\mu}{\alpha}\,\left[\ell(\ell+1)\,H_{\ell m} - \partial_r(r\,H_{\ell m}) - r\,\partial_r^2(r\,H_{\ell m})\right] = 0 \tag{A.68}$$

By substituting eqs (A.64)-(A.67) into eq. (A.68), after some straightforward algebra, we achieve

$$v_j = \frac{x_j - X_j + (x_j+2)\,\zeta}{\ell(\ell+1)(\zeta+1) - x_j\,X_j} \tag{A.69}$$

where

$$X_j = x_j(x_j+1) - \ell(\ell+1) \tag{A.70}$$

$$\zeta = \frac{\beta - \kappa_0}{\mu} \tag{A.71}$$

and κ_0 is the compressional bulk modulus, eq. (2.4). Eq. (A.63) can be arranged in form of a second-order polynomial in X

$$a_0 + a_1\,X_j + a_2\,X_j^2 = 0 \tag{A.72}$$

with

$$a_0 = -\ell(\ell+1)\,\left[1 + \zeta\,\left(4\,\frac{\mu}{\kappa_0} - 1\right)\right] \tag{A.73}$$

$$a_1 = -2\,\frac{\zeta\,\mu}{\kappa} \tag{A.74}$$

$$a_2 = 1 + \frac{\zeta\,\mu}{\kappa} \tag{A.75}$$

Denoting the two roots of eq. (A.72) by X_1 or X_3 and X_2 or X_4,

$$X_1 = X_3 = \frac{-a_1 + \sqrt{a_1^2 - 4\,a_0\,a_2}}{2} \tag{A.76}$$

$$X_2 = X_4 = \frac{-a_1 - \sqrt{a_1^2 - 4\,a_0\,a_2}}{2} \tag{A.77}$$

and from the definition of X_j, eq. (A.70), we obtain four distinct expressions for x_j

$$x_j = -\frac{1}{2} - \frac{1}{2}\sqrt{1 + 4\,\ell(\ell+1)\,X_j} \tag{A.78}$$

$$x_{j+2} = -\frac{1}{2} + \frac{1}{2}\sqrt{1 + 4\,\ell(\ell+1)\,X_{j+2}} \tag{A.79}$$

with $j = 1, 2$. In this way, we have obtained the analytical expressions for both scalars, v_j and x_j, which enter the expressions for the four independent solutions of the radial and tangential momentum equations, eqs (A.66)-(A.67).

In order to solve the surface loading problem, we define the spheroidal 4-vector solution $\boldsymbol{y}$ in the Laplace domain

$$\boldsymbol{y} = \begin{pmatrix} U_{\ell m} \\ V_{\ell m} \\ R_{\ell m} \\ V_{\ell m} \end{pmatrix} \tag{A.80}$$

After substitution of eqs (A.64)-(A.65) into eq. (A.80), we thus obtain the analytical expression for the spheroidal vector solution $\boldsymbol{y}$

$$\boldsymbol{y}(r,s) = \tilde{\mathbf{Y}}(r,s)\,\mathbf{C} \tag{A.81}$$

where $\mathbf{Y}$ is the fundamental matrix and $\mathbf{C}$ is the 4-vector consisting of the four constants of integration

$$\tilde{\mathbf{Y}}(r,s) = (\boldsymbol{y}_1,\, \boldsymbol{y}_2,\, \boldsymbol{y}_3,\, \boldsymbol{y}_4) \tag{A.82}$$

$$\mathbf{C} = (C_1,\, C_2,\, C_3,\, C_4)^T \tag{A.83}$$

with T standing for the transpose. Here, $\tilde{\boldsymbol{y}}_j$ are the four independent spheroidal vector solutions that we obtain by substituting U_j and V_j, eqs (A.66)–(A.67), for U and V into eq. (A.80).

The four constants of integration $\mathbf{C}$ must be determined imposing boundary conditions at the CMB ($r = r_C$) and at the Earth surface ($r = a$). The boundary conditions at the CMB for the simple gravitating problem are given by

$$\tilde{\boldsymbol{y}}(r_C, s) = \mathbf{I}_C\, \mathbf{D} \tag{A.84}$$

where $\mathbf{I}_C$ is the following 4×2–matrix describing isostatic compensation (first column) and free-slip (second column)

$$\mathbf{I}_C = \begin{pmatrix} 1 & 0 \\ 0 & 1 \\ \rho\, g & 0 \\ 0 & 0 \end{pmatrix} \tag{A.85}$$

and $\mathbf{D}$ are two constants of integration

$$\mathbf{D} = (D_1,\, D_2)^T \tag{A.86}$$

The boundary conditions for loading at the Earth surface take the following form

$$\mathbf{P}_1 \boldsymbol{y}(a,s) = \boldsymbol{b} = \begin{pmatrix} -\frac{(2\,\ell+1)\,g}{4\,\pi\,a^2} \\ 0 \end{pmatrix} \tag{A.87}$$

where $\mathbf{P}_1$ is the projector for the third and forth components. By eliminating the constants of integration $\mathbf{C}$ from eq. (A.81) by making use of the above boundary conditions, eqs (A.84) and (A.87), we thus obtain the analytical solution of the viscoelastic Love numbers $\tilde{\mathbf{k}}$ in the Laplace domain

$$\tilde{\mathbf{k}}(r,s) = \begin{pmatrix} \tilde{h}(r,s) \\ \tilde{l}(r,s) \end{pmatrix} = \frac{G}{a\,g} \frac{[\mathbf{P}_2\,\mathbf{\Pi}(r,r_C,s)]\;[\mathbf{P}_1\,\mathbf{\Pi}(a,r_C,s)]^{\dagger}}{\Delta(s)}\,\boldsymbol{b} \tag{A.88}$$

where † stands for the matrix of the minors, $\tilde{h}$ and $\tilde{l}$ are the radial and tangential Love numbers, and Δ is the secular determinant

$$\Delta(s) = \det\left[\mathbf{P}_1\mathbf{\Pi}(a,r_C,s)\right] \tag{A.89}$$

with

$$\mathbf{\Pi}(r,r_C,s) = \mathbf{Y}(r,s)\,\mathbf{Y}(r_C,s)^{-1}\,\mathbf{I}_C \tag{A.90}$$

A.3.1 Analytical approximations

By definition, the poles s_{C_m} of the compositional modes are roots of the secular determinant

$$\Delta\left(s_{C_m}\right) = 0 \tag{A.91}$$

and, from the residue theorem, the residues $\mathbf{k}_{C_m}$ are given by

$$\mathbf{k}_{C_m} = \begin{pmatrix} \tilde{h}_{C_m} \\ \tilde{l}_{C_m} \end{pmatrix} = \lim_{s\to s_{C_m}} (s - s_{C_m})\,\tilde{\mathbf{k}}(r,s) =$$

$$= \left. \frac{[\mathbf{P}_2\,\mathbf{\Pi}(r,b,s)]\;[\mathbf{P}_1\,\mathbf{\Pi}(a,b,s)]^\dagger}{\partial_s \Delta(s)} \right|_{s=s_{C_m}} \boldsymbol{b} \tag{A.92}$$

As discussed in the main text, the origin of the Laplace domain $s = 0$ is the cluster point of the compositional modes. To investigate the behaviour of the independent solutions, eqs (A.66)-(A.67), we consider the Taylor series of the exponents x_j at the origin of the Laplace domain. We define the non-dimensional variable $\delta(s)$ as follow

$$\hat{\mu}(s) = -\ell(\ell+1)\,\epsilon\,\kappa_0\,\delta^4(s) \tag{A.93}$$

With respect to the variable $\delta(s)$, which goes to zero for $s \to 0$, the Taylor series take the following forms

$$x_1 = -i\,\delta^{-1} - \frac{1}{2} + i\,F\,\delta + O\left(\delta^3\right) \tag{A.94}$$

$$x_2 = -\delta^{-1} - \frac{1}{2} - F\,\delta + O\left(\delta^3\right) \tag{A.95}$$

$$x_3 = i\,\delta^{-1} - \frac{1}{2} - i\,F\,\delta + O\left(\delta^3\right) \tag{A.96}$$

$$x_4 = \delta^{-1} - \frac{1}{2} + F\,\delta + O\left(\delta^3\right) \tag{A.97}$$

with

$$F = \frac{4\,\ell(\ell+1)+5}{8} - \frac{\kappa_0}{2\,\kappa} \tag{A.98}$$

Note that the leading terms of the above Taylor expansions diverge in the limit for $\delta \to 0$. Particularly, x_1 and x_3 go to $-i\,\infty$ and $i\,\infty$, respectively, and they are responsible for the oscillating pattern of the perturbations through the mantle shown in fig. 2.7. Instead, x_2 and x_4 goes to $-\infty$ and ∞, respectively.

We then determine the analytical approximations for the poles s_{C_m} by expanding the secular equation (A.91) in Taylor series with respect to δ and neglecting vanishing terms

like

$$\lim_{\delta\to 0}\left(\frac{r_C}{a}\right)^{\delta^{-1}} = 0 \tag{A.99}$$

for $r > r_C$. After much straightforward algebra, we thus obtain

$$s_{C_m} = -\ell(\ell+1)\,\frac{\epsilon\,\kappa_0}{\nu}\,\left(\frac{\log\left(\frac{b}{a}\right)}{\pi\,m}\right)^4$$
$$\left\{1 - \frac{2\,\log\left(\frac{b}{a}\right)\left[\left(\ell(\ell+1)+\epsilon+\frac{1}{4}\right)\,\log\left(\frac{b}{a}\right)-3\,\epsilon\right]}{(\pi\,m)^2}\right\} + O\left(m^{-5}\right) \tag{A.100}$$

Similarly, from eq. (A.92), we obtain the analytical approximations for the radial, h_{C_m}/s_{C_m}, and tangential, l_{C_m}/s_{C_m}, strengths

$$\frac{h_{C_m}}{s_{C_m}} = (2\,\ell+1)\,\sqrt{\frac{a}{r}}\left(-\frac{\sin\theta_m}{\pi\,m} + \frac{\epsilon\left(3\,\log\left(\frac{b}{r}\right)-2\,\log\left(\frac{b}{a}\right)\right)\,\cos\theta_m+\log\left(\frac{b}{a}\right)(\cos\theta_m-\sin\theta_m)}{2\,(\pi\,m)^2}\right.$$
$$\left.-\frac{e^{-\theta_m}\,\log\left(\frac{b}{a}\right)+(-1)^m\,e^{-\alpha_m}\,(1-3\,\epsilon)\,\log\left(\frac{b}{a}\right)}{2\,(\pi\,m)^2}\right) + O\left(m^{-3}\right) \tag{A.101}$$

$$\frac{l_{C_m}}{s_{C_m}} = \frac{2\,\ell+1}{\ell(\ell+1)}\,\sqrt{\frac{a}{r}}\left(-\frac{\cos\theta_m}{\log\left(\frac{b}{a}\right)} - \frac{\log\left(\frac{b}{a}\right)(\cos\theta_m+2\,\sin\theta_m)+3\,\epsilon\,\log\left(\frac{b}{r}\right)\,\sin\theta_m}{2\,\log\left(\frac{b}{a}\right)\pi\,m}\right.$$
$$\left.+\frac{e^{-\theta_m}+(-1)^m\,e^{-\alpha_m}\,(1-3\,\epsilon)}{2\,\pi\,m}\right) + O\left(m^{-2}\right) \tag{A.102}$$

where θ_m and α_m also depend on the radial distance from the Earth centre r

$$\theta_m = \pi\,m\,\frac{\log\left(\frac{r}{a}\right)}{\log\left(\frac{b}{a}\right)} \tag{A.103}$$

$$\alpha_m = \pi\, m\, \frac{\log\left(\frac{b}{r}\right)}{\log\left(\frac{b}{a}\right)} \tag{A.104}$$

A.4 The special case of the harmonic degree one

Here we derive the boundary conditions to deal with the global ocean layer of PREM, that we discuss in Chapter 3, section 3.2.2, in the special case of seismic perturbations of harmonic degree $\ell = 1$. As it concerns the top of the ocean, in addition to eqs (3.50)-(3.51), we must also impose the conservation of the center of mass that, following Farrell [1972], pp. 774-777, results in

$$\Phi_{1m}(b) = \Phi^{(1)}_{1m}(b) + \Phi^{(2)}_{1m}(b) = 0 \tag{A.105}$$

Then, from eqs (3.55)-(3.56) evaluated at the top of the ocean, $r = b$, we obtain

$$B_2 = -B_1 \tag{A.106}$$

and

$$\Phi^{(1)}_{1m} = B_1\, r^{-2} \qquad \Phi^{(2)}_{1m} = -B_1\, r^{-2} \tag{A.107}$$

$$q^{(1)}_{1m} = 0 \qquad q^{(2)}_{1m} = 0 \tag{A.108}$$

The absence of potential stresses within the ocean, eq. (A.108), together with the consistency relation proposed by Farrell (1972), pg. 775, allows us to impose the following boundary condition at the interface between solid Earth and ocean

$$\mathbf{P}_2 \left[\mathbf{\Pi}(a, r_C)\, \mathbf{I}_C, -\mathbf{I}_O^{(\ell=1)}\right] [\mathbf{C}_4, \mathbf{O}_3] = \mathbf{P}_2\, \boldsymbol{b}(a) \tag{A.109}$$

where $\mathbf{O}_3$ and $\mathbf{I}_O^{(\ell=1)}$ are the $3-$vector of constants and the $8 \times 3-$matrix

$$\mathbf{O}_3 = (B_1,\, B_3,\, B_4)^T \tag{A.110}$$

$$\mathbf{I}_O^{(\ell=1)} = \begin{pmatrix} 0 & 0 & 1 \\ 0 & 1 & 0 \\ 0 & 0 & \rho_w\, g(a) \\ 0 & 0 & 0 \\ a^{-2} & 0 & 0 \\ 0 & 0 & 0 \\ -a^{-2} & 0 & 0 \\ 0 & 0 & C\,\rho_w \end{pmatrix} \tag{A.111}$$

while $\mathbf{P}_2$ is the projector for all the components, except for the $4-$th component, which refers to the tangential stress. Indeed, the consistency relation of Farrell (1972) assures us that, once the boundary conditions for the other components are satisfied, the tangential stress is null at the interface between solid Earth and ocean

Acknowledgments

My principal debt is to Roberto Sabadini whose enthusiasm pushed me forward. Special thanks go to Yanick Ricard, Dave Yuen, Carolina Lithgow-Bertelloni and Volker Klemann who blessed my work with their attention. Last but not least I owe much to Detlef Wolf, Anna Maria Marotta, Bruno Crippa, Mauro Giudici, Riccardo Barzaghi, Mirko Reguzzoni, Valentina Roberta Barletta, Andrea Bordoni, Giorgio Dallavia, Manuel Roda, Raffaele Splendore, Lorenzo Colli, Filippo Satolini, Alessandra Casati and Wu Zedong which have been a constant reference and a source of inspiration.

I also thank for the support given to me by the Italian Space Agency (ASI), the COST Action ES0701 “Improved constraints on models of Glacial Isostatic Adjustment”, the University of Lyon 1, the University of California Santa Cruz, the German Research Centre for Geosciences, the University College London, and the European General Assembly.

Bibliography

[1] Alessandrini, B., 1989. The hydrostatic equilibrium figure of the Earth – an interative approach, *Phys. Earth Planet. Inter.*, **54**, 180–192.

[2] Ammon, C. J. *et al.*, 2005. Rupture process of the 2004 Sumatra–Andaman earthquake, *Science*, **308**, 1133–1139.

[3] Ammon, C. J., T. Lay, H. Kanamori, and M. Cleveland, 2011. A rupture model of the great 2011 Tohoku earthquake, *Earth Planets Space*, **63**, 693–696.

[4] Barletta, V. R., Bordoni, A., Aoudia, A. and Sabadini, R., 2011 (submitted). Squeezing more information out of Time Variable Gravity data: a global screening tool and a validation test for global hydrology models.

[5] Bassin, C., G. Laske, and G. Masters, 2000. The current limits of resolution for surface wave tomography in North America, *EOS Trans. AGU*, *81*, S12A03.

[6] Baur, O., Kuhn, M. and Featherstone, E., 2009. GRACE–derived ice–mass variations over Greenland by accounting for leakage effects, *J. geophys. Res.*, **114**, B06407.

[7] Becker, T. W. and L. Boschi, 2002. A comparison of tomographic and geodynamic mantle models, *Geochem. Geophys. Geosyst.*, **3**, 1003.

[8] Ben–Menahem, A., and Singh, S. J., 1981. *Seismic Waves and Sources*, Springer–Verlag, New York, Heidelberg, Berlin.

[9] Besse, J. and Courtillot, V., 1991. Revised and synthetic apparent polar wander paths of the African, Eurasian, North American, and Indian Plates, and true polar wander since 200 Ma', *J. Geophys. Res.*, **96**, 4029–4050.

[10] Besse, J. and Courtillot, V., 2002. Apparent and true polar wander and the geometry of the geomagnetic field over the last 200 Myr, *J. geophys. Res.*, **107**, 2300.

[11] Birch, F., 1952. Elasticity and constitution of the earth's interior, *J. Geophys. Res.*, **57**, 227–286.

[12] Birch, F., 1964. Density and composition of mantle and core, *J. Geophys. Res.*, **69**, 4377–4388.

[13] Broerse, D. B. T., L. L. A. Vermeersen, R. E. M. Riva, and W. van der Wal, 2011. Ocean contribution to co–seismic crustal deformation and geoid anomalies: Application to the 2004 December 26 Sumatran–Andaman earthquake, *Earth Planet. Sci. Lett.*, **305**, 341–349.

[14] Cambiotti, G., Barletta, V. R., Bordoni, A. and Sabadini, R., 2009. A comparative analysis of the solutions for a Maxwell Earth: the role of the advection and buoyancy force, *Geophys. J. Int.*, **176**, 995–1006.

[15] Cambiotti, G. and Sabadini, R., 2010. The compressional and compositional stratifications in Maxwell Earth models: the gravitational overturning and the long period tangential flux, *Geophys. J. Int.*, **180**, 475–500.

[16] Cambiotti, G., Ricard, Y. and Sabadini, R., 2010. Ice age True Polar Wander in a compressible and non–hydrostatic Earth, *Geophys. J. Int.*, **183**, 1248–1264.

[17] Cambiotti, G., A. Bordoni, R. Sabadini, and L. Colli, 2011a. GRACE gravity data help constraining seismic models of the 2004 Sumatran earthquake, *J. geophys. Res.*, **116**, B10403.

[18] Cambiotti, G., Y. Ricard and R. Sabadini, 2011b. New insights into Mantle Convection True Polar Wander and rotational bulge readjustment, *Earth Planet. Sciences Lett.*, **310**, 538–543.

[19] Chambat, F. and Valette, B., 2001. Mean radius, mass, and inertia for reference Earth models, *Phys. Earth Planet. Inter.*, **124**, 237–253.

[20] Chambat, F., Ricard, Y. and Vallette, B., 2010. Flattening of the Earth: further from hydrostaticity than previously estimated, *Geophys. J. Int.*, **183**, 727–732.

[21] Chambers, D. P., 2006. Evaluation of new GRACE time–variable gravity data over the ocean, *Geophys. Res. Lett.*, **33**, L17603.

[22] Chinnery, M. A., 1975. The static deformation of an earth with a fluid core: a physical approach, *Geophys. J. R. astr. Soc.*, **42**, 461–475.

[23] Chlieh, M., Avouac, J. P., Hjorleifsdottir, V. *et al.*, 2007. Coseismic slip and afterslip of the Great M_w 9.15 Sumatra–Adaman earthquake of 2004, *BSSA*, **97**, S152Ű-S173.

[24] de Linage, C., Rivera, L., Hinderer, J., Boy, J. P., Rogister, Y., Lambotte, S. and Biancale, R., 2009. Separation of coseismic and postseismic gravity changes for the 2004 Sumatran earthquake from 4.6 yr of GRACE observations and modelling of the coseismic change by normal mode summation, *Geophys. J. Int.*, **176**, 695–714.

[25] Denis, C., 1989. The hydrostatic figure of the Earth, in *Gravity and Low Frequency Geodynamics* (chap. 3), *Physics and Evolution of the Earth's Interior*, vol. 4, ed. R. Teisseyre, Elsevier, Amsterdam.

[26] Denis, C., Almavict, M., Rogister, Y., and Tomecka–Suchon, S., 1998. Methods for computing internal flattening, with applications to the EarthŠs structure and geodynamics, *Geophys. J. Int.*, **132**, 603–642.

[27] Dziewonski, A. M. and Anderson, D. L., 1981. Preliminary reference earth model, *Phys. Earth Planet. Inter.*, **25**, 297–356.

[28] Dziewonski, A. M., Chou, T. A. and Woodhoouse, J. H., 1981. Determination of earthquake source parameters from waveform data for studies of global and regional seismicity, *J. geophys. Res.*, **21**, 2825–2852.

[29] Ekström, G., Dziewonski, A. M., Maternovskaya, N. N. and Nettles, M., 2003, Global seismicity of 2001, centroid–moment tensor solutions for 961 earhquakes, *Phys. Earth Planet. Inter.*, **136**, 165–185.

[30] Fang, M. and Hager, B. H., 1995. The singularity mystery associated with a radially continuous Maxwell viscoelastic structure, *Geophys. J. Int.*, **123**, 849–865.

[31] Farrell, W. E., 1972. Deformation of the Earth by Surface Loads, *Rev. Geophys.*, **10**, 761–797.

[32] Farrell, W. E. and Clark, J. A., 1976. On Postglacial Sea Level, *Geophys. J. R. astr. Soc.*, **46**, 647–667.

[33] Gilbert, F. and Backus, G., 1968. Elastic–gravitational vibrations of a radially stratified sphere, in *Dynamics of Stratified Solids*, pp. 82–95, ed. Herrmann, G., American Society of Mechanical Engineers, New York.

[34] Gilbert, F., and A. M. Dziewonski, 1975. An application of normal mode theory to retrieval of structural parameters and source mechanisms from seismic spectra, *Phil. Trans. R. Soc. Lond. A*, **278**, 187–269.

[35] Gross, R.S., and B. F. Chao, 2001. The gravitational signature of earthquakes, in *Gravity, Geoid, and Geodynamics 2000*, **123**, pp. 205-Ű210, eds. Sideris, M.G., IAG Symposia, 384 Springer–Verlag, New York.

[36] Gross, R. S. and Chao, B. F., 2006. The rotational and gravitational signature of the December 26, 2004 Sumatran earthquake, *Surv. Geophys.*, **27**, 615–632.

[37] Han, D. and Wahr, J., 1995. The viscoelastic relaxation of a realistically stratified earth, and a further analysis of postglacial rebound, *Geophys. J. Int.*, **120**, 278–311.

[38] Han, S. C., Shum, C. K., Bevis, M., Ji, C. and Kuo, C. Y., 2006. Crustal dilatation observed by GRACE after the 2004 Sumatran–Andaman eartquake, *Science*, **313**, 658–662.

[39] Han, S. C., C. K. Shum, M. Bevis, C. Ji, and C. Y. Kuo, 2010. Regional gravity decrease after the 2010 Maule (Chile) earthquake indicates large–scale mass redistribution, *Geophys. Res. Lett.*, **37**, LL23307.

[40] Hanyk, L., Matyska, C. and Yuen, D. A., 1999. Secular gravitational instability of a compressible viscoelastic sphere, *Geophys. Res. Lett.*, **26**, 557–560.

[41] Heki, K. and K. Matsuo, 2010. Coseismic gravity changes of the 2010 earthquake in central Chile from satellite gravimetry, *Geophys. Res. Lett.*, **37**, L24306.

[42] Jeffreys, M., 1952. *The Earth*, Cambridge Univ. Press, Cambridge.

[43] Jurdy, D.M., 1978. An alternative model for early Tertiary absolute plate motions, *Geology*, **6**, 469–472.

[44] Kanamori, H., 1971. Seismological evidence for a lithospheric normal faulting – the Sanriku earthquake of 1933, *Phys. Earth Planet. Interiors*, **4**, 289–300.

[45] Kanamori, H. (1973) Mode of Strain Release Associated with Major Earthquakes in Japan, *Annual Review of Earth and Planetary Sciences*, **1**, 213–239.

[46] Klemann, V., Wu, P., and Wolf, D., 2003. Compressible viscoelasticity: stability of solutions for homogeneous plane–earth models, *Geophys. J. Int.*, **153**, 569–585.

[47] Klemann, V., Ivins, E. R., Martinec, Z. and Wolf, D., 2007. Models of active glacial isostasy roofing warm subduction: Case of the South Patagonian Ice Field, *J. geophys. Res.*, **112**, B09405.

[48] Kusche, J., 2007. Approximate decorrelation and non–isotropic smoothing of the time–variable GRACE–type gravity field models, *J. Geod.*, **81**, 733–749.

[49] Kusche, J., R. Schmidt, S. Petrovic, and R. Rietbroek, 2009. Decorrelated GRACE time–variable gravity solutions by GFZ, and their validation using a Hydrological Model, *J. Geod.*, **83**, 903–913.

[50] Lay, T., C. J. Ammon, H. Kanamori, L. Xue, and M. J. Kim, 2011a. Possible large near–trench slip during the great 2011 Tohoku ($M_W = 9.0$) earthquake, *Earth Planets Space*, **63**.

[51] Lay, T., Y. Yamazaki, C. J. Ammon, K. F. Cheung, and H. Kanamori, 2011b. The great 2011 off the Pacific coast of Tohoku ($M_W\,9.0$) Earthquake: Comparison of deep–water tsunami signals with finite–fault rupture model predictions, *Earth Planets Space*, **63**.

[52] Lithgow–Bertelloni, C., Richards, M.A., Ricard, Y., O'Connell, R. and Engebreston, D.C., 1993. Torodial–Poloidal partitioning of plate motions since 120 MA, *Geophys. Res. Lett.*, **20**, 375–378.

[53] Longman, I. M., 1962. A Green's function for determining the deformation of the earth under surface mass loads 1. Theory, *J. Geophys. Res.*, **67**, 845–850.

[54] Longman, I. M., 1963. A Green's Function for Determining the Deformation of the Earth under Surface Mass Loads 2. Computations and numerical results, *J. geophys. Res.*, **68**, 485–496.

[55] Love, A. E. H., 1911. *Some Problems of Geodynamics*, Dover reprint, New York, 1967, pg. 180.

[56] Mansinha, L., Smylie, D. E. and Chapman, C. H., 1979. Seismic excitation of the Chandler wobble revisited, *Geophys. J. R. astr. Soc.*, **59**, 1–17.

[57] Martinec, Z., Thoma, M., and Wolf, D., 2001. Material versus local incompressibility and its influence on glacial–isostatic adjustment, *Geophys. J. Int.*, **144**, 136–156.

[58] Matsuo, K., and K. Heki, 2011. Coseismic gravity changes of the 2011 Tohoku–Oki earthquake from satellite gravimetry, *Geophys. Res. Lett.*, *38*, L00G12.

[59] McCarthy, D.D. and Luzum, J.B., 1996. Path of the mean rotational pole from 1899 to 1994, *Geophys. J. Int.*, **125**, 623–629.

[60] Melini, D., Spada, G. and Piersanti, A., 2010. A sea level equation for seismic perturbations, *Geophys. J. Int.*, **180**, 88–100.

[61] Mikhailov, V., Tikhotsky, S., Diament, M., Panet, I. and Ballu, V., 2004. Can tectonic processes be recovered from new gravity satellite data?, *Earth planet. Sci. Lett.*, **228**, 281–297.

[62] Mitrovica, J. X. and Milne, G. A., 1998. Glacial–induced perturbations in the Earth's rotation: a new appraisal, *J. Geophys. Res.*, **103**, 985–1005.

[63] Mitrovica, J. X., Wahr, J., Matsutyama, I. and Paulson, A., 2005. The rotational stability of an ice–age earth, *Geophys. J. Int.*, **161**, 491–506.

[64] Mosengard, K., and Tarantola, A., 2002. Probabilistic Approach to Inverse Problems in *International Handbook of Earthquake & Engineering Seismology (Part A)*, Academic Press, pp. 237Ű-265.

[65] Munk, W. H. and MacDonald, G. J. F., 1960. *The rotation of the Earth: a geophysical discussion*, Cambridge University Press, London, New York, Melbourne.

[66] Nakada, M., 2002. Polar wander caused by the Quaternary glacial cycles and fluid Love number, *Earth and planetary science letters*, **200**, 159–166.

[67] Nakiboglu, S.M., 1982. Hydrostatic theory of the Earth and its mechanical applications, *Phys. Earth planet. Int.*, **28**, 302Ű-311.

[68] Okubo, S., 1992. Gravity and Potential Changes due to Shear and Tensile Faults in a Half–Space, *J. geophys. Res.*, **97**, 7137–7144.

[69] Otha, K., 2010. *Electrical and thermal conductivity of the Earth's lower mantle*, PhD. Thesis, Tokyo Institute of Technology.

[70] Pekeris, C. L. and Accad, Y., 1972. Dynamics of the liquid core of the earth, *Philos. Trans. Roy. Soc. Lond., Ser. A*, **273**, 237–260.

[71] Peltier, W. R., 1974. The Impulse Response of a Maxwell Earth, *Rev. Geophys. Space Phys.*, **12**, 649–669.

[72] Plag, H.–P. and Jüttner, H. –U., 1995. Rayleigh–Taylor instabilities of a self–gravitating Earth, *J. Geodynamics*, **20**, 267–288.

[73] Pollitz, F.F., Burgmann, R. and Banerjee, P., 2006. Post–seismic relaxation following the great 2004 Sumantran–Andaman earthquake on a compressible self–gravitating Earth, *Geophys. J. Int.*, **167**, 397–420.

[74] Ray, R. D. and Luthcke, S. B., 2006. Tide model errors and GRACE gravimetry: towards a more realistic assessment, *Geophys. J. Int.*, **167**, 1055–1059.

[75] Ricard, Y. and Sabadini, R., 1990. Rotational instabilities of the Earth induced by mantle density anomalies, *Geophys. Res. Lett.*, **17**, 627–630.

[76] Ricard, Y., Spada, G. and Sabadini, R., 1993a. Polar wandering of a dynamic Earth, *Geophys. J. Int.*, **113**, 284–298.

[77] Ricard, Y., Richards, M.A., Lithgow–Berteloni, C. and Le Stunff, Y., 1993b. A geodynamic model of mantle mass heterogeneities, *J. geophys. Res.*, **98**, 21.895–21.909.

[78] Richards, M., Bunge, H.P., Ricard, Y. and Baumgardner, J. R., 1999. Polar wandering and inertial interchange events in mantle convection models, *J. Geophys. Lett.*, **26**, 1777–1780.

[79] Richards, M.A., Y. Ricard, Lithgow–Bertelloni, C., Spada, G. and Sabadini, R., 1997. An Explanation for EarthŠs Long–Term Rotational Stability, *Science*, **275**, 372–375.

[80] Richards, M.A., Bunge, H.–P., Ricard, Y. and Baumgardner, J.R., 1999. Polar wandering in mantle convection models, *Geophys. Res. Lett.*, **26**, 1777–1780.

[81] Rouby, H., Greff–Lefftz, M. and Besse, J., 2010. Mantle dynamics, geoid, inertia and TPW since 120 Myr, *Earth Planet. Sci. Lett.*, **292**, 301–311.

[82] Sabadini, R. and Peltier, W.R., 1981. Pleistocene deglaciation and the EarthŠs rotation: implication for mantle viscosity, *Geophys. J. R. astr. Soc.*, **66**, 553–578.

[83] Sabadini, R., Yuen, D. A. and Boschi, E., 1982. Polar wandering and the forced responses of a rotating, multilayered, viscoelastic planet, *Geophys. J. Int.*, **87**, 2885–2903.

[84] Sabadini, R. and Vermeersen, L. L. A., 2004. *Global Dynamics of the Earth: Applications of Normal Mode Relaxation Theory to Solid–Earth Geophysics*, 1st edn, Kluwer Academic Publisher, Dordrecht, Boston, London.

[85] Sabadini, R., Dalla Via, G., Hoogland, M. and Aoudia, A., 2005. A Splash in Earth Gravity from the 2004 Sumatra Earthquake, *Eos Trans. AGU*, **86**.

[86] Sabadini, R., Riva, R. E M. and Dalla Via, G., 2008. Coseismic rotation changes from the 2004 Sumatran earthquake: the effects of Earth's compressibility versus earthquake induced topography, *Geophys. J. Int.*, **171**, 231–243.

[87] Schaber, K., Bunge, H. P., Schubert, B. S. A., Malservisi, R. and Horbach, A., 2009. Stability of the rotation axis in high–resolution mantle circulation models:

Weak polar wander despite strong core heating, *Geochem. Geophys. Geosyst.*, **10**, Q11W04.

[88] Simons, F. J., F. A. Dahlen, and M. A. Wieczorek, 2006. Spatiospectral Concentration on a Sphere, *SIAM Review*, **48**, 504–536.

[89] Smylie, D. E. and Manshina, L., 1971. The Elastic Theory of Dislocations in Real Earth Models and Changes in the Rotation of the Earth, *Geophys. J. R. astr. Soc.*, **23**, 329–354.

[90] Spada, G., Sabadini, R., Yuen, D. A. and Ricard, Y., 1992a. Effects on postglacial rebound from the hard rheology in the transition zone, *Geophys. J. Int.*, **109**, 683–700.

[91] Spada, G., Ricard, Y. and Sabadini, R., 1992b. Excitation of True Polar Wander by subduction, *Nature*, **360**, 452–454.

[92] Steffen H., Petrovic, S., Mueller, J., Schmidt, R., Wuensh, J., Barthelmes, F. and Kusche, J., 2009. Significance of secular trends of mass variations determined from GRACE solutions, *J. Geod.*, **48**, 157–165.

[93] Steinberger, B. and O'Connell, J., 1997. Changes of the Earth's rotation axis owing to advection of mantle density heterogeneities, *Nature*, **387**, 169–173.

[94] Steinberger, B. and Torsvik, T. H., 2010. Toward an explanation for the present and past locations of the poles, *Geochem. Geophys. Geosyst.*, **11**, Q06W06.

[95] Sun, W. K., and S. H. Okubo, 1993. Surface–potential and gravity changes due to internal dislocations in a spherical earth – 1. Theory for a point dislocation, *Geophys. J. Int.*, **114**, 569–592.

[96] Takahaski, N., S. Kodaira, T. Tsuru, J.–O. Park, Y. Kaneda, K. Suyehiro, H. Kinoshita, S. Abe, M. Nishino, and R. Hino, 2004. Seismic structure and seismogenesis off Sanriku region, northeastern Japan, *Geophys. J. Int.*, *159*, 129Ű145.

[97] Takeuchi, H. and Saito, M., 1972. Seismic surface waves, *Meth. comput. Phys.*, **11**, 217–295.

[98] Tanaka, Y., Okuno, J. and Okubo, S., 2006. A new method for the computation of global viscoelastic post–seismic deformation in a realistic Earth model (I) – vertical displacement and gravity variation, *Geophys. J. Int.*, **164**, 273–289.

[99] Tarantola, A., 2005. *Inverse Problem Theory and Methods for Model Parameter Estimation*, Society for Industrial and Applied Mathematics, Philadelphia, Pennsylvania.

[100] Torsvik, T. H., Smethurst, M. A., Borke, K. and Steinberger, B., 2006. Large igneous provinces generated from the margins of the large low–velocity provinces in the deep mantle, *Geophysis. J. International*, **167**, 1447–1460.

[101] Tsai, V. C., Nettles, M., Ekström, G. and Dziewonsi, A. M., 2005. Multiple CMT source analysis of the 2004 Sumatran earthquake, *Geophys. Res. Lett.*, **32**, L17304.

[102] van der Meer, D. G., Spakman, W., van Hinsbergen, D. J. J., Amaru, M. L., and Torsvik, T. H., 2010. Towards absolute plate motions constrained by lower–mantle slab remnants, *Nature Geoscience*, **3**, 36–40.

[103] Van Hoolst, T., Rambaux, N., Karatekin, O., Dehant, V. and Rivoldini, A., 2008. The libration, shape, and icy shell of Europa, *Icarus*, **195**, 286–399.

[104] Vermeersen, L. L. A., Sabadini, R. and Spada, G., 1996. Compressible rotational deformation, *Geophys. J. Int.*, **129**, 735–761.

[105] Vermeersen, L. L. A. and Sabadini, R., 1997a. A new class of stratified viscoelastic models by analytical techniques, *Geophys. J. Int.*, **129**, 531–570.

[106] Vermeersen, L. L. A., Fournier, A. and Sabadini, R., 1997b. Changes in rotation induced by Pleistocene ice masses with stratified analytical Earth models, *J. Geophys. Res.*, **102**, 27689–27702.

[107] Vermeersen, L. L. A. and Sabadini, R., 1999. Polar Wander, sea–level variations and Ice Age cycles, *Surv. Geophys.*, **20**, 415–440.

[108] Vermeersen, L. L. A. and Mitrovica, J. X., 2000. Gravitational stability of spherical self–gravitating relaxation models, *Geophys. J. Int.*, **142**, 351–360.

[109] Zhou X., Sun, W., Zhao, B., Fu, G., Dong, J. and Nie, Z., 2011 (submitted). Geodetic observations detected co–seismic displacements and gravity changes caused by the Tohoku–Oki earthquake (Mw=9.0).

[110] Wahr, J., Molenaar, M. and Bryan, F., 1998. Time variability of the Earth's gravity field: hydrological and oceanic effects and their possible detection using GRACE, *J. geophys. Res.*, **108**, 30205–30229.

[111] Werth, S., Güntner, A., Schmidt, R. and Kusche, J., 2009. Evaluation of GRACE filter tools from a hydrological perspective, *Geophys. J. Int.*, **179**, 1499–1515.

[112] Wolf, D., 1991. Viscoelastodynamics of a stratified, compressible planet: incremental field equations and short– and long–time asymptotes, *Geophys. J. Int.* (1991) **104**, 401–417.

[113] Wolf, D. and Kaufmann, G., 2000. Effects due to compressional and compositional density stratification on load–induced Maxwell–viscoelastic perturbations, *Geophys. J. Int.*, **140**, 51–62.

[114] Wolf, D. and Li, G., 2002. Compressible viscoelastic earth models based on Darwin's law, in *Glacial Isostatic Adjustment and the Earth System: Sea–Level, Crustal Deformation, Gravity and Rotation*, edited by J. X. Mitrovica and L. L. A. Vermeersen, pp. 275–292, American Geophysical Union, Washington, D. C.

[115] Wu, P. and Peltier, W. R., 1982. Viscous gravitational relaxation, *Geophys. J. R. astr. Soc.*, **70**, 435–485.

[116] Wu, P. and Peltier, W. R., 1984. Pleistocene deglaciation and the Earth's rotation: a new analysis, *Geophys. J. R. astr. Soc.*, **76**, 753–791.